Summer 7-15-2019

Studying The Properties Of SF6 Gas Mixtures For Directional Dark Matter Detection

Randy J. Lafler
University of New Mexico - Main Campus

Randy Lafler

Candidate

Physics And Astronomy

Department

This thesis is approved, and it is acceptable in quality and form for publication:

Approved by the Thesis Committee:

Dinesh Loomba , Chairperson

Michael Gold

Paul Schwoebel

Keith Rielage

Studying The Properties Of SF_6 Gas Mixtures For Directional Dark Matter Detection

by

Randy Lafler

M.S., Physics, University of New Mexico, 2014

B.S. Physics, University of New Mexico, 2012

DISSERTATION

Submitted in Partial Fulfillment of the

Requirements for the Degree of

Doctor of Philosophy

Physics

The University of New Mexico

Albuquerque, New Mexico

July, 2019

Dedication

To my bride for encouraging me, believing I could finish, and loving me despite my stress. You are my cuteness.

Acknowledgments

I would like to thank my advisor, Professor Dinesh Loomba, for his support, direction, honest opinions, and for keeping me on track. I would like to thank Eric Lee, who designed many of the gadgets and detectors I used in this thesis. We will miss you. I would like to thank PhD. Nguyen Phan for his advice with data analysis, experimental techniques, and his development of the Tilted GEM. Thank you Alex Mills for designing cool contraptions for us and for having creative insights.

Studying The Properties Of SF_6 Gas Mixtures For Directional Dark Matter Detection

by

Randy Lafler

M.S., Physics, University of New Mexico, 2014
B.S. Physics, University of New Mexico, 2012

Phd., Physics, University of New Mexico, 2019

Abstract

Although dark matter comprises approximately 85% of the matter content of the universe, direct detection of dark matter remains elusive. As the available parameter space for dark matter candidates is pushed to lower and lower limits, the demand for larger, more sensitive detectors continues to grow. Although upscaling the detector improves the sensitivity, it greatly increases the cost and complexity of the experiment. Even after a dark matter signal is detected, there remains the possibility that an unknown background mimics the dark matter signal. Consequently, verifying the dark matter origin of a detection signal is an issue for any dark matter experiment. The solution is to search for the so-called "smoking gun" signatures for dark matter. There is the annual modulation of the event rate, and the modulation of the recoil direction over a sidereal day. The directional modulation is the more robust signal. It would not only unambiguously confirm the existence of dark matter, but pave the way for characterizing the properties of dark matter.

This thesis describes research toward advancing low pressure gas Time Projection Chamber (TPC) technology for directional dark matter detection. It begins by measuring the thermal negative ion behavior of the novel TPC gas, SF_6, and thereby confirming SF_6 as an ideal gas for directional dark matter experiments. The disadvantage of SF_6 is the low fiducialization efficiency due to the relatively small secondary drift species, SF_5^-. This motivated studies of CF_4-SF_6 gas mixtures that led to the discovery of a new negative ion species hypothesized to be CF_3^-. We show that the relative production of the new species can be tuned by adjusting the SF_6 concentration and the drift field. We also propose a model for CF_3^- production in CF_4-SF_6 gas mixtures that makes qualitative predictions, which are consistent with our measurements. Our studies show that a 20-3 CF_4-SF_6 mixture results in low thermal diffusion and a factor two enhancement of the fiducialization efficiency relative to that measured for pure SF_6. Using this mixture our measurements demonstrate gamma/electron discrimination down to 15 $keVee$ and head-tail directionality down to 30 $keVee$. These are the first such measurements in TPCs with SF_6-based gases, and the first utilizing a 1D readout in any gas.

Contents

List of Figures

List of Tables

Glossary

Discrimination The ability to identify the interacting particle.

Directionality The ability to measure the recoil direction.

Fiducialization The ability to location where the event occurred within the detector.

"$Cathode - side$" DD neutron generator oriented on by the cathode.

"$GEM - side$ DD neutron generator oriented on the GEM-side (anode-side) of the detector.

DM Abbreviation for dark matter

NITPC Abbreviation for Negative Ion Time Projection Chamber

Chapter 1

Introduction

1.1 What is Dark Matter?

What is Dark Matter? This is one of the biggest questions in modern physics today. It is known to constitute 25% of the energy density and 84% of the total mass of the universe, and yet it is far from understood. What is known is the non-luminous nature of dark matter and its gravitational interaction with ordinary matter. While its gravitational influence on ordinary matter has been seen on cosmological scales, the interaction or the production of dark matter within a detector has not been observed. This chapter will briefly describe the evidence for dark matter, giving a brief history in the process. It will also describe the most popular dark matter candidates, direct detection techniques, and the directional dark matter experiment DRIFT (Directional Recoil Identification From Tracks). The studies detailed in the chapters that follow are motivated with the goal to improve the sensitivity of the DRIFT detector and to characterize the properties of the low energy events expected within the range of dark matter interactions.

1.2 Evidence For Dark Matter

1.2.1 First Evidences

The first hints for the presence of dark matter came in the form of missing matter. In the 1930s, Oort measured the velocities of stars in the Milky Way using their Doppler shifts and discovered, based on the gravitational attraction of the visible matter, the stars should escape their orbits. Since this was not the case, Oort proposed that there must be more mass within the Milky Way to provide the needed gravitational attraction to maintain the orbits [2]. Zwicky later studied the Coma cluster and, by employing the virial theorem, also determined there must be additional non-visible matter in the system [3]. These measurements were not taken seriously until 40 years later, when Vera Rubin and collaborators studied the rotation curves of isolated galaxies [4]. Based on the Newtonian gravity of the visible matter, the orbital velocity of stars about their galactic center should obey

$$v(r) = \sqrt{\frac{Gm(r)}{r}}. \tag{1.1}$$

Equation 1.1 predicts once a star is beyond the visible disk of the galaxy $m(r)$ is a constant and the orbital velocity falls as the inverse square root of r. However, this was not observed. Instead, the velocity curves were "flat" for orbital distances greater than the visible central bulge of the galaxy. This behavior is depicted in Figure 1.1. There are two common resolutions to this problem. One solution is to suppose the galaxy is immersed in a nearly spherical halo of non-luminous matter with a density profile proportional to $1/r$. This solution implies the mass within the orbit continues to increase at a rate proportional to the radius as the orbital distance increases . Therefore, the ratio $m(r)/r$ is constant and so is the orbital velocity. This non-luminous matter is called dark matter.

The other solution is to propose modifications to the force of gravity which are apparent only on large scales. This is called Modified Newtonian Dynamics (MOND) [6]. Although the theory can predict "flat" rotation curves, there are two main issues with the theory compared to dark matter theories. One issue is MOND is unmotivated by other theories, whereas many extensions to the Standard Model (such as Supersymmetry) naturally have a dark matter-like particle. Another issue is MOND cannot explain the Bullet Cluster, the Cosmic Microwave Background (CMB), or other similar measurements. How the Bullet Cluster and the CMB pertain to dark matter will be discussed next.

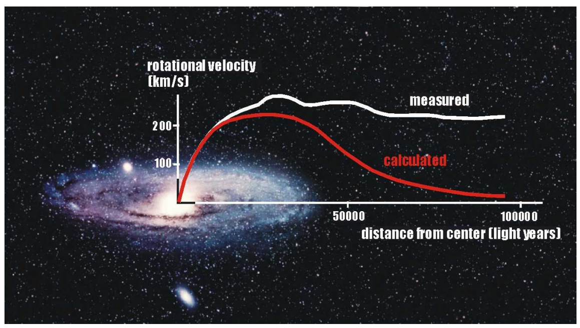

Figure 1.1: The predicted orbital velocity of stars about their galactic center (red) and the observed orbital velocities (white). Credit: Ref. [5].

1.2.2 Bullet Cluster

The Bullet Cluster is the name given to the collision of the two galaxy clusters shown in Figure 1.2 [7]. During the collision the intergalactic gases of the two clusters interact, are heated, emit X-rays (pink), and are slowed. The intergalactic gases are the dominant ordinary matter component of galaxies. The star component of each cluster is neutral and point-like compared to the size of the clusters, which results in each star component passing unhindered through the other. The net result is the spacial separation between the intergalactic gas and star components. Next consider gravitational lensing. Measurement of the gravitational lensing (blue) should trace the dominant matter component. Therefore, without dark matter the gravitational lensing should be coincident with the x-ray emission from the intergalactic gas. Instead, the gravitational lensing is coincident with the star component. This is strong evidence for a hidden matter component to the system that also was not slowed during the collision. If the clusters are immersed in a halo of dark matter before the collision and the dark matter has no self-interactions, the dark matter would not be slowed by the collision and could constitute the hidden matter. These measurements cannot be explained by MOND. Also, the Bullet Cluster reveals an important property of dark matter; the dark matter must have negligible self-interaction.

Figure 1.2: The Bullet Cluster showing the X-ray emission (pink) and the gravitational lensing (blue). Credit: Ref. [8].

1.2.3 Cosmic Microwave Background

The Cosmic Microwave Background (CMB) provides precise measurements of cosmological parameters, and it measures the dark matter abundance when constrained by other measurements. To begin understanding the CBM, one must consider the dynamics of the hot dense photon-baryon plasma of the early universe. A brief overview of the dynamics and how they relate to dark matter will be provided next.

The dynamics of an over dense region of space in the early universe are depicted in Figure 1.3 [9]. Waynehu models the dynamics with massive balls on springs in a potential well. The over density of the plasma (potential well) causes electrons and protons (massive balls) to fall into the gravitational potential wells. Through repeated Compton scattering with the electrons the photons (springs) are also drawn into the well. This infall of matter continues until the photon pressure is large enough that it overcomes the force of gravity (the springs are maximally stretched). At this point the plasma (mass) begins to be forced out of the well. This is called rarefaction. The rarefaction continues until the force of gravity (spring at the bottom of the well) overcomes the photon pressure and the cycle repeats. The resulting oscillations are called "acoustic oscillations", because the period of oscillation depends on the speed of sound within the plasma. In this context the speed of sound defines the rate a signal is transferred in the medium. However, if dark matter is included in the model the dynamics change considerably. Since dark matter does not interact with the photons it does not feel the photon pressure and is not rarefied. Therefore, dark matter continues to fall into the well regardless of the cycle and enhances the depth of the well. Including each component, the final model for the dynamics is that of a forced, damped harmonic oscillator.

The acoustic oscillations continue as the universe expands until the universe is cool enough for electrons to bind to protons to form neutral atoms. At this epoch in time, called Recombination, the photons become decoupled from the plasma, freestream, and redshift. This relic radiation is present today as a low temperature background radiation. Information about the size of the over dense regions is imprinted in the CMB at the time of Recombination. Regions where the plasma was maximally compacted or rarefied are imprinted into the CMB as slightly hotter or colder spots in the sky. The greater the over density the greater the temperature fluctuation in the CMB. Consequently, the CMB is sensitive to each matter component of the universe, including dark matter.

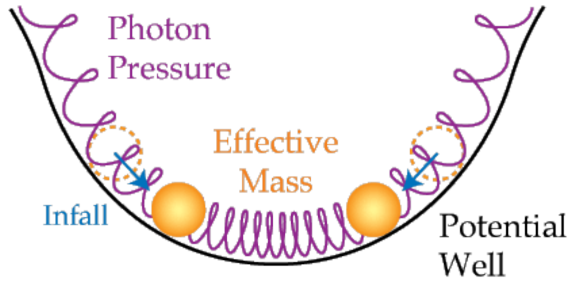

Figure 1.3: Graphical depiction of gravitational infall competing against radiation pressure. The cycle that ensues is called "acoustic oscillations." Credit: Ref. [9].

The CMB was first discovered by Penzias and Wilson in 1964 and measured to have the nearly uniform temperature of 2.73 K [10]. Later, the WMAP experiment measured the temperature fluctuations of the CMB to be 1 part in 10^5. A related evidence for dark matter comes from the measured angular size of the temperature fluctuations combined large scale structure measurements. Simply put, the size of the density fluctuations at the time of Recombination under the influence of ordinary matter alone would not have had the time during the age of the universe to grow and form the structure we observe today. Dark matter is needed to efficiently grow the density fluctuations. Figure 1.4a shows the temperature fluctuations, also called anisotropies, in the WMAP 9 year all sky map. Figure 1.4b shows the power spectrum of the fluctuations. It is from the power spectrum that quantities such as the total, baryonic, and dark matter densities can be calculated to high precision; $\Omega_m h^2 = 0.1334 \pm 0.0055$, $\Omega_b h^2 = 0.02260 \pm 0.00053$, $\Omega_{dm} h^2 = 0.1123 \pm 0.0035$ [11].

1.2.4 Other Evidence

Another cosmological evidence for dark matter is found in Big Bang Nucleosynthesis (BBN) [13]. BBN describes the period from a few seconds to several minutes after the Big Bang when the universe was very hot and protons and neutrons were fus-

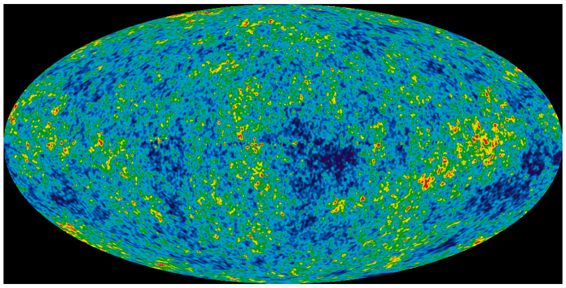

(a) 9 Year WMAP all sky map of the Cosmic Microwave Background Anisotropies. Credit: Ref. [12].

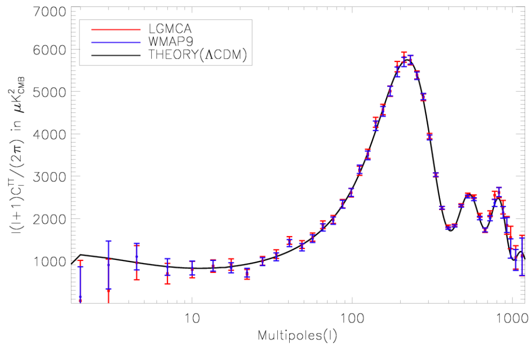

(b) 9 Year WMAP Cosmic Microwave Background power spectrum. Credit: Ref. [11].

Figure 1.4: The Cosmic Microwave Background temperature anisotropies (1.4a) and power spectrum (1.4b).

ing together to form light elements like deuterium and helium. By employing nuclear physics and reaction rates, BBN predicts the abundances of these light elements. The predictions of BBN match well with measurements of elemental abundances. For example, the deuterium in stars is rapidly converted into ^4He, and therefore the amount of deuterium in the universe today is a lower limit on the amount created during BBN. The deuterium abundance is estimated by observing regions of space with low levels of elements heavier than lithium. These regions of space are assumed to not have changed significantly since the Big Bang, so the measured ratio of deuterium to hydrogen (D/H abundance) can be estimated right after BBN. The D/H abundance is heavily dependent on the baryon density during BBN. Therefore, measuring D/H is a measure of the overall baryon abundance. Measurements of D/H reveal that the baryon density only accounts for about 20% of the total matter density of the universe, further supporting the existence for dark matter.

Other evidences for dark matter are large scale structure observations such as galaxy counts, and N Body simulations [14]. These also require a dark matter-like particle to produce the small scale structure that is observed in the universe. They indicate dark matter must be moving non-relativistically and be Cold Dark Matter (CDM). In fact, the ΛCDM cosmological model has been highly successful in predicting the structure of the universe on large scales. However, it fails on small scales. CDM, which assumes dark matter has no self-interactions, tends to produce too much small scale structure. This is the so called "small scale structure crisis" of the ΛCDM model [15].

1.3 What can Dark Matter be?

This section discusses several theoretical motivations for a new fundamental dark matter-like particle and a few of the most popular dark matter candidates. First consider known particles within the Standard Model. The only particle with weak interactions and no electromagnetic interactions is the neutrino. However, neutrinos are relativistic. A neutrino dominated universe would suppress structure formation and create a "top-down" (large-scale structures first) formation of the universe. This is not the case. The "bottom-up" formation of the universe is more consistent with observations and simulations [16]. Another strike against the neutrino is constraints on the mass of the neutrino. With the constraints on the neutrino mass the number density of the neutrino is much lower than the measured dark matter density.

What about composite Standard Model candidates such as Massive Compact Halo Objects (MACHOs)? MACHOs are massive objects, such as black holes or neutron stars, that do not emit radiation and are therefore "ordinary" dark matter. These objects can be found with gravitational microlensing, which occurs when the MACHO passes between a distant star and the earth. When this happens there is a characteristic brightening and dimming of the star. The MACHO Collaboration and the EROS-2 Survey have searched for these objects [17]. They found only a small number of candidate MACHOs, much too few to constitute a significant component of dark matter. For these reasons, the search is shifted toward a yet undiscovered non-baryonic dark matter particle.

Due to the lack of constraints on non-barionic dark matter, there are many theories, some with more theoretical motivation than others. Figure 1.5 shows the wide variety of dark matter candidates. The most popular candidates include the Weakly Interacting Massive Particles (WIMPs), Axion, Sterile Neutrino, and Kaluza-Klein particles. Also gaining popularity are dark sector dark matter theories, such as Asymmetric Dark Matter and Dark Photon theories which incorporate small dark matter self-interactions. More exotic forms of dark matter have also been proposed, such as WIMPzillas, GIMPs, Q-balls. The WIMPs, Kaluza-Klein, Axion, Dark Sector, and Sterile Neutrino theories will be discussed next. For a review of dark matter candidates see Ref. [19].

1.3.1 WIMP DM

The most popular and highly searched for dark matter candidate over the past several decades is the WIMP [26]. WIMP dark matter is electrically neutral, interacts very weakly with ordinary matter, and is CDM. As such, it naturally provides the necessary "bottom up" formation of large scale structure. Initially, WIMPs were very attractive candidates because of the so-called "WIMP Miracle". If WIMPs have a weak-scale mass and were created in thermal equilibrium during the early universe, they would "miraculously" produce the measured relic abundance of dark matter. WIMPs are also attractive because they can be applied with Supersymmetric theories (SUSY).

Here is a brief description of SUSY and how it naturally produces a WIMP candidate. SUSY proposes every particle in the Standard Model has a corresponding bosonic or fermionic partner. This symmetry between bosons and fermions solves the hierarchy problem (why the Planck and electroweak energy scales are so different), and the fine-tuning problem (why the Higgs mass is so small). Also attractive about SUSY is there appears to be a unification of the electroweak and strong forces at the unification scale ($\approx 10^{16}$ GeV), which does not occur without SUSY extensions to the Standard Model. SUSY is considered a broken symmetry because the mass of the SUSY particles are much larger than their partner particles. If this were not the case SUSY particles like the selectron (SUSY counterpart to the electron) would have the same mass as the electron and been discovered long ago. Consequently, SUSY must undergo symmetry breaking similar to electroweak symmetry breaking, and all SUSY particles must be very massive. However, the difference in SUSY masses must not be larger than a few TeV for SUSY to naturally explain the small Higgs mass. For this reason, the typical WIMPs is 10 GeV to 1 TeV. The Lightest Supersymmetric Particle (LSSP), often the neutralino, is stable, electrically neutral, and thus a popular WIMP candidate.

Despite the theoretical motivation, experimental searches at the Large Hadron Collider (LHC) and other experiments for WIMPs or other SUSY particles have proven elusive. In fact the parameter space where WIMPs naturally occur continues to diminish. Figure 1.8 shows that soon the WIMP cross-section will reach the "neutrino floor", where coherent neutrino scattering with the target nucleus will be an irreducible background; more on this in Section 1.4.3. In recent years there is a push toward "light" WIMPs with masses of order 1 GeV. These are not naturally predicted by SUSY theories, but are possible with the inclusion of other theories such as dark sector dark matter or universal extra dimensions. Nevertheless, traditional WIMPs remain an interesting dark matter candidate.

1.3.2 Kaluza-Klein DM

In universal extra dimension theories (UED) Standard Model fields can propagate in compact extra dimensions. These extra dimensions are compactified on a circle of small radius. This is appealing because UED proposes a mechanism to unify the electroweak and gravitational forces. It is also attractive because String theory, which is currently the most promising theory of quantum gravity, is a multi-dimensional theory consistent with UED. Momentum conservation in the extra dimensions leads to the lightest Kaluza-Klein mode (LKP) being stable, electrically neutral, non-baryonic, and thus a viable WIMP dark matter candidate [27].

1.3.3 Axion DM

The axion was proposed by Roberto Peccei and Helen Quinn in 1977 to solve the "strong-CP problem" of Quantum Chromodynamics (QCD) [28]. The Lagrangian for the strong force contains a term which gives an electric dipole moment to the neutron. Since no electric dipole moment has been observed, they proposed a new symmetry that prevents the CP violating term from appearing in the Lagrangian. As a consequence, a light scalar particle, the axion, is produced. Experiments such as ADMX and CARRACK have have set limits for the axion. They search for the Axion by using radio frequency cavities and waiting for the excess power produced in the cavity when an axion is converted into a photon within the magnetic field. Theories place the mass to be in the μeV range. Despite the light mass, the axion can be CDM because it is produced non-thermally in the early universe.

1.3.4 Dark Sector DM

Dark sector dark matter models are growing in popularity because they can solve many discrepancies of the Standard Model using different methods [29]. Hidden forces in the dark sector can be used to explain the strong CP-problem and the anomalous magnetic moment of the muon. Also, dark sector physics can solve the "small scale crisis" of ΛCDM with the coupling between the dark photon and dark matter. The solution requires reconsidering the dynamics of the early universe with the inclusion of the dark photon. The result are "dark acoustic oscillations", where the dark photon acts as radiation pressure for dark matter. Moreover, specific dark sector theories can solve very specific conundrums of the Standard Model. For example, asymmetric dark matter solves the matter-antimatter asymmetry of the universe, which is otherwise unexplained. Unlike other dark matter theories, dark sector models have many testable predictions on structure formation and the CMB. Several experiments, such as high intensity beam and electron beam dump experiments, have been proposed to search for rare particles like the dark photon.

1.3.5 Sterile Neutrino ND

Since neutrinos have a small but nonzero mass they can undergo neutrino flavor mixing, which is not predicted in the Standard Model. This leads to the possibility of sterile neutrinos, which have right-handed helicities allowing them only to interact gravitationally. The sterile neutrino, although neutral, could interact with ordinary matter by mixing with the three observed left-handed neutrinos [30]. If the sterile neutrino exists and is the dominant component of dark matter, it must have a keV scale mass because it is a fermion obeying the Pauli exclusion principle. This ensures it cannot be packed into an infinitely small volume and cannot have an arbitrarily small mass. The upper limit is set to a few tens of keV due to the sterile neutrino's observationally small mixing with neutrinos. Despite their light mass, sterile neutrinos are often theoretically predicted to be non-relativistic, and therefore they are another important theory in the search for dark matter.

1.4 Detection Techniques

The focus of this work is WIMP-like dark matter, although the techniques and experiment discussed in this section may be sensitive to other types of dark matter. Consequently, the term dark matter and WIMP will be used interchangeably for the remainder of this work. Typically WIMPs are hypothesized to interact with ordinary matter via two types of interactions with the target nucleus. For the first type of WIMP-nuclear interaction the WIMP and target nucleus exchange a scalar particle,

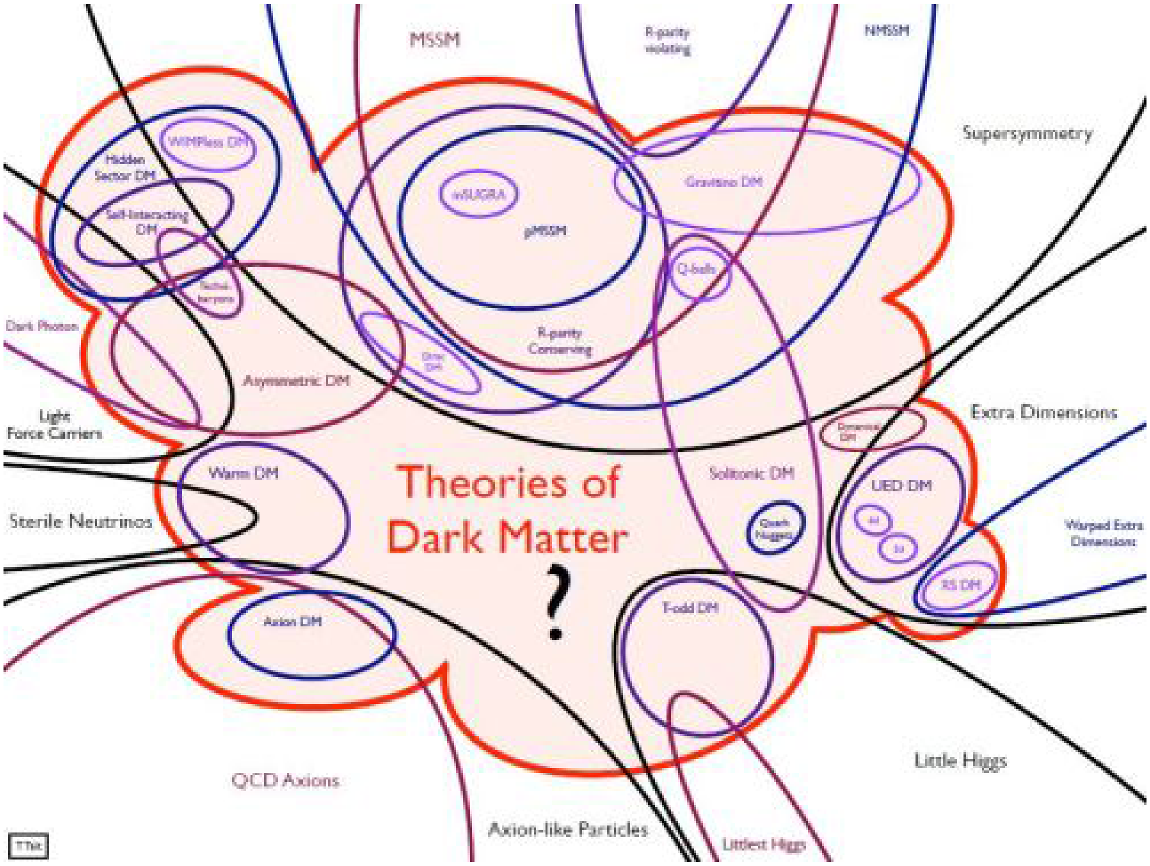

Figure 1.5: Theoretical particle dark matter candidates. Credit: Ref. [18].

leading to a spin independent (SI) interaction. For the second type they exchange a vector boson, which is a spin dependent (SD) interaction. The SI interaction cross-section is proportional to the target atomic number squared A^2. Therefore, it is advantageous for experiments searching for SI WIMP-nuclear interactions to choose target materials with large A. However, if the WIMP mass is much lighter than the target nucleus, less energy is transfered from the WIMP to the target nucleus due to kinematics. Experiments may attempt to lower the energy threshold to maintain sensitivity, but this results in an increase in the rate of low energy backgrounds. Consequently, experiments focusing on SI must balance enhancing the WIMP-nuclear cross-section with the difficulties and consequences of lowering the energy threshold.

Searching for SD WIMP interactions requires a target nucleus with a net nuclear spin. Refs. [20, 21, 22, 23, 24, 25] describe several SD targets. Among them are ^{129}Xe, ^{127}I, ^{23}Na, and ^{19}F. Regardless of the type of WIMP-nuclear interaction searched for, experiments utilize three different types of detection schemes: indirect detection, direct detection, and production. Briefly discussed in the following sections are the pros and cons and several experiments employing each detection technique.

1.4.1 Indirect Detection

For the indirect detection technique the main assumption is dark matter has a dark matter-dark antimatter symmetry, unlike baryons, and they annihilate when they encounter each other. In this case, the annihilation interaction produces ordinary particles, such as photons, charged leptons, or neutrinos. The presence of dark matter is inferred based on the characteristic properties of the observed ordinary particles. Experiments search regions of space where the dark matter density is expected to be significantly enhanced, such as the sun, the galactic center, or other massive objects. One such experiment is the IceCube experiment searching for dark matter annihilation to neutrinos in the sun [31]. Others include earth and satellite based gamma ray telescope experiments searching for the dark matter annihilation to gamma rays. One satellite experiment is the Fermi Large Area Telescope searching in the energy range between 100 MeV to hundreds of GeV [32]. One major requirement for these indirect detection experiments is an extensive understanding of all astrophysical sources of the ordinary particles detected by the experiment and residing within the signal region. This is important for indirect experiment to convince the greater scientific community of a detected WIMP signal.

1.4.2 Production Detection

Similar to indirect detection, the production detection technique detects ordinary particles and infers the existence of dark matter. The particle accelerator, the

Large Hadron Collider (LHC), collides two high energy particle beams and studies the resulting reactions and created particles. It is reasonable to expect, that in this high energy, high luminosity environment, dark matter will be occasionally produced through its unknown couplings to ordinary matter. Since Standard Model interactions have been precisely measured and are well understood, a WIMP signal in the LHC would consist of a cascade of ordinary particles, missing energy and momentum carried away by the created WIMP particle, and an interaction inconsistent with known Standard Model Interactions [33]. The LHC has yet to detect any hints of WIMP or other SUSY particles, but hopes are physics beyond the Standard Model will be found with the LHC upgrade and its increased center of mass energy (14 TeV).

1.4.3 Direct Detection

A robust detection technique in terms of background rejection is direct detection. Direct detection experiments wait for a WIMP particle passing through the detector to interact with the target nucleus, and deposit energy. Since WIMPs are non-relativistic, they have low kinetic energy and depending on the mass of the WIMP will typically transfer tens of keV to target nuclei. The low energy transferred ensures an elastic recoil. However, measurement requires low energy thresholds, high efficiency discrimination, and the ability to maintain low background rates. Discrimination is the ability to identify particles based on the properties of the recoiling particle.

There are several standard approaches to lower the background rate. First, the cosmic rays interacting within the detector are suppressed by operating the experiment deep underground. The rock overburden attenuates the cosmic ray flux in the experiment. Second, ultra-pure detector materials with very low concentration of radioactive elements are used. The low radioactivity of detector components is crucial to reduce Radon Progeny Recoils (RPRs) and other backgrounds, which can mimic WIMP signals. Third, the detector is fiducialized. Fiducialization is the restriction of the detection region in order to reject background events originating along detector surfaces, such as the inner walls of the vessel or the detector cathode and anode. One such background are RPRs. Fourth, the experiment is surrounded by water, polyethylene, or other hydrogen-rich materials to suppress low energy neutrons originating from alpha-n reactions occurring in the cavern walls, or those induced by muon interactions near the experiment. The hydrogen-rich materials are ideal to suppress the low energy neutrons because hydrogen's similar mass to the neutron is kinematically favored for optimal energy transfer. As a result, the flux of neutrons entering the detector with enough energy to produce a detectable interaction can be made as small as required by increasing the material thickness. Therefore, the neutrons stop short of the detector. In addition to these backgrounds, particular experiment-based backgrounds must be suppressed or characterized.

After employing these and other background reduction techniques, direct detection experiments compare their measured event rate with an estimation of their background. This is often done per energy bin. Indication of a dark matter signal is a significant excess of events above the predicted background. Since it is impossible to account for all potential backgrounds, direct detection experiments search for so-called "smoking gun" signals. These are the annual modulation of the event rate, and the sidereal (daily) modulation of the nuclear recoil direction [36], [37]. These signatures are difficult for a background to imitate, so if measured they would constitute a definitive proof of dark matter originating from the galaxy.

Annual Modulation To understand annual modulation consider Figure 1.7 (left). The Milky Way Galaxy is immersed in a non-corotating halo of dark matter. Due to the solar system's motion though the galaxy, an Earth-bound detector experiences a flux of dark matter appearing to come from the constellation Cygnus [36], [37]. This flux of dark matter is called the "WIMP Wind". From the earth's orbit around the sun, the earth has the maximal component of its velocity toward

Cygnus in June and has the maximal component in the opposite direction of Cygnus in December. Consequently, there is a greater flux of WIMPs in June compared to December. The periodic change of flux causes a yearly modulation in the event rate of an earth bound detector. As long as there are no backgrounds which modulate with a yearly cycle, annual modulation is a characteristic signature for dark matter.

The DAMA/LIBRA experiment claims to have detected the annual modulation signal [34]. Figure 1.6 shows the DAMA/LIBRA modulation consists of a few percent, yearly periodic signal that is consistent with a dark matter interpretation of the signal. Unfortunately, the parameter space corresponding to their signal has been ruled out by several orders of magnitude by the null results of other experiments. The DAMA/LIBRA collaboration deliberately has no background rejection in order to be sensitive also to non-standard dark matter-electron interactions. They claim if dark matter interacts primarily with electrons other null experiments will not see dark matter because they reject all electronic events. Other groups have developed theoretical models such as dark matter inelastic collisions to reconcile the null result of other experiments. Nevertheless, the issue will likely not be resolved until experiments similar to DAMA/LIBRA are built. Although many experiments continue to search for an annual modulation, the DAMA/LIBRA controversy demonstrates the need for another more definitive dark matter signature.

Daily (Sidereal) Modulation The second "smoking gun" signal is the sidereal or daily modulation of the WIMP-induced nuclear recoil directions over the course of a sidereal day [37]. Figure 1.7 (right) shows the "WIMP Wind" entering a ground-based detector from left to right. At one time of day the WIMP-induced nuclear recoils are preferentially directed downward, and 12 hours later due to the rotation of the earth the nuclear recoils are rightward. This is a robust signal, because unlike annual modulation there are no known backgrounds that can mimic the signal. Consider the following common background situations. First, a point source

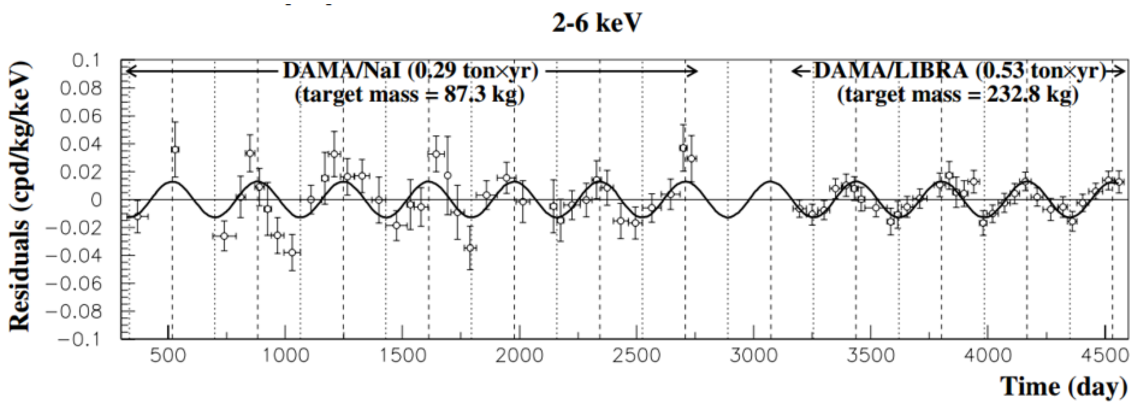

Figure 1.6: DAMA-LIBRA annual modulation signal. Credit: Ref. [34].

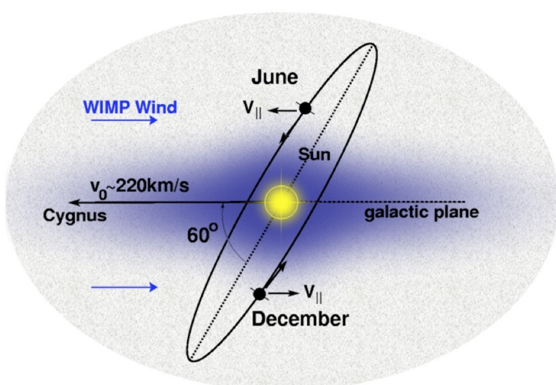

(a) Annual modulation

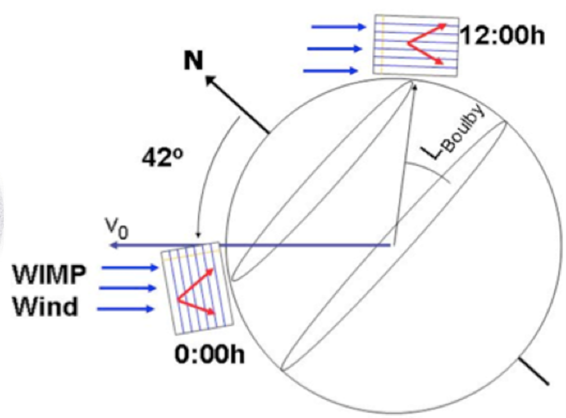

(b) Sidereal modulation

Figure 1.7: (a) The solar system moving through the halo of dark matter experiences a "WIMP Wind" from the direction of the constellation Cygnus. (b) Sidereal modulation of the WIMP-induced nuclear recoil direction. Credit: Ref. [35].

in the lab emits particles that interact in the fiducial volume. This background is easily identified because the direction of events in the detector is preferentially directed away from the source, regardless of the direction of the WIMP Wind. Second, an isotropic background. An isotropic background is distinguishable as well, because it generates an isotropic distribution of event directions in the detector. Both of these backgrounds are uncorrelated with the location of Cygnus. The difficulty with the sidereal modulation is in the detection of the event direction. Currently the best directional detectors are gas-based Time Projection Chambers (TPCs), which can reconstruct the direction of the track based on the orientation of the primary ionization trail [42, 43]. Other techniques such as nuclear emulsions are under development [38].

1.5 Characterizing Progress: Limit Curves

In order to characterize the progress of WIMP searches and to compare results from experiment with different target nuclei, the standard approach is to summarize all results on limit curves in terms of the WIMP-nuclear interaction cross-section and the WIMP mass. For each experimental curve the parameter space above the curve is excluded by the experiment at the 95% confidence level. The parameter space below each curve is unprobed by the experiment and is the location where WIMPs might exist. Figure 1.8 shows the limits for the spin-independent (SI) case for several prominent experiments. The solid and dashed curves represent current experimental limits and the predicted next generation limits. Notice the next generation experiments will approach the so-called "neutrino floor". The neutrino floor indicates where coherent nuclear scattering of solar, atmospheric, and supernova neutrinos become an irreducible background [39]. In other words, below the neutrino floor the rate of background neutrino interactions in a detector is greater or equal to the expected rate of WIMP interactions in the detector. Consequently, the neutrino floor represents a serious problem for direct detection experiments. Creative ideas are in development toward searching below the neutrino floor [40, 41]. One idea is to develop an ultra-sensitive directional detector, able to measure directionality down to or below a keV. Such a detector might be able to separate the neutrino background from the directional WIMP signal.

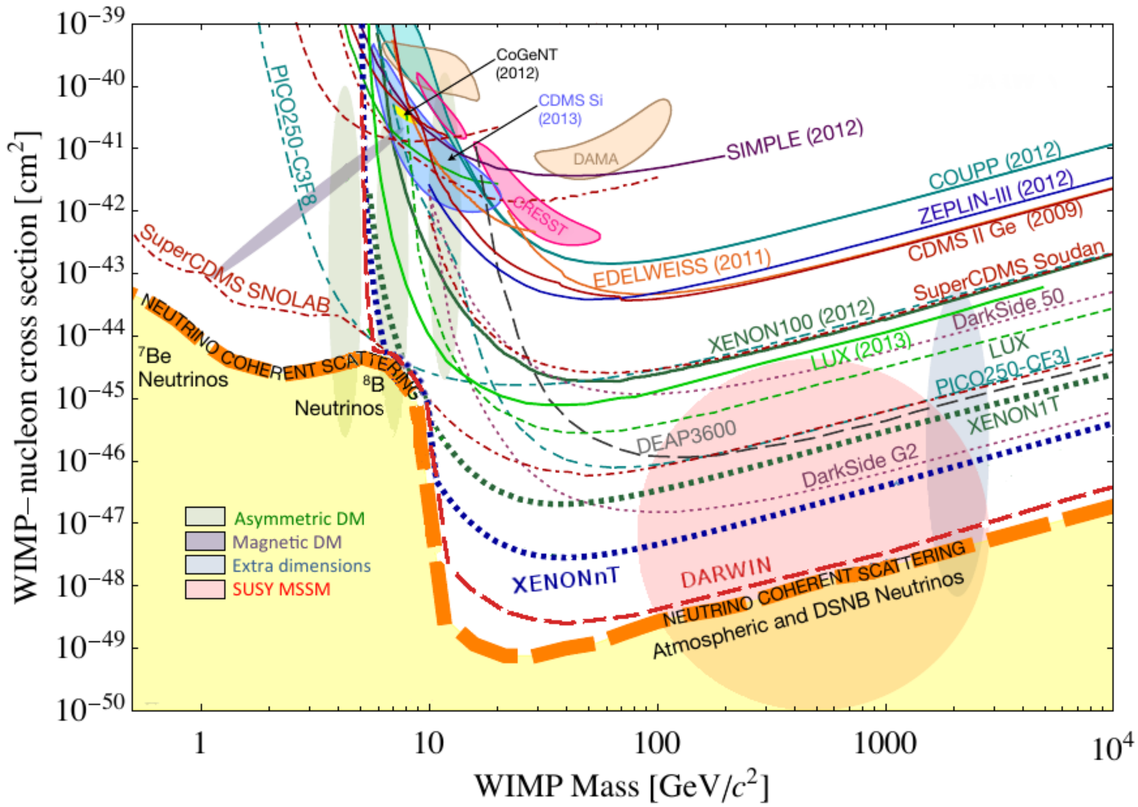

Figure 1.8: Current SI WIMP-nucleon limits curve. Note that next generation experiments will be approaching the "neutrino floor". Credit: Ref. [55].

1.6 DRIFT

This section discusses the Directional Recoil Identification From Tracks (DRIFT) experiment and its search for the sidereal modulation of WIMP-induced nuclear recoils [44, 45, 46, 57]. The DRIFT-IId detector is shown in Figure 1.9. It is operated at a depth of 1.1 km in the STFC Boulby Underground Science Facility [52]. It is a 1 m^3 TPC with a 0.9 μm thick, texturized, aluminized-Mylar central cathode dividing the detector into two 50 cm drift regions. At the end of each is a 1 m^2 Multiwire Proportional Chambers (MWPCs). They are comprised of a 2 mm pitch, 20 um wire anode plane sandwiched between two grid planes 1 cm on either side of the anode plane. A field cage with periodic stainless steel rings is utilized to maintain a uniform drift field of 580 V/cm. The detector is operated within a steel vacuum vessel.

1.6.1 DRIFT Gas Mixture

The DRIFT experiment utilizes the gas mixture 30-10-1 Torr CS_2-CF_4-O_2. The F atoms of the CF_4 component of the gas mixture are the target for spin-dependent (SD) WIMP-nucleon interactions (WIMP interacts with the net spin of the nucleus). The CS_2 component of the gas is electronegative and is utilized to achieve negative ion drift. Negative ion drift is important in order to achieve low diffusion (a few hundred μm [44, 53]) without magnetic fields and to have slow drift velocity. The O_2 component of the gas causes the production of minority species, which is required for fiducialization. Section 1.6.3 will describe fiducialization and how it is utilized for background rejection.

1.6.2 DRIFT Operating Principle

The DRIFT detector operates in the following manner. Particles enter the right or left drift region and interact with the gas. If the particle is absorbed excitations can also occur resulting in scintillation. If the interaction is elastic an electron or a nucleus are sent recoiling through the gas depending on the type of interacting particle. As the recoiling particle moves through the gas it interacts with the neutral molecules of the bulk gas and leaves behind a trail of ionization. The recoil direction is correlated with the incident direction of the interacting particle, and thus it gives information about the incident direction. Next, the CS_2 quickly captures the electrons, are drifted to the closest MWPC, and are readout. Meanwhile, the positive ions drift to the cathode. The DRIFT collaboration was the first to use this Negative Ion Time Projection Chamber (NITPC) technology ([53, 54]) to measure the energy deposited, the track length, and the track direction for low energy nuclear recoils.

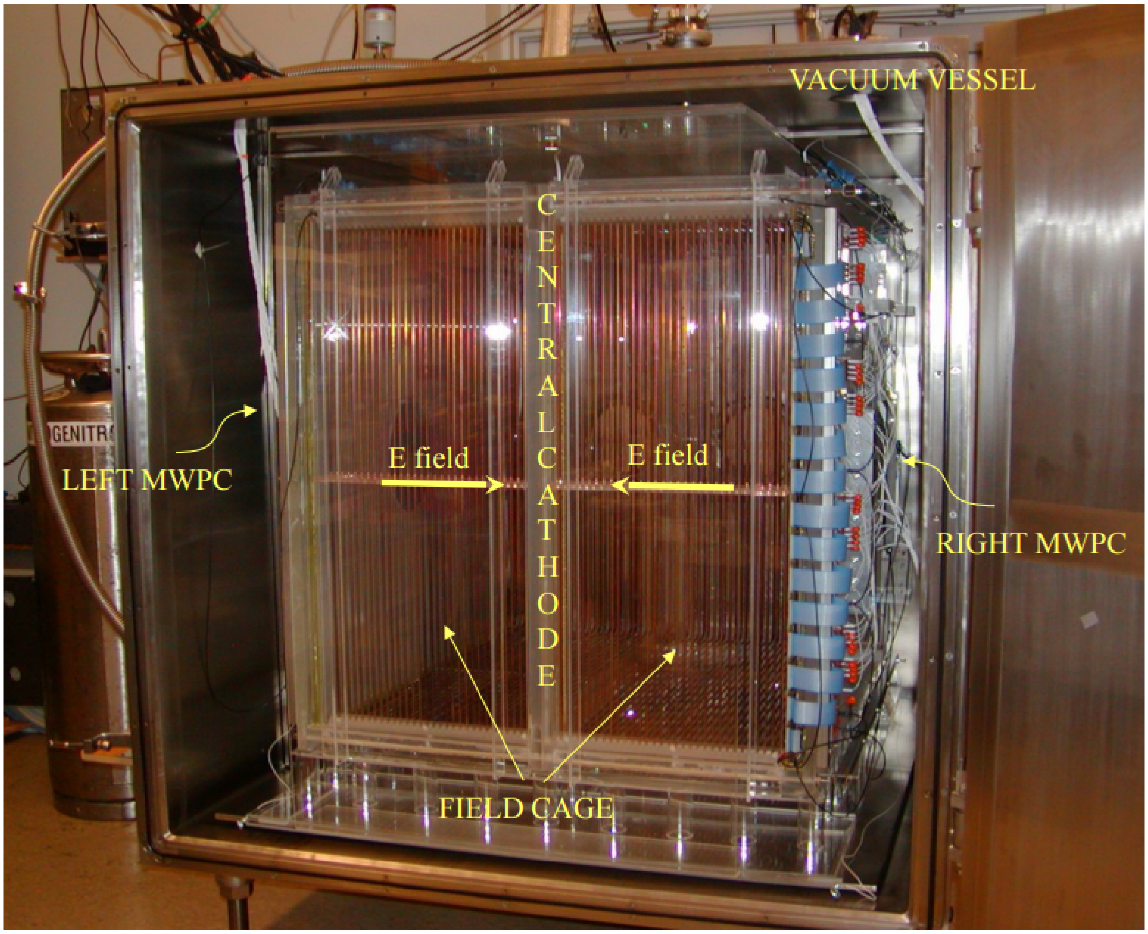

Figure 1.9: Interior view DRIFT detector. Credit: Ref. [56].

In the software the track and the recoil direction are reconstructed from the readout signal. Since typical track lengths for low energy tracks (expected for WIMP-nuclear interactions) are a few mm at this pressure, in order to efficiently reconstruct the track the diffusion must be small in comparison. The diffusion with negative ions is only a few hundred μm [45]. Although low diffusion is also possible in traditional electron drift TPCs, they require the addition of a complex and a costly magnetic field [42, 43]. The benefit of drifting negative ions such as CS_2^- is the low diffusion is achieved without magnetic fields. Also, the slower drift velocity of the negative ions reduces the requirement of fast readout electronics in order to resolve the track.

When the drift field is not too large, the negative ions remain in near thermal equilibrium with the bulk gas and their diffusion is given by:

$$\sigma^2_{ThermDiff} = \frac{2kTL}{eE}, \tag{1.2}$$

where k is the boltzmann constant, L is the distance over which diffusion occurs (drift distance), E is the applied drift field, and T is the temperature of the gas. Equation 1.2 represents the theoretical minimum diffusion (without a magnetic field). The negative ion diffusion can deviate from this at high E, as the ions enter a non-thermal regime. Figure 1.10 depicts a WIMP-induced nuclear recoil, the creation of primary ionization, and the capture of primary electrons by CS_2.

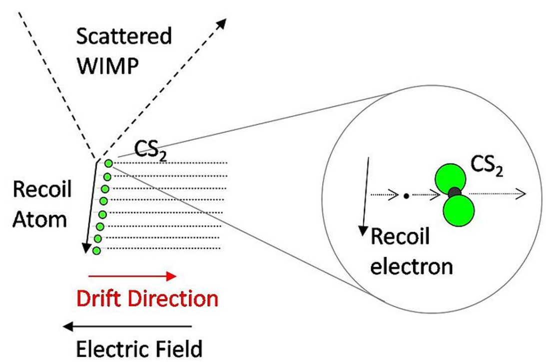

Figure 1.10: WIMP-induced nuclear recoil within DRIFT detector, subsequent electron capture, and drift of CS_2^- toward MWPC readout. Credit: Ref. [56].

1.6.3 Background Reduction

This section describes the background suppression for the DRIFT experiment [46]. Similar to other direct detection experiments, the DRIFT experiment has taken the following steps to reduce known backgrounds, which include neutron-induced recoils, cosmic rays, gamma-rays, and radon progeny recoils (RPRs) [47, 48, 49, 50]. In order to remove cosmic ray backgrounds the detector is operated 1.1 km underground in the STFC Boulby Underground Science Facility [52]. To prevent ambient and cosmic ray muon induced neutrons emanating from the cavern walls from entering the detector, the detector is surrounded by 67 cm polyethylene pellets with a density of 40 g/cm^2 taking into account the mean pellet packing fraction. The shielding thickness was chosen based on GEANT4 simulations of the neutron background [51]. DRIFT measures the neutron flux to be < 4 neutron recoils/day by comparing the shielded and unshielded data [47]. Software cuts based on the track length reject gamma-ray interactions [47].

A troublesome background are RPRs, because they are potentially indistinguishable from a WIMP signal. The following description is based on Refs. [47, 48]. ^{222}Rn is unstable to alpha decay and is present in low quantities in the detector. Its decay daughter is ^{218}Po, which is charged and is attracted to the negative potential of the cathode. On the surface of the cathode the ^{218}Po alpha decays with a half-life of 3.05 minutes to ^{214}Pb. The recoiling ^{214}Pb creates a nuclear recoil event observed with one of the MWPCs. Due to momentum conservation, the alpha particle recoils in the opposite direction and is observed by the other MWPC. Consequently, the ^{214}Pb recoil can be "tagged" with the alpha track at the other MWPC and rejected. However, since the alpha particle is emitted isotropically, the alpha particle can range out in the cathode and go undetected. Consequently, the "untagged" RPRs can represent an irreducible background. To eliminate them, the DRIFT collaboration searched for a means of fiducializing the detector and excluding the cathode from the fiducial region. Ultimately, the fiducialization was accomplished by introducing a small amount of O_2 to the CF_4-CS_2 gas mixture. The result is the appearance of several minority drift species. Although their identity is unknown, these minority species have distinct drift velocities faster than the dominant CS_2^- peak. Consequently, the

Z location of the interaction can be determined by:

$$Z = \frac{V_{pri} V_{min}}{V_{min} - V_{pri}} \Delta T_{pri-min} \tag{1.3}$$

where V_{pri} is the drift velocity of the primary species (CS_2^-), V_{min} is that of the minority species (identity unknown) [46], and $\Delta T_{pri-min}$ is the arrival time difference between the primary and minority species. This process wherein the interaction site in the detector is determined is known as fiducialization, where Equation 1.3 is utilized to fiducialize the detector along the drift dimension Z. Consequently, the ability to fiducialize is important for dark matter detectors employing the TPC technology. In fact, utilizing these techniques and the ability to fiducialize along Z, the DRIFT experiment achieves zero background [46].

1.6.4 Results and Conclusion

DRIFT is the leading directional dark matter detector, setting SD limits several orders of magnitude better than other directional detectors, such as NEWAGE and DMTPC [46]. Figure 1.11 shows the factor 4 improvement of the 2016 DRIFT limits over previous results [57, 58]. Despite the success of the DRIFT experiment, the use of low pressure gas has the obvious drawback of low target mass compared to liquid or solid state detectors. DRIFT also has the disadvantage that only a fraction of the low pressure gas in the detector is useful target for SD WIMP searches; of the 41 Torr gas mixture only the F component of the 10 Torr CF_4 is target for WIMPs. Although required for thermal diffusion and fiducialization, the other components of the gas mixture (30 Torr CS_2 and 1 Torr O_2) are "wasted" space in the detector. They provide no SD target for WIMPs. In the chapters that follow this work presents research toward a new gas mixture better optimized for SD WIMP detection that maintains the other benefits of the DRIFT gas mixture. Again, these are low thermal diffusion, slow drift velocity, and the presence of minority peaks for fiducialization.

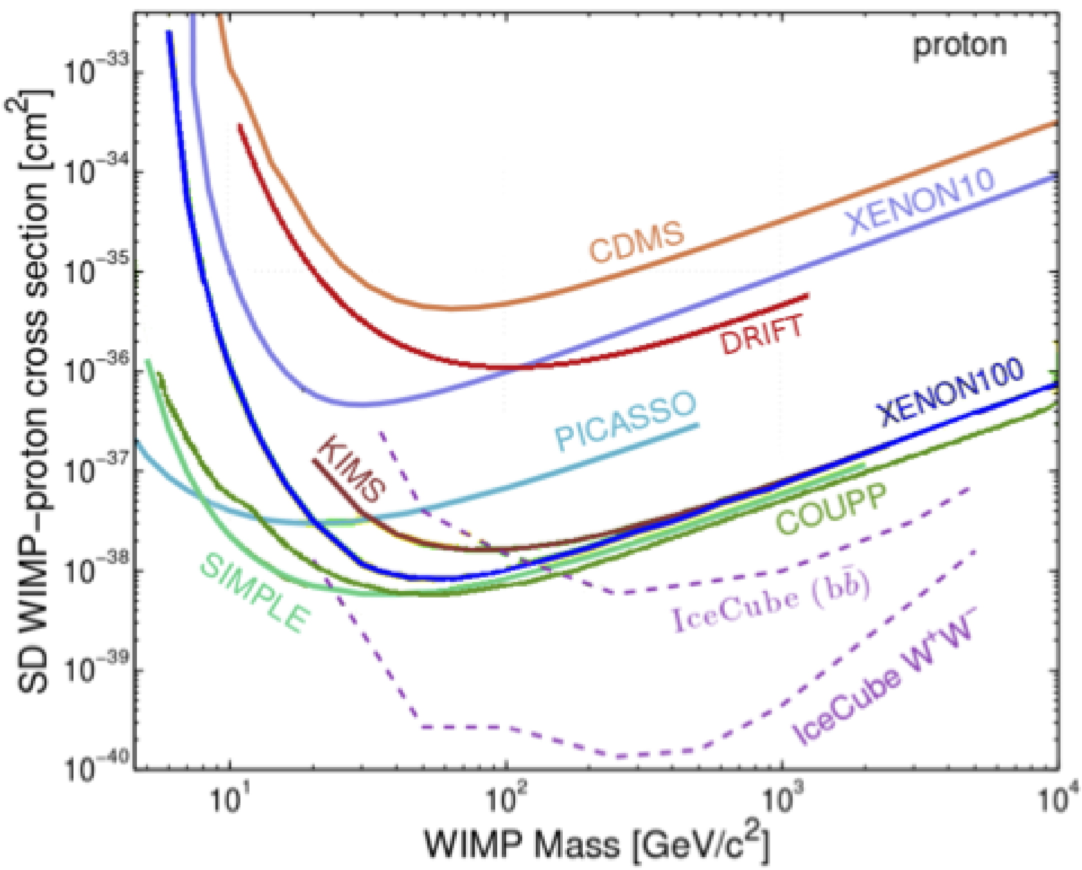

Figure 1.11: Current SD limits for DRIFT (black) and other leading SD experiments. Credit: Ref. [58].

Chapter 2

Characterization of SF_6 in Time Projection Chamber Technology

2.1 Introduction

In this chapter a low pressure SF_6 TPC is utilized to measure the smearing (broadening) of the events due to the diffusion, the capture length, and the pitch of the Thick Gas Electron Multipliers (THGEMs) as a function of the pressure, the drift field, and the drift distance. These measurements and the choice of SF_6 were motivated with the goal of improving the DRIFT experiment [44, 45], which was discussed in Section 1.6 and is briefly presented here. DRIFT is a 1 m^3 Negative Ion Time Projection Chamber (NITPC) that searches for directional dark matter. Although DRIFT is the leading directional dark matter experiment, like other directional dark matter TPCs it suffers from low target mass. This is compounded because the CS_2 and O_2 components of the DRIFT gas mixture, although required for low diffusion (a few hundred μm [44]) and for fiducialization, provide no target for SD WIMP interactions. Low diffusion and fiducialization are important properties for track resolution (typical low energy tracks in DRIFT are a few mm [44]), and background rejection, respectively. With the goal of optimizing the gas mixture, our group began searching for a new negative ion gas that is a good target for SD WIMP interactions, has low diffusion, and has a minority species for fiducialization. Ultimately, our focus turned to SF_6 [101].

SF_6 has been extensively studied with applications as a gaseous high voltage dielectric insulator [59, 60], in plasma etching of silicon [61, 62], and thermal and sound insulation due to its high electron affinity [63, 64]. Until recently SF_6 was not considered for use in Negative Ion Time Projection Chambers (NITPCs). Although the electronegativity of SF_6 was well known, it was assumed the high electronegativity that makes SF_6 attractive for other applications would make gas gain in SF_6 difficult. Mainly, the electrons cannot be stripped from SF_6^- even in the high field region of gaseous amplification devices such as Multi-Wire Proportional Counters (MWPCs).

However, recently our group demonstrated gas gains in SF_6 utilizing Thick Gas Electron Multipliers (THGEMs) [101]. In addition to demonstrating gas gain, our group verified two crucial properties of SF_6 for NITPCs: SF_6 has low gas diffusion, and the existence of the faster secondary drift species, SF_5^-. The production of a secondary species with a distinct drift velocity is necessary for fiducialization (recall Equation 1.3). Our conclusion was the low diffusion, the ability to fiducialize, and the non-toxicity make SF_6 an ideal gas for WIMP searches with NITPCs.

This chapter studies SF_6 in TPCs with the following two goals. The primary goal is to verify the thermal drift behavior of the primary negative ion SF_6^- as a function of the drift field E_{Drift}, the drift distance Z, and the gas pressure P. This includes measuring the diffusion σ_{Diff}. The second goal is to precisely measure two quantities that are discuss in detail in Section 2.4. They are the contribution to the effective diffusion (or the broadening of the track) due to the capture length of the primary electrons (σ_{Capt}) and the contribution due to the THGEM pitch (σ_{THGEM}).

σ_{Capt} and σ_{THGEM} are useful quantities to measure in their own right, because σ_{Capt} is applicable to any SF_6 TPC regardless of the amplification device and the readout electronics, and σ_{THGEM} is applicable to any TPC utilizing THGEMs regardless of the gas. In order to achieve these goals, the experiment consists of a series of experiments performed in either 20, 30, and 40 Torr SF_6 with each of the following E_{Drift} and Z; $E_{Drift} = 200\ V/cm, 400\ V/cm$, $600\ V/cm, 800\ V/cm$, and $1000\ V/cm$ and $Z = 3.175\ cm$, $8.255\ cm$, $13.335\ cm$, $18.415\ cm$,$23.495\ cm$, and $28.575\ cm$.

The chapter proceeds by first describing the experiment and the data acquisition. Next, the data analysis and the typical signals are discussed. After this, two independent "measurement" techniques are presented which combine the data (collected at different P, E_{Drift}, or Z) in order to extract σ_{Diff}, σ_{Capt}, and σ_{THGEM} . Then, an experimental complication involving the non-δ-function nature of the ionization source is discussed and the effect modeled. In order to overcome this complication, two "extraction" techniques are discussed. Lastly, the results are presented and discussed.

2.2 Experimental Setup and Data Acquisition

This section presents the experiment and the data acquisition. Figure 2.1 shows the NITPC detector schematically. The detector has a 2.54 cm thick, 30 cm long acrylic, cylindrical tube capped on the ends with an anode consisting of a THGEM (right green) and an aluminum cathode (left). Along the length of the cylinder interior is the PCB mylar film that supports the 1.3 cm thick, 2.54 cm pitch copper strips for the field cage (bronze). Between each field ring is a 56 $M\Omega$ resistor, allowing a smooth step-down of the cathode voltage. The field cage ensures the uniformity of E_{Drift}, which is important to preserve the shape of the charge distribution as it diffuses and drifts to the THGEM readout. Spaced between the field rings and along the length of one side of the cylinder are 2.54 cm diameter circular holes. A

^{210}Po alpha source is mounted on an adjustable, motor-driven slider (designed by Eric Lee). Through a narrow collimator the ^{210}Po alpha source emits alpha particles into the detection region at specific Z locations defined by the holes. The detector is place inside the large "MiniDRIFT" vacuum vessel (Figure 2.1, right), where it can operate in a controlled, low pressure gas environment. The vacuum vessel is called "MiniDRIFT" due to its use as a prototype DRIFT-like detector (see Section 1.6.4 for the DRIFT experiment).

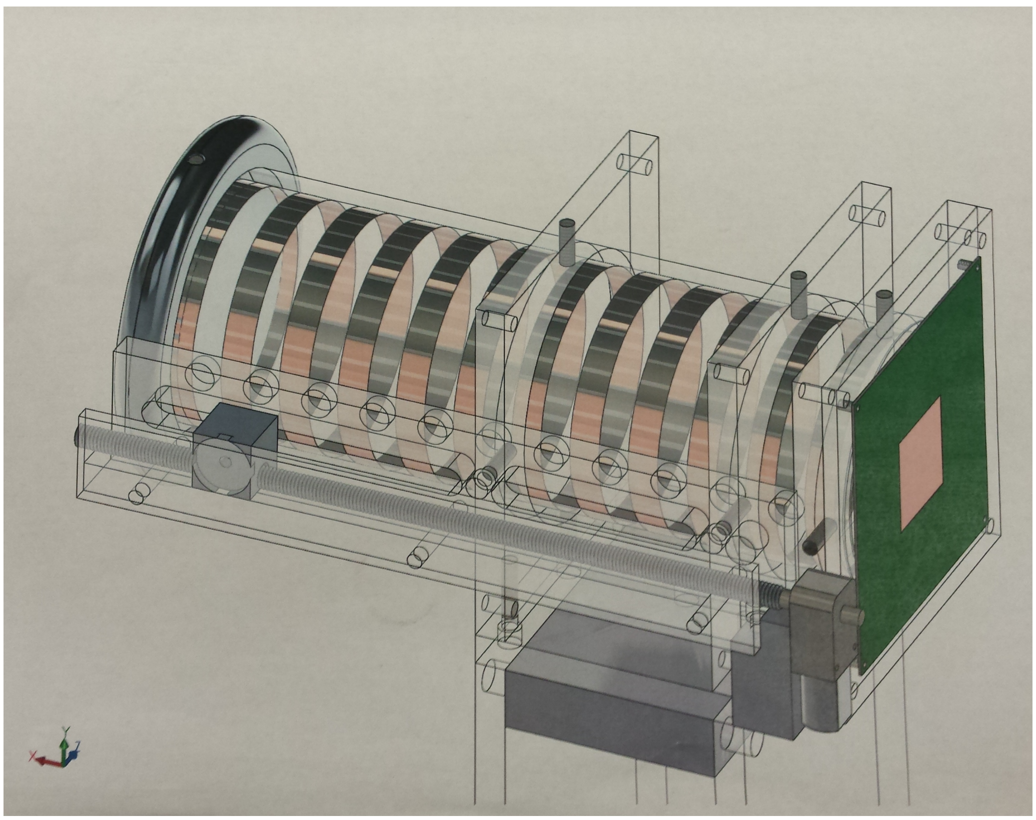

Figure 2.1: Schematic of the 30 cm acrylic cylindrical detector. The THGEM (right green PCB) and aluminum cathode (left) cap the ends. Along the interior of the cylinder are periodically spaced fields rings, and between the rings along the front side of the cylinder are periodically spaced circular holes. With the motor-driven slider designed by Eric Lee, the ^{210}Po can fire alpha particles at different Z locations into the detector.

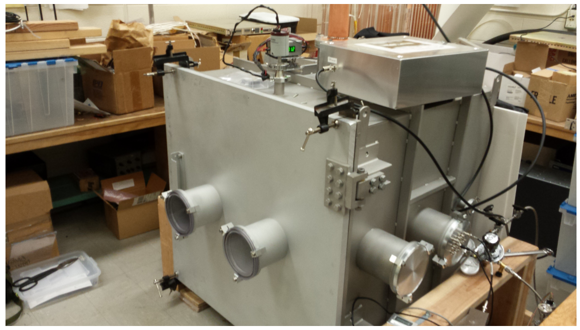

Figure 2.2: MiniDRIFT vacuum vessel used to house the 30 *cm* acrylic cylindrical detector. The high frequency filter box is seen resting on top of the vessel (top right).

The detector is powered with two separate power supplies. The cathode power supply is able to supply a voltage up to $-60kV$. In order to remove much of the high frequency noise introduced by the power supply, the high voltage is directed through a low pass filter box. Since the filter box capacitors have a breakdown voltage of 36 kV, the negative high voltage applied to the cathode is maintained below 30 kV. The THGEM performs the dual function of charge amplification and signal readout; i.e., no separate readout is utilized. The THGEM surface facing the drift volume is grounded and the opposite surface is powered to positive high voltage. The THGEM has a 3 *cm* by 3 *cm* amplification region surrounded by copper plating out to 9.5 *cm* by 9.5 *cm*. This additional copper area helps preserve the uniformity of the drift field near the THGEM. The high voltage surface of the THGEM is read out using an ORTEC 142 charge sensitive preamplifier. The voltage signals from the preamplifier are then collected with the Tektronix TDS 3054C digital oscilloscope and written to text with the provided National Instruments software.

2.3 Measuring the Track Width (σ'_Z)

This section describes what the signals are and the steps of the data analysis leading up to the measurement of the signal width. It will be shown in Section 2.4 that measuring the signal width is the first step toward determining σ_{Diff}, σ_{Capt}, and σ_{THGEM}. The measured signal width is referred to as σ'_Z. In summary, the steps are: the voltage baseline removal, the conversion of the voltage signal to the current signal, the noise reduction with a Gaussian filter, and the fitting of the SF_6^- charge distribution.

2.3.1 Baseline Removal

Since the voltage signals from the preamplifier are negatively offset from zero, the first step of the data analysis is the baseline removal. The baseline is calculated and removed on an event-by-event basis with the follow procedure. The average voltage for three regions of the time window is calculated. The three regions are 1000 samples long and begin and end at the array indexes: 100 to 1100, 1100 to 2100, and 8900 to 9900. The total number of data samples is $10,000$. The location of the three regions are specifically chosen to exclude all portions of the track, which typically start at 4000 and end by 8000. The first and final 100 samples are excluded to avoid edge effects. Next, the regions are averaged together, and the result is subtracted from each sample of the voltage signal. The resulting baseline subtracted voltage is referred to as V_{Raw}. Figure 2.3 shows a typical V_{Raw} in 40 Torr SF_6, $E_{Drift} = 400$ V/cm, and alpha source location $Z_{Source} = 28.575$ cm. The vertical green lines in Figure 2.3b mark the locations in time where the rise time cut (RT cut) is calculated. The RT cut is described in Section 2.6.1.

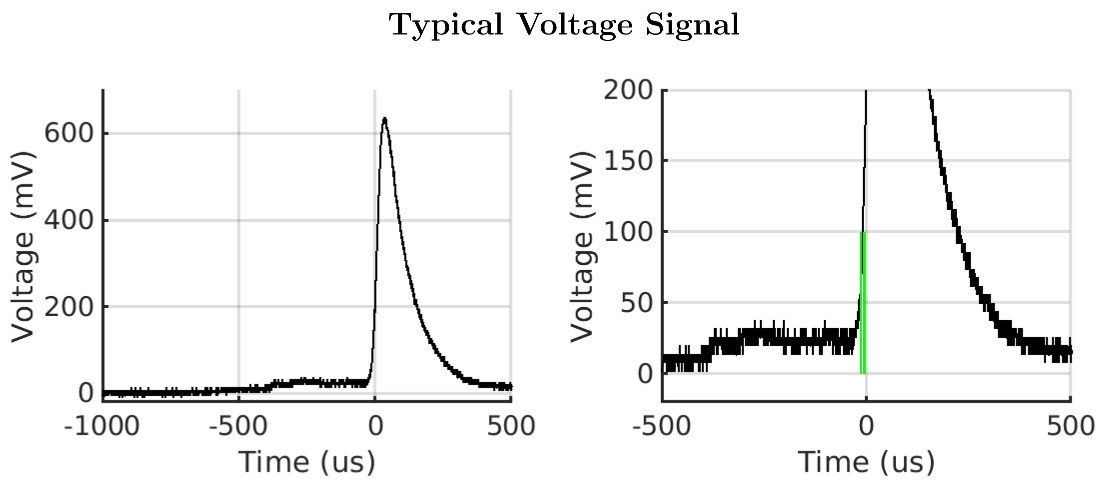

(a) (b)

Figure 2.3: Typical voltage signal at 40 Torr SF_6 for 400 V/cm and $Z_{Source} = 28.575\ cm$ (2.3a), and a closeup view of the voltage rise time (RT) (2.3b).

2.3.2 Current Conversion

Consider Figure 2.3a and notice the preamplifier decay tail. In order to calculate track properties such as the track length, the energy, and other track properties the preamplifier decay time must be removed from the signal. Often this is done with a hardware shaper. Unfortunately, although the hardware shaper removes the decay time, it makes track properties such as the event energy difficult to measure. Since the event energy is vital for this work, an alternative approach is used. The voltage signal is converted in software to a signal proportional to the current I:

$$I \propto \frac{dV}{dt} - \frac{V}{\tau}, \tag{2.1}$$

where V is the preamplifier voltage and τ is the decay time of the preamplifier. The decay time is measured to be $\tau = 90\mu s$. Due to the time derivative in Equation 2.1, the point to point fluctuations in the current are large and Gaussian filtering (or other noise reduction) is required to bring the signal out of the noise. Figure 2.4a shows I after the Gaussian filtering step (Section 2.3.3). Equation 2.1 is an essential step for all data analysis in this work, and thus is referred to repeatedly.

Typical Current Signal

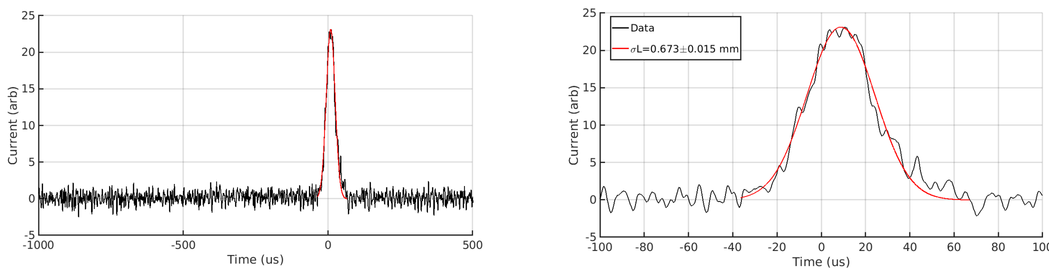

(a) (b)

Figure 2.4: Typical current signal I at 40 Torr, $E_{Drift} = 400\ V/cm$, and $Z_{Source} = 28.575\ cm$ with 0.044 mm Gaussian smoothing. The red curve is the Gaussian fit for the SF_6^- charge distribution.

2.3.3 Gaussian Filtering

The current signal I is Gaussian filtered to bring the signal out from the noise. Gaussian filtering (smoothing) is equivalent to convolving the signal with a normalized Gaussian kernel. The convolution operation takes the signal and replaces each sample of the signal with the Gaussian average of the sample and the surrounding points. The extent and degree of filtering is characterized by the width σ_{Filt} of the kernel. The smallest σ_{Filt} is selected in order to minimize the signal broadening and distortion brought about by the filter. For the experiments performed at $E_{Drift} = 400$ V/cm, 600 V/cm, 800 V/cm, and 1000 V/cm, a $\sigma_{Filt} = 0.044\ mm$ is chosen. For $E_{Drift} = 200\ V/cm$, a $\sigma_{Filt} = 1\ mm$ is selected, because these experiments are noisier and required increased filtering. The broadening of the track width due to σ_{Filt} will be shown to be small in comparison to the other contributions to the track width.

2.3.4 Measurement Of The Track Width (σ'_Z)

Next, the track width σ'_Z is measured. For this, the SF_6^- charge distribution is fit with a Gaussian, where the fitted σ is σ'_Z. The fit region is determined by locating the maximum current I_{Max} and iteratively searching for the location where the signal to the left of I_{Max} and to the right of I_{Max} drops to zero. Consequently, the fit region includes the entire SF_6^- charge distribution. The motion of positive ions away from the THGEM and toward the cathode has a distortion effect on the right-side of the SF_6^- charge distribution. However, for this experiment the effect is assumed to be small based on the low χ^2 resulting from the fit to the entire charge distribution. Therefore, the motion of the positive ions is ignored.

2.4 Two "Measurement" Techniques

This section presents how the primary goal (verifying the negative ion behavior of SF_6) and the secondary goal (measuring σ_{Diff}, σ_{Capt}, and σ_{THGEM}) are accomplished by means of combining experiments performed at different P, E_{Drift}, and Z. Consider again Figure 2.4, which shows the current signal of a typical track arriving at the anode. The signal width (σ'_Z) has a number of contributions that are assumed to be uncorrelated. In this case, they add together in quadrature:

$$\sigma'^2_Z(P, Z, E) = \sigma^2_{Diff}(Z, E) + \sigma^2_{Capt}(P, E) + \sigma^2_{THGEM} + \sigma^2_{Filt} + \sigma^2_{\Delta Z_0}, \tag{2.2}$$

where in parenthesis the explicit dependencies of each quantity are written. P is the total gas pressure, E (E_{Drift}) is the drift field, and Z (L) is the drift distance. σ_{Diff} is the contribution to σ'_Z from the diffusion, which is given by Equation 1.2. Notice σ_{Diff} depends on Z and E but not on P. The other terms that contribute to σ'_Z are: σ_{Capt}, the capture distance of the electron by the SF6 molecule; σ_{THGEM}, from the smearing due to the THGEM pitch; σ_{Filt}, which is due to the Gaussian noise reduction filter (discussed in Section 2.3.3); and $\sigma_{\Delta Z_0}$, which is the term arising from the non-δ-function nature of the alpha source. For the time being, the $\sigma_{\Delta Z_0}$ contribution is ignored because it is independent of the techniques described in this section. It is discussed separately in Section 2.5. Consequently, define the quantity σ_Z such that:

$$(\sigma'_Z)^2 = \sigma_Z^2 + \sigma_{\Delta Z_0}^2, \tag{2.3}$$

where σ_Z is:

$$\sigma_Z^2(P, Z, E) = \sigma_{Diff}^2(Z, E) + \sigma_{Capt}^2(P, E) + \sigma_{THGEM}^2 + \sigma_{Filt}^2. \tag{2.4}$$

2.4.1 "Constant E_{Drift} Technique"

The first "measurement" technique is referred to as the "Constant E_{Drift} Technique", because the data is considered jointly for a fixed E_{Drift} and P. For this technique, the σ_Z^2 for all data at a given P and E_{Drift} are plotted as a function of Z. Consider the Z dependence of each contribution: σ_{Diff} depends on Z through Equation 1.2; σ_{Capt} depends on the capture length of the primary electrons, which is independent of Z; σ_{THGEM} is independent of Z, and σ_{Filt} is a constant. Since all contributions except σ_{Diff} are independent of Z, extrapolating the curve to $Z = 0$ gives the quadratic sum of σ_{Capt} and σ_{THGEM}. Recall σ_{Filt} is small and can be ignored. If the intercept is called "b", then $b = \sigma_Z^2(Z = 0) = \sigma_{Capt}^2 + \sigma_{THGEM}^2$. Also calculated is T_{Ion}:

$$T_{Ion} = \frac{meE_{Drift}}{2k}, \tag{2.5}$$

where T_{Ion} is the effective temperature of the drifting negative ions, the slope m of the fit line, k is the boltzmann constant, and e is the fundamental charge. Along with other quantities, T_{Ion} will be utilize to characterize the thermal nature of the negative ion drift.

Next, consider the P and E_{Drift} dependencies of σ_{Capt}. σ_{Capt} depends on the SF_6 capture cross-section, which can have a complicated dependence on E_{Drift}. In SF_6 the cross-section peaks at zero electron energy, or $E_{Drift} = 0$. Also, σ_{Capt} should decrease as the gas pressure increases. This is because the number density decreases and the electron travels a longer distance before encountering a gas molecule. Conversely, if the gas pressure is very high the electron is quickly captured. Therefore, as E_{Drift} goes to zero and P becomes large the capture length goes to zero, resulting in $\sigma_{Capt}(E_{Drift} = 0 \& P \rightarrow \infty) = 0$. Consequently, σ_{THGEM} is extracted by measuring σ_Z over a range of pressures and extrapolate the curve of σ_Z^2 simultaneously to $Z = 0$ & $E_{Drift} = 0$ ($\sigma_{THGEM} = \sqrt{\sigma_Z^2(Z = 0 \& E_{Drift} = 0)}$). Once σ_{THGEM} is determined, σ_{Capt} follows from b ($\sigma_{Capt} = \sqrt{b - \sigma_{THGEM}^2}$).

2.4.2 "Constant Z Technique"

Although the Constant E_{Drift} Technique is sufficient to measure σ_{THGEM} and σ_{Capt}, the following second procedure was developed as an independent check. This procedure begins with the assumption that the negative ions drift thermally for all E_{Drift}. Although this assumption is not strictly true, results from the Constant E Technique verify that it is approximately true. This assumption implies that σ_{Diff} is approximately thermal ($\sigma_{Diff} \approx \sigma_{ThermDiff}$) for all E_{Drift}. Next, the σ_Z of the data at a fixed Z and a given P are combined to plot σ_Z as a function of E_{Drift}. The curve is then fit with the function $\sigma_Z = \sqrt{\sigma_{DiffTherm}^2 + c}$, where the only fit parameter c equals the quadratic sum of σ_{Capt} and σ_{THGEM} ($c = \sigma_{Capt}^2 + \sigma_{THGEM}^2$). Taking the σ_{THGEM} from the Constant E_{Drift} Technique, σ_{Capt} is measured. The results will be shown to be consistent with the Constant E_{Drift} Technique.

2.5 Complication: Non-δ-Function Nature of The Initial Ionization Track

Here the consequences of the non-δ-function nature of the alpha source are discussed. The alpha particles enter the detector with a nonzero spread in Z. To discover how this affects the measured σ_Z, consider Figure 2.5. It depicts the cone of alpha particles entering the detector and the subsequent shape of the charge distribution along Z upon readout at the THGEM. Let the Z-axis point toward the GEM (right) and the X-axis point toward the top of the page. The blue alpha track is the track fired along the X-axis (perpendicular to Z). This track is a line charge in the XZ plane, and a point track in Z. Therefore, it has no initial spread in Z ($\Delta Z_0 = 0$). The green tracks represent all other tracks within the cone which exit the collimator at some angle relative to the X-axis. When projected onto the XZ plane, the green tracks are square pulses. Projecting further along Z they are line tracks with $\Delta Z_0 > 0$. Consequently, the primary ionization created by the alpha particles has an initial spread $\Delta Z_0 \geq 0$. The frequency of each ionization track ΔZ_0 depends on the collimation angle, the length of the collimator, the ^{210}Po distance to THGEM active region, and other detector geometries. Let the probability distribution for ΔZ_0 be $\rho(\Delta Z_0)$.

Next, consider the drift of the point track $\Delta Z_0 = 0$ (blue) and the line tracks $\Delta Z_0 > 0$ (green) to the THGEM. The net effect of diffusion can be approximated with the convolution of ΔZ_0 with a Gaussian of width equal to σ_{Diff}. Consequently, the point track diffuses into a perfect Gaussian, while the line tracks are elongated. Therefore, each track has an additional ΔZ_0 contribution to its measured width (σ_Z), which is always greater or equal to the result of Equation 2.4.

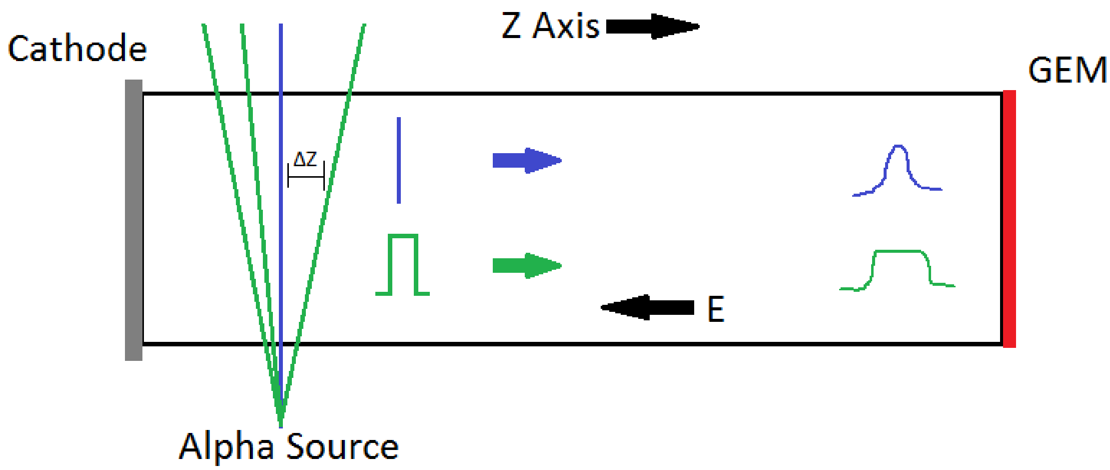

Figure 2.5: Diagram of the gas diffusion comparing the diffused track at the readout for $\Delta Z_0 = 0$ (blue) and $\Delta Z_0 > 0$ (green).

Since our interest is in the extraction of σ_{Diff} from the data, we need to know how the ΔZ_0 distribution effects the measured track width σ'_Z. To answer this question, a geometrical monte carlo simulation is performed to estimate the shape of $\rho(\Delta Z_0)$ and the largest possible ΔZ_0. The steps of the monte carlo are the following. First, the location of the emitted alpha particle is randomly chosen within a circle of diameter equal to that of the collimator ($D_{Collimator} = 0.251\ cm$). The origin of the simulation is the center ($X = 0, Y = 0$) and the base ($Z = 0$) of the collimator (intersection of collimator and the source). Next, the direction of the emitted alpha particle is selected isotropically by uniformly selecting the azimuthal angle ϕ and cosine of the polar angle $cos(\theta)$ between 0 and 2π[1]. Next, the alpha particle is linearly propagated to the edge of the collimator ($Z = l_{Collimator}$), where the length of the collimator is $l_{Collimator} = 1.955\ cm$. Define the 2D radial distance at the Z location of the collimator $r(Z = l_{Collimator}) = \sqrt{X(Z_{Collimator})^2 + Y(Z_{Collimator})^2}$. If $r(Z = l_{Collimator}) < D_{Collimator}/2$ the alpha particle successfully exits the collimator

[1]Note it is important to select $cos(\theta)$ from a uniform distribution and not θ, otherwise the frequencies are overly concentrated at the poles ($\theta = 0, \pi$).

and enters the detector. If $r(Z = l_{Collimator}) \geq D_{Collimator}/2$ the particle strikes the collimator. For the later case, the trajectory is aborted and the previous steps are repeated for another alpha particle. For the trajectories that enter the detector, ΔZ_0 is calculated by propagating the particle from $Z = l_{Collimator}$ to $Z = l_{Collimator} + l_{GEM}$, where the length of the active region of the THGEM is $l_{GEM} = 3\ cm$. Notice only the additional propagation distance across the THGEM L_{GEM} is necessary to consider for ΔZ_0. Therefore, $\Delta Z_0 = Z(l_{Collimator} + l_{GEM}) - Z(l_{Collimator})$. Six million alpha particles are simulated in this manner. The resulting probability distribution $\rho(\Delta Z_0)$ is shown in Figure 2.6. $\Delta Z_0 = 0$ is the most probable initial track extent. For $\Delta Z_0 \geq 0$, $\rho(\Delta Z_0)$ monotonically decreases to zero, where the maximal ΔZ_0 occurs near $(\Delta Z_0)_{max} = 3.5\ mm$.

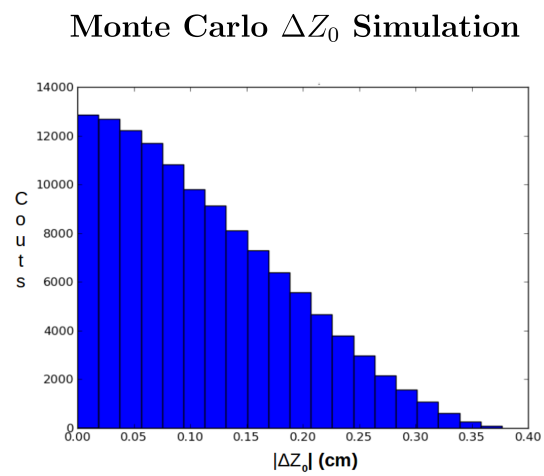

Figure 2.6: Monte Carlo (MC) simulation for ΔZ_0, where $|\Delta Z_0|$ is the absolute value of ΔZ_0.

The shape of $\rho(\Delta Z_0)$ and the range of ΔZ_0 indicate that the contribution of ΔZ_0 to measured track width σ'_Z cannot be ignored. For this reason it is essential to develop a method either to decrease $\sigma_{\Delta Z_0}$, to extract the σ_Z from the measured σ'_Z distribution, or to locate the $\sigma_{\Delta Z_0} \approx 0$ tracks. The former is possible by narrowing the cone opening angle, either by decreasing $D_{Collimator}$ or by increasing $l_{Collimator}$.

Although increasing the collimation lowers the effect of $\sigma_{\Delta Z_0}$, it also reduces the rate of alpha particles entering the detector. Since the event rate with the current collimation is already low ($\approx 1Hz$), increasing the collimation is not an ideal option. Another method measures σ_Z from σ'_Z with the statistics technique commonly referred to as bootstrapping. This "Bootstrapping Technique" is further discussed in Section 2.7. The third method extends the Monte Carlo simulation and attempts to simulate σ'_Z for a given σ_{Diff} (Section 2.6.3). We refer to this technique with the shorthand, "MC Technique".

2.6 "Extraction" Techniques

In this section the techniques to extract σ_Z from the measured σ'_Z distribution are discussed. Prior to employing either technique a troublesome class of events are removed with the so-called Rise Time (RT) Cut. On the remaining data, two independent techniques measure the underlying σ_Z at the particular P, E_{Drift}, and Z of the experiment from the σ'_Z distribution.

2.6.1 Rise Time (RT) Cut

The first step is to apply the following cut to the data, which rejects "unphysically" fast RTs. In this work RT is the time the voltage signal takes to increase from 10% to 25% of the maximum voltage V_{Max}. The RT calculation is depicted by the vertical green lines in Figure 2.7, where the left and right lines intersect the X-axis where V_{Raw} crosses the 10% and the 25% thresholds respectively. Typical voltage signals have $RT \approx$ few μs, whereas the fast-RT events have $RT \leq 0.2\ \mu s$, which equals the oscilloscope digitization rate $= \frac{1}{0.2\mu s} = 5\ MHz$. For example the nuclear recoil signal in Figure 2.7 has $RT = 9\ \mu s$. The fast-RT events are detrimental to the analysis because their shape is distorted; they are positively skewed. Consequently, if they are not rejected the σ'_Z distribution is misshaped in the crucial small σ'_Z region of the distribution. Therefore, the RT cut removes events with $RT \leq 0.2\mu s$.

Unfortunately, these fast-RT events occur in all experiments in this work. For this reason, a brief digression into possible causes/sources of these events is presented next. First, there are several variations/classes of the fast-RT events. The simplest class is sparks or micro-sparks, where the voltage jumps from $0V$ to V_{Max} in $\approx 0.2\mu s$. The second class has structure in the voltage signal above the 25% threshold, and thus unlikely to be sparks or micro-sparks. One possible origin for this class is that they are events originating very close to the THGEM, perhaps even inside a THGEM hole. In the high field region close to, or inside the THGEM, it is possible that not all of the primary electrons are captured by the SF6 molecules. Thus, the uncaptured part of the track produces the fast portion of the signal, with the negative ions responsible for the subsequent structure. Nevertheless, since all classes of fast-RT events can be removed with $RT \leq 0.2\mu s$, the discovery of their source is left for future work.

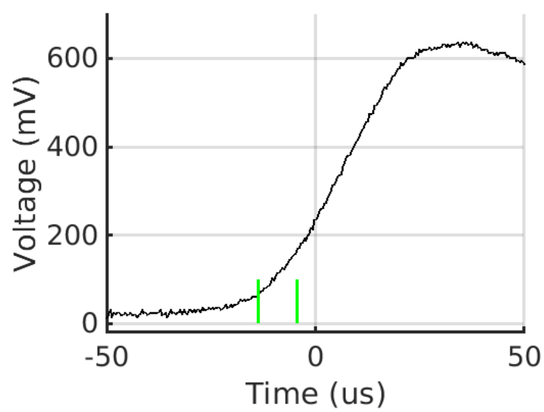

Figure 2.7: The same voltage signal in Figure 2.3, but focused on the RT measurement.

2.6.2 Bootstrap Technique

Before describing the bootstrap technique [65] to measure σ_Z, the technique is briefly motivated. In order to extract σ_Z, the location in the σ'_Z distribution where the $\sigma_{\Delta Z_0}$ contribution is approximately zero will correspond to $\sigma_Z \approx \sigma'_Z$. Consider a typical σ'_Z distribution: Figure 2.8, which is the result of the experiment performed at $P = 40$ Torr, $E_{Drift} = 400\ V/cm$, and $Z = 3.175\ cm$. Also, recall that the ΔZ_0 distribution decays for large ΔZ_0 (see Figure 2.6). Based on the ΔZ_0 distribution, the right side of the distribution consists of tracks whose width is dominated by $\sigma_{\Delta Z_0}$. Therefore, σ_Z does not correspond to the tail.

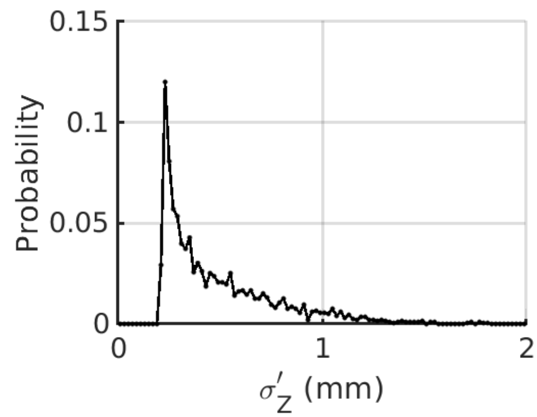

Figure 2.8: The measured distribution of track widths (σ'_Z) for the experiment performed at $P = 40$ Torr, $E_{Drift} = 400\ V/cm$, and $Z = 3.175\ cm$.

Next, consider the peak of the distribution, which corresponds to the most frequently measured track width. Even though the most frequent ΔZ_0 is zero, any small, unconsidered contribution to the width (such as fluctuations in $\frac{dE}{dx}$, inhomogeneous fields, non-straight trajectories from alpha scatters) will only act to increase the track width. The net effect of these contributions and $\sigma_{\Delta Z_0} > 0$ is to make the most frequently measured track width greater than σ_Z. Ultimately, the tracks with the smallest σ'_Z correspond to σ_Z, and σ_Z is determined by precisely identifying where the σ'_Z distribution on its left side begins to deviate from zero. In order to quantify this location and its uncertainty, the 0.05 quantile statistic and the bootstrap technique are utilized.

Here is a brief description of the bootstrap technique and how it is utilized to determine σ_Z, based on Refs. [65, 66, 67]. The first step is to randomly sample the data distribution N times with *replacement*, obtaining N bootstrap samples. We chose N to equal the total number of events in the distribution, which is a common choice. The result is a "new" bootstrap distribution derived from the data distribution. The bootstrap distribution is distinct from the data distribution with high probability, but it should be representative of the data distribution. Next, the 0.05 quantile statistic is calculated over the bootstrap distribution. This bootstrap statistic represents a single estimation of σ_Z. The procedure is repeated ten thousand times, resulting in a distribution of bootstrap σ_Z's. It is from this final bootstrap σ_Z distribution that σ_Z is determined. σ_Z is given by the mean of the distribution, and the measurement uncertainty by the standard error of the mean. Figure 2.9 shows the bootstrap σ_Z distributions for 40 Torr, 400 V/cm, and the six Z. The distributions suggest the bootstrap technique provides a good estimate of σ_Z and its measurement error, because they are roughly symmetric about a central value and their widths are narrow. An indication of the "failure" of the bootstrap technique would be non-convergence of bootstrap statistic.

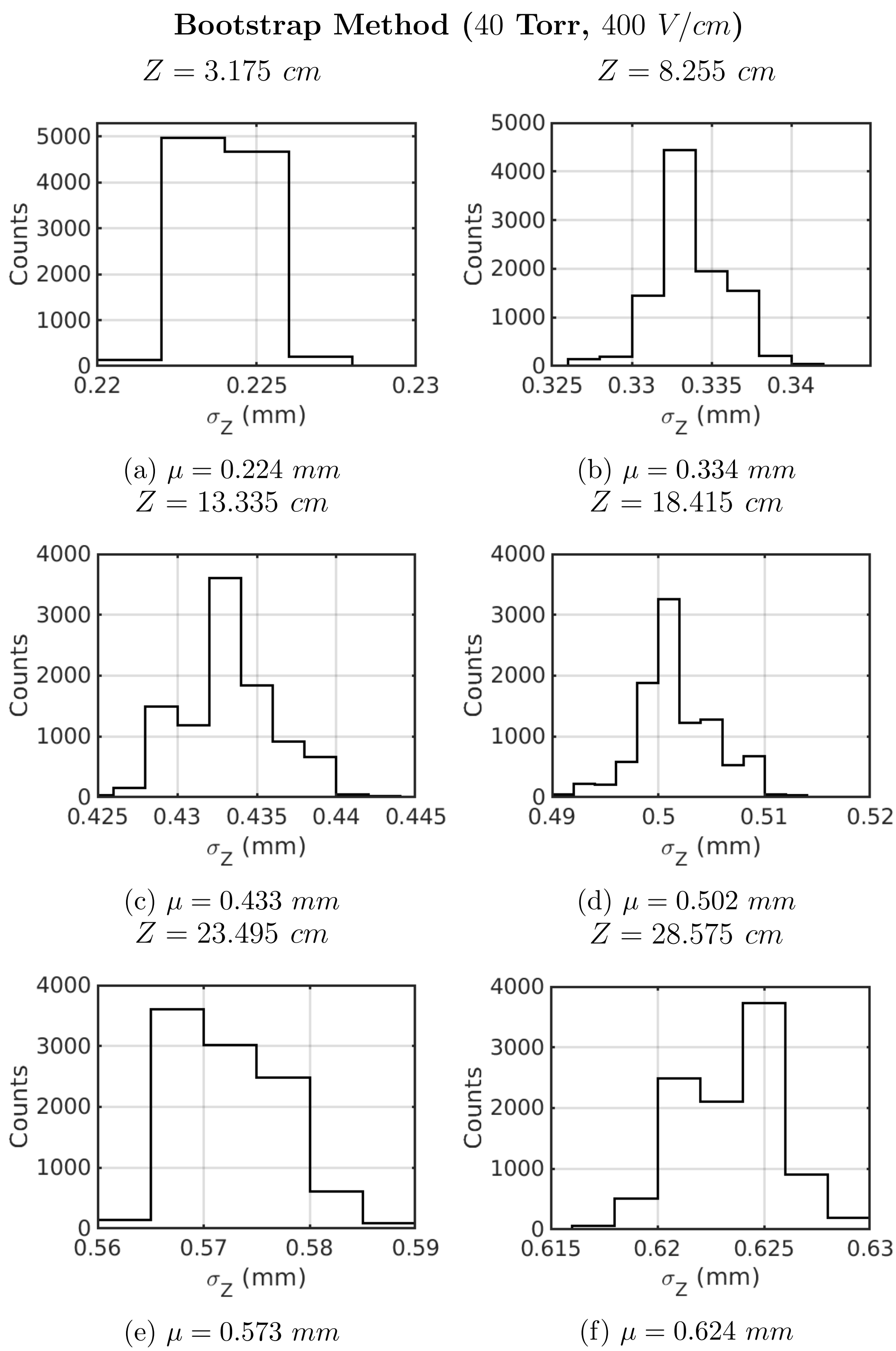

Figure 2.9: σ_Z is extracted from the σ'_Z distribution utilizing the Bootstrap Technique and the 0.05 quantile statistic. Shown are the bootstrap σ_Z distributions for 40 Torr, 400 V/cm for each Z. The mean and standard error of the mean for these distribution gives σ_Z and its associated measurement error.

2.6.3 Monte Carlo (MC) Technique

The second "extraction" technique extends the Monte Carlo simulation discussed in Section 2.5. First, unit height square-wave pulses are generated with lengths (widths) randomly selected from $\rho(\Delta Z_0)$. Second, each square pulse is convolved with a Gaussian of σ_{Sim}. This procedure is repeated over the range $\sigma_{Sim} = 0.15mm$ to $0.9mm$ in steps of $0.01mm$, which encompass the complete range of possible σ_Z based on the results of the Bootstrap Technique. Since σ_{Diff} is greater than or equal to $\sigma_{ThermDiff}$, the simulation starts with $\sigma_{Sim} = \sigma_{ThermDiff}$ and iteratively increases σ_{Sim} through the remaining range of σ_{Sim}. For each σ_{Sim} the test statistic χ is evaluated, where χ is the sum of the absolute difference between the measured distribution and the σ_{Sim} distribution; $\chi = \sum_i(|Data_i - Sim_i|)$, where i is the bin number. The best match is the σ_{Sim} distribution where χ is a minimum. Figure 2.10 shows the χ's at 40 Torr, 400 V/cm, and each Z. Unfortunately, this technique assumes σ_{Capt} and σ_{THGEM} are Gaussian effects which can be simulated with a single Gaussian, which is not strictly true. For example, the electron capture length, σ_{Capt} is likely to obey an exponential distribution. The shape of the σ_{THGEM} is unknown, and could be complicated. Also, not considered are the effects of nonuniform fields, charge loss, fluctuations in $\frac{dE}{dx}$, and non-straight trajectories due to alpha scatter.

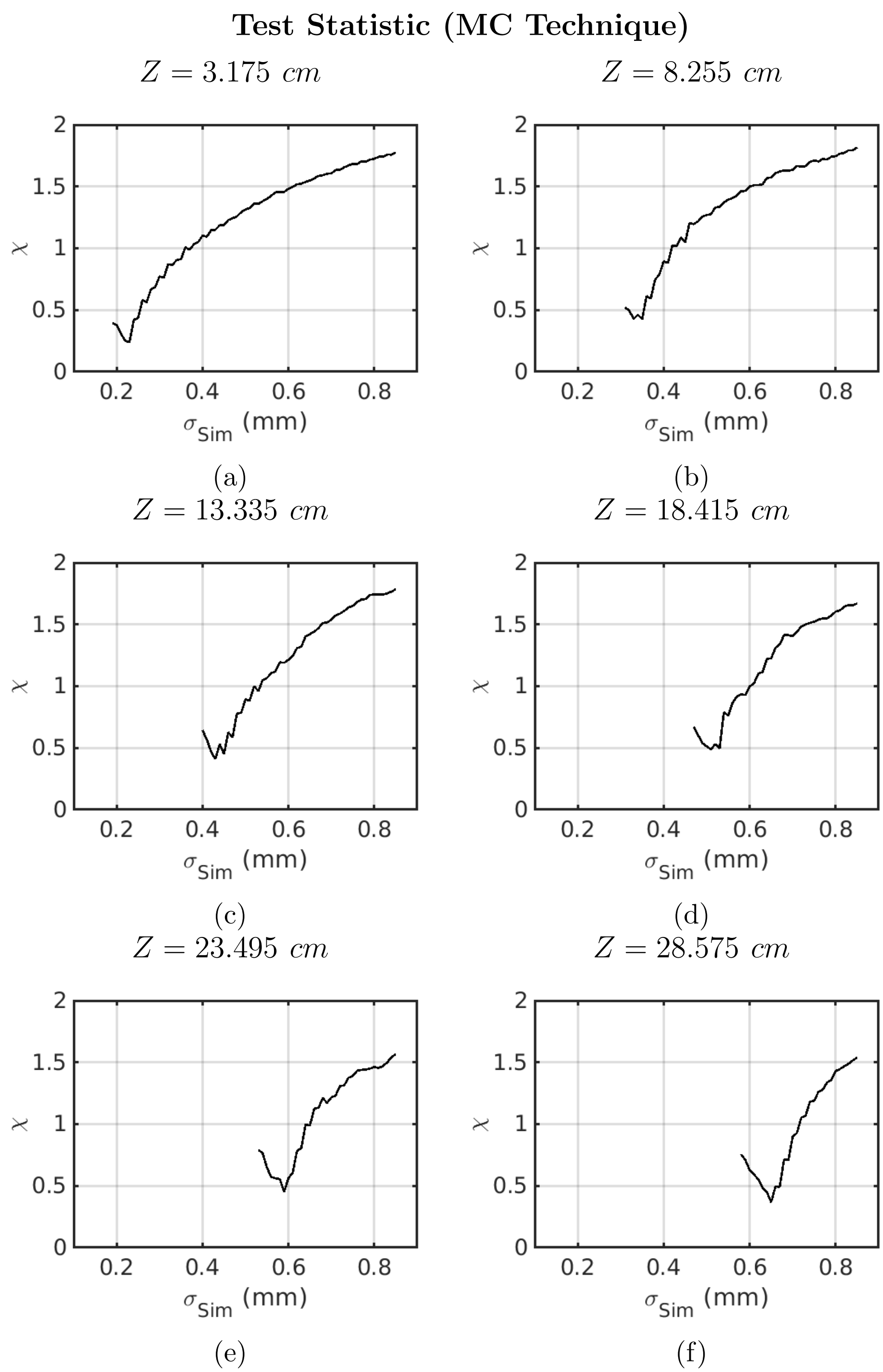

Figure 2.10: Test statistic χ for the MC Technique best-match σ_{Sim} at 40 Torr, and 400 V/cm.

Figure 2.11 shows the best-matched σ_{Sim} distribution (red) compared with the measured σ'_Z distributions at 40 Torr and $E_{Drift} = 400\ V/cm$ (black). Although the measured σ'_Z distributions are well matched in the large σ'_Z tail region, the measured σ'_Z distributions often have a slower rising time than predicted by the σ_{Sim} distributions. The mismatch for the small σ'_Z edge is more severe at large Z. Since $\Delta Z_0 \approx 0$ and σ_Z are expected to have the smallest σ'_Z, the MC Technique may be overestimating σ_Z for large Z. This would lead to a systematic increase in T_{Ion}. Future work is required to determine the cause and fix for the systematic. Nevertheless, the MC Technique is an independent check of the Bootstrap Technique.

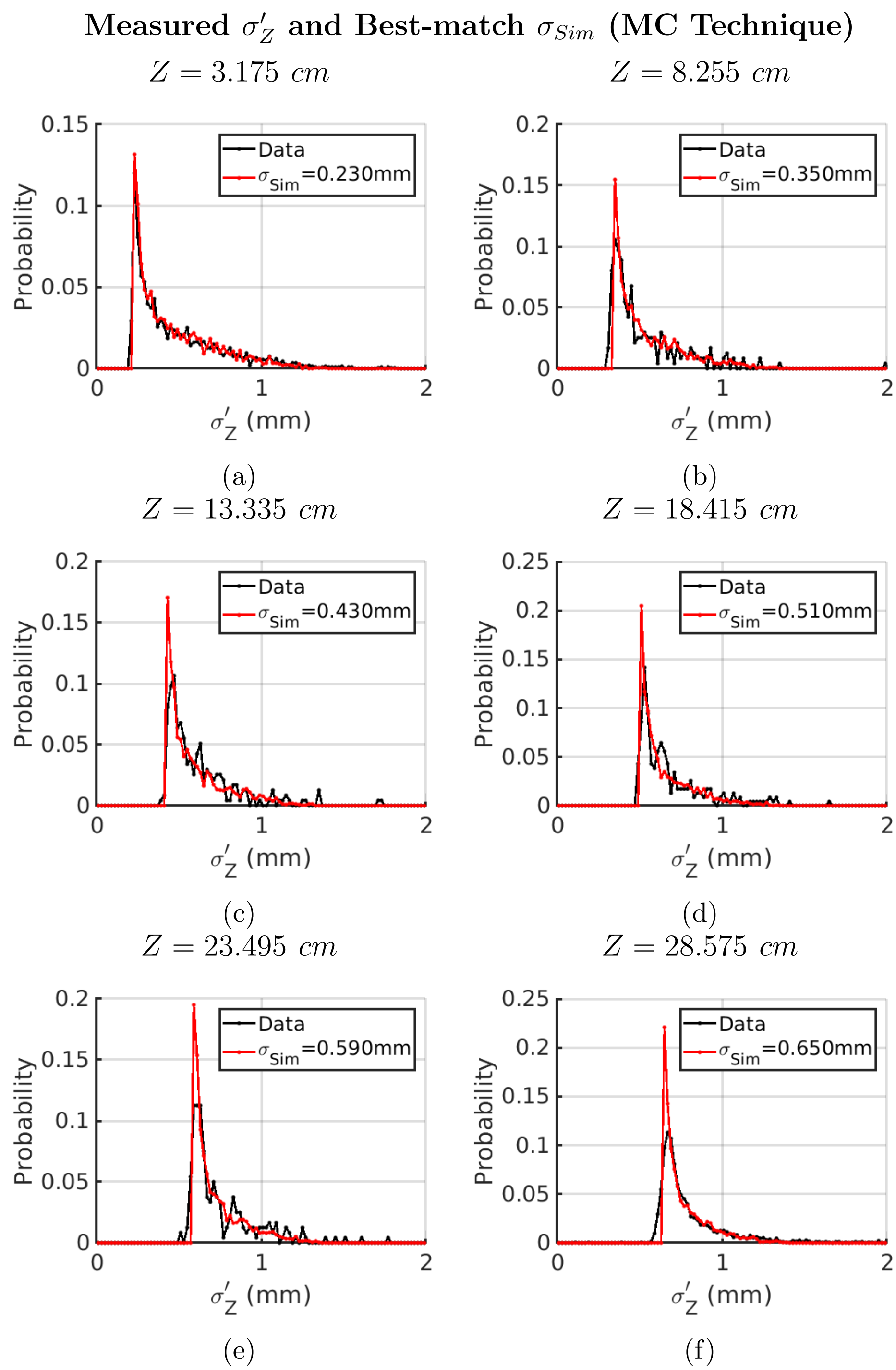

Figure 2.11: Best match σ_{Sim} distribution (red) compared to the experiment at 40 Torr and $E_{Drift} = 400\ V/cm$ (black).

2.7 Discussion and Results: Bootstrap Technique

This section discusses how the Bootstrap Technique is utilized to measure σ_{Diff}, σ_{Capt}, and σ_{THGEM}. In order to quantify the thermal behavior of the gas, T_{Ion} is measured and based on T_{Ion} the quantity $E_{NonTherm}$ is estimated. $E_{NonTherm}$ is the E_{Drift} corresponding to significant deviation from thermal behavior. $E_{NonTherm}$ is said to be "estimated" because its resolution is 200 V/cm (the granularity of the data) and its value is subjectively based on the E_{Drift} where T_{Ion} has deviated "significantly" from room temperature ($300K$). Consequently, the criteria for the transition to non-thermal behavior will be defined to be the E_{Drift} where $T_{Ion} > 350$. Also, the important quantity for the detector operation is the diffusion σ_{Diff}, which could potentially be small ($\approx 200\mu m$) even for "high" T_{Ion}.

These measurements are performed with two different techniques; the Constant E_{Drift} Technique and the Constant Z Technique. T_{Ion} is measured exclusively with the Constant E_{Drift} Technique with Equation 2.5. b is identified with the intercept, and σ_{Capt} and σ_{THGEM} are measured from b. The Constant Z Technique fits the curve of σ_Z versus E_{Drift} with the function $\sqrt{\sigma^2_{ThermDiff} + c}$, where c is the only fit parameter. It assumes $\sigma_{Diff} \approx \sigma_{ThermDiff}$, which is shown to be valid with the Constant E_{Drift} Technique.

2.7.1 Results: Constant E_{Drift} Technique

First, consider the thermal behavior at $P = 20$ Torr and the curve of σ^2_Z versus Z. Figure 2.12 shows the results for $E_{Drift} = 400\ V/cm$ (red), 600 V/cm (blue), and 800 V/cm (green). Since room temperature T_{Room} is 300 K, the T_{Ion}'s indicate non-thermal behavior by $E_{Drift}(P = 20Torr) = 600\ V/cm$ and the deviation increases with E_{Drift}. Consequently, $E_{NonTherm}(P = 20Torr) \leq 600\ V/cm$. Next, consider the results for $P = 30$ Torr in Figure 2.13. It suggests $E_{NonTherm}(P = 30Torr) \leq 800$ V/cm. The final pressure tested is 40 Torr. Similarly, Figure 2.14 shows the 40 Torr

$E_{NonTherm} \leq 800\ V/cm$. The T_{Ion}s are summarized in Figure 2.16, and $E_{NonTherm}$: $E_{NonTherm}(P = 20Torr) \leq 600\ V/cm$, $E_{NonTherm}(P = 30Torr) \leq 800\ V/cm$, and $E_{NonTherm}(P = 40Torr) \leq 800\ V/cm$.

20 **Torr** SF_6

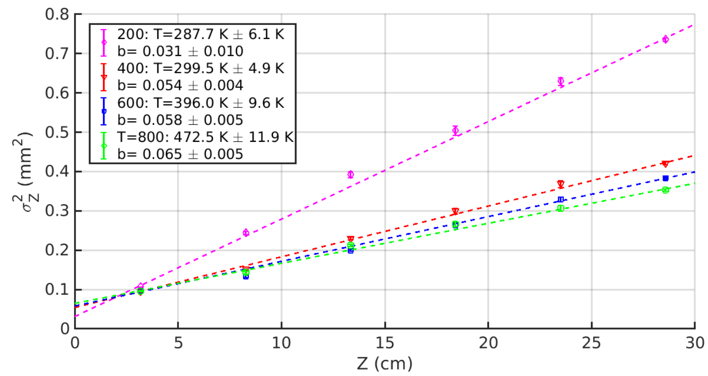

Figure 2.12: σ_Z^2 versus Z location for 20 Torr SF_6 and $E_{Drift} = 200\ V/cm$ (magenta), $400\ V/cm$ (red), $600\ V/cm$ (blue), and $800\ V/cm$ (green).

30 **Torr** SF_6

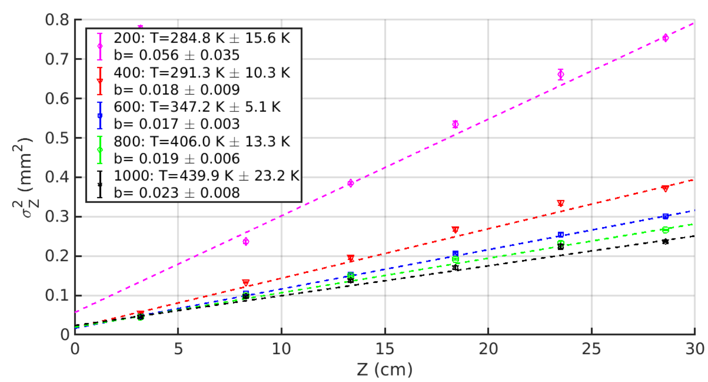

Figure 2.13: σ_Z^2 versus Z location for 30 Torr SF_6 and $E_{Drift} = 200\ V/cm$ (magenta), $400\ V/cm$ (red), $600\ V/cm$ (blue), $800\ V/cm$ (green), and $1000\ V/cm$ (black).

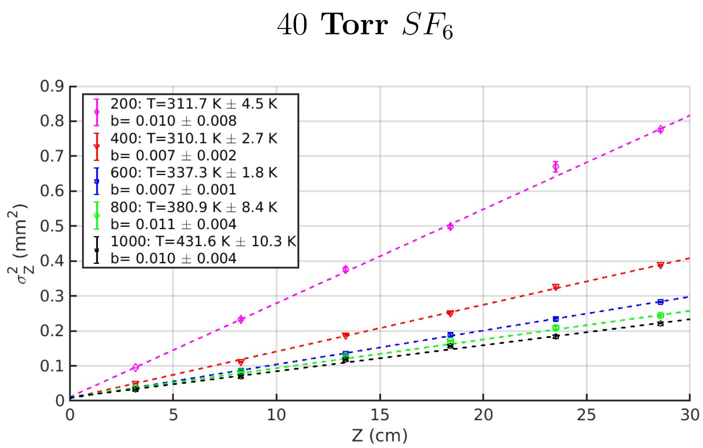

Figure 2.14: σ_Z^2 versus Z location for 40 Torr SF_6 and $E_{Drift} = 200\ V/cm$ (magenta), 400 V/cm (red), 600 V/cm (blue), 800 V/cm (green), and 1000 V/cm (black).

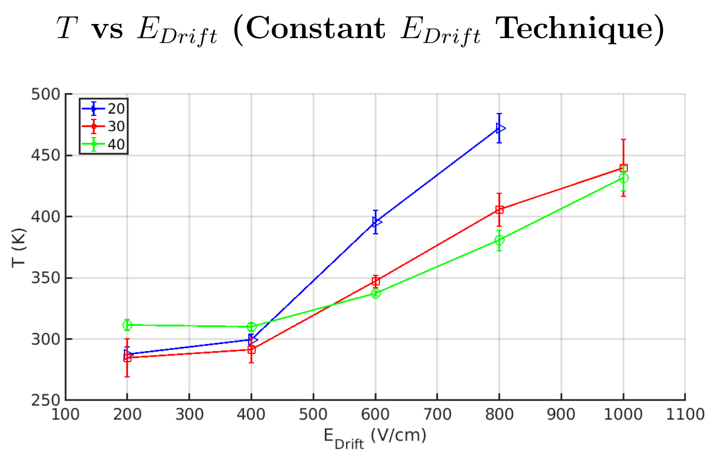

Figure 2.15: Summary of T vs E_{Drift} utilizing the Constant E_{Drift} Technique.

Next consider the intercept b, which is plotted for each pressure as a function of E_{Drift} in Figure 2.16. The 20 Torr experiment (blue) has the largest slope. The 30 Torr is next, and 40 Torr is approximately flat. There was a mistake during the data collection for the 30 Torr, 200 V/cm data, so this data is removed from the analysis. The reason for the trend of the increasing slope is σ_{Capt} dependence on E_{Drift} through the capture cross-section. Also, the results indicate as P decreases

σ_{Capt} increases. This is consistent with the capture length increasing with decreasing P due to the lower number density of the gas. Figure 2.16 supports the supposition that as P goes to large pressures σ_{Capt} goes to zero. Unfortunately, only three pressures were studied. Consequently, the intercept b_b cannot be plotted versus P and extrapolated to $P \to \infty$. Since $\sigma_{Capt}(P \to \infty) \to 0$, it is possible such a curve would asymptote toward a constant b_b. In any case, the best that can be done is the following assumption. Since the 40 Torr data is the largest pressure, assume a high pressure curve if measured would be not too far from the 40 Torr curve. If so, let the 40 Torr curve approximate the high pressure curve and take $E_{Drift} \to 0$. The result is $b_b(P = 40Torr)$ (dotted green), the intercept of the fit line for the 40 Torr data. Therefore, with this assumption/approximation $\sigma_{THGEM} = \sqrt{b_b(P = 40Torr)} = 99\mu m \pm 11\ \mu m$. This measurement is consistent with our prior rough estimation of the upper limit of σ_{THGEM} ($\sigma_{THGEM} < 0.2mm$), where the effect of σ_{Capt} was ignored entirely so that $b \approx \sigma^2_{THGEM}$ [101].

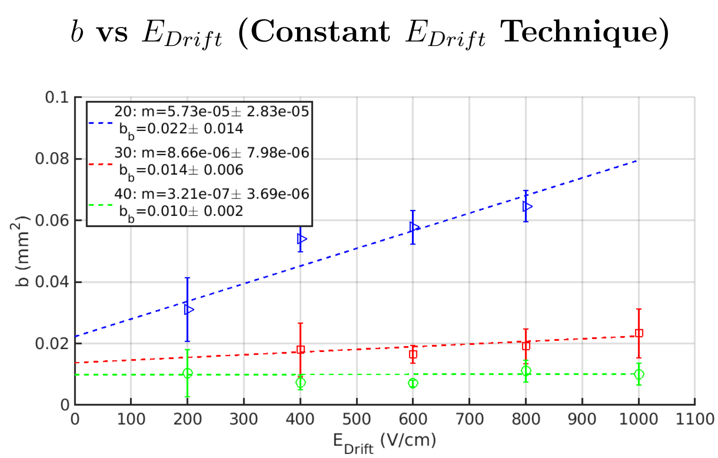

Figure 2.16: $b = \sigma^2_{Capt} + \sigma^2_{THGEM}$ is plotted versus E_{Drift} utilizing the Constant E_{Drift} Technique.

If this value for σ_{THGEM} is used, σ_{Capt} can be determined from b as a function of E_{Drift} ($\sigma_{Capt} = \sqrt{b - \sigma^2_{THGEM}}$). The result is shown in Figure 2.17. The σ_{Capt} are consistent with the capture cross-section for SF_6, which estimates the capture length to be of order 1 μm to 10 μm [101, 112]. Unfortunately, the data points at 40 Torr 400 V/cm and 600 V/cm are zero since for those experiments b is slightly less than $b_b(P = 40Torr)$. Lastly, σ_{Diff} is estimated by subtracting in quadrature σ_{Capt} and σ_{THGEM} from σ_Z. The result is summarized in Figure 2.18, where each Figure plots σ_{Diff} as a function of E_{Drift} for a fixed Z.

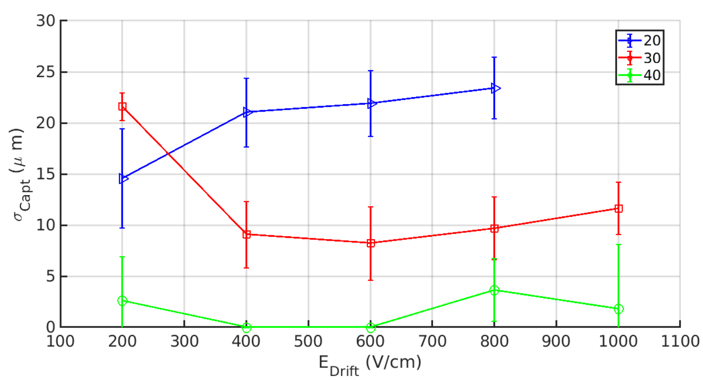

Figure 2.17: Using the Constant E_{Drift} Technique, σ_{Capt} versus E_{Drift} for 20 (blue), 30 (red), and 40 (green) Torr. The measurement of σ_{THGEM} utilizing the Constant E_{Drift} Technique is used; $\sigma_{THGEM} = 99 \pm 11$ μm.

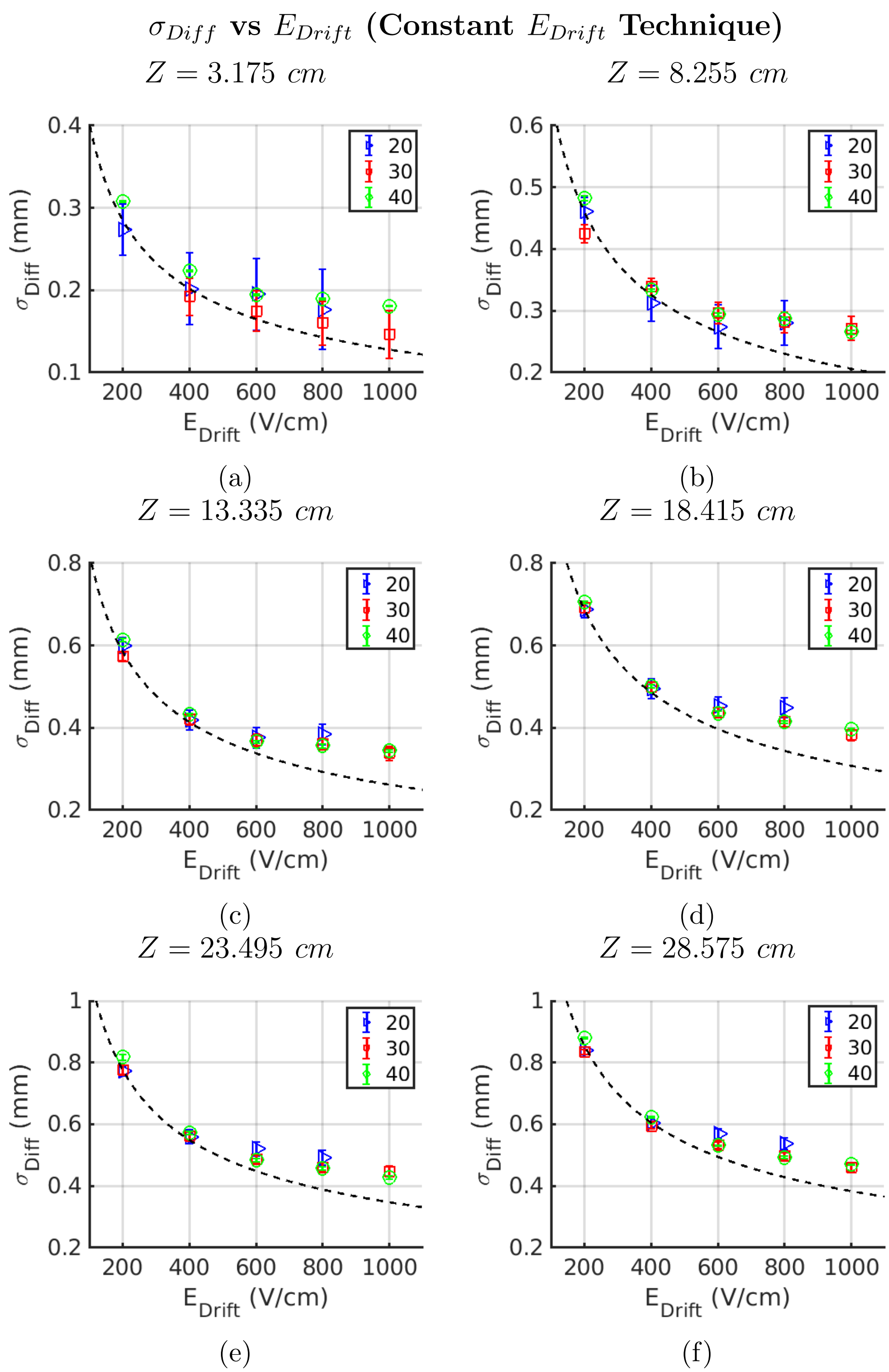

Figure 2.18: σ_{Diff} vs E_{Drift} for 20 Torr (blue), 30 Torr (red), and 40 Torr (green), where σ_{THGEM} and σ_{Capt} are taken from the Constant E_{Drift} Technique: $\sigma_{THGEM} = 99\mu m \pm 11\ \mu m$ and σ_{Capt} from Figure 2.17.

2.7.2 Constant Z Technique

The following is a redundant measurement of $E_{NonTherm}$ and σ_{Capt} utilizing the Constant Z Technique. It is meant to be a verification of the measurements from the Constant E Technique. The first step is to plot σ_Z versus E_{Drift} for a fixed (constant) Z. Figure 2.19 shows the results, where the black dotted line represents $\sigma_{ThermDiff}(E_{Drift})$ at $L = Z_{Source}$. Assuming $\sigma_{Capt}(E_{Drift}) \approx const$ and $\sigma_{Diff} = \sigma_{ThermDiff}$, the red (30 Torr) and green (40 Torr) dashed curves are the fits to the function $\sqrt{\sigma^2_{ThermDiff} + c}$. The only fit parameter $c = \sigma^2_{Capt} + \sigma^2_{THGEM}$. The 20 Torr experiment is not fitted because it is highly non-thermal for at least half the data points ($E_{Drift} \geq 600\ V/cm$). Based on when the 30 Torr and 40 Torr curves begin to deviate significantly from the fits, $E_{NonTherm}(P = 30Torr) \approx 800\ V/cm$ and $E_{NonTherm}(P = 40Torr) \approx 1000\ V/cm$. These measurements are consistent with the Constant E Technique.

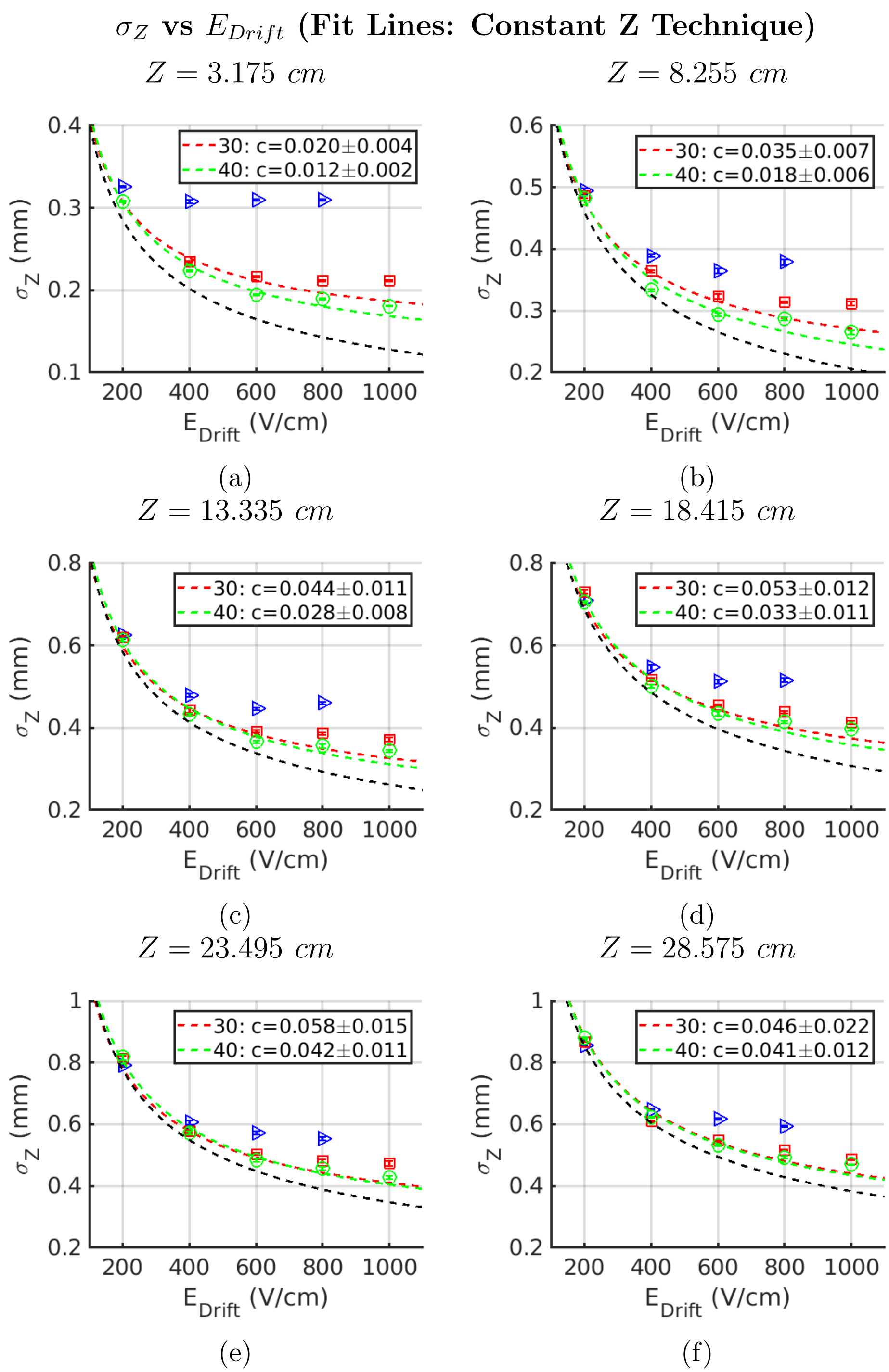

Figure 2.19: σ_Z vs E_{Drift} for 20 Torr (blue), 30 Torr (red), and 40 Torr (green). The black dashed line is $\sigma_{ThermDiff}(E_{Drift})$ at each Z. The red (30 Torr) and green (40 Torr) dashed lines are the fit curves for the function $\sqrt{\sigma^2_{DiffTherm} + c}$, where c is the only fit parameter.

Figure 2.20 shows the c parameter at each Z for 30 Torr (red) and 40 Torr (green). Several trends are clear from the Figure. The first is that c increases linearly with Z. The linear dependence is because $\sigma^2_{ThermDiff} \propto Z$. The red and green dashed lines are the linear fits. The second trend is $c(P = 30Torr) > c(P = 40Torr)$. The intercept of the fits are $b_c(P = 30Torr) = 0.017mm^2 \pm 0.007mm^2$ and $b_c(P = 40Torr) = 0.007mm^2 \pm 0.003mm^2$. Similarly taking $\sigma_{Capt}(P = 40Torr) \approx 0$ results in the measurement $\sigma_{THGEM} = \sqrt{b_c(P = 40Torr)} = 82\mu\ m \pm 20\ \mu m$. Using this value of σ_{THGEM}, gives $\sigma_{Capt}(P = 30Torr) = 8.5\mu \pm 4.2um$. Both of these measurements are consistent with the Constant E Technique.

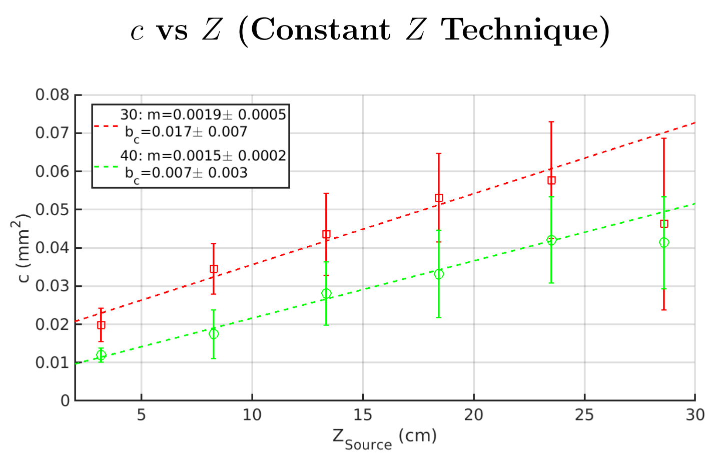

Figure 2.20: Utilizing the Constant Z Technique c is plotted versus Z, where the fit curve is $\sigma_Z = \sqrt{\sigma^2_{DiffTherm} + c}$ and c is the fit parameter.

2.8 Comparison with MC Technique

This section briefly discusses the results of the MC Technique and compares with the Bootstrap Technique. Figures 2.21, 2.22, and 2.22 utilize the Constant E Technique to measure T_{Ion} and $E_{NonTherm}$. Figure 2.21 summarizes the results and indicates non-thermal behavior at much lower E_{Drift} than the Bootstrap Method. The reason for the discrepancy is likely related to the slower rise time of the data compared to the simulation, which results in a poor matching of the left edge of the distributions. Consequently, additional work is required to improve the Monte Carlo simulation so that effects such as charge loss, non-uniform fields, fluctuations in $\frac{dE}{dx}$, non-straight trajectories, etc., which might effect large Z more than small Z.

20 **Torr** SF_6 **(MC Technique)**

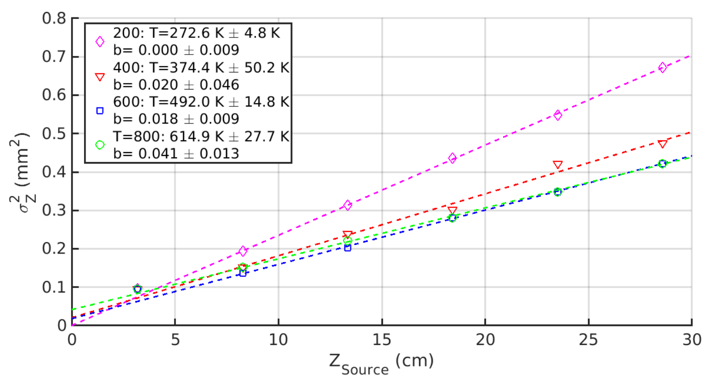

Figure 2.21: Utilizing the MC Technique, σ_Z^2 versus Z location for 20 Torr SF_6 and $E_{Drift} = 200\ V/cm$ (magenta), $400V/cm$ (red), 600 V/cm (blue), and 800 V/cm (green).

30 **Torr** SF_6 **(MC Technique)**

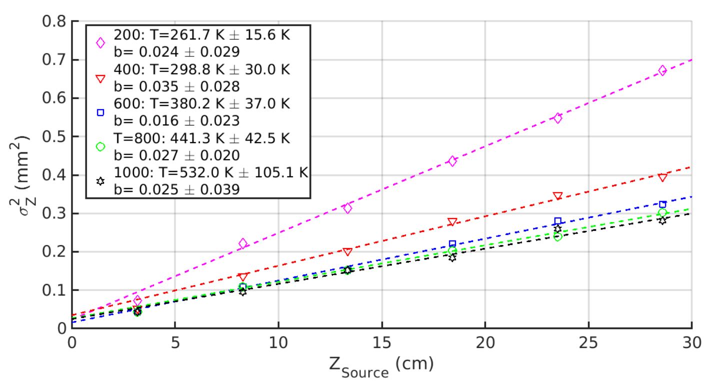

Figure 2.22: Utilizing the MC Technique, σ_Z^2 versus Z location for 30 Torr SF_6 and $E_{Drift} = 200\ V/cm$ (magenta), 400 V/cm (red), 600 V/cm (blue), 800 V/cm (green), and 1000 V/cm (black).

40 **Torr** SF_6 **(MC Technique)**

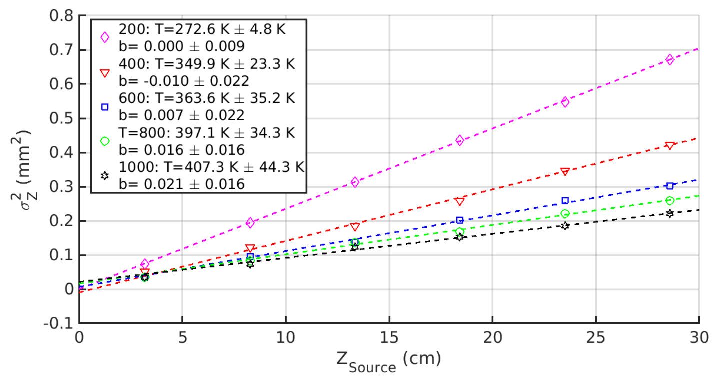

Figure 2.23: Utilizing the MC Technique, σ_Z^2 versus Z location for 40 Torr SF_6 and $E_{Drift} = 200\ V/cm$ (magenta), 400 V/cm (red), 600 V/cm (blue), 800 V/cm (green), and 1000 V/cm (black).

T **vs** E_{Drift} **(MC Technique)**

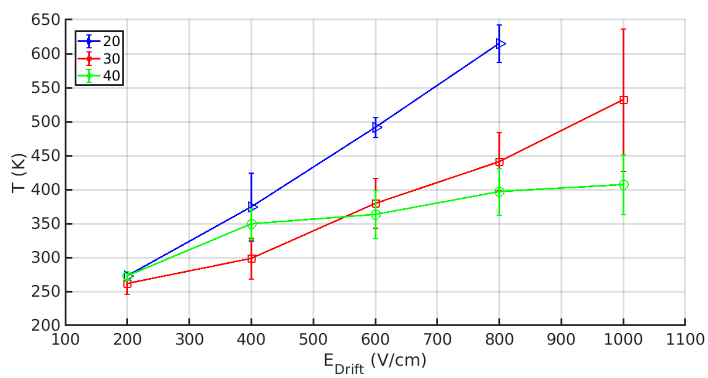

Figure 2.24: Utilizing the MC Technique, summary of T versus E_{Drift}.

2.9 Conclusion

In this chapter the thermal negative ion nature of SF_6 was tested at 20, 30, and 40 Torr. The measurements were performed using two independent techniques. The first technique measured the square of the total width of the track σ_Z^2 versus the ^{210}Po

alpha source location Z. Utilizing this technique, the effective temperature of the negative ions T_{Ion} and the drift field E_{Drift} where significant deviation from thermal behavior begins was measured. The results are: $E_{NonTherm}(P = 20Torr) \leq 600$ V/cm, $E_{NonTherm}(P = 30Torr) \leq 800$ V/cm, and $E_{NonTherm}(P = 40Torr) \leq 800$ V/cm. The quadratic sum of the track spreading due to the capture length σ_{Capt} and the THGEM pitch σ_{THGEM} was measured with the parameter $b = \sigma^2_{Capt} + \sigma^2_{THGEM}$ and extrapolated to $Z = 0$. Assuming $\sigma_{Capt}(P = 40Torr) \approx 0$, σ_{THGEM} was measured from b; $\sigma_{THGEM} = 99\mu m \pm 11$ μm. Using the measured σ_{THGEM}, σ_{Capt} was measured as a function of E_{Drift}. The second measurement technique assumed thermal diffusion and fit the curve of σ_Z versus E_{Drift} at constant Z with the function $\sqrt{\sigma^2_{ThermDiff} + c}$. This method yielded the following measurements; $\sigma_{THGEM} = 81.5$ $\mu m \pm 20$ μm, and $\sigma_{Capt}(P = 30Torr) = 8.5\mu m \pm 4.2$ μm.

In hindsight, the measurements could be improved with the following changes to the experiment. The first improvement is to use a narrower collimator, despite the rate reduction. The narrower collimation is the most direct method to decrease the spot size of the alpha tracks and the errors associated with extracting σ_Z from the measured σ'_Z distribution. Another improvement is to increase the statistics, especially for the intermediate Z region. Also, performing experiments at higher pressures in order to more effectively extrapolate to $P \rightarrow \infty$ and $E_{Drift} \rightarrow 0$, where $\sigma_{Capt} \rightarrow 0$. Another idea is to reduce the experimental noise by placing a readout board behind the THGEM and reading the charge from the readout board instead of the THGEM. Lastly, collect data with a faster data acquisition system in order to better resolve the structure of the shortest tracks and utilize less filtering.

Chapter 3

Discrimination and Directionality in SF_6

3.1 Introduction

This chapter presents the studies of the discrimination and the directionality of a 1D TPC operated in 30 Torr SF_6 gas. This pressure was selected because we could operate the TPC without gas breakdown at the highest drift field (1029 V/cm), where diffusion was found to be the lowest. The measurements presented in this chapter are the first discrimination and directionality measurements in a SF_6 TPC for any type of readout scheme, and they are the first measurements of discrimination and directionality in any TPC utilizing 1D readout.

First consider discrimination. Discrimination is the ability to distinguish particles based on the measured properties of the recoiling particle. The interacting particle can deposit energy through scintillation [68, 69], phonons [70, 71], and ionization [72, 73, 74] into the detection material. In the case of scintillation, the particle interacts inelastically with an atom, exciting it a to higher electronic or vibrational mode. When the atom deexcites it can emit a scintillation photon. Phonons are produced through an elastic scatter with the target material, exciting the crystal or depositing heat. Ionization consists of the electron-ion pairs created when radiation (photons or charged particles) strip an electron from a neutral atom. For a review of particle energy loss in matter see Ref. [75, 76, 77].

Often discrimination involves designing the experiment to measure the energy deposited into multiple channels. The ratio of the energy measured through each channel is different depending on the interacting particle [78, 79, 80]. Discrimination techniques involving the measurement of a single channel can involve pulse shape analysis [81, 82, 83], pulse duration [49], and scintillation timing [84]. In the case of low pressure TPC detectors, the energy and the length of the ionization signal can be utilized for discrimination. This is because electronic recoils in a low pressure gas tend to lose less energy per unit length of track ($\frac{dE}{dx}$) than nuclear recoils at the same energy. Consequently, electronic recoil tracks tend to be longer than nuclear recoils for a given energy. As a result, discrimination in low pressure TPCs is possible based on range (track length) versus energy.

The interesting regime for WIMP searches is the low energy regime, where electronic recoil and nuclear recoil tracks begin to look similar. This is the result of several factors. The first is that track lengths get shorter with energy and eventually become unresolved due to diffusion or the granularity of the readout electronics. Another factor is the charge of the recoiling ion. The following description is taken from Hitachi [86]. The primary interaction creates the ion with a certain charge. At low energies, the ion tends to acquire electrons as it recoils and neutralize. When the ion is neutral no more ionization is created and the remaining energy is deposited through collisions with other neutral molecules (heat). At this point discrimination is lost. We define the energy at which this occurs to be E_{Disc}. In terms of the range versus energy E_{Disc} is where the electronic and the nuclear recoil distributions overlap. This work is the first to study discrimination in a TPC detector that utilizes SF_6.

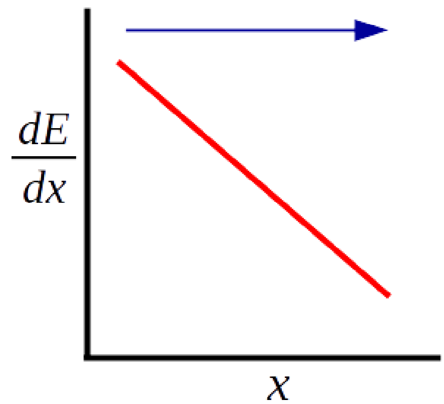

Figure 3.1: A depiction of the ionization energy lose per unit length $\frac{dE}{dx}$is for nuclear recoils. There is ionization $\frac{dE}{dx}$ at the start (left) compared the end (right). The arrow represents the direction of the nuclear recoil.

The other measurements discussed in this chapter involve the directionality of nuclear recoils in SF_6. Directionality comes in two forms: axial and vector (head-tail). This work measures the latter, which is due to an intrinsic asymmetry in the ionization charge profile along the recoil track. Previous measurements indicate that the ionization $\frac{dE}{dx}$ decreases with the recoil energy [85, 87, 88, 89, 90]. Consequently, the level/power of the directional signal also decreases with the recoil energy. The energy where the directionality disappears will be referred to as E_{Skew}.

Directionality is a crucial step in our track reconstruction procedure. Track reconstruction begins by constraining the track to lie along an axis. For 2D readout the axis lies in the readout plane, and for 1D readout the axis is along the readout dimension. In either case, the result is a track with axial direction, where the vector direction of the track has two options. The ambiguity is resolved by exploiting the

Bragg curve (specifically the ionization channel) for low energy nuclear recoils. The ionization Bragg curve shows the ionization energy loss $\frac{dE}{dx}$ along the track is higher at the start (tail) of the track compared to the end (head) [85, 87, 88, 89, 90]. The charge distribution is depicted for 1D in Figure 3.1. It shows the vector direction of the track starts from the region of ionization $\frac{dE}{dx}$ (left) and points toward the region of low ionization $\frac{dE}{dx}$ (right). In 1D, the skewness can be either positive (more charge at the start of the track), or negative (more charge at the end of the track). Figure 3.2 shows an example negatively skewed signal (left) and a positively skewed signal (right).

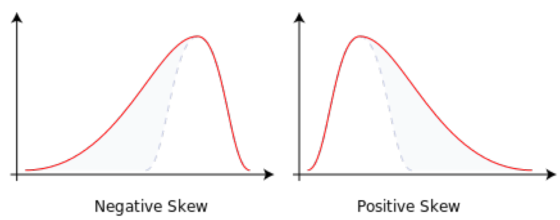

Figure 3.2: Diagram depicting negative (left) and positive (right) skewness. Credit: Ref. [91].

Other factors affecting discrimination and directionality in TPCs are the gas pressure and the quenching factor Q [85, 87, 88, 89, 90]. Since we have measured the track lengths to decrease as the gas pressure increases, the level/power of the discrimination at a given energy decreases with pressure. Consequently, discrimination is often better for low gas pressures. As for the quenching factor, it is defined to be:

$$Q = \frac{E_{ee}}{E_R}, \tag{3.1}$$

where E_{ee} and E_R are respectively the energy deposited into the ionization channel (electron equivalent energy) and the kinetic energy of the recoil [87]. Of interest in this work are nuclear quenching factors, which mainly depend on the target material, and the energy of the recoil [87]. Consequently, Q must be measured for the target and the energy range of interest. If Q is known the recoil energy can be extracted from the measured E_{ee} of the track. For electronic recoils Q is approximately 1. Affecting the discrimination and the directionality is the energy dependence of Q, which typically decreases monotonically with energy at low energies [85, 87]. As a result, at a particular recoil energy the nuclear $\frac{dE}{dx}$ and the electronic $\frac{dE}{dx}$ converge, resulting in no discrimination even with perfect track reconstruction and track resolution. Consequently, the recoil energy where discrimination disappears depends on the Q factor. Q's have been measured for many nuclei, recoil energy ranges, and target gases. For example, Hitachi measures Q's for: He, Ne, and Ar and the ions Xe and C, N, O, Ar, and Pb in Ar [85]. He also proposes theoretical models for Q in Ref [86]. Due to their importance in the dark matter community, there are facilities dedicated to measuring nuclear quenching factors. One such facility is the SICANE facility, which measures Q's for cryogenic detectors using nuclear recoils induced by monoenergetic neutron beams [87]. Unfortunately, Q has yet to be measured for the gas mixtures and pressures utilized in this work. Therefore, this work quotes the track energies in terms of the electron equivalent energy E_{ee} in units of $keVee$.

This chapter characterizes the discrimination and directionality of SF_6 by measuring E_{Disc} and E_{Skew} with a simple 1D readout scheme. Often the discrimination level/power is characterized by the rejection factor, which is the number of nuclear recoils per electronic recoil that reside in the nuclear recoil band. For reasons that will be come clear, the rejection factor is not calculated in this chapter. Instead, it will be returned to in Chapter 5. Although the nuclear and electronic recoil populations merge at higher energy in 1D compared to 2D or 3D readout, the 1D readout is an extremely low-cost option that has not been investigated for directional dark matter experiments. The 1D readout requires 1 electronic channel whereas 2D or 3D readouts require many 1000's to instrument strips or pixels, greatly increasing the cost and complexity of the experiment. The 1D TPC detector is described in Section 3.2.

3.2 Experimental Apparatus

The experimental setup is identical to our setup in Ref. [101]. The TPC detector is comprised of the 60 *cm* acrylic cylindrical tube, 2.54 *cm* thick with a 30.5 *cm* inner diameter, sealed on the ends with the aluminum anode and cathode plates. In this way the acrylic vessel serves as both the vacuum vessel and the TPC. The cathode is connected to the high voltage power supply, which is able to provide a maximum voltage of -60 kV. Field rings along the length of the interior of the cylinder ensure the uniformity of the drift field along the detector axis. Each resister connecting adjacent field rings is $56M\Omega$. The detector and the detailed SolidWorks schematic of the detector (Eric Lee) are shown in Figures 3.3 and 3.4 respectively. The acrylic high voltage shield is positioned over the cathode side of the detector for safety.

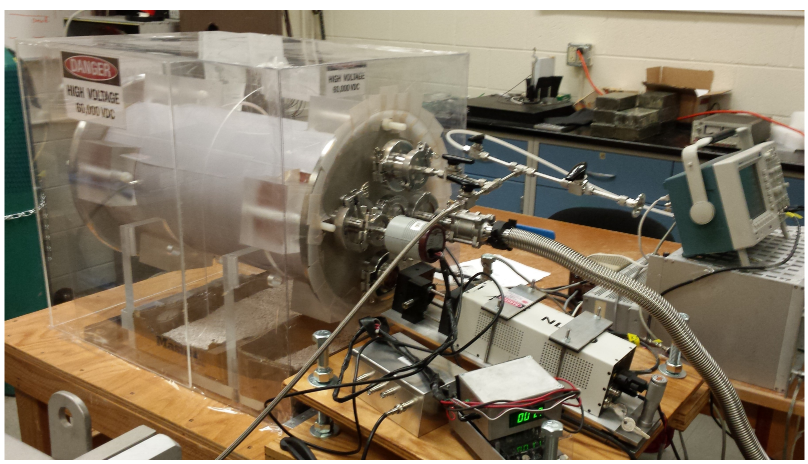

Figure 3.3: The 60 *cm* acrylic cylindrical vacuum vessel, aluminum anode (right), and cathode plate (left). The NL100 laser is mounted in front of the anode plate, and the digital oscilloscope for data acquisition is on the right edge.

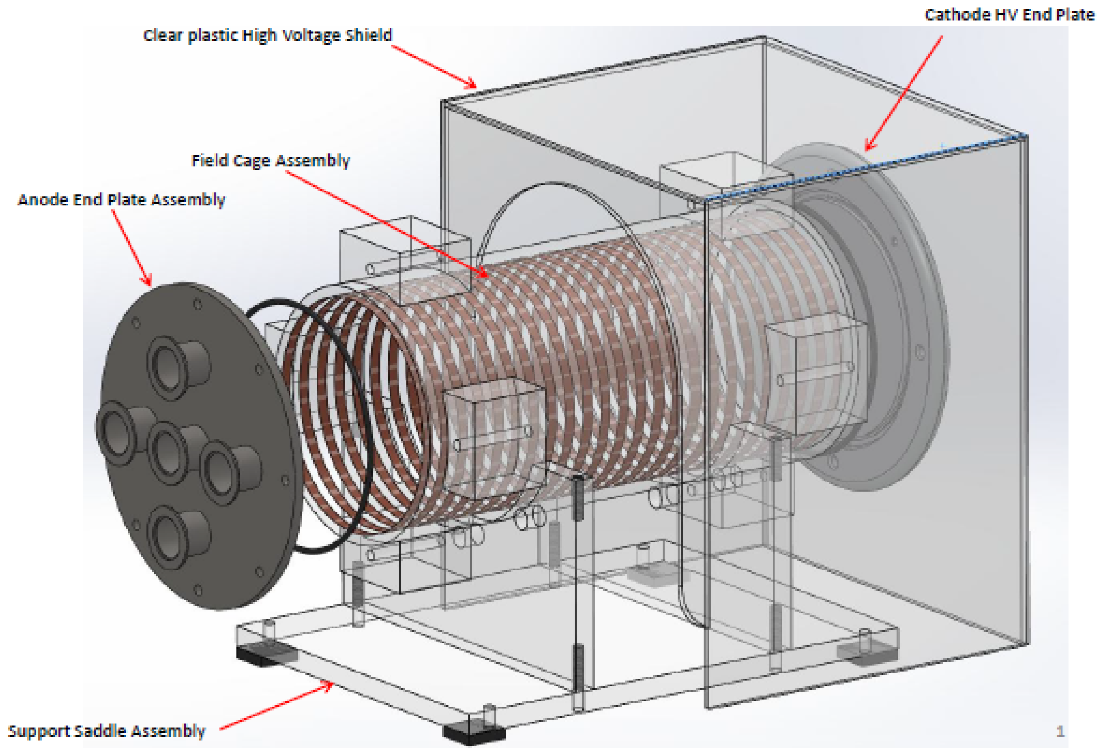

Figure 3.4: Schematic of the detector components of the 60 *cm* acrylic cylindrical detector. Credit: Ref. [101].

Similar to the TPC experiment discussed in Section 2.2, a THGEM with 3 *cm* by 3 *cm* active region and 9.5 *cm* by 9.5 *cm* copper plating serves as both the gain stage and 1D readout for the primary ionization of recoil tracks produced in the TPC volume. The surface facing the detector interior is grounded and the anode-facing surface is raised to high voltage and connected to the ORTEC 142 charge sensitive preamplifier. The voltage signal from the preamplifier is acquired with the Tektronix TDS 3054C digital oscilloscope and the National Instruments software. Figure 3.5 shows the THGEM and the switchable on/off ^{55}Fe source used for the energy calibrations.

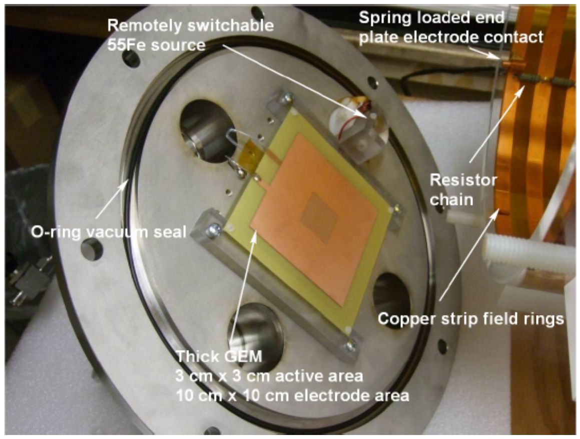

Figure 3.5: Interior surface of the 60 *cm* acrylic cylindrical detector anode plate. Credit: Ref. [101].

3.3 Detector Preparation and Water Contamination

This section describes the motivation for the acrylic cylindrical design of the detector and an unforeseen drawback. The DRIFT detector (see Section 1.6) is composed of a steel vacuum vessel that houses the TPC. The vacuum vessel has sharp corners and is grounded, requiring an insulating gap between it and the TPC. The cylindrical design is employed to avoid sharp corners where large electric fields are created and gas breakdown can occur. The acrylic material is utilized because of its low cost, ability to hold vacuum, and electrical insulation, which allows the vacuum vessel and TPC to be integrated into a single unit. Although the acrylic cylindrical detector design improves upon the DRIFT detector design, it was discovered that the acrylic absorbs water and suffers from a large amount of outgassing. Since acrylic is porous, it easily absorbs gas molecules into its surfaces. Consequently, it is known to be a "dirty" material. These ingassed molecules can later be outgassed and contaminate the gas mixture. For this reason, acrylic is generally avoided in vacuum systems. Contaminates typically include low levels of water, nitrogen, oxygen, and other compounds. Water vapor is especially troublesome because it has a strong tendency to coat surfaces in a thin molecular layer and thus is difficult to remove. A common technique to remove surface level contaminants like water from detector components is to bake them. However, this technique cannot be applied to acrylic because acrylic warps when heated to the high temperatures needed for baking. This section describes the significant issue of water contamination and the procedure implemented to minimize it.

The following technique is employed to reduce outgassing contamination into the detector. First, the detector is pumped on with the roughing pump for several days prior to experiments. Second, the detector is placed in a low humidity environment by surrounding it with a thin, plastic shell containing desiccant. Next, the detector is flushed two times with 200 Torr SF_6 and pumped to baseline. This reduces the residual contamination in the vessel by a factor of about $(\frac{1}{200})^2$. Then the detector is quickly raised to pressure and voltage to minimize the time the acrylic can outgas into the vessel before the experiment begins. Once the detector is ready, a short laser calibration (described in Section 3.4) is performed to verify the signal waveforms are as expected, indicating minimal water contamination. A detailed description of the strong distortion of the waveforms due to water vapor is described in Ref [101]. This procedure works to stabilize the gas for 3 or 4 hours, which is long enough for the studies in this work. Consequently, water contamination is bad for all gas mixture, but is especially bad for SF_6-based mixtures. T Therefore, future designs of the TPC should take this into consideration and some thought should be given to using other materials such as glass [1].

[1]Recommendation based on conversation with Dr. Paul Schwoebel.

3.4 Charge Creation

The experiment requires the following ionization sources: the δ function ionization tracks, which are produced via the ejection of electron from the cathode by the Stanford Research Systems (SRS) NL100 337.1 nm pulsed nitrogen laser; the DD generator, which produces neutron-induced nuclear recoils within the drift volume; the ^{55}Fe source, which create 5.9 $keVee$ x-rays for the energy calibration (described below); the ^{60}Co source, which creates gamma-ray induced electronic recoils within the drift volume; and the background radiation, which consists mostly of cosmic rays and occasional Radon Progeny Recoils (RPRs). See Section 1.6.3 for a description of RPRs. This section describes in detail the use of each source.

The laser is utilized to repeatedly create identical point-like primary ionization events along Z. This is done as is depicted in Figure 3.6. The laser is mounted in front of the anode plate such that the laser pulses passes through a quartz window located on the anode plate. The laser pulses travel through the gas volume and are impingent on the inner surface of the cathode. This causes photoelectrons to be ejected from the cathode and subsequently captured by SF_6. Since each laser pulse impinges on the same location on the cathode, each ionization cluster and resulting signal are nearly identical. As Chapter 2 verified, starting with a δ function ionization event is preferred in order to precisely measure the diffusion, which is the broadening of the charge distribution as the charge drifts to the readout. Since the ionization generated at the cathode is point-like and occurs at the same Z, 58.3 cm (total length of drift volume), this technique is ideal to measure the diffusion and the drift velocity of each negative ion drift species. In Ref [101], the reduced mobilities (see Equation 3.2) for SF_6^- and SF_5^- and the diffusion are measured. Also, performing a laser experiment is important in order to verify the quality (low water content) of the gas. The issue of water contamination is presented in Section 3.3. In order to verify the drift velocity, the diffusion, and the gas quality, a laser calibration experiment is performed before and after all science experiments. In Section 3.5 the mobilities and the diffusion measured in this work are compared to Ref [101].

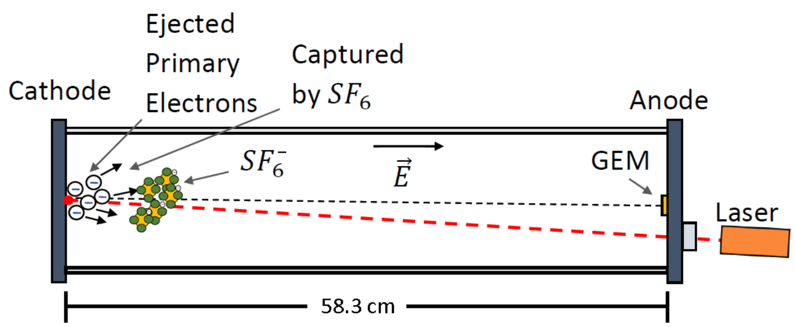

Figure 3.6: Schematic of NL100 laser ejecting electrons from the cathode and subsequent capture by SF_6^-.

The DD generator produces an isotropic beam of 2.2 MeV neutrons. These neutrons are utilized to create nuclear recoils within the drift volume, where the nuclear recoils are the events of interest in order to characterize the detector response to prospective WIMP induced nuclear recoils. The DD generator is positioned near the GEM-side and the Cathode-side of the detector and approximately aligned such that the target plane coincides with the detector axis. The shorthand "GEM" and "Cathode" will be used to refer to runs with the DD Generator positioned on the GEM-side and the Cathode-side respectively. The placement of the DD generator on each side of the detector allows for the directional study of low energy nuclear recoil tracks maximally projected onto the readout dimension. Unfortunately, it also produces a high rate of gamma-rays, which frequently interact in the detector and create electronic recoils. Therefore, due to the slow acquisition rate of the oscilloscope the data collected is predominately electronic recoils. This makes acquiring nuclear recoil statistics difficult. In order to help alleviate the problem, I developed a custom python module to operate the oscilloscope, which increased the data collection rate by a factor of 2 to 3 over the provided Labview software. Unfortunately, this decrease in the oscilloscope dead-time was not sufficient for the low energy regime of interest (tens of $keVee$). Also, we performed several DD neutron experiments with lead bricks in place in order to shield the detector from the gamma-rays. We observed that, although the overall acquisition rate is reduced, the neutron-induced nuclear recoil rate did not appear to increase relative to the electronic recoil rate. Therefore, it was unclear how beneficial it was to incorporate the lead bricks. The solution that is utilized in this chapter is to raise the detector energy threshold until the rate of nuclear recoils and electronic recoils are comparable. The results are described in Section 3.9.

In order to determine the nuclear recoil energy, an ^{55}Fe calibration experiment is performed. First, the remote-switchable ^{55}Fe source located on the anode plate is opened and the 5.9 $keVee$ X-rays are allowed to interact in the detector. Next, the charge (area) for each ^{55}Fe current signal is calculated and the result is histogrammed. Since the all events correspond to 5.9 $keVee$, distribution is fit with a Gaussian, where the peak corresponds to 5.9 $keVee$. The result is a conversion factor from the measured charge to energy. Figure 3.7 shows a typical ^{55}Fe spectrum fit with a Gaussian, where the mean X_0 is the conversion factor. The energy resolution is σ_A/X_0; 30% for Figure 3.7. ^{55}Fe runs are typically performed before and after the experiment and the average between the two is utilized for the conversion. Averaging the factors helps to incorporate changes to the gas gain due to the gas aging.

The final two sources are the ^{60}Co source and the ambient background (no-source). For the ^{60}Co source, the ^{60}Co nucleus decays to ^{60}Ni, emitting an electron at 317.9 $keVee$ and two gamma-rays with energies 1.173 MeV and 1.332 MeV [97]. These gamma-rays can Compton scatter with an electron bound to an atom in the drift volume, causing the electron to recoil through the gas. This work measures these electronic recoils to have typical energies less than 25 $keVee$. Therefore, a ^{60}Co experiment consists almost exclusively of electronic recoils, which is useful to identify the electronic recoil band for discrimination and to characterize the electron

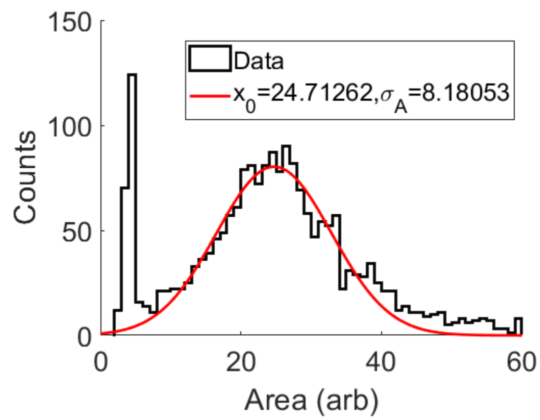

Figure 3.7: ^{55}Fe charge (area) spectrum taken before the "GEM-side" DD neutron experiment.

rejection factor. Lastly, ambient background experiments help to identify Radon Progeny Recoils (RPRs). Each experiment is utilized to guide the selection cuts for discrimination and directionality measurements.

3.5 Diffusion, Mobility, and Waveforms

This section summaries the reduced mobility and the diffusion measurements, which are important calibration measurements used to compare with our previous results [101]. The reduced mobility u_0 is defined by

$$u_0 = \frac{V_d N}{E N_0}, \tag{3.2}$$

where V_d is the drift velocity, $N_0 = 2.68710^{19}\ cm^3$ is the gas density at STP, and N is the gas density. Unfortunately, Figures 4.8 and 3.8b show this work measures u_0 and the effective diffusion σ_Z to be slightly larger than Ref. [101]. The percent difference for μ_0 and σ_Z are roughly 1% and 7% respectively. Much effort was devoted to discovering the cause, but no differences of analysis or of experimental procedure were discovered. Regardless, the minor discrepancy is not an issue for this work because differences in the mobilities merely scale the length of the tracks. Consequently, the discrepancy does not affect discrimination and directionality.

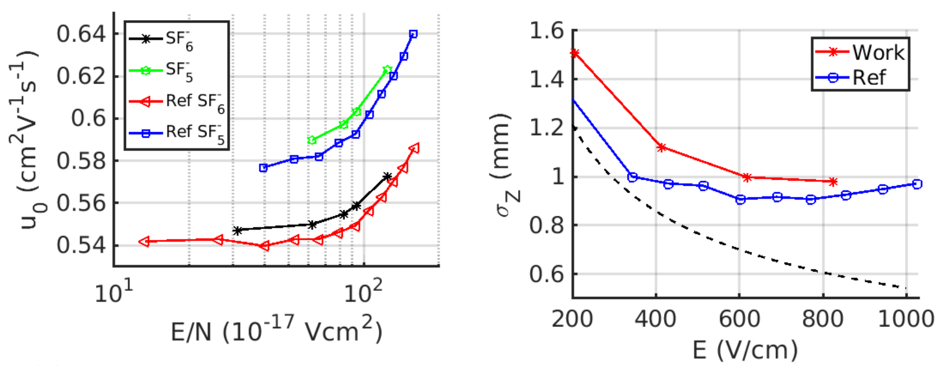

(a) Reduced mobilities μ_0 compared with Ref [101]. The percent difference for both SF_6^- and SF_5^- is approximately 1%.

(b) σ_Z (effective diffusion) compared with Ref [101]. The percent difference is approximately 7%.

Figure 3.8: Comparison of this work's measurements of the reduced mobility μ_0 (left) and the track width σ_Z (right) with our prior results in Ref [101].

Lastly, Figure 3.9 shows the laser-induced average waveforms at 20 Torr and $E_{Drift} = 200\ V/cm$, $400\ V/cm$, $600\ V/cm$, and $800\ V/cm$. They show that the E_{Drift} dependence of the waveforms are consisted with previous results [101]. Figure 3.9 will be referred to later in Section 4.4 as a comparison with the waveforms in low pressure CF_4-SF_6.

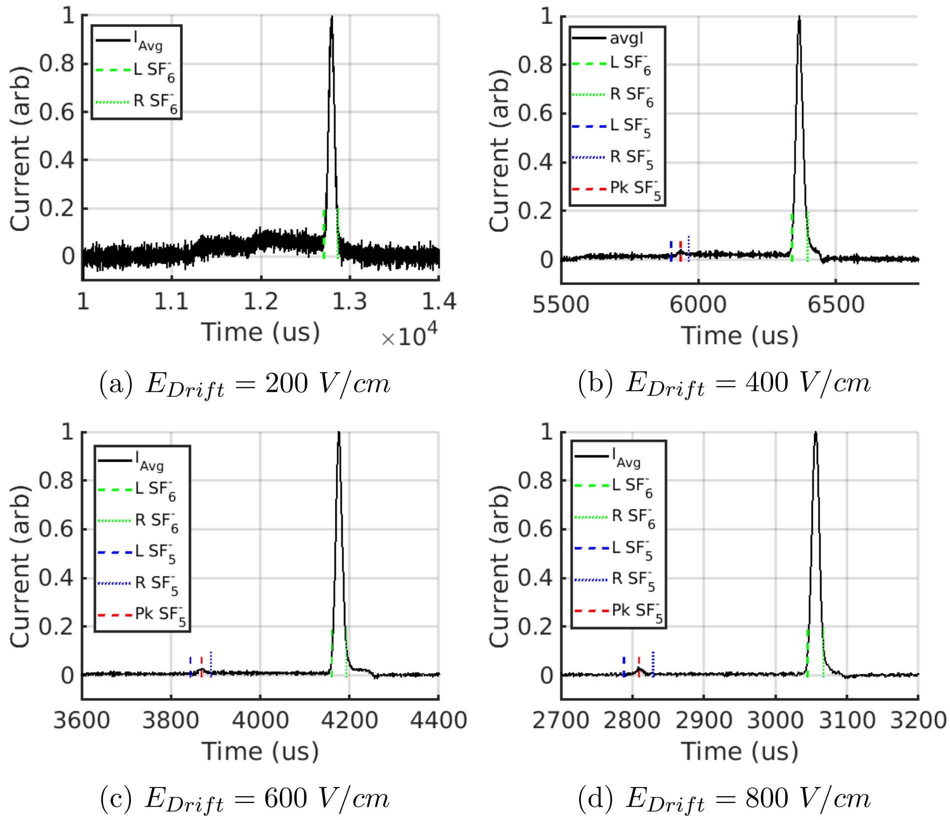

(a) $E_{Drift} = 200\ V/cm$

(b) $E_{Drift} = 400\ V/cm$

(c) $E_{Drift} = 600\ V/cm$

(d) $E_{Drift} = 800\ V/cm$

Figure 3.9: Average current waveforms at 20 Torr.

3.6 Data Analysis Method

This section describes the method for analyzing the data. Each step is shown for the example nuclear recoil track in Figure 3.10. The first step is to remove the voltage baseline. The reader is referred to Section 2.3.1 for details. The baseline subtracted voltage is labeled "Raw" in Figure 3.10a.

3.6.1 Noise Reduction Algorithm

In order to measure the track properties the preamplifier decay time must be removed from the signal. The selected methodology is to convert the voltage signal to a current signal in software with Equation 2.1. Unfortunately, this method greatly

Example "Cathode-side" Nuclear Recoil Event

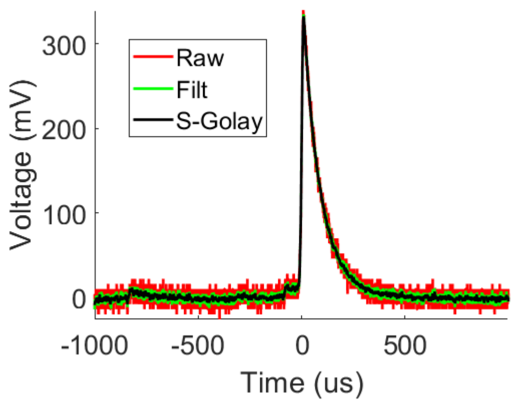

(a) Voltage output from the preamplifier, where the "Raw" voltage the baseline subtracted preamplifier voltage signal, the "Filt" voltage is the signal after the removal of periodic noise features, and the "S-Golay" voltage is the signal after the Savitzky-Golay filter is applied.

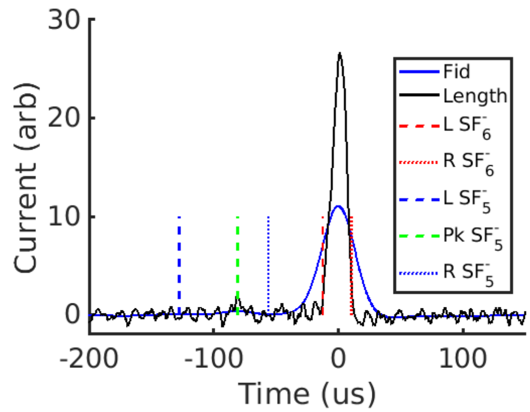

(b) Two versions of the current signal, the "Fid" and the "Length", are calculated. The Fid has an additional $10\mu s$ Gaussian smoothing. The red and blue dashed lines identify the left and right edges of the track and the minority peak SF_5^-. The green dashed line identifies the peak location of the minority peak, which is utilized for the fiducialization.

Figure 3.10: Example nuclear recoil track collected during the "Cathode-side" DD neutron experiment.

increases the noise in the signal. This is because the point-to-point fluctuations of the voltage signal are enhanced by the discrete time derivative. For this reason it is advantageous and typically easier to reduce the signal noise before the current conversion. Therefore, before the current conversion the voltage V_{Raw} is processed with the noise reduction algorithms. Several different algorithms were tested, but the following algorithm was the most successful in terms of reducing noise without distorting the waveforms.

After the baseline subtraction, two periodic noise features induced by the cathode power supply are removed with notch filters at $53kHz$ and $72kHz$. Experiments conducted in the MiniDRIFT detector do not have this noise because of the high voltage filter box (see Section 2.2). In Figure 3.10a the resulting filtered signal is called V_{Filt}. The next step is to utilize a special type of filter called the "Savitzky-Golay" (SG) filter [92, 93, 94]. The SG filter is a digital filter that takes adjacent subsets of data points and fits each subset with a polynomial using the least squares method. Since the data samples are equally spaced in time, the operation is equivalent to convolving the data with the coefficients kernel, which depends on the polynomial order O and length L of the subsets. The optimal O and L were determined qualitatively to be the parameters that reduce the noise with minimal distortion of the signal shape compared to the unfiltered signal. For this experiment the optimal parameters are $O = 3$ and $L = 25$. The voltage V_{SG} is used for V in Equation 2.1 (which defines the V to I conversion).

Next the discrete voltage time derivative is calculated. It is this step that introduces the worst noise into the current signal. Again, several discrete derivative methods were tested. The first method was the 3-point central derivative [95], but the results were very noisy unless additional Gaussian filtering was applied. Gaussian filtering tends to remove the skewness, especially at low energies, and can broaden the tracks [96]. Higher order n-Point central derivative methods had only slightly better results. Ultimately, the optimal method again utilizes the SG filter. However, in this case the SG filter is utilized to calculate the derivative with

$$\frac{dV}{dt} = V * g'/(-dt), \tag{3.3}$$

where g' is the derivative of the SG kernel, $V = V_{SG}$, and $*$ represents the convolution operator [92]. The parameters for the SG filter derivative are $O = 4$ and $L = 25$. Although the order and window size must be carefully selected, the SG filter derivative effectively reduces noise while preserving the overall features of the derivative. Now the signals are ready be converted to the current signal with Equation 2.1. The current I is shown in Figure 3.10b, where I_{Fid} and I_{Length} are defined in the next section.

3.7 Track Property Algorithm

The track properties are measured from the current signal with the following algorithms. First, it is necessary to calculate two versions of the current signal; one with no additional filtering and the other with $\sigma = 10\mu s$ Gaussian filtering. They are labeled "Fid" and "Length" respectively in Figure 3.10b. The I_{Fid} is utilized to precisely localize the minority peak SF_5^-, which requires more filtering to extract from the noise, and I_{Length} is utilized to determine the SF_6^- pulse. Each edge of SF_6^- is found with the following algorithm. First, calculate the quantity $I_{Length}\frac{dI_{Length}}{dt}$, which is the current multiplied by its derivative. Since the boundaries in I_{Length} typically have jitter to them, it is advantageous to consider $I_{Length}\frac{dI_{Length}}{dt}$ where the edges are enhanced. Next, Matlab's "peakfind" algorithm is utilized to find the positive and the negative peaks in $I_{Length}\frac{dI_{Length}}{dt}$. The negative and positive peaks correspond to falling and rising edges in I_{Length} respectively. Between each positive-negative peak combination there is a local maxima or minima in I_{Length}. Starting with the largest positive peak in $I_{Length}\frac{dI_{Length}}{dt}$, the left edge of the SF_6^- charge distribution is found by iteratively searching through positive-negative peak combinations until the local maxima in I_{Length} drops below 10% of I_{Max}. When this occurs the loop is broken and the prior local maxima in I_{Length} is considered. The left edge is identified with the location preceding the local maxima that I_{Length} drops below 10% of I_{Max}. Similarly, the right edge of SF_6^- is located by iteratively searching to the right. The SF_5^- pulse is identified with this algorithm by replacing I_{Length} with I_{Fid}. Lastly, the track length ΔZ is calculated as the difference in time of the SF_6^- edges multiplied by the drift velocity of SF_6^-. Other algorithms were developed and test, but this algorithm has proven to be the most reliable for track length reconstruction. It is crucial the algorithm reliably reconstructs the track length, otherwise the discrimination is reduced.

The final track property to consider is the track skewness (directionality). The skewness measure utilized in this work is related to the third central moment of the distribution but adapted for discrete curves. The population skewness for sample distributions $Skew_{Dist}$ is given by

$$Skew_{Dist} = \frac{m_3}{s^3} = \frac{\frac{1}{n}\sum_i^n (x_i - \bar{x})^3}{[\frac{1}{n-1}\sum_i^n (x_i - \bar{x})^2]^{\frac{3}{2}}}, \tag{3.4}$$

where x_i is the ith element of the distribution, $\bar{x}$ is the mean of the distribution, and n is the number of samples. The numerator m_3 is the sample third central moment, and the denominator s^3 is the cube of the sample standard deviation. Equation 3.4 is modified to be applicable to discrete curves of time ordered samples. After careful study, the skewness measure was adapted to

$$Skew(x, y) = \frac{\frac{\sum_i^n (x_i - \frac{\sum_i^n x_i y_i}{\sum_i^n y_i})^3 y_i)}{\sum_i^n y_i}}{(\frac{\sum_i^n (x_i - \frac{\sum_i^n x_i y_i}{\sum_i^n y_i})^2 y_i}{\sum_i^n y_i - 1}])^{\frac{3}{2}}}, \tag{3.5}$$

where y and x are the data and time axis respectively, y_i and x_i are the ith elements of y and x, and n is the total number of samples. Qualitatively, the equivalence can be understood as follows. The term $\frac{\sum_i^n x_i y_i}{\sum_i^n y_i}$ is the weighted mean of the curve along x, and y_i behaves as the weighting factor. The division by $\sum_i^n y_i$ normalizes the weights y_i. The term $\sum_i^n y_i$ is the sum of all the data values, which is the same as n when y is normalized to n. The numerator of Equation 3.5 is equivalent to m_3

and similarly the denominator to s^3. Nevertheless, Equation 3.5 defines the skewness utilized in this work.

3.8 30 Torr SF_6 Selection Cuts

In order to measure discrimination the following five discrimination cuts must be applied first to the data. The effect of each is shown in Figure 3.11 for the parameter $ln(\eta)$ versus energy E, where η is the ratio of I_{Max} to the track length ΔZ. The importance of the $\ln(\eta)$ parameter is be described shortly. The 1st cut removes tracks where the voltage saturates the vertical scale of the oscilloscope. These tracks are not entirely captured by the oscilloscope and their properties cannot be reconstructed. For the neutron experiments the voltage saturates near $1.25V$. The "saturation" cut rejects events where the peak voltage is greater than $1.25V$. Their location in $ln(\eta)$ is shown in Figure 3.11a, where "All" is every track in the "GEM-side" data set and "NS" are the events passing the saturation cut ("Not Saturated").

Occasionally, tracks will have an "unphysically" fast rise in the voltage signal. This type of event and the rise time (RT) cut employed to remove them was discussed in detail in Section 2.6.1. It is important to remove these tracks with the RT cut, because they are characteristically positive skewed and have the shortest reconstructed tracks lengths. Consequently, they lie in the nuclear recoil band and bias the skewness distribution toward positive skewness. Since they have the shortest track lengths, they are in the upper-most band of the $ln(\eta)$ parameter as shown in Figure 3.11b. The red points pass the saturation cut, but fail the RT cut. The black points pass both cuts and proceed to the next cut.

The next cut is designed to reject events where more than one track is contained in the time window, or the tracks are cut short due to incorrect track reconstruction. It removes events that have a peak greater than 2 ADC units preceding the SF_5^- pulse or trailing the SF_6^- pulse. The 2 ADC unit threshold is about 3σ above the noise in I_{Length}. The cut is referred to as the "Other Peak" (OP) cut. Figure 3.11c shows the removal of these tracks.

The 4th cut utilizes the parameter $ln(\eta)$ and is shown in Figure 3.11d. Since nuclear recoils have larger $\frac{dE}{dx}$ than electronic recoils, they have shorter track lengths and larger I_{Max} at a given energy. Consequently, nuclear recoils tend to reside at larger values of $ln(\eta)$ than electronic recoils. The blue dotted line is the $ln(\eta)$ cut boundary line. Nuclear recoils are selected to be the tracks above the boundary line. The location of the boundary line is based on the ^{60}Co experiment, and once it is selected it is utilized for all experiments. Since the ^{60}Co source produces exclusively gamma-rays, all tracks in the ^{60}Co data set are electronic recoils. For the ^{60}Co experiment the trigger threshold has to be lowered to $E_{Trig} \approx 12\ keVee$ in order to include the low energy electronic recoils. Figure 3.12a shows $ln(\eta)$ versus energy E for the ^{60}Co experiment. The $ln(\eta)$ boundary line is selected so that all tracks except the background RPRs lie below the boundary. For comparison, a voltage minimum cut equivalent to the neutron trigger threshold was applied to the ^{60}Co experiment in software. Figure 3.13a shows the ^{60}Co ΔZ versus E with the voltage minimum cut. The black points passing the $ln(\eta)$ cut are likely RPRs. The result verifies the boundary cut is effective at the same trigger threshold as the neutron experiments. In order to maintain statistics, the directionality cuts stop after the $ln(\eta)$ cut. However, for the discrimination measurement an additional cut (the fiducialization cut) is applied.

Selection Cuts For Directionality And Discrimination Measurement

Saturation Cut

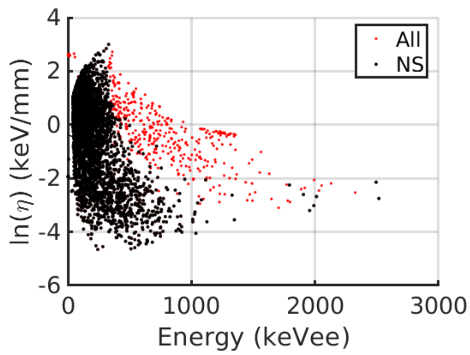

(a) Voltage saturation cut removing events in red with peak voltage greater than $1.25V$. "All" and "NS" refer to all data and to the tracks that pass the saturation cut respectively.

Rise Time (RT) Cut

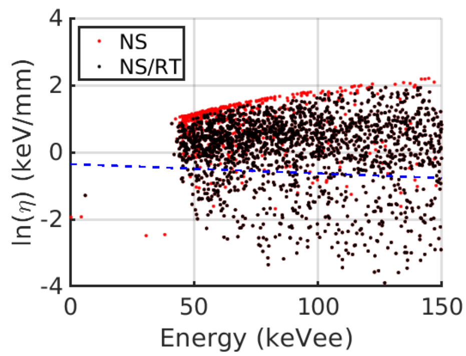

(b) Rise time (RT) cut removing fast-RT events. The red points (NS) pass the saturation cut but fail the RT cut, while the black points (NS/RT) pass the saturation cut and the RT cut.

Other Peak (OP) Cut

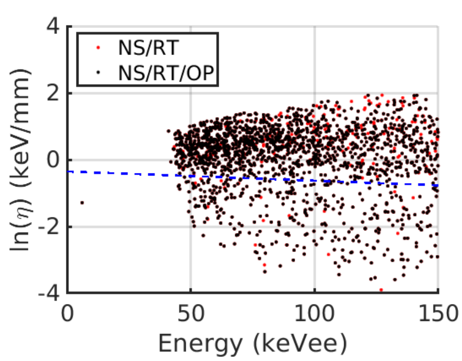

(c) Other peak (OP) cut removing events with a large peak outside the event region. The red points (NS/RT) pass the saturation cut and the RT cut but fail the OP cut, while the black points (NS/RT/OP) pass the saturation cut, the RT cut, and the OP cut.

$\ln(\eta)$ **Cut**

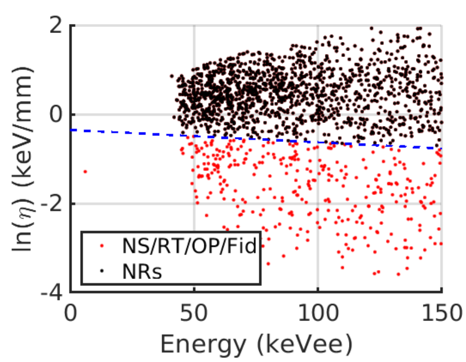

(d) The $ln(\eta)$ cut accepts events that lie above the $ln(\eta)$ cut boundary (blue dotted line).

Figure 3.11: The effect of each successive selection cut on the "GEM-side" data. The red and black markers are the events that fail and pass each cut respectively. The blue dotted line marks the $ln(\eta)$ cut boundary. NS, RT, OP, and Fid refer to the points that pass the saturation, rise time, other peak, and the fiducialization cut. Refer to Section 3.8 for the description of each cut.

^{60}Co **Experiment With** $E_{Trig} \approx 12\ keVee$

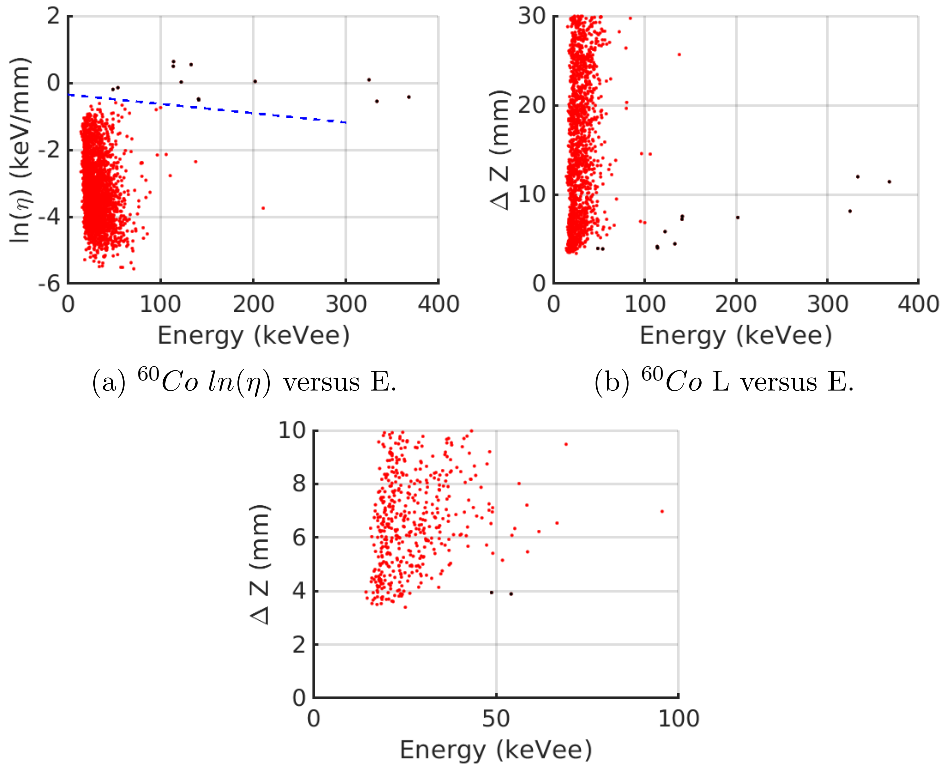

(a) ^{60}Co $ln(\eta)$ versus E.

(b) ^{60}Co L versus E.

(c) ^{60}Co L versus E focus low energy.

Figure 3.12: (3.12a) $ln(\eta)$ versus E for the ^{60}Co experiment after the fiducialization cut. (3.12b and 3.12c) Range ΔZ vs energy E for the ^{60}Co experiment with the fiducialization cut. Red points pass all cuts except the $ln(\eta)$ cut (blue dashed line). The black are nuclear recoil-like RPRs which pass the $ln(\eta)$ cut.

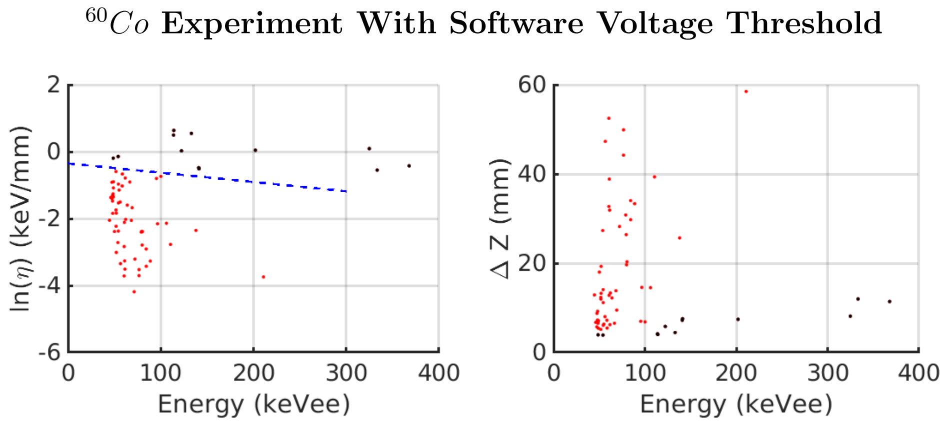

(a) $ln(\eta)$ versus E.

(b) ΔZ versus E.

Figure 3.13: (3.13a) $ln(\eta)$ and (3.13b) range ΔZ vs energy (E) for the ^{60}Co experiment with the fiducialization cut and the $160mV$ software voltage cut (equivalent to the DD Neutron Experimental hardware voltage threshold). Red points pass all prior cuts but fail the $ln(\eta)$ cut. The black are the nuclear recoil-like RPRs which pass the $ln(\eta)$ cut.

The 5th cut is the fiducialization cut, which requires the Z location of the track to be greater than 10 cm and less than 62 cm. Z is estimated with Equation 1.3 and the peak location of the SF_5^- charge distribution. The 10 cm lower limit removes events where the SF_5^- charge distribution is beginning to overlapping with the SF_6^- charge distribution, which would positively bias the track skewness. Since the maximum Z is limited by the length of the detector (58.3 cm), the upper limit rejects incorrectly fiducialized events while allowing for jitter in the measured SF_5^- peak location. Figure 3.14 shows the results of the fiducialization cut. Unfortunately, it is clear by comparing Figure 3.14 with Fig 3.11d the fiducialization cut greatly reduces the overall statistics. Since the directionality measurement requires a large number of statistics, the fiducialization cut is not utilized for the directionality measurement. The advantage of the fiducialization cut for the discrimination measurement is described in Section 3.9.1.

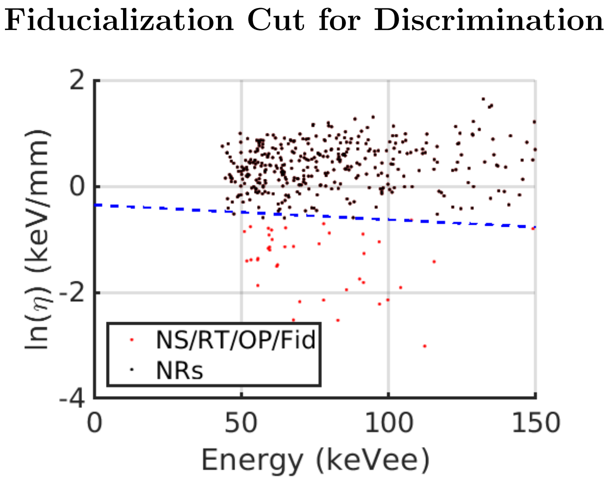

Figure 3.14: The fiducialization cut is applied to the data in Figure 3.11d to enhance the discrimination measurement, where the black points are the remaining points within the nuclear recoil band and the red points correspond to points outside the nuclear recoil band.

3.9 Discrimination and Directionality Results

The discrimination and directionality in 30 Torr SF_6 is presented in this section. In order to quantify the discrimination, the minimum energy required to discriminate E_{Disc} is measured. Another quantity that quantifies the amount or the power of the discrimination is the rejection factor, which is the number of nuclear recoils per electronic recoil that lie in the nuclear recoil band. Unfortunately, due to the low nuclear recoil rate (see Section 3.4) the rejection factor is not quantified in this chapter. However, the rejection factor is returned to in Chapter 5. The directionality is quantified with the minimum energy required to measure directionality E_{Skew} and the skewness difference, which is the difference between the "GEM-side" and the "Cathode-side" skewness distributions.

3.9.1 Discrimination

E_{Disc} is estimated based on the location in the range ΔZ versus energy E plots where the vertical electronic recoil band merges with the nuclear recoil band. Figure 3.15b shows the ΔZ versus E plots for the "GEM-side" and the "Cathode-side" experiments without the fiducialization cut. Unfortunately, there is a "haze" of events between the bands which blurs E_{Disc}. The events in the "haze" are greatly reduced after the fiducialization cut. Although the source of the "haze" remains unknown, here are several ideas. First, these tracks are not properly reconstructed. For this case, when the actual SF_5^- is included with the SF_6^- change distribution the track length is overestimated, or when a portion of the SF_6^- distribution is misidentified as SF_5^- the track length is underestimated. Such tracks would have incorrect or no fiducialization. Another possibility are alpha tracks crossing the entire THGEM active region. The "haze" could also be neutron-induced proton recoils produced when the neutron liberates a proton from the acrylic. Nevertheless, the "haze" must be removed to obtain a measurement of E_{Disc}.

Figures 3.16a and Figure 3.17a show the entire measured energy range for ΔZ versus E for the "Cathode-side" and the "GEM-side" experiments with the fiducialization cut. Before focusing on the low energy region of the nuclear recoil bands, consider the high energy behavior of the nuclear recoil bands. They increase monotonically with energy and have a maximum nuclear recoil energy of about 400 $keVee$, which is almost the kinematic maximum energy transfer between the 2.2 MeV neutrons and a F atom (420 $keVee$). Also, the nuclear recoil bands show a sudden decrease in density after about 250 $keVee$, which is consistent with the expected 260 $keVee$ maximum energy transfered to a S atom. Consequently, below 250 $keVee$ the nuclear recoil band is denser because it consists of F and C nuclear recoils, and above 250 $keVee$ the nuclear recoil band consists entirely of F atoms. Since the "haze" is gone, E_{Disc} can be measured from the low energy region of the nuclear recoil bands.

"GEM-side" and "Cathode-side" Experiments Without Fiducialization Cut

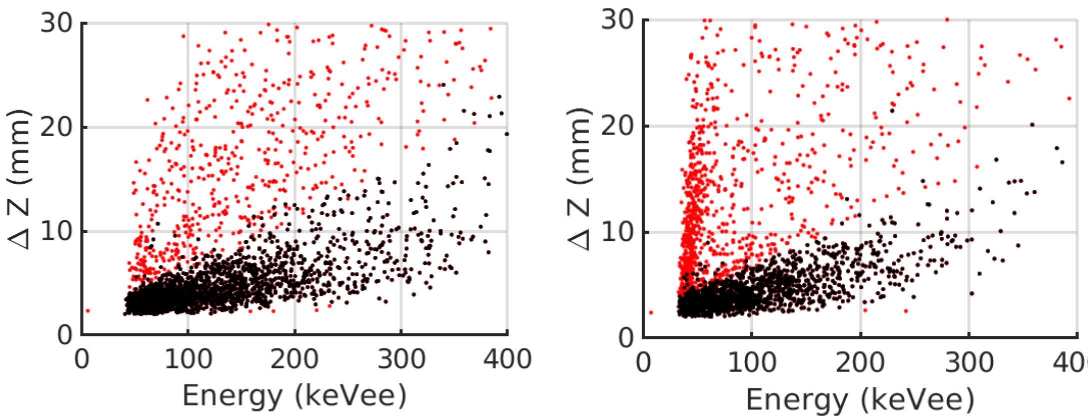

(a) "GEM-side" ΔZ versus E.

(b) "Cathode-side" ΔZ versus E.

Figure 3.15: Range ΔZ vs energy E for the "GEM-side" and the "Cathode-side" neutron experiments without the fiducialization cut. Red events pass the 1st, 2nd, and 3rd Cuts, but fail the $ln(\eta)$ cut. The black events pass the $ln(\eta)$ cut and are used to measure directionality.

Figures 3.16b and 3.17b indicate there is separation between the electronic and nuclear recoil distributions until about 50 $keVee$. However, if only the shortest ΔZ are considered at a given energy then discrimination can be pushed down to about 30 $keVee$. Since the trigger threshold cannot be lowered below about 25 $keVee$, it is difficult to determine if $E_{Disc} < 30$ $keVee$. In order to gain some insight below 25 $keVee$, consider the low threshold ^{60}Co experiment in Figure 3.12c. The electron recoil band has few events below $\Delta Z = 4$ mm at $E = 20$ $keVee$, whereas the 2 RPRs are below 4 mm at 50 $keVee$. This suggests E_{Dist} could have been measured to be lower than 30 $keVee$ if the trigger level for the neutron experiments was lowered.

3.9.2 Directionality

The directionality for the nuclear recoil band without the fiducialization cut is calculated with the following procedure. For the neutron experiments with the DD

“Cathode-side” Fiducialization Cut

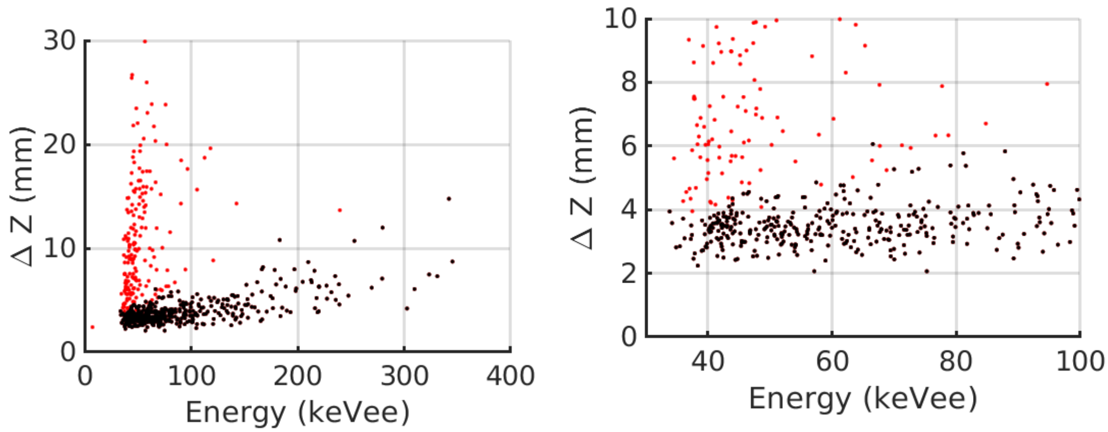

(a) Entire measured nuclear recoil band.

(b) Closeup for low energy discrimination.

Figure 3.16: Track range ΔZ vs energy E for the “Cathode-side” neutron experiment with the fiducialization cut applied. The red events pass the 1st, 2nd, and 3rd Cuts, but fail the $ln(\eta)$ cut. The black are the nuclear recoil tracks utilize to measure discrimination.

“GEM-side” Fiducialization Cut

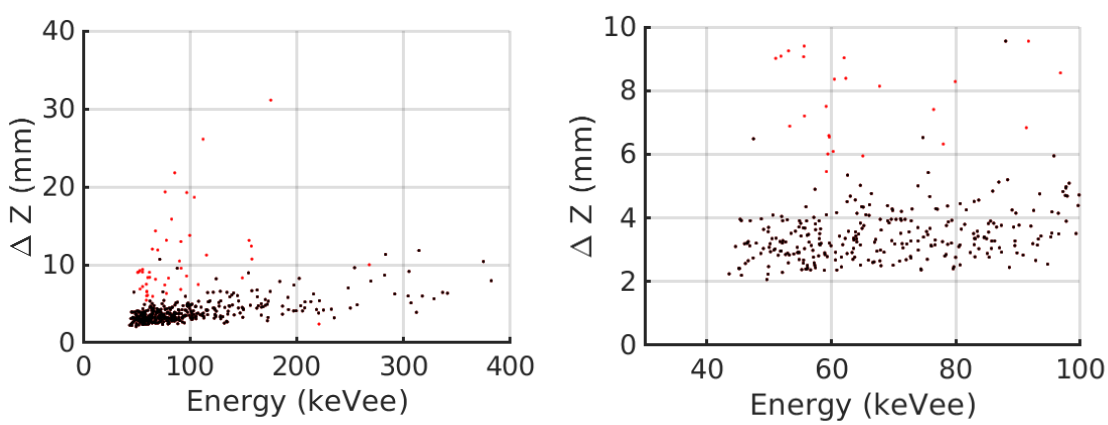

(a) Full nuclear recoil band.

(b) Focus low energy discrimination.

Figure 3.17: Range ΔZ vs energy E for the “GEM-side” neutron experiment with the fiducialization cut applied. Red events pass all prior cuts, but fail $ln(\eta)$ cut. The black are the nuclear recoil events.

generator on the GEM-side of the detector, the nuclear recoils are preferentially directed away from the GEM. The highest ionization density tends to be closest to the GEM, and therefore the "GEM-side" experiment should have positive overall skewness. Similarly, the "Cathode-side" experiment should have negative skewness. In order to subtract away any experimental systematics, the interesting parameter is the difference between the "GEM-side" and the "Cathode-side" skewness distributions ($Skew_{GEM} - Skew_{Cathode}$). If the experiment is sensitive to the intrinsic skewness, the skewness difference is greater than zero ($Skew_{GEM} - Skew_{Cathode} > 0$).

The nuclear recoil bands are divided into three energy bins; 30 to 70 $keVee$, 70 to 110 $keVee$, and 110 to 150 $keVee$. Figure 3.18 shows the "GEM" (red) and "Cathode" (blue) skewness distributions for each energy range. The mean skewness and standard deviation of the mean are calculated for each energy range, and the results are plotted in Figure 3.19a. The black points are the sum of the skewnesses ($Skew_{GEM} + Skew_{Cathode}$) for each energy range. The horizontal bars represent the extent of the energy bin at each point. Although the errors are large, the sum curve is not equal to zero. This indicates there is a systematic biasing signal shapes toward negative skewness. The systematic could be an artifact of the electronics or the analysis. Nevertheless, Figure 3.19a indicates the expected trends; the "GEM-side" and the "Cathode-side" skewnesses are positive and negative respectively, and diverging with energy.

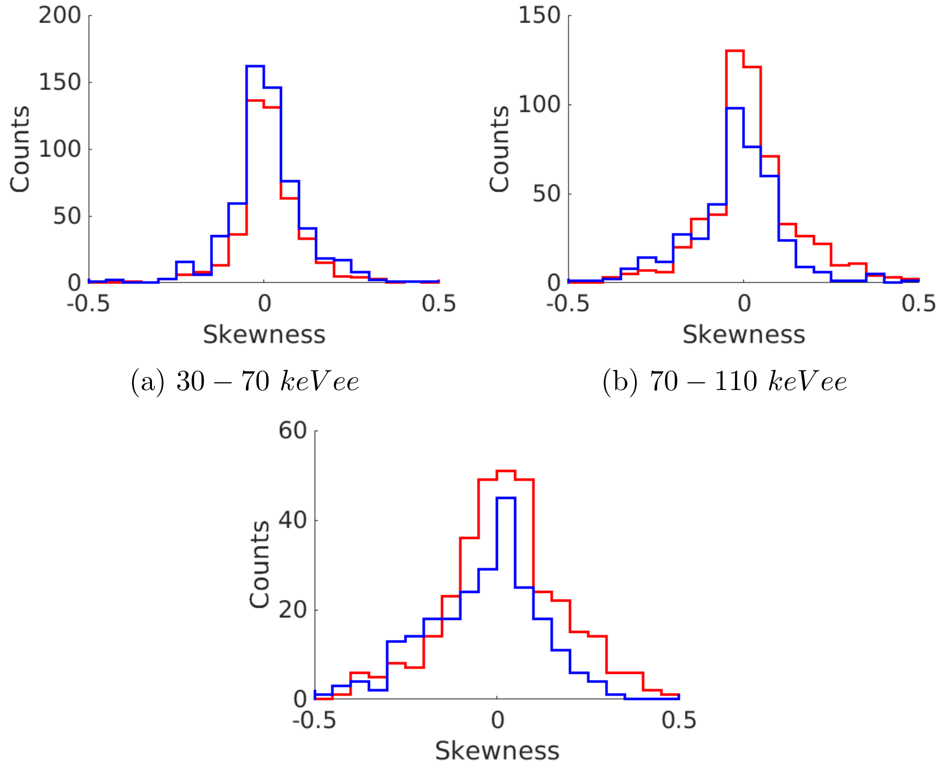

(a) $30-70\ keVee$

(b) $70-110\ keVee$

(c) $110-150\ keVee$

Figure 3.18: Skewness distributions for the directionality nuclear recoil band. The "Cathode-side" and the "GEM-side" are blue and red respectively.

The skewness difference is plotted in Figure 3.19b. The NR curve is measured over the entire nuclear recoil band, and the "1/3-1" curve is the calculation for the upper 2/3-longest nuclear recoil tracks. The result shows there is statistically significant skewness down to the lowest energy bin 30 to 70 $keVee$. The skewness difference is enhanced for the "1/3-1" curve because it is easier to reconstruct the intrinsic skewness from the longer population of tracks in a given energy bin [98]. There are a few possible reasons why the shortest tracks have no skewness. The first is the filtering removes the skewness because the shortest tracks consist of about 10 samples. Another possibility is the tracks are directed parallel to the "GEM-side" and the skewness is difficult to measure along Z. Nevertheless, since the skewness difference is statistically greater than zero in the lowest energy bin, E_{Skew} is at most 50 $keVee$, and perhaps the intrinsic E_{Skew} is even lower.

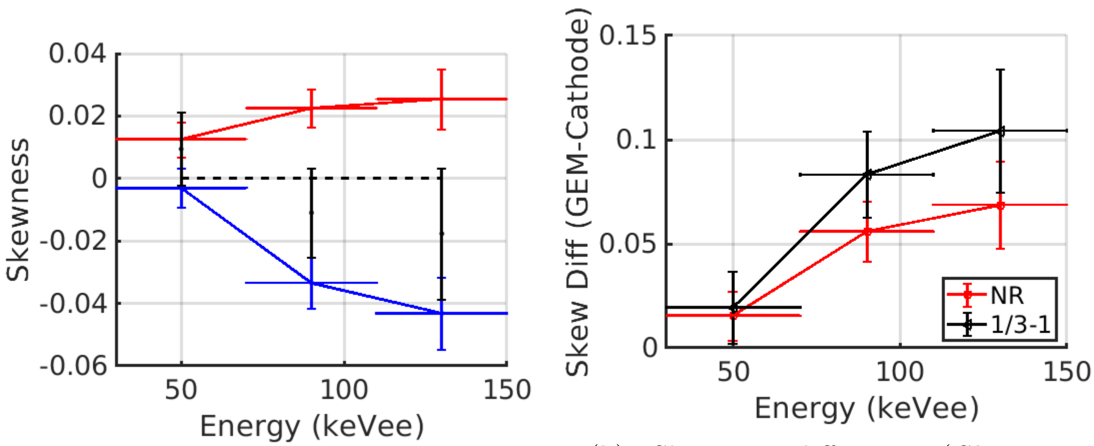

(a) Skewness in the "GEM" (red) and the "Cathode" (blue), and the sum of the skewness (black) versus energy in 40 $keVee$ bins.

(b) Skewness difference ($Skew_{GEM}$-$Skew_{Cathode}$) versus energy in 40 $keVee$ energy bins for the longest nuclear recoil events ("1/3-1") and for the entire nuclear recoil band (NR).

3.9.3 Conclusion

In this chapter the discrimination and the directionality in a 30 Torr SF_6 TPC is measured in 1D. These measurements are the first in SF_6 using any type of readout. They are quantified with the quantities E_{Disc}, E_{Skew}, and the directionality level/power with the skewness difference between the "GEM-side" and the "Cathode-side" experiments. The results are $E_{Disc} \leq 30$ $keVee$ and $E_{Skew} \leq 50$ $keVee$. The skewness difference is shown in Figure 3.19b as a function of energy. Unfortunately, these measurements might be intrinsically better, but the 25 $keVee$ neutron trigger threshold due to the low nuclear recoil rate makes determining this difficult. The directionality measurement might be improved if the fiducialization cut could have been applied to the directionality data without heavily reducing the nuclear recoil statistics. It is possible the non-fiducialized "haze" events are diluting the directionality. The level/power of discrimination is often quantified with the rejection faction, but for this data it could not be determined due to the low nuclear recoil rate.

A solution to the low nuclear recoil rate is to introduce a thick layer of lead shielding between the detector and the DD neutron generator in order to reduce the gamma-ray interaction rate within the detector. We performed several experiments with the lead bricks. However, even with the addition of lead bricks, we observed that the acquisition rate of electronic recoils continued to overwhelm the acquisition rate of nuclear recoils. Also, we reasoned the initial directionality of the neutrons would be diluted due to scatters in the lead. Therefore, the advantage of the lead shielding was unclear. Future work could involve determining the optimal shielding thickness required to reduce the electronic recoil rate relative to the nuclear recoil rate. Another method is to utilize a digitization system with less dead-time, which would increase the number of collected nuclear recoil events per unit time.

Although this chapter may not have measured the minimum for E_{Disc} and E_{Skew} in SF_6^- in 1D, it did verify an issue with the use of SF_6 in TPCs used for directional dark matter experiments. The low production of SF_5^- relative to SF_6^- reduces the fiducialization efficiency. In order to fiducialize, the SF_5^- charge distribution must be localized accurately with respect to that of SF_6^-, which is about 2.5% of SF_6^- [101]. This work demonstrated the low fiducialization efficiency in SF_6 when the peak-to-peak noise in the track is similar in amplitude to the SF_5^- charge distribution. An ideal WIMP TPC would select the relative production of the fiducialization species to be 8% to 10% or have better signal to noise. Therefore, there has been a push toward discovering a means to enhance the SF_5^- charge distribution in SF_6. Chapter 4 presents an unexpected discovery that resolves this issue.

Chapter 4

Tunable Negative Ion Species In Low Pressure CF_4-SF_6 Gas Mixtures

4.1 Introduction

This chapter presents the discovery and the characterization of an unexpected negative ion species in a low pressure CF_4-SF_6 TPC operated with low SF_6 concentration. Before discussing this result, here is a brief review of what has been discussed in this work thus far. In Chapter 2 SF_6 was demonstrated to have many of the properties desired for directional dark matter experiments that employ the TPC technology. However, Chapter 3 discusses a significant drawback of SF_6: the minority peak SF_5^- is very small (2.5%), making fiducialization in SF_6 difficult on an event-by-event basis. Recall the importance of the detector fiducialization for background rejection, which was discussed for the DRIFT experiment in Section 1.6.3 and verified by this work in Chapter 3. Ideally, the minority species should be approximately 8% to 10% of the total charge to reliably fiducialize. Consequently, there has been a push in the community to discover a means to enhance the relative production of SF_5^- in low pressure SF_6 TPCs.

With this objective, we decided to study gas mixtures involving SF_6, but with SF_6 only as a minor component. The motivation for this was that the electron capture would occur with a larger mean-free path, thereby increasing the relative contribution of SF_5^- [101]. A secondary objective was to characterize the capture length and the effective diffusion of SF_6 in low concentrations. As verified in Chapter 2, the capture length decreases with pressure in pure SF_6. However, the capture length in a CF_4-SF_6 mixture was expected to depend on the SF_6 partial pressure and the total pressure of the gas in a complex way. Therefore, measuring the capture length and the effective diffusion of SF_6 in low concentrations is interesting in its own right. The bulk gas was selected to be CF_4 because it is electrically stable and under most conditions is not electronegative. Like for SF_6, there are many studies of the electrical properties of CF_4 [102, 103, 104, 98, 112]. CF_4 is known to be resonantly electronegative, and has electron attachment resonances at 6.8 eV and 7.5 eV [104]. These energies are much greater than the electron affinity for SF_6, which is 1.05 ± 0.1 eV [105]. Also, CF_4 has no stable negative ion state, and it will immediately dissociate into CF_3^- or F^- [102]. Based on these properties of CF_4 and our own prior experience, the negative ion behavior in $CF_4 - SF_6$ was expected to be similar to the negative ion behavior in pure SF_6 [101], where the bulk CF_4 gas acts only to dilute the SF_6.

Instead, an additional negative ion species was discovered with mobility faster than SF_5^-. This was very unexpected. We have extensive experience utilizing CF_4 in low pressure TPCs and have never encountered negative ion behavior in CF_4. This chapter describes the results and develops a model for the production of the new species, and asserts the new species is CF_3^-. In Section 4.4.1, the preliminary experiment that discovered the new species is presented. In Section 4.4.2, an experiment with the SF_6 pressure P_{SF_6} less than 0.1 Torr is presented. These experiments demonstrate not only electron capture for $P_{SF_6} \leq 0.1$ Torr but the predominate production of the new species. Immediately after its discovery work began toward characterizing the new species; i.e. the dependence of the relative signal amplitude and the relative charge of the new species on the P_{SF_6}, the CF_4 pressure P_{CF_4}, and the reduced field E/N. This begins in Section 4.4.3, where the signal waveforms are shown to be highly dependent on the P_{SF_6}. Next, in Section 4.4.4 the dependence of the relative charge and the signal amplitude of the new species on P_{SF_6} is described. These measurements show the new species is tunable and its relative production depends on P_{SF_6} and E/N. In fact, the new species is produced in the optimal range for efficient fiducialization (8%-10%) at 20-3 Torr CF_4-SF_6. Following this, in Sections 4.4.5, and 4.4.6 the reduced mobility μ_0 and the effective diffusion σ_Z are measured as a function of P_{SF_6} and the drift field E_{Drift}. The fiducialization with the new species is presented in Section 4.4.8, where it is shown to be more efficient than fiducialization with SF_5^-. The chapter ends with a brief characterization of the CF_4-SF_6 gas stability over time in Section 4.4.9. The stability of the gas with time is another benefit of the CF_4-SF_6 compared to SF_6, where Ref. [101] measured that the SF_6 waveforms suffered from large distortions as the gas ages due to the outgassing of water vapor [101]. Chapter 5 characterizes the discrimination and directionality of the 20-3 Torr CF_4-SF_6 mixture.

4.2 Experimental Setup, Data Analysis, and the Resulting Waveforms

4.2.1 Experimental Setup and Operation

The experimental setup is identical to that described in Section 3.2 and Ref. [101] except for the backfill procedure. The reader is referred to Section 3.2 for the experimental setup, the powering scheme, and the data acquisition system. The backfill procedure requires the following steps. After a two day pump-down the detector is flushed twice with 200 Torr CF_4. When the baratron reads 1 Torr above the desired CF_4 partial pressure on the second pump-down, pump-down rate is decreased to 0.1 Torr per two or three seconds in order to avoid overshoot. Once P_{CF_4} is reached the detector is allowed to equilibrate for several minutes. Next, the SF_6 is slowly introduced into the detector, where again the rate for the last 1 Torr is reduced. If SF_6 is introduced too quickly the equilibrium pressure after the mixture settles is typically lower than the initial reading and the desired P_{SF6}. This backfill procedure is the most reliable to prevent overshoot, to reduce the detector fill time, and to minimize the outgassed the contamination.

The primary ionization is created with the Stanford Research Systems (SRS) NL100 337.1 nm pulsed nitrogen laser, where each laser-induced track drifts from the creation site on the cathode to the THGEM (58.3 cm). Consequently, the laser source is ideal to measure the effective diffusion, the fiducialization, and the relative production of each negative ion species in a reproducible manner.

4.2.2 Data Acquisition, Analysis

The signals are converted to current with the procedure discussed in Section 2.3 and analyzed using the algorithms in Section 3.9. The only changes are to the Savitky-Golay (SG) filter parameters Order O and Window W, and to the width of the Gaussian filter applied to the fiducialization current I_{Fid}. These changes to the filter parameters compensate for the slightly different noise and drift velocities of the experiments. The SG filter applied to V_{Filt} is $O = 4$ and $W = 25$, and the SG filter applied to the current signal I_{Length} is $O = 4$ and 101. I_{Fid} utilizes a 12 μs Gaussian filter.

The laser is utilized as described in Section 3.4 to create repeatable, point-like ionization events from the cathode. The laser-induced current signals are added together to reduce noise. The resulting average current signals are referred to in this chapter as waveforms. The effective diffusion is measured by Gaussian fitting the rising edge of the waveform from 20% to 60% of I_{Max}. The charge distributions for the new species and the SF_5^- are located, and the relative charge of each species is measured. The charge of each species is calculated with the "trapz" function in Matlab. The edges of the new species are defined to be the location where the waveform drops below 10% of the new species peak amplitude. For SF_5^- the threshold is 30% of the SF_5^- peak amplitude because it is surrounded by "inter-peak" charge. The inter-peak charge is all the charge that is not contained in the SF_6^-, the SF_5^-, and the new species charge distributions. The fraction of the total charge in the inter-peak charge changes with P_{SF_6} and E/N. In fact, there are certain experiments where the inter-peak charge is greater than these thresholds and the charge of the species cannot be calculated. The inter-peak charge is discussed further in Section 4.3. Lastly, the reduced mobility u_0 is calculated from the drift velocity V_d and Equation 3.2, where V_d for each negative ion species is the arrival time of its peak divided by the length of the detector (58.3 cm).

4.2.3 The Unexpected Signal Waveform

Figure 4.1 shows the resulting waveform for the case where $P_{CF_4} = 40$ Torr, $P_{SF_6} = 0.1$ Torr, and $E_{Drift} = 617\ V/cm$. The negative ion species constituting the peak at $T = 4600\mu s$ is the new negative ion species, CF_3^-. This species has never been observed under these or similar conditions by our group or any other groups, and it was entirely unexpected. We were attempting to discover a means to enhance the SF_5^- peak for fiducialization in SF_6, but with the discover of the CF_3^- species we pursued this as an alternative path toward fiducialization in CF_4-SF_6 mixtures. The shoulder on the right side of the CF_3^- peak at $T \approx 4700\mu s$ demonstrates the dual-peak nature of what we call the CF_3^- peak. The shoulder likely represents another drift species, perhaps F^-. The dual-peak nature of the CF_3^- peak will be discussed further in conjunction with the experimental results in Section 4.4. The peaks at $T = 5200\mu s$ and $T = 5500\mu s$ are the SF_5^- and the SF_6^- species, respectively.

One immediate advantage of the CF_3^- peak over the SF_5^- peak is that it is even faster than SF_5^-. This means greater time separation from the SF_6^- peak, which should give better fiducialization. We were excited by the possibilities of the new peak, so wanted to study its potential. However, before describing the experimental results further, a proposed model for the new peak will be discussed, which predicts the behavior of the CF_3^- peak as a function of P_{SF_6} and E_{Drift}. After the model, a series of experiments that study the new peak's behavior as a function of P_{SF_6} and E_{Drift} are presented. Also, for the remainder of the chapter the entirety of the double-peak is referred to as CF_3^-, unless mentioned otherwise.

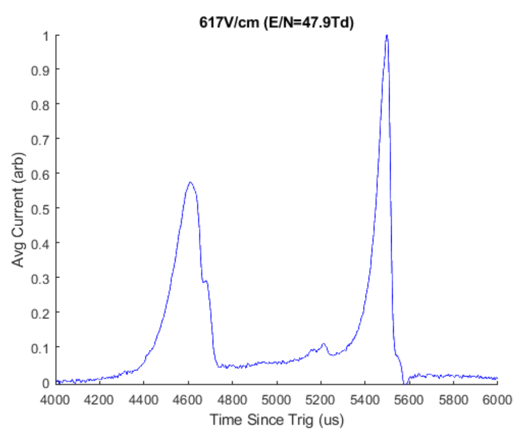

Figure 4.1: Signal waveform at 40-0.1 Torr CF_4-SF_6 and $E_{Drift} = 617\ V/cm$, where the left most peak is the unexpected, new species, hypothesized to be CF_3^-. The shoulder on the right side of the CF_3^- peak shows the double-peak nature of the CF_3^- peak. The second peak might be F^-.

4.3 A Proposed Model For The Production Of CF_3^-

Before discussing the experimental results, this section presents a production model for the new species and concludes the new species is CF_3^-. This model is based on Refs. [103, 105], where the essential process is electron transfer. Consider the reaction:

$$A^- + B \underset{k_b}{\overset{k_c}{\rightleftharpoons}} (A^-.B)^* \rightarrow A^-(E_\nu).B \rightarrow A.B^- \rightarrow A + B^-, \tag{4.1}$$

where a negatively charged molecular ion A^- interacts with a neutral molecule B [105]. Through several intermediate molecular complexes the electron is transfered from A^- to B. The success and rate for the electron transfer to B depends on several factors. The upper limit for the transfer rate is the collision rate of molecules A^- and B. However, the following conditions suppress the reaction; if the reaction is endothermic (requiring energy), or if there is a significant change in the geometry of the molecules from the initial state to the intermediate molecular complexes, and from the complexes to the final state.

It was discovered in Ref [103] that when $A = SF_6^-$ the electron transfer to a variety of neutral molecules B is highly suppressed. In addition, when $A = SF_6^-$ and $B = SF_6$ the transfer does not occur at all. They concluded there must be a large geometry change between the neutral SF_6 (known to be octahedral) and SF_6^-. Two possibilities for the change are that the $S - F$ bond is longer for SF_6^-, or the SF_6^- exists in a $SF_5 - F^-$ bound state. In either case, electron transfer from SF_6^- is slow and highly suppressed.

Immediately after SF_6 captures an electron it is in an excited state $(SF_6^-)^*$, where the $*$ denotes excited state [105, 100, 101]. The $(SF_6^-)^*$ can collisionally deexcite with $B = SF_6$ and produce SF_6^-. Consider what happens for the situation $A = (SF_6^-)^*$ encounters $B = CF_4$ instead of SF_6. There are two possible outcomes. Outcome 1 is:

$$\textbf{Outcome 1}: (SF_6^-)^* + CF_4 \rightarrow SF_6^- + CF_4, \tag{4.2}$$

where $(SF_6^-)^*$ collisionally deexcites with CF_4, and no new species are created. Outcome 2 is depicted by the reaction coordinate shown in Figure 4.2. The reaction coordinate is an abstract method of representing the progress of a reaction, where the X-axis depicts the progression of time and the Y-axis represents the internal energy of the system.

Outcome 2

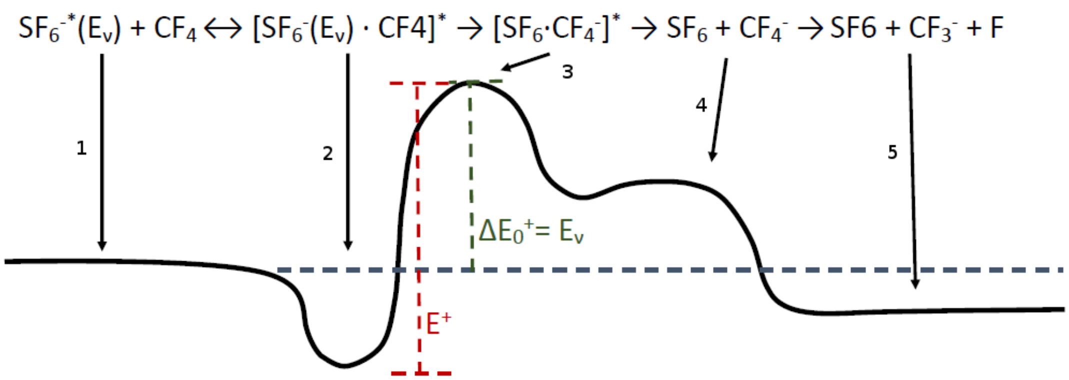

Figure 4.2: The reaction coordinate for Outcome 2, where 1 through 5 indicates the state of the system. The reaction proceeds from the initial state (State 1), over the internal energy barrier E^+ (State 2), through several intermediate states (State 3 and State 4), and to the final state (State 5). Notice CF_3^- in the final state.

For Outcome 2, the reaction begins in State 1, where the $(SF_6^-)^*$ encounters a CF_4 molecule and the system has an initial internal energy given by the solid line at State 1. As the molecules the internal energy of the system decreases due to the van der waals attraction between the molecules. When the system is in State 2, the internal energy is a minimum. Between State 2 and State 3, as the molecules move closer the force between them becomes repulsive and the internal energy of the system increases. In order for the system to transition into the State 3 the internal energy barrier E^+ must be overcome, hence the reaction is endothermic. If the vibrational energy E_ν of the $(SF_6^-)^*$ is greater than the difference between the barrier and the initial system energy ($E_\nu > \Delta E_0^+$), then the $(SF_6^-)^*$ can give up E_ν in order to overcome E^+ and the system transitions into State 3. If this does not happen, the system either moves back to State 1 or undergoes Outcome 1. For the case where $E_\nu > \Delta E_0^+$, the system reaches State 3, where the electron has been successfully transfered to the CF_4 side of the molecular complex. At this point the molecular complex is $(SF_6 \cdot CF_4^-)^*$. Between State 3 and State 4 the molecules begin to move apart and the internal energy of the system decreases. This decrease in the internal energy of the system is the reverse of the situation between State 1 and State 2, where the moving apart of the constituent molecules of the complex is resisted by their van der waals attraction. Eventually the complex is broken and the system is in State 4, where the system consists of the separate molecules SF_6 and CF_4^-. Since the CF_4^- is unstable, it subsequently auto-dissociates into State 5, where the CF_3^- and F are products. Although the production of CF_3^- is most probable, it is important to note the products can also be CF_3 and F^-. In fact, the F^- production could explain the dual-peak nature of the new species that is apparent for several experiments discussed in Section 4.4.

An important question to consider is: once the charge is in one of the final states SF_6^-, SF_5^-, CF_3^-, or F^- can the electron be transfered again to a neutral molecule? In no additional charge transfer reactions occur, the total charge in each charge distributions is unchanged as it drifts to the readout. This results in each species forming a peak in the signal. The arrival time of each distinct species then depends only on the drift velocity of the species. However, if electron transfer reactions occur during the drift there will be charges that arrive at the readout outside of these peaks. This is because the charges spend a fraction of the drift as more than one negative ion, which each have their own unique drift velocity. This charge is referred to as “inter-peak” charge. Since there are at least three negative ion species, the inter-peak charge between any two signal peaks could involve two or more species and its shape depend on the energy barriers for each reaction. The situation different in pure SF_6 where the inter-peak charge is believed to be due to or mediated by water contamination [101].

Importantly, this model has several experimentally testable predictions. Namely, it predicts the behavior of each negative ion species as a function of P_{SF_6} and E/N. The underlying factor is the vibrational energy E_ν of the $(SF_6^-)^*$, which can have different values along the track for each $(SF_6^-)^*$. The result is a distribution of E_ν, where the part of the distribution above ΔE_0^+ contributes to CF_3^- production. The distribution of E_ν along the track depends on the energies of the primary electrons when they are captured by SF_6, where larger electron energies results in the distribution of E_ν shifted to larger values. Consequently, any process that tends to increase the primary electron energies along the track will more readily produce CF_3^-.

The energies of the primary electrons can be increased by: raising the drift field E_{Drift}, and thereby increasing the electron acceleration between collisions; increasing the capture length, where the electron is accelerated by E_{Drift} for a longer distance before being captured by SF_6; or to higher order increasing the mean free path between collisions with CF_4, i.e. raising the pressure of the bulk gas P_{CF_4}. The dependence on P_{CF_4} is a higher order effect than P_{SF_6}, because even with more frequent collisions with CF_4 the electrons still reach very fast drift velocities, and the effect of P_{CF_4} is small compared to P_{SF_6}. Consequently, the main factors that increase the CF_3^- production are higher E_{Drift} and lower P_{SF_6}. Additional consequences of the model will be explained with the discussion of the experimental results in Section 4.4.

Briefly, here are several reasons why other negative ions cannot be associated with the new species. First, CF_4^- cannot be the new species and cannot perform the initial electron capture, because (except the electron attachment resonances at $6.8eV$ and $7.5eV$ [104]) CF_4 is not electronegative and has no known stable negative ion state [102, 103, 104, 98, 112]. However, Ref. [104] does propose a theoretical metastable C_s configuration for CF_4^-, which is $1.22eV$ greater than the ground state of neutral CF_4. This theoretical state for CF_4^- has not been observed and requires the bulk CF_4 to be in an initially excited state to capture the primary electrons. Since the bulk gas in this work is at room temperature, CF_4 cannot initially capture the electrons and CF_4^- can only exist for a short time before auto-dissociation. Also, all our experimental work with pure CF_4 used in TPCs has always produced electron drift behavior [98]. Therefore, at the conditions probed by our TPC experiments, SF_6 must perform the initial electron capture. Another species is CF_4^- in clusters of $(CF4)_n$, which have been observed and found stable [106]. Neither can this be the new species, because they have slow drift velocities and the new species is faster than SF_5^- [107]. Therefore, CF_3^- is the best explanation for the identity of the new species, and the new species will be referred to as CF_3^- for the remainder of the chapter.

4.4 Experimental Results and Discussion

This section describes the experiment that discovered CF_3^- and the series of experiments to characterize its behavior. For each experiment the waveforms are presented and the results are compared with the production model in Section 4.3. In Section 4.4.3 the effect of P_{SF_6} on the waveform shape is presented. In sections 4.4.4, 4.4.5, and 4.4.6 the relative charges and the relative peak amplitudes, the reduced mobilities μ_0, and the effective diffusion are measured for CF_3^-, SF_6^-, and SF_5^- as a function of P_{SF_6} and E_{Drift}. The results of the fiducialization with CF_3^- are presented and compared to fiducialization with SF_5^- in Section 4.4.8. The last property discussed is the stability of the gas over time in Section 4.4.9.

4.4.1 40 Torr CF_4, 0.1 Torr SF_6

The 40-0.1 Torr CF_4-SF_6 gas mixture was the first where the new negative ion species CF_3^- was observed. First, consider the average laser waveforms from 103 V/cm to 1029 V/cm in Figure 4.3. At $E_{Drift} = 103\ V/cm$, Figure 4.3a demonstrates that even with such a low P_{SF_6} all the charge is captured. Also, the signal contains a lot of inter-peak charge, which is similar to the low drift field waveforms in pure SF_6 (see Figure 3.9a and Ref. [101]). However, there is an unexpected change in the waveforms compared to the SF_6 waveforms at $E_{Drift} = 412\ V/cm$. Figure 4.3b shows the onset of CF_3^- production and the CF_3^- peak at $T = 7100\ \mu s$. The small feature to the right of CF_3^- at $T = 7200\ \mu s$ is another negative ion species. This feature could be F^-; its lower amplitude compared to the peak amplitude of CF_3^- is consistent with the lower production rate of F^- compared to CF_3^- [103]. Similar to pure SF_6, the shoulders near $T = 7400\ \mu s$ and $T = 7800\ \mu s$ are an unknown feature and the SF_5^- peak. The unknown feature is another unidentified negative ion species, where the left edge represents the charge that did not undergo charge transfer with another species. The shoulder to the right is the inter-peak charge resulting from electron transfer with the slower drift species, perhaps SF_5^- and SF_6^-. As the E_{Drift} is further increased, in Figures 4.3c and 4.3d the CF_3^- peak grows quickly and by $E_{Drift} = 1029\ V/cm$ becomes the dominant negative ion species. Similar to 30 Torr SF_6 the inter-peak charge decreases as E_{Drift} is increased. At $E_{Drift} = 1029\ V/cm$ all three negative ion species are prominent and the inter-peak charge is minimal, which is important for fiducialization. Also clear from Figure 4.3d is the dual-peak nature of CF_3^-, where the smaller amplitude peak overlapping with the CF_3^- peak is likely F^-.

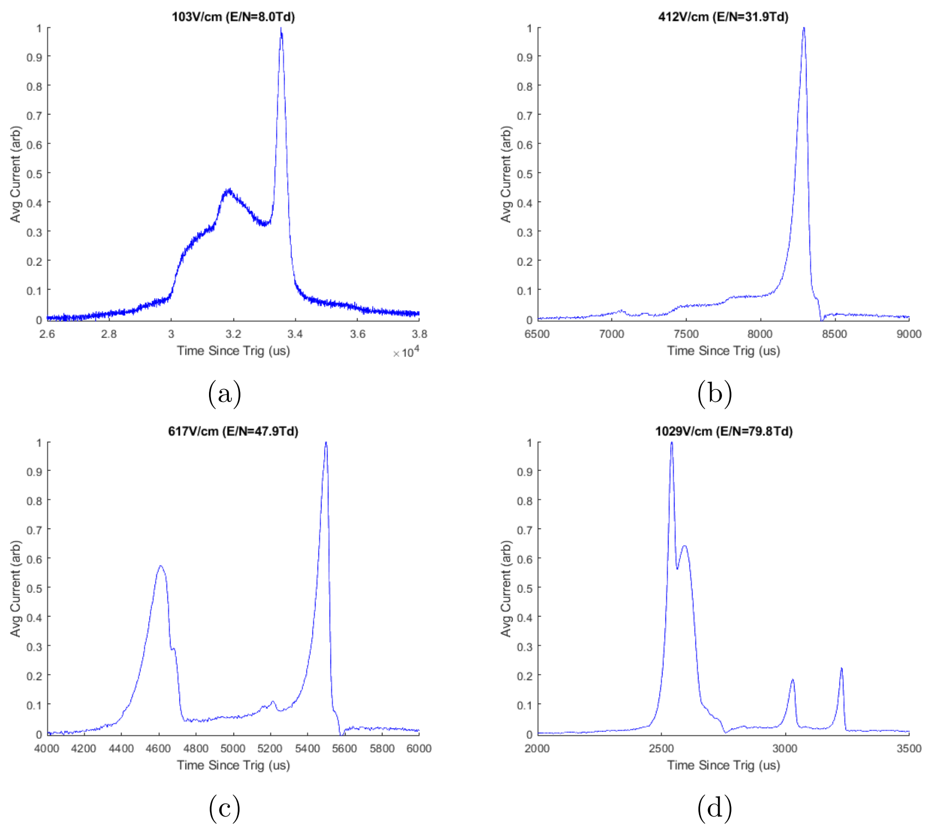

Figure 4.3: Averaged laser current waveforms at 40-0.1 Torr CF_4-SF_6 and $E_{Drift} = 100\ V/cm$, $400\ V/cm$, $600\ V/cm$, and $1000\ V/cm$.

The behavior of the negative ion species are consistent with the production model. At low E_{Drift}, the low energy electrons are captured by SF_6 and the resulting $(SF_6^-)^*$ is excited to low vibrational energy E_ν. Consequently, $E_\nu < \Delta E_0^+$ and CF_3^- is not readily produced. Instead, $(SF_6^-)^*$ collisionally stabilizes and produces SF_6^- or SF_5^-. When E_{Drift} is increased the electrons are captured at higher energies, the fraction of $(SF_6^-)^*$ with $E_\nu > \Delta E_0^+$ increases, and the CF_3^- production increases.

4.4.2 "Pure" CF_4 (Trace SF_6)

The unexpected negative ion species at 40-0.1 Torr CF_4-SF_6 in Section 4.4.1 led to the experiment described in this section. The experiment is 40 Torr CF_4 with the goal of verifying whether the new negative ion species identified as CF_3^- is due to the introduction of SF_6, consistent with our model in Section 4.3. Unfortunately, even after a long pump down the negative ion behavior of the experiment indicates the presence of SF_6 (we know based on prior experiments that at these conditions CF_4 never experiences negative ion behavior). The SF_6 contamination comes from SF_6 outgassed into the detector, and thus polluting the CF_4 with trace amounts of SF_6. The P_{SF_6} contaminating the gas is estimated to be less than 0.1 Torr because the pressure remains constant during the experiment and the baratron resolution is ±0.1 Torr. Since it is known that SF_6 is difficult to purge from the detector and requires long pump-down times, the following experiments are performed in order to study the negative ion behavior when P_{SF_6} is as low as can be obtained.

Figure 4.4 shows the average laser current waveforms from $E_{Drift} = 257\ V/cm$ (Figure 4.4a) to $E_{Drift} = 823\ V/cm$ (Figure 4.4f). The Figures 4.4a, 4.4b, and 4.4c are logarithmic scale. At $E_{Drift} = 257\ V/cm$ the dominant, off-scale, sharp peak is the fast arriving electrons that are never captured. The electron peak is followed by the slow, very low amplitude negative ion signal, which arrives over a long time period. The right edge indicates charge that drifts the entire length of the detector as a negative ion. The inter-peak charge spent a fraction of the drift time as electrons and negative ions. The negative ion species at $E_{Drift} = 257\ V/cm$ is believed to be SF_6^-, because SF_6 has an electron capture resonance at zero electron energy, and the drift velocity is consistent with SF_6^-.

At $E_{Drift} = 386\ V/cm$, Figure 4.4b shows a different negative ion species is produced. The production of the negative ion species increases with E_{Drift} until all the charge is captured at $E_{Drift} = 515\ V/cm$ (Figure 4.4d). Based on u_0, the dominant negative ion species at $E_{Drift} \geq 386\ V/cm$ is CF_3^-. At $E_{Drift} = 515\ V/cm$ there are clearly three species. The slowest species is SF_6^- and the faster species between CF_3^- and SF_6^- is SF_5^-. Similar to pure SF_6 [101], the charge that arrives more lowly than SF_6^- are likely SF_6-SF_6^- clusters. When E_{Drift} is increased further, the SF_6^- peak disappears entirely and SF_5^- emerges prominently above the inter-peak charge. This negative ion behavior is consistent with the production model for the same reasons as the 40-0.1 Torr CF_4-SF_6 experiment. Namely, increasing E_{Drift} or decreasing P_{SF_6} increases the E_ν distribution and the production of CF_3^-. Also, SF_5^- is produced more readily with increasing E_{Drift} due to the higher probability of auto-dissociation when E_ν is larger.

Figure 4.4e shows at $E_{Drift} = 1029\ V/cm$ the waveforms are similar to the waveforms in 40-0.1 Torr at 1029 V/cm (Figure 4.3d). In both experiments the peak associated with CF_3^- separates into two species; CF_3^- and likely F^-. The prominence of SF_5^- above the inter-peak charge is also similar. A difference is the absence of SF_6^- in 40-<0.1 Torr, which is explainable with the production model. Due to the increase in the electron capture length in 40-<0.1 Torr, the distribution of E_ν is greater in 40-<0.1 Torr than in 40-0.1 and SF_6^- production is suppressed.

Although the 40-<0.1 and the 40-0.1 results demonstrate the tunability of each negative ion species, these mixtures do not produce negative ion species that resolve the fiducialization issue in pure SF_6. At the largest E_{Drift}, CF_3^- is the dominate negative ion species and the charge distribution is too broad due to its overlap with the slightly slower negative ion species, which we have referred to as the F^- peak. If CF_3^- is utilized for the track length reconstruction and SF_6^- or SF_5^- for fiducialization, the reconstructed track lengths might have large even-by-event fluctuations even for point-size tracks due to the intrinsic broadness of the charge distribution. Instead, the behavior of the negative ion species at larger P_{SF_6} are studied with the objective of finding an optimal SF_6-CF_4 mixture for fiducialization.

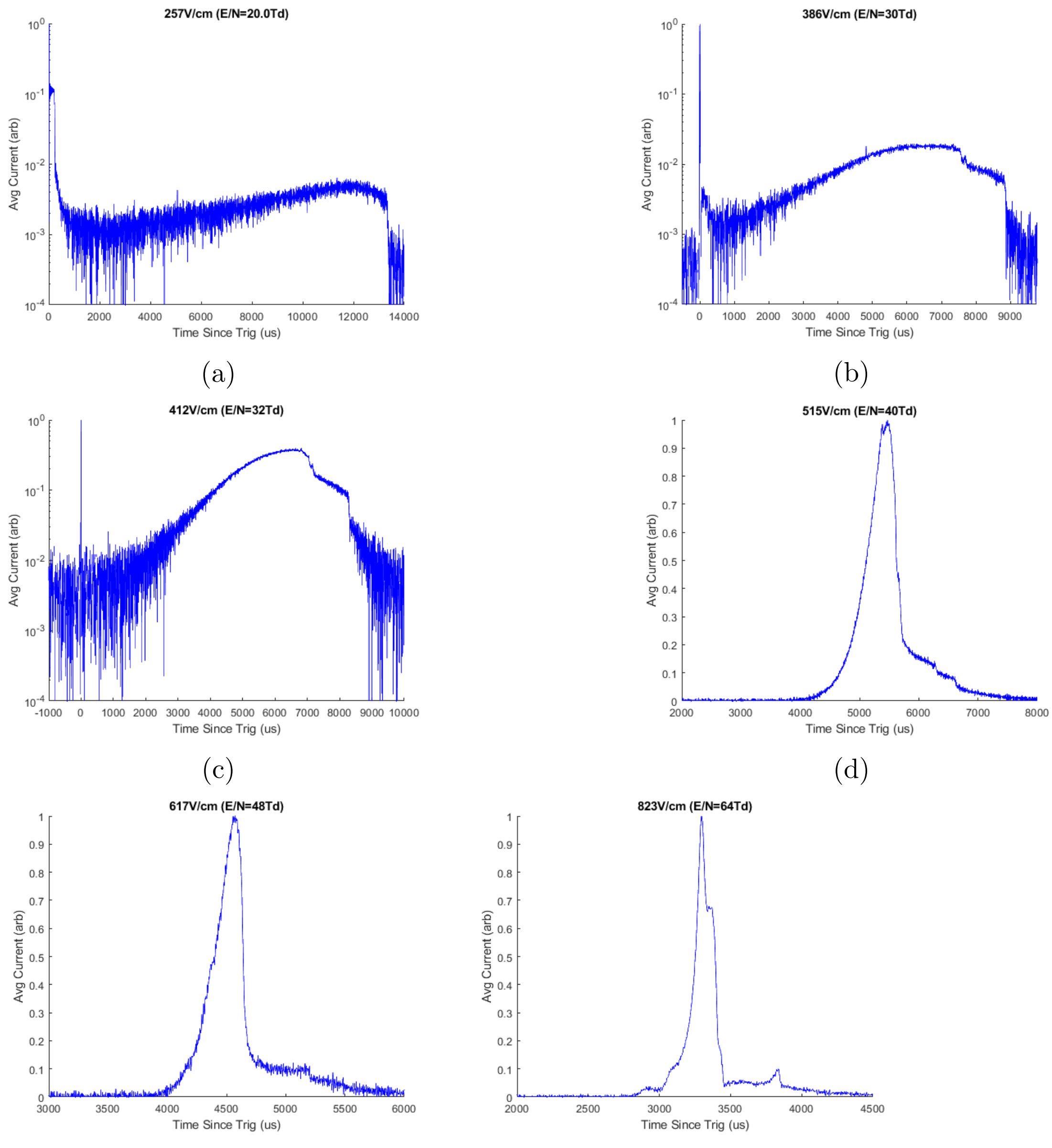

Figure 4.4: Average laser current waveforms for 40-< 0.1 Torr CF_4-SF_6 for increasing drift field. Note the vertical scale changes from log to linear.

4.4.3 The Effect of P_{SF_6} at Constant P_{CF_4} and E/N

This section describes a series of experiments aimed at characterizing the behavior of SF_6^-, SF_5^-, and CF_3^- as P_{SF_6} is increased while maintaining P_{CF_4} and constant reduced field E/N. The E/N will be expressed in units of Td, where $1Td = 10^{-17}$ $Vcm^{-}2$. P_{SF_6} is increased from ≈ 0 Torr to 10 Torr at $P_{CF_4} = 20$ Torr and $E/N = 95Td$. P_{CF_4} is lowered to 20 Torr to reach the highest possible E/N without causing the gas to breakdown. E/N is held fixed by slightly adjusting the high voltage to compensate for the pressure increase as SF_6 is added. Figure 4.5 shows the waveforms for several P_{SF_6}. The waveforms show that as P_{SF_6} is increased the SF_6^- production increases at the expense of CF_3^- and SF_5^-, which is expected based on the production model. As P_{SF_6} increases the primary electrons encounter SF_6 earlier (capture length decreases), and thus the distribution of E_ν is lowered. Consequently, collisional stabilization is the dominant deexcitation method and SF_6^- production is favored. Also favoring the production of SF_6^- over CF_3^- is the increased likelihood of $(SF_6^-)^*$ encountering SF_6 instead of CF_4.

4.4.4 Relative Peak Amplitude and Charge

This section discusses the behavior of the relative amplitude ($\frac{A_{minority}}{A_{SF_6^-}}$) and the relative charge ($\frac{C_{minority}}{C_{CF_3^-}+C_{SF_5^-}+C_{SF_6^-}}\%$), where $C_{minority}$ is one of the negative ion species: SF_6^-, SF_5^-, and CF_3^-. Recall from Figure 4.1 the CF_3^- peak is really two unresolved peaks; CF_3^- and another peak (perhaps F^-). Consequently, for the case of CF_3^- the amplitude refers to the amplitude of the larger peak (presumed to be CF_3^-), and the charge is the sum of the charge contained in both peaks ($CF_3^- + F^-$). First, consider the series of experiments described in Section 4.4.3, where $P_{SF_6} =$ 0-10 Torr, $P_{CF_4} = 20$ Torr, and $E/N = 95Td$. Figure 4.6 shows the relative amplitude and charge for these experiments versus $\%SF_6 = \frac{P_{SF_6}}{P_{SF_6}+P_{CF_4}}\%$. The curves for the relative charge in Figure 4.6a are blue for CF_3^-, red for SF_5^-, and black for SF_6^-. When

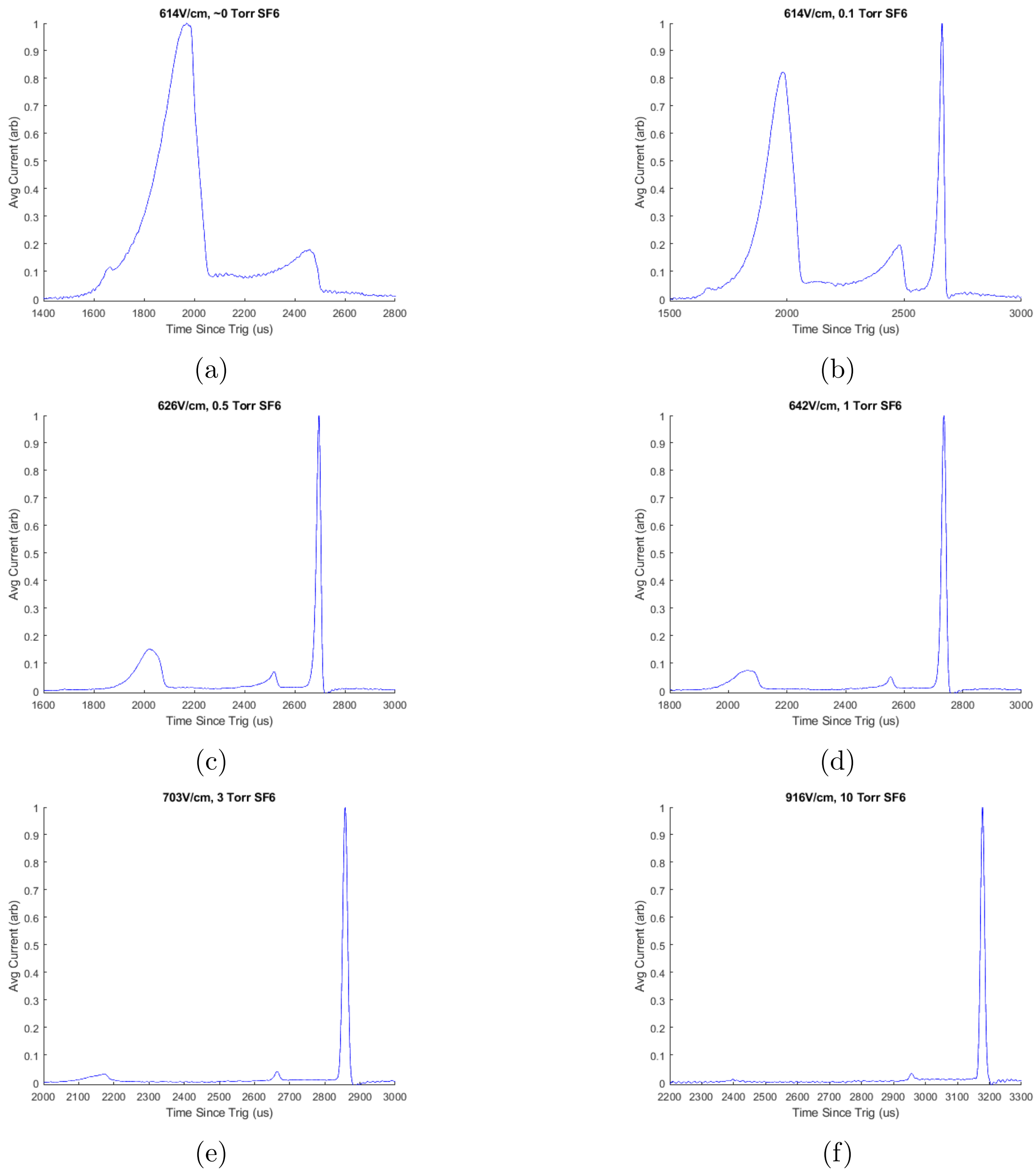

Figure 4.5: Average laser waveforms at 20 Torr CF_4 and 0 Torr to 10 Torr SF_6 at $E/N = 95Td$.

$\%SF6 < 4\%$, most of the charge is contained in CF_3^-. As $\%SF_6$ increases, SF_6^- production rapidly increases and when $\%SF_6 > 4\%$ it overtakes CF_3^- as the dominant charge species. The CF_3^- production quickly decreases until for $\%SF_6 > 30\%$ CF_3^-

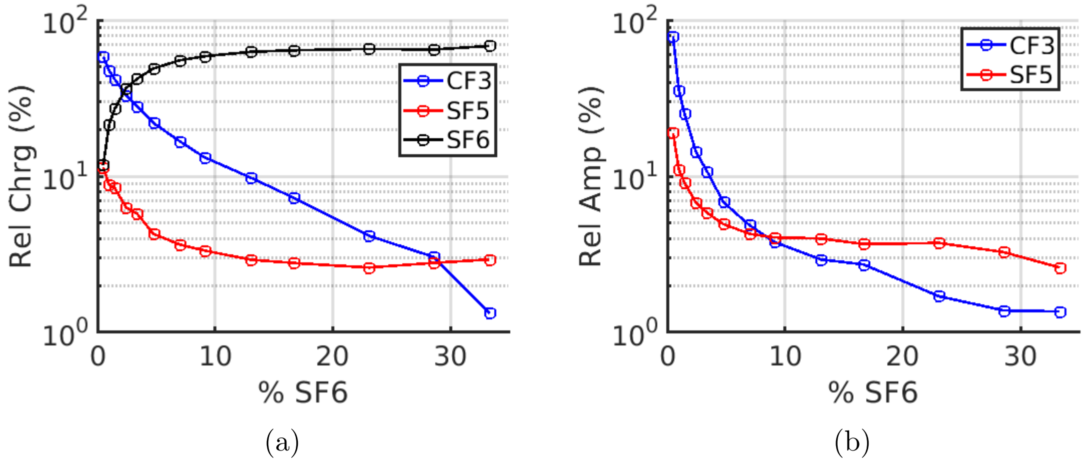

Figure 4.6: At $P_{CF_4} = 20$ Torr and $E/N = 95Td$ the relative charge and the relative amplitude versus the relative SF_6 pressure $\%SF_6$.

is difficult to identify. The SF_5^- decreases with $\%SF_6$ and asymptotes to 2.5%. The difference between the total charge (all charge between left edge of CF_3^- peak and right edge of SF_6^- peak) and the sum of the three species is the inter-peak charge. The inter-peak charge remains roughly constant at slightly less than 20%, which is expected since E/N is unchanging.

Next, consider the relative amplitudes shown in Figure 4.6b. Although the relative charge is dominated by CF_3^- for $\%SF_6 < 4\%$, the dominant amplitude species is always SF_6^- (see Figure 4.5), so the amplitudes are normalized to SF_6^- (not shown). Similar to the relative charge, the CF_3^- is nearly as high as SF_6^- for $P_{SF_6} < 0.1$ Torr, but it quickly decreases as $\%SF_6^-$ increases. The SF_5^- decreases more slowly and is larger than CF_3^- for $\%SF_6 > 10\%$. The CF_3^- relative amplitude is order 1% for $\%SF_6 > 30\%$.

In summary the trends are the following: as $\%SF_6$ is increased, the relative CF_3^- production decreases rapidly, the relative SF_5^- production decreases more slowly than CF_3^- and asymptotes to a constant, and the relative SF_6^- production increases rapidly. Each of these trends are consistent with the production model because as

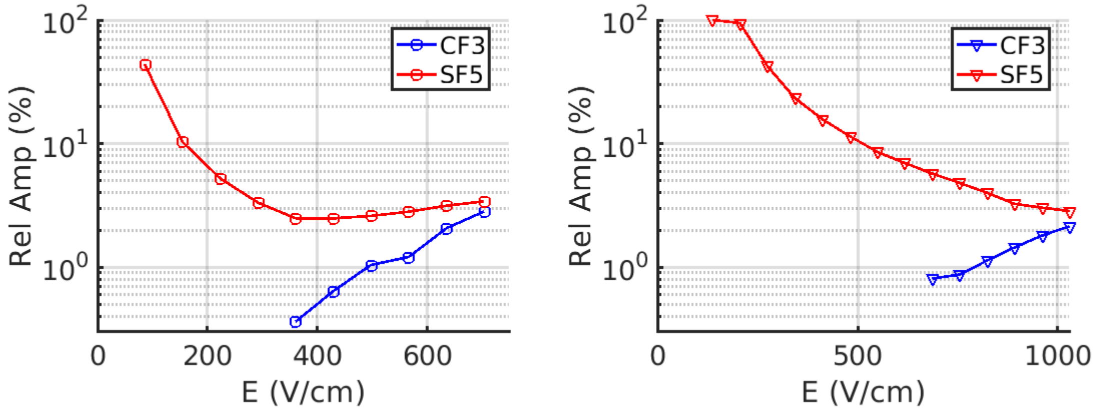

(a) 20-3 Torr CF_4-SF_6.

(b) 50-3 Torr CF_4-SF_6.

Figure 4.7: Relative amplitudes for CF_3^- (blue) and SF_5^- (red) versus the drift field E.

the SF_6 density increases, the electron capture length decreases and the electron energies are correspondingly lower when they are captured.

Lastly, consider the behavior of CF_3^- and SF_5^- when the gas composition is held fixed and E_{Drift} is increased. Figure 4.7a and 4.7b show the relative amplitude of CF_3^- (blue) and SF_5^- (red) for 20-3 Torr CF_4-SF_6 and 50-3 Torr CF_4-SF_6 respectively. The trends are similar for both mixtures. For E_{Drift} equal to a few hundred V/cm, SF_5^- is large and CF_3^- is not produced. When E_{Drift} is increases, SF_5^- gradually decreases to a few % and CF_3^- steadily increases. This behavior is predicted in our model in Section 4.3, where the increasing E_{Drift} increases the E_ν distribution which in turn increases the CF_3^- production.

4.4.5 Reduced Mobility μ_0

This section focuses on the reduced mobility u_0 (see Equation 3.2)of the three negative ion species SF_6^-, SF_5^- and CF_3^-. The behavior of u_0 for each species is characterized versus E/N and $\%SF_6$. Figures 4.8, 4.9, and 4.10 compare u_0 for SF_6^-, SF_5^- and CF_3^- in two gas mixtures: 20-3 Torr CF_4-SF_6 (blue) and 50-3 Torr CF_4-

SF_6 (red). Figure 4.11 compares u_0 versus $\%SF_6$. Consider first $u_0(SF_6^-)$ versus E/N in Figure 4.8. The location where u_0 changes from flat to positive sloping indicates the transition from thermal to nonthermal drift behavior (see [101] and the Nernst-Townsend-Einstein relation). For the 20-3 (50-3) Torr CF_4-SF_6 mixtures, the $u_0(SF_6^-)$ transition is $60Td$ ($70Td$). The high E/N transition at the higher total pressure is due to the increase in gas density, which tends to increase the interaction rate and to maintain the negative ions in thermal equilibrium with the bulk gas. The dotted curves are other measurements of $u_0(SF_6^-)$ for 1% $\%SF_6$ (upper) and 3.75% $\%SF_6$ (lower) [100]. The $\%SF_6$ for the 20-3 and the 50-3 mixtures are 13% and 5.6% respectively, indicating this work measures u_0 faster for a given $\%SF_6$ than Ref. [100]. This discrepancy might be due to a difference in the total pressure, since the measurements of Ref. [100] are at higher total pressure. Nevertheless, the trend for $\%SF_6$ is the same; the drift velocity of SF_6^- decreases monotonically as $\%SF_6$ increases. Ref. [100] asserts the slowing is the result of much stronger SF_6^--SF_6 interactions than SF_6^--CF_4 interactions. Figure 4.11 further corroborates this behavior, where SF_6^- (black) slows with increasing $\%SF_6$.

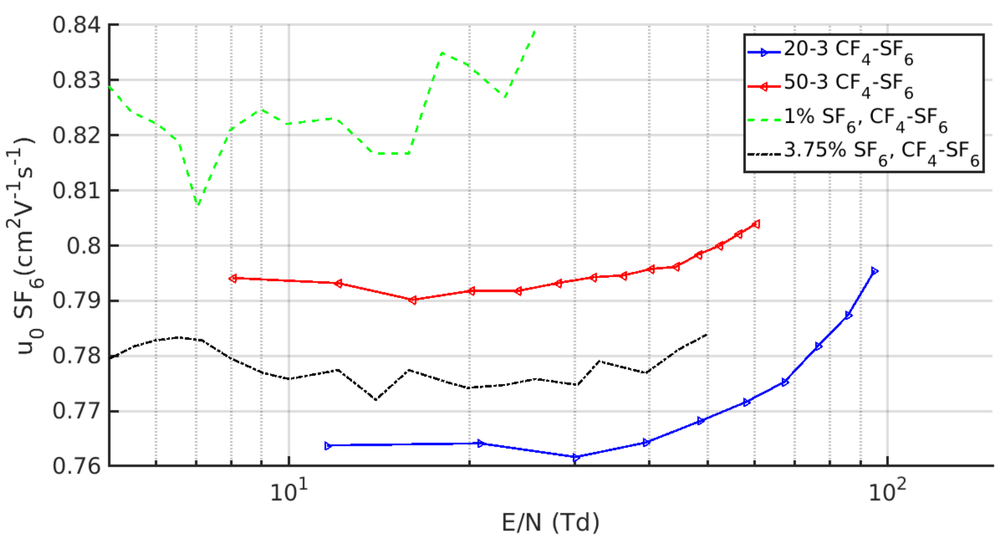

Figure 4.8: Reduced mobilities μ_0 for SF_6^-. The curves for 1% SF_6 and 3.75% SF_6 are measurements from Ref. [100]

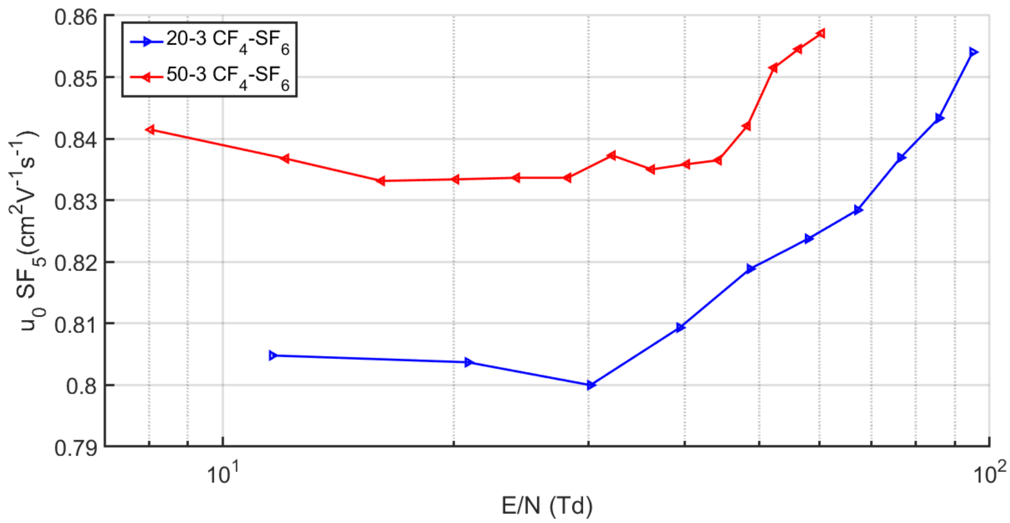

Figure 4.9: Reduced mobilities μ_0 for SF_5^-.

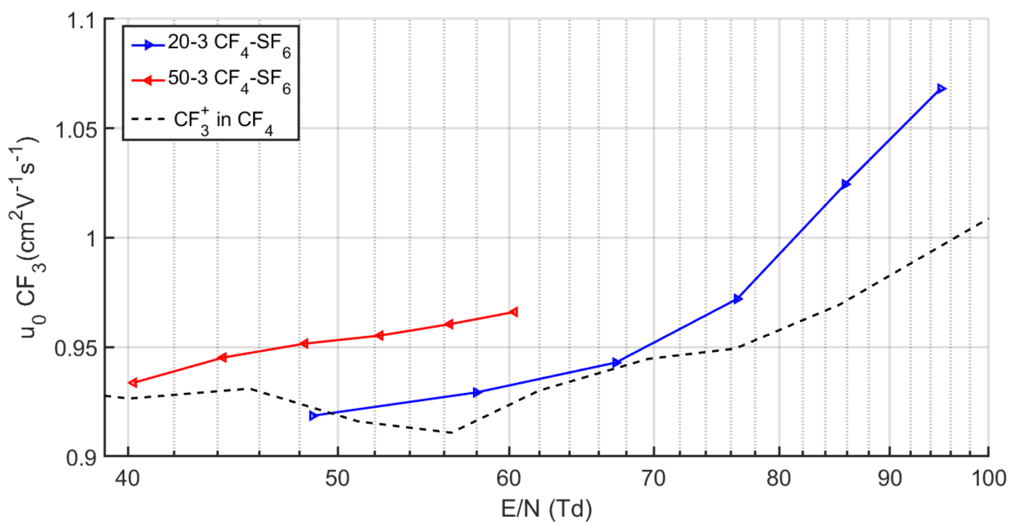

Figure 4.10: Reduced mobilities μ_0 for CF_3^-, where the curve CF_3^+ are measurements from Ref. [99].

Figure 4.9 shows $u_0(SF_5^-)$. Compared to calculating $u_0(SF_6^-)$ the measurement of $u_0(SF_5^-)$ has the difficulty of SF_5^- being lower amplitude, broader, and surrounded by inter-peak charge. The two left most data points in the 50-3 curve (red) might have been miscalculated due to the increase in the inter-peak charge. Nevertheless, the deviation from the thermal behavior is consistent with SF_6^-. Also similarly to SF_6^-, $u_0(SF_5^-)$ is higher for the 50-3 mixture and decreases linearly with $\%SF_6$ (Figure 4.11 red).

Lastly, consider the behavior of $u_0(CF_3^-)$ with E/N and $\%SF_6$. Based on the production model, CF_3^- is not created until $E_\nu > \Delta E_0^+$, and thus E/N must be greater than some threshold value. Figure 4.10 shows the behavior of $u_0(CF_3^-)$ with E/N for 20-3 CF_4-SF_6 (blue) and 50-3 CF_4-SF_6 (red). The 20-3 and the 50-3 curves terminate at $40Td$ and $48Td$ respectively because the CF_3^- peak amplitude drops below 1% (see Figure 4.7a) and is difficult to identify. Consequently, the onset for CF_3^- production is likely close to $E/N = 40Td$. The sharp positive slope for both 20-3 (blue) and 50-3 (red) indicate the ion behavior is nonthermal from the onset. Unfortunately, no measurements of $u_0(CF_3^-)$ in CF_4 or CF_4-SF_6 mixtures were discovered to compare with our measurements. The best comparison to make are measurements of $u_0(CF_3^+)$ in CF_4 using a drift tube mass spectrometer [99]. Since typically u_0 for the positive ion counterpart to the negative ion are similar to the u_0 for the negative ion, $u_0(CF_3^+)$ in CF_4 is a useful comparison with our measurements of $u_0(CF_3^-)$. Although $u_0(CF_3^+)$ is slower than our measured $u_0(CF_3^-)$, their trend with E/N is consistent. The behavior of CF_3^- with $\%SF_6$ is the same as the behavior of SF_6^- and SF_5^-. $u_0(CF_3^-)$ decreases linearly with $\%SF_6$.

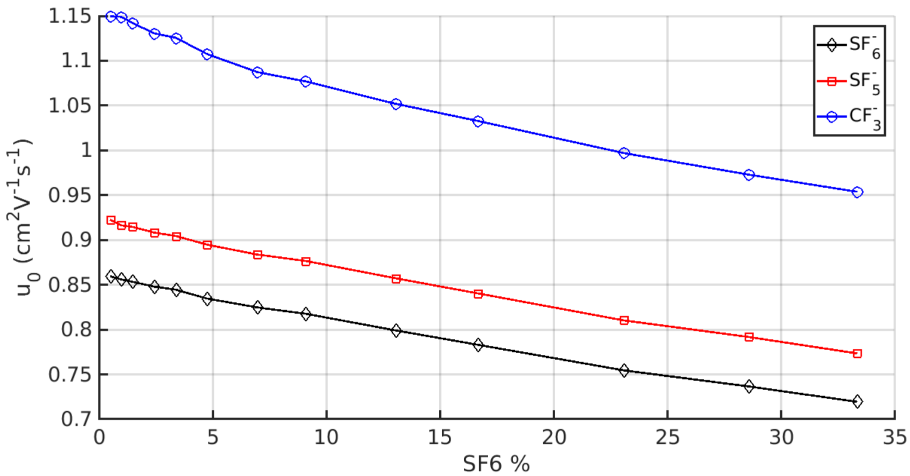

Figure 4.11: At a constant 95Td and 20 Torr CF_4 the mobilities of SF_6^-, SF_5^-, and CF_3^- versus the SF_6 percentage of the total pressure.

4.4.6 Diffusion

The next important quantity to describe is the effective diffusion σ_Z of the primary negative ion. Figure 4.12a shows σ_Z versus E_{Drift} for several $P_{CF_4} = 50$ Torr and $P_{CF_4} = 20$ Torr mixtures, and Figure 4.12b shows σ_Z versus E_{Drift} for several $P_{CF_4} = 50$ Torr and $P_{CF_4} = 20$ Torr mixtures. σ_Z is measured with:

$$\sigma_Z = \sigma_T V_d, \tag{4.3}$$

where σ_T is the fitted Gaussian of the SF_6^- peak on its left edge from 30% to 50% its amplitude after the smoothing time is removed, and V_d is the drift velocity. The smoothing time is subtracted in quadrature from σ_{fit}. Unfortunately, this subtraction method is only approximately valid because the measured σ_{fit} is not strictly Gaussian. In Chapter 2 the broadening of the waveforms due to the THGEM pitch σ_{THGEM} is measured to be $99\mu m \pm 11\mu m$, and the broadening due to the capture length σ_{Capt} is measured to be order $10\mu m$ for the range of E_{Drift} in this section. Comparing these measurements to the measurements of σ_Z in Figure 4.12a and 4.12b, they are small compared to σ_Z. Consequently, the effect of σ_{THGEM} and σ_{Capt} are ignored.

Consider Figure 4.12a, where the dotted line represents thermal diffusion (Equation 1.2). For the 20-0.8 CF_4-SF_6 mixture (black squares), the $\%SF_6$ concentration is low (3.8%) and the deviation from thermal behavior occurs early in E_{Drift} (about 300 V/cm). Next, the 20-1 mixture (magenta) and the 20-1.2 mixture (green) have 4.8 and 5.7 $\%SF_6$ respectively. The E_{Drift} where the onset of nonthermal behavior occurs is largest for 20-1.2. This is where $\%SF_6$ is the highest. For the 20-3 mixture (blue) $\%SF_6$ is the largest of all the mixtures (13%) and the diffusion appears to be thermal until $E_{Drift} \approx 400$ V/cm. The 20-3 mixture is further studied in Section 4.4.8 measuring fiducialization and in Chapter 5 measuring discrimination and directionality. The trend of σ_Z implies that thermal behavior is maintained to higher E_{Drift} as the $\%SF_6$ is increased. As shown in Figure 4.12a, the 50-2 and 50-3 trend to have σ_Z larger for lower $\%SF_6$. The cause for the deviation from thermal below 500 V/cm in the 50-3 is unknown but could be the result of contamination during the run or peak misidentification due to the increase of the inter-peak charge.

Next consider the dependence of σ_Z on $\%SF_6$ shown in Figure 4.12b, where E/N is held fixed at $95Td$. σ_Z decreases exponentially with increasing $\%SF_6$ and approaches the minimum value 1 mm. The behavior is the result of the following two contributions. First recall from Equation 2.4 the contributions to σ_Z are the diffusion σ_{Diff}, the capture length σ_{Capt}, the THGEM σ_{THGEM}, and $\sigma_{Software}$. The σ_{Diff} may decrease as $\%SF_6$ increases for the same reason as $u_0(SF_6^-)$; the SF_6^- interacts more strongly with neutral SF_6 than CF_4 and the increased interaction rate better maintains SF_6^- in equilibrium with the bulk gas. Another contribution is σ_{Capt}. The primary electron capture length will decrease as the number density of SF_6 increases,

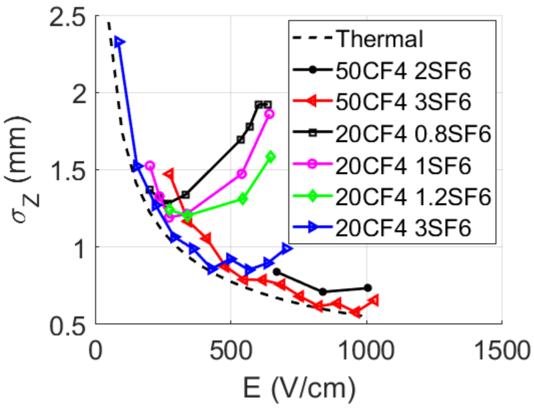

(a) The effective diffusion σ_Z versus E/N.

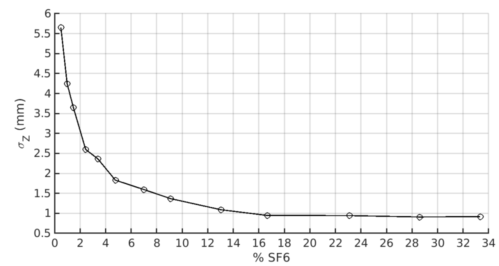

(b) The effective diffusion σ_Z at E/N = $95Td$ and $P_{CF_4} = 20$ Torr versus $\%SF_6$.

Figure 4.12: The dependence of the effective diffusion σ_Z on E_{Drift} (4.12a) and $\%SF_6$ (4.12b).

and as the capture length decreases so will the lengthening of the track before capture σ_{Capt}. However, given that SF_6 captures at very low $\%SF_6$ (Figure 4.4a) the capture length is likely very short above a few $\%SF_6$. The continued downward trend of σ_Z above a few $\%SF_6$ is then almost exclusively due to the increasing SF_6^- interaction rate with the bulk gas.

4.4.7 Broadness of the CF_3^- Spatial Distribution

In this section the broad nature of the CF_3^- charge distribution is discussed. There are two potential causes for this, but the second is the more likely. The first is complex and involves the production of the negative ion. If all the steps for the CF_3^- production occur quickly (efficiently), then the ions will be clustered in time and the peak will be narrow. However, if any of the steps require a significant or varying amount of time, then the peak will broaden. There are two steps which might be inefficient. The first is the electron transfer between the intermediate complexes, which might depend on the distribution of E_ν. The second is the time for the auto-dissociation of CF_4^- to CF_3^-, which might be altered and lengthened because of the

CF_4^- proximity to the SF_6, its internal energy, or another means. Another potential cause for the broadness is the overlap of the CF_3^- charge distribution with the charge distribution of another species. Figure 4.3d and 4.4f indicate there is another negative ion species (perhaps F^-) that separates itself from CF_3^- at high E/N. It is unclear if this species is present at low E/N and high $\%SF_6$. Future work is required to determine its effect on the width of CF_3^-, and how to minimize it.

4.4.8 Fiducialization

This section discusses the optimal mixture for fiducialization and, using this mixture, presents results on fiducialization. In order to select the optimal mixture, consider the following trends. In Section 4.4.4 the production of CF_3^- rapidly drops with $\%SF_6$ and disappears entirely for $\%SF_6 > 35\%$. However, not yet discussed is that as $\%SF_6$ is increased the mixtures are more stable and can achieve higher gas gains. Therefore, the optimal mixture for fiducialization must take into account the trade-off between gain and CF_3^- production. For the CF_3^- fiducialization to be more reliable than SF_5^- fiducialization in SF_6 given the current signal to noise of our detector, the CF_3^- production must be greater than 2.5% (by amplitude). This work asserts the optimal relative production is 8% to 10%, which is large enough to reliably fiducialize without taking too much charge from the SF_6^- charge distribution. The SF_6^- charge distribution should contain the majority of the charge in order to best measure all other track properties needed for directional dark matter searches. With these considerations, the 20-3 Torr mixture at $E_{Drift} = 702\ V/cm$ is selected, which has a relative CF_3^- production of 9.8% and low effective diffusion ($\sigma_Z < 1mm$ over $58.3cm$). The waveform is shown in Figure 4.5e. Also important, the relative SF_5^- production in the 20-3 Torr mixture and in 30 Torr SF_6 is the same at 2.5%. This allows the SF_5^- fiducialization in the 20-3 Torr mixture to represent the fiducialization characteristics in SF_6. In other words, the conclusions about the fiducialization in the 20-3 Torr mixture can be directly compared with the fiducialization in SF_6.

Next, the effectiveness of the CF_3^- fiducialization is compared to the SF_5^- fiducialiation in the 20-3 Torr mixture. Recall the fiducialization is given by

$$Z = \frac{v_s v_p}{v_s - v_p} \Delta T_{p-s}, \tag{4.4}$$

where Z is the location of the track, v_s and v_p are the drift velocities of the secondary species and SF_6^- respectively, and ΔT_{p-s} is the arrival time difference between the secondary and SF_6^-. First, consider the CF_3^- and the SF_5^- fiducialization using the laser to produce ionization at the cathode ($Z = 58.3\ cm$). Figure 4.13 shows the fiduzialization utilizing the CF_3^- (blue) and the SF_5^- (red). Each laser-induced track drifts the length of the detector, so the reconstructed Z should be centered on 58.3 cm. Unfortunately, the intrinsic broadness of the CF_3^- charge distribution (Section 4.4.7) causes the reconstructed Z distribution to be broader than the SF_5^- Z distribution. This means the resolution in Z utilizing CF_3^- is worse than SF_5^- for this mixture. However, what Figure 4.13 does not demonstrate is the higher CF_3^- fiducialization *efficiency* compared to SF_5^- fiducialization.

In order to characterize the efficiency of the CF_3^- and the SF_5^- fiducialization, the DD neutron generator is utilized to create low energy nuclear recoils at Z locations distributed throughout the detector. Figure 4.14 shows the reconstructed Z distributions for the "GEM-side" (Figure 4.14a) and the "Cathode-side" (Figure 4.14b) locations for the DD neutron generator. The reader is referred to Section 3.4 for the description of the DD generator. Notice the CF_3^- fiducialization is red and the SF_5^- fiducialization is blue. Both Figures show several benefits of the CF_3^- fiducialization. Since each track is fiducialized independently for CF_3^- and SF_5^-, a given track can be fiducialized for CF_3^- and SF_5^-, for one and not the other, and for neither (not fiducialized). Consequently, the greater statistics in the CF_3^- fiducialization qualitatively demonstrates the improved fiducialization efficiency of CF_3^-

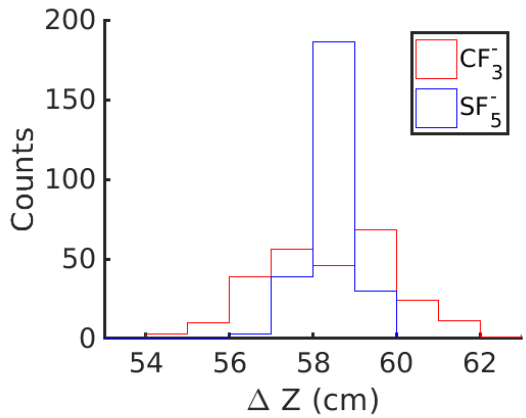

Figure 4.13: Reconstructed track Z for the laser generated tracks utilizing the SF_5^- (red) and the CF_3^- (blue). For the laser $Z = 58.3\ cm$.

compared to SF_5^-. Quantitatively, when utilizing CF_3^- fiducialization 70% and 76% of all "GEM-side" and the "Cathode-side" tracks respectively are fiducialized. This is compared to 38% and 50% using SF_5^- to fiducialize from the "GEM-side" and the "Cathode-side", respectively.

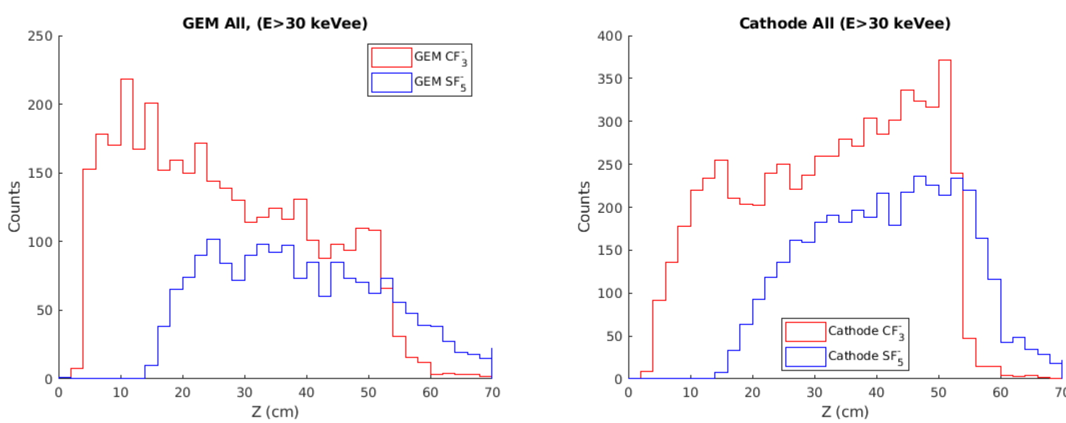

(a) (b)

Figure 4.14: ΔZ for the SF_5^- and CF_3^- peaks. Ionization created by DD generator.

Another benefit of the CF_3^- fiducialization is not only that the CF_3^- charge distribution is easier to identify, but it is harder to misidentify. Since the SF_5^- production is small and the SF_5^- charge distribution is immersed in the inter-peak charge, the likelihood of falsely identifying a noise peak as SF_5^- is significant. In order to have a qualitative understanding of the frequency of misidentification of both the SF_5^- and the CF_3^- peaks, we consider their reconstructed Z distribution above 58.3 cm, which is the maximum drift distance. For both the "GEM-side" and the "Cathode-side" experiments, the SF_5^- Z distribution has a tail that extends far beyond 58.3 cm. This is in contrast with the CF_3^- distribution, which has a much smaller fraction of events with $Z > 58.3$ cm.

In addition, another advantage of using CF_3^- over SF_5^- for fiducialization is the larger detector volume that can be fiducialized. Since Equation 4.4 shows that Z is proportional to ΔT_{p-s} and CF_3^- is faster than SF_5^-, ΔT_{p-s} is larger for CF_3^- than SF_5^- at a given Z. The detector and the data analysis combined have a minimum time difference between the arrival of two species ΔT_{min} required to resolve them. Consequently, ΔT_{min} corresponds to a smaller Z_{min} for CF_3^- than for SF_5^-. Figure 4.14 shows $Z_{min} = 5$ cm for CF_3^- and $Z_{min} = 10$ cm for SF_5^-. Therefore, the fiducial volume of the detector available for the dark matter search is higher with CF_3^-, thereby increasing the sensitivity of the experiment.

A final point to note is that the shape of the CF_3^- "GEM-side" and "Cathode-side" fiducialization distributions clearly indicate the location of the DD generator. This is because the solid angle for neutron interactions in the 3 cm by 3 cm active region decreases as the interaction distance from the DD generator is increased. Consequently, a greater number of neutron interactions are expected on the side of the detector closest to the DD generator. Figure 4.14 shows the "GEM-side" Z distribution has a greater number of tracks at short Z and is positively skewed. The opposite situation results for the "Cathode-side" Z distribution, because the DD generator is on the Cathode-side of the detector. The CF_3^- fiducialization reflects the inherent shape of the Z distribution better than the SF_5^- fiducialization. The small peak/excess of events in the CF_3^- fiducialization is likely due to the occasional misidentification of the CF_3^- peak with SF_5^-.

4.4.9 Waveform Stability over 24 Hours

The final property of the CF_4-SF_6 mixtures discussed in this chapter is the stability of the waveforms over time compared to those of SF_6. Section 3.3 and Ref. [101] describe the changing negative ion behavior of SF_6 gas over time. In SF_6 the inter-peak charge increases dramatically over the course of six hours. The reason was attributed to SF_6^--H_2O interactions during the drift of SF_6^-, which produce one or more unknown negative ion species that reside in the inter-peak charge. The amount of water contamination gradually increases as the acrylic of the detector outgases over the duration of the experiment. This section presents the negative ion behavior of the 20-3 CF_4-SF_6 mixture at three time intervals over the course of 24 hours.

Figure 4.15 shows the shape of the average laser waveforms for 2 hours (blue), 11 hours (red), and 24 hours (black) after the introduction of fresh gas. The inter-peak charge between the CF_3^- and the SF_5^- and between the SF_5^- and the SF_6^- begins low and remains unchanged for 24 hours. The only significant change is to the drift velocity of CF_3^-, which after 24 hours (black) is slower by 1.7% compared to after 2 hours (blue). Although this change in the drift velocity over a 24 hour period has little effect on the Z fiducialization, it requires further study. It is possible that the slowing of the CF_3^- species is due to outgassing of SF_6, because as shown in Figure 4.11 each negative ion species is slowed as SF_6 is added to the mixture. Since the drift velocities of the SF_5^- and the SF_6^- species do not much over time (see Figure 4.15), the drift velocity of the CF_3^- species may be much more sensitive to the SF_6 concentration than the other species. Also, since the detector was operated under similar conditions (pressure, pump down procedure, etc.) to the 20 Torr SF_6 experiments, the rate of water outgassing can be assumed similar. Therefore, the stability of the inter-peak charge in 20-3 Torr CF_4-SF_6 compared to SF_6 is most likely due to the lower SF_6 concentration in 20-3 Torr CF_4-SF_6.

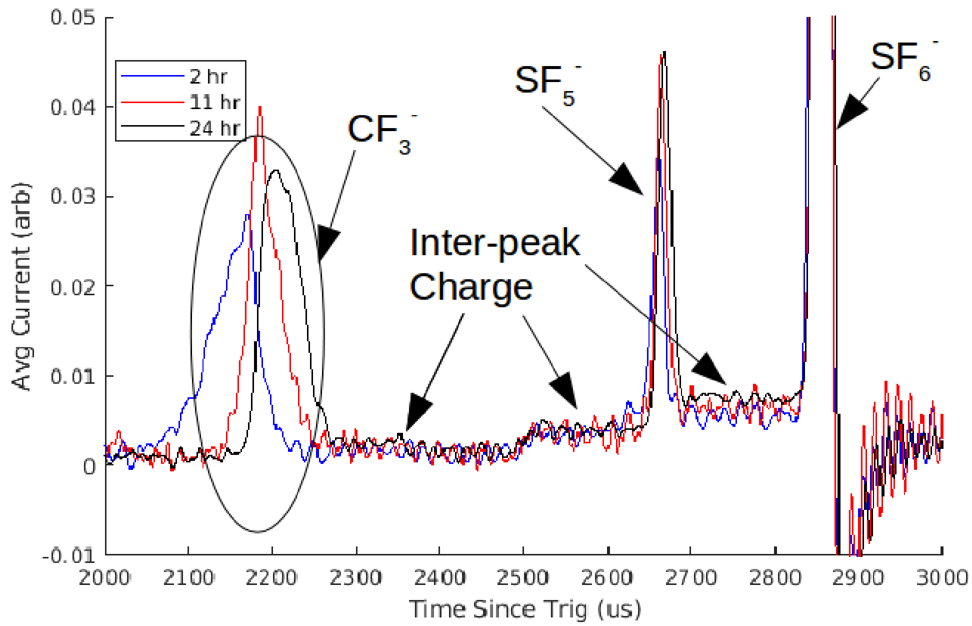

Figure 4.15: Average laser waveforms at 20-3 Torr CF_4-SF_6 demonstrating the stable production of the negative ion species and the inter-peak charge.

4.5 Conclusion

This chapter discusses the discovery and characterization of a new, tunable negative ion species in mixtures of CF_4-SF_6. The new species resolves the issue of the small SF_5^- production in pure SF_6 used to fiducialize TPCs along the drift direction. The new species is hypothesized to be CF_3^- and a model is proposed for its production and behavior in our TPC experiments. Next, we preformed a series of experiments to characterize the properties and relative production of the three negative ion species (SF_6^-, SF_5^-, and CF_3^-) as a function of SF_6 concentration $\%SF_6$ and reduced field E/N. The results show the CF_3^- production increases at the expense of SF_6^- as either $\%SF_6$ is decreased or E/N is increased. Base on these measurements, we found that the optimal mixture for fiducialization is 20-3 Torr CF_4-SF_6 at $E = 702\ V/cm$, where the relative production of CF_3^- is 9.8%. This mixture is utilized to measure the fiducialization with CF_3^- and to compare it with the fiducialization measured with SF_5^-. The results demonstrate the improved efficiency and the increase in fiducial volume for the CF_3^- fiducialization compared to the SF_5^- fiducialization. Lastly, the 20-3 Torr mixture is shown to be stable over at least a 24 period, which is much better than in pure SF_6. In Chapter 5 the 20-3 mixture is further utilized in experiments where we measure discrimination and directionality, the key quantities used in directional dark matter experiments.

Chapter 5

Discrimination and Directionality in Novel CF_4-SF_6 Gas Mixture

5.1 Introduction

In this chapter the discrimination and the directionality are measured in 20-3 Torr CF_4-SF_6 utilizing a 1D readout. These measurements are motivated by the work presented in Chapter 4, where the unexpected discovery of a tunable negative ion species in CF_4-SF_6 mixtures is characterized and found to be a solution for the small SF_5^- fiducialization peak in SF_6. The relative production of the species is found to increase from 0% to more than 50% of the total charge either by decreasing the SF_6 concentration ($\%SF_6$) or by increasing the reduced field (E/N). In Section 4.3 the production model for the new species is described, and its identity is asserted to be CF_3^-. The model predicts CF_3^- to be produced through dissociative electron transfer, where the excited $(SF_6^-)^*$ can transfer the electron to CF_4 if the vibrational energy E_ν of $(SF_6^-)^*$ is greater than the internal energy barrier. When the electron transfer occurs the CF_4^- subsequently auto-dissociates to CF_3^- and F, or to F^- and CF_3.

Although the CF_3^- production can be arbitrarily set by tuning $\%SF_6$ or E/N, the increase of the CF_3^- production comes at the expense of the SF_6^- production. Consequently, the CF_3^- production should be large enough to reliably fiducialization and to maximize SF_6^- production, where the SF_6^- peak is utilized to measure track properties such as the track length and the track skewness. The 20-3 Torr CF_4-SF_6 mixture at drift field $E_{Drift} = 702\ V/cm$ is selected for further study because the relative CF_3^- production (by charge) is 9.8% (see 13% $\%SF_6$ in Figure 4.6a), which is large enough to reliably fiducialize without detriment to other track properties.

In Chapter 3 the discrimination and the directionality are quantified utilizing a 1D TPC readout with the quantities E_{Disc} and E_{Skew}, which are the threshold energies above which the data demonstrates discrimination and directionality, respectively. Similarly, in this chapter the discrimination and directionality are measured and quantified with E_{Disc} and E_{Skew} in 20-3 Torr CF_4-SF_6 at $E_{Drift} = 702\ V/cm$ using a TPC with a 1D readout. The issue of the oscilloscope dead-time and the high gamma-ray production from the DD generator (see Section 3.4) causes at low energies the rate of gamma-ray induced electronic recoils to be much greater than the rate of neutron-induced nuclear recoils. In order to lower the rate of gamma-ray induced electronic recoils the detector must either be shielded with lead bricks in order to reduce the gamma-ray flux entering the detector, or the trigger threshold for the data acquisition must be increased. The solution was to measure the discrimination and the directionality in separate, dedicated experiments. For the discrimination measurement the detector is shielded with lead bricks and the trigger threshold is set at the ^{55}Fe level ($\approx 5.9\ keVee$). Whereas, for the directionality measurement no lead shielding is utilized and the trigger threshold is increases to the point where the nuclear recoil rate is about as large as the electronic recoil rate. This threshold was experimentally determined to be $\approx 20\ keVee$. The motivation for these experimental setups for the discrimination and the directionality experiments are discussed in Sections 5.3 and 5.4, respectively.

The chapter proceeds by describing the detector, the data acquisition, and the data analysis in section 5.2. The discrimination measurement is discussed in Section 5.3; where the four discrimination selection cuts and their effect on the data are presented in Section 5.3.1, the procedure to define the electronic recoil band and the nuclear recoil band is discussed in Section 5.3.2, and the resulting discrimination measurement presented in Section 5.3.3. The directionality measurement is discussed in Section 5.4; where the effect of the four directionality selection cuts and the resulting nuclear recoil band are presented in Section 5.4.1, and the resulting directionality measurement is presented in Section 5.4.2. Finally, this chapter presents in Section 5.5 the first range versus energy measurement in 20-3-100 Torr CF_4-SF_6-He, where 100 Torr He is added to the 20-3 Torr CF_4-SF_6 mixture. The addition of He is interesting for low mass WIMP searches with TPCs (see Section 5.5). The 100 Torr He pressure was selected in order to have a high He concentration without incurring instability, and it was meant merely as a starting point. Since the experiment had very poor signal to noise, a ^{60}Co experiment and a long background experiment (needed to define the electronic recoil band and the electronic recoil band) were not performed and other He pressures were not pursued. Consequently, although a notion of the discrimination is given based on the range versus energy for the DD neutron experiment, a full discrimination measurement cannot be performed.

5.2 Data Acquisition and Analysis

The experiments in this chapter utilize the same 1D detector, preamplifier, and oscilloscope acquisition as Chapter 3 and Chapter 4. Figure 5.1 shows the detector with the lead shielding (bricks) in place in order to reduce the gamma-ray flux from the DD generator for the discrimination experiment. The nuclear recoils are generated by orienting the DD generator in front of the THGEM ("GEM") and the cathode ("Cathode") as discussed in Section 3.4. For the data analysis, the algorithms are described in detail in Section 3.6. The filter parameters are summarized in Table 5.1, where SG_V is the Savitzky-Golay (SG) filter applied to the filtered voltage signal V_{Filt}, and SG_I is the SG derivative filter utilized to calculate the current I_{Length}. The discrimination experiment "Disc" has a larger filter window W than the directionality experiment "Skew". This is because the discrimination experiment can trigger on lower energy tracks than the directionality experiment. The low energy tracks have worse signal-to-noise and require additional filtering.

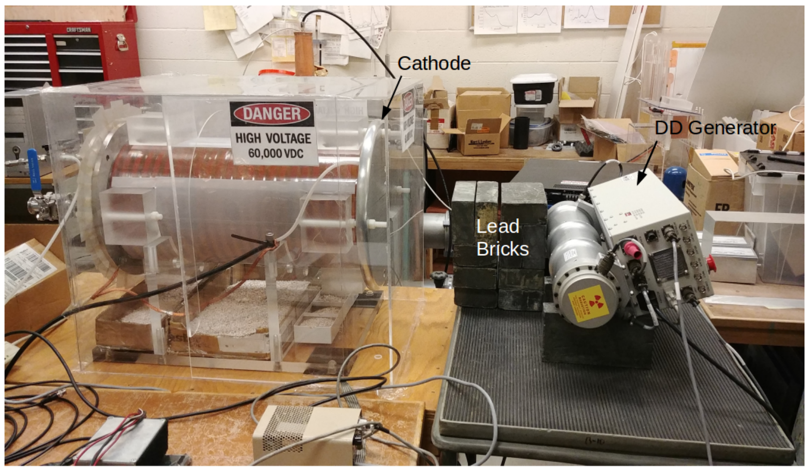

Figure 5.1: Experimental setup for the "Cathode-side" discrimination experiment, where the lead bricks are in place to reduce the gamma-ray flux.

Filtering Algorithm

	Skew	Disc
Notch (kHZ)	53,72	53,72
SG_V O	4	2
SG_V W	25	51
SG_I O	4	2
SG_I W	101	101

Table 5.1: The parameters for the Savitsky Golay (SG) filters. SG_V refers to the SG filters applied to V_{Filt} and SG_I refers to the SG derivative filter to calculate I_{Length}.

Track Property Algorithm

	Skew	Disc
$(I \cdot \frac{dI}{dt})_{min}$	3E-4	1E-4
$\%Edge$ (%)	10	10

Table 5.2: The thresholds and parameters for the track property algorithm.

The track property algorithm is similar to the algorithm described in Section 3.7. The thresholds to define the track length are summarized in Table 5.2, where $\%Edge$ is the percentage of I_{Max} where the track edges are located. The fiducialization algorithm is modified to require each potentially located minority charge distribution to pass amplitude and charge (area) qualifications. The qualifications are shown in Table 5.3, where A and H refer to area and amplitude, and "min" and "max" are the minimum and maximum values allowed for SF_5^- and CF_3^-. The amplitude and charge qualifications are selected based on measurements in Chapter 4. Although they reduce the fiducialization efficiency for low energy tracks, they prevent noise peaks from being misidentified as a minority species. Lastly, the track skewness is defined by Equation 3.5.

Fiducialization Algorithm

	Skew	Disc
$\sigma_{Fid}(us)$	12	15
$A_{CF_3^-,min}(\%)$	5	5
$A_{SF_5^-,min}(\%)$	2	2
$H_{CF_3^-,min}(\%)$	2	2
$H_{SF_5^-,min}(\%)$	2	2
$A_{CF_3^-,max}(\%)$	40	40
$A_{SF_5^-,max}(\%)$	40	40
$(I_{Fid} \cdot \frac{dI_{Fid}}{dt})_{min}$	1E-4	1E-5
$\%Edge$	10	10

Table 5.3: The parameters and thresholds for the fiducialization algorithm.

The energy calibrations are performed according to Section 3.4. A typical ^{55}Fe charge (area) spectrum is shown in Figure 5.2. The area-to-energy conversion factor is $5.9keV/x_0$, where $x_0 = 14.9$ is the mean location for the Gaussian fit. σ_A is the width of the Gaussian fit. Unfortunately, the energy resolution is often worse than 30% due to the poor signal-to-noise and the noise artifacts in the signal. In Figure

5.2 the energy resolution is $\sigma/x_0 = 44\%$. Most of the noise is introduced from the high voltage power supply for the cathode, which cannot be removed with the high voltage filter box utilized in Chapter 2 because the filter box has a break voltage of $36kV$. Therefore, reducing the noise and improving the energy calibration is crucial in future work.

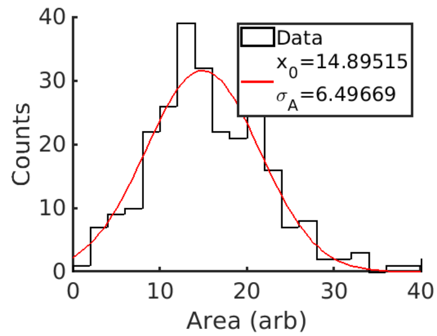

Figure 5.2: Typical area spectrum for $5.9keV$ ^{55}Fe X-rays.

5.3 Discrimination Measurement

In this section a series of experiments are presented that were performed in order to define the electronic and the nuclear recoil bands and to measure the discrimination in 20-3 Torr CF_4-SF_6 utilizing a 1D readout. These experiments consist of: a DD neutron generator experiment, where the neutron-induced nuclear recoils within the detector are used to measure the discrimination; a ^{60}Co experiment, where the gamma-rays induce electronic recoils which are used to define the electronic recoil band; and a background (ambient radiation) experiment, which in conjunction with the ^{60}Co experiment is utilized to define the nuclear recoil band. The defining of the electronic and nuclear recoil bands will be discussed in Section 5.3.2.

Here are several details concerning the experimental setup for these experiments. For each experiment the trigger threshold is set so that the acquisition system triggers consistently on ^{55}Fe x-rays ($\approx 5.9\ keVee$). For the ^{60}Co experiment, the ^{60}Co source is placed on top of the acrylic shield of the detector, halfway between the cathode and the anode. For the background experiment no ionization source is placed near the detector. Instead, the background experiment contains cosmic ray induced electronic recoils and RPRs originating from the detector materials. For the DD neutron generator experiment, since the focus is on the discrimination measurement the DD generator is oriented on the Cathode-side of the detector only and lead bricks are placed between the DD generator and the detector in order to reduce the gamma-ray flux entering the detector. A "GEM-side" experiment is not performed, because the directionality measurement, which is quantified by the skewness difference between the "GEM-side" experiment and the "Cathode-side" experiment, is not pursued. This is because the directionality measurement requires a greater number of nuclear recoil statistics than can be obtained (in a reasonable amount of time) with a ≈ 5.9 $keVee$ trigger threshold. The directionality measurement is performed is a dedicated series of experiments that will be presented in Section 5.4.

5.3.1 Discrimination: Selection Cuts

This section presents the four cuts leading up to the identification of the nuclear recoil band: the saturation cut, the Rise Time (RT) cut, the fiducialization cut, and the $ln(\eta)$ cut ($\eta = \frac{I_{Max}}{dZ}$). These cuts are similar to the selection cuts utilized for the 30 Torr SF_6 discrimination and directionality measurements (see Section 3.8). In this section a brief description of each cut is provided. The reader is referred to Section 3.8 for the complete description and the motivation for each cut. First, the effect of each cut on the data is shown for the DD neutron generator experiment in Figure 5.3 in terms of the $ln(\eta)$ versus energy E parameters space. After each cut is described, in Section 5.3.2 the ^{60}Co experiment, the background experiment, and how the nuclear recoil band is defined based on them is discussed. The blue dotted line in Figure 5.3 represents the boundary line between the nuclear recoil band (above) and the electronic recoil band (below), which will be defined in Section 5.3.2.

Saturation Cut: The first cut is the saturation cut, which is utilized to reject all tracks with peak voltage V_{max} greater than $76mV$ (red). For tracks with $V_{max} > 76mV$ the signal extends beyond the vertical scale of the oscilloscope. The tracks that pass the saturation cut (black) are shown in Figures 5.3a. Notice the saturated tracks reside on the upper right. This is because the peak current is roughly constant (numerator of η), while the length of the track continues to increase with the track energy (denominator of η). Consequently, the saturated tracks have $ln(\eta)$ progressively decreasing with energy.

Rise Time (RT) Cut: On the events that pass the saturation cut, the rise time (RT) cut is applied. RT is defined as the time it takes the voltage signal to increase from 10% to 25% of V_{max}. The RT cut removes tracks with $RT < 5\ \mu s$. Figure 5.3b shows the rejected tracks (red) after the saturation cut. Notice the band of events along the top of the $ln(\eta)$ distribution (with the largest $ln(\eta)$). This band consists entirely of "unphysically" fast events and is completely removed with the RT cut.

Fiducialization Cut: Next is the fiducialization cut, whose effect is shown in Figures 5.3c. The fiducialization cut places the following two requirements on the reconstructed fiducialization Z. It requires the reconstructed Z estimated with CF_3^- and SF_5^- to be less than 60 cm and greater than 10 cm (60 $cm < Z_{CF_3^-} <$ 10 cm and 60 $cm < Z_{SF_5^-} <$ 10 cm). The requirements $Z_{CF_3^-} < 60\ cm$ and $Z_{SF_5^-} < 60\ cm$ ensure that each track is fiducialized within the detector volume. The $Z_{CF_3^-} > 10\ cm$ and $Z_{SF_5^-} > 10\ cm$ requirement conservatively rejects events where the SF_5^- charge distribution might be overlapping with the SF_6^- charge distribution, which would distort calculated track properties such as the track skewness (shape of SF_6^- charge distribution) and the track length (extent of the SF_6^- charge distribution along Z). Although the statistics are greatly reduced, the fiducialization cut ensures only the highest quality tracks proceed to the $ln(\eta)$ Cut.

$ln(\eta)$ **Cut:** The first three cuts reject tracks which may not have been incorrectly reconstructed. The final cut is the $ln(\eta)$ cut, which takes the remaining tracks, separates the electronic recoil band and the nuclear recoil band (with the boundary line defined in Section 5.3.2), and selects the nuclear recoil band (all events above the boundary line). The $ln(\eta)$ cut is successful because nuclear recoil tracks tend to have high $\frac{dE}{dx}$ and short track lengths ΔZ compared to electronic recoil tracks. Consequently, the nuclear recoil band resides at high $ln(\eta)$. Figure 5.3 shows the $ln(\eta)$ cut, where all tracks above the boundary line (dotted blue line) are considered part of the nuclear recoil band and pass the $ln(\eta)$ cut. The location of the boundary line will be discussed in Section 5.3.2. All tracks that lie below the boundary line (fail the $ln(\eta)$ cut) reside either in the electronic recoil band (defined in Section 5.3.2) or the "haze". The "haze" will be discussed along with the results of the discrimination measurement in Section 5.3.3.

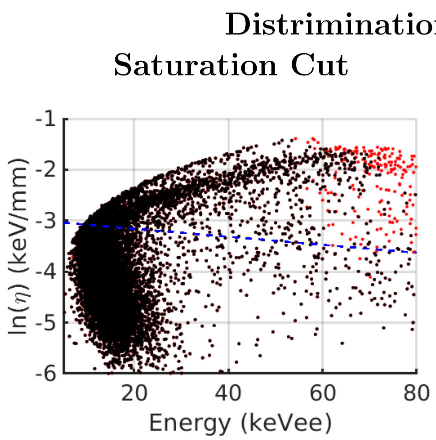

(a) The saturation cut rejects the events where the voltage signal saturates the vertical scale of the oscilloscope ($76mV$).

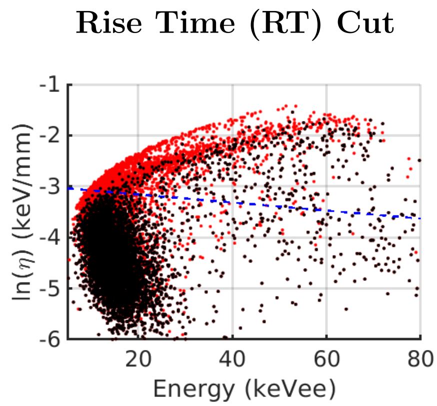

(b) The Rise time (RT) cut rejects events with $RT < 5\ \mu s$.

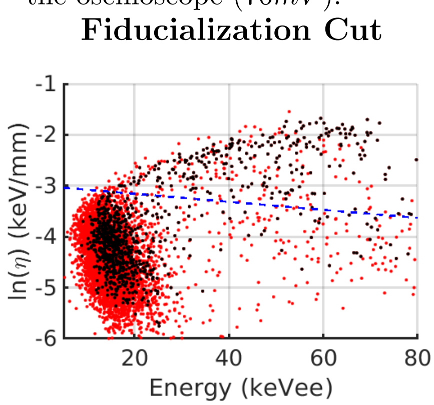

(c) The fiducialization cut rejects events where $Z_{CF_3^-}$ or $Z_{SF_5^-}$ lie outside of ($10\ cm < Z_{CF_3^-} < 60\ cm$) or ($10\ cm < Z_{SF_5^-} < 60\ cm$).

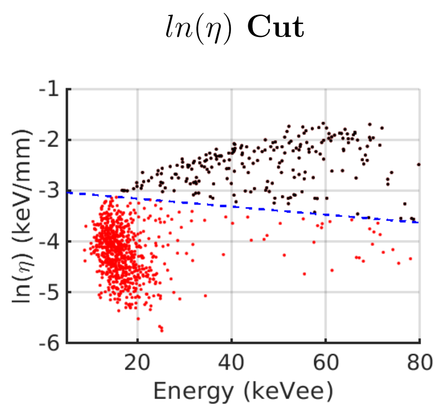

(d) The $ln(\eta)$ cut, where the nuclear recoil band lies above the boundary line (blue dotted line).

Figure 5.3: Discrimination: The selection cuts for the DD neutron generator experiment in 20-3 Torr CF_4-SF_6, where the black events pass the given cut and the red events pass all previous cuts but fail the given cut. The blue dotted line represents the boundary line defined in Section 5.3.2.

5.3.2 Defining The Nuclear Recoil Band

This section describes how the boundary line (blue dotted line in Figure 5.3 that divides the electronic recoil band from the nuclear recoil band) is defined. First, an approximately 10 hour ^{60}Co experiment was performed. Since the ^{60}Co induces only electronic recoils within the detector, a band should be present in the ^{60}Co experiment that corresponds to the electronic recoil band. For the ^{60}Co experiment, Figure 5.4 shows the effect of the saturation cut (5.4a), the RT cut (5.4b), the fiducialization cut (5.4c), and the $ln(\eta)$ cut (5.4d) in terms of $ln(\eta)$ versus energy. Figure 5.4d shows the band at low energy and small $ln(\eta)$ is the electronic recoil band. The few events at larger $ln(\eta)$ are likely RPR backgrounds, which occur during all experiments (see 1.6.3).

Next, an approximately 10 hour background (ambient radiation) experiment was performed. Figure 5.5 shows the effect of each cut on the background experiment. Similar to the ^{60}Co experiment, the background experiment consists mostly of electronic recoils (induced from ambient gamma-rays) and the occasional RPR. This is confirmed in Figure 5.5d. The nuclear recoil band is defined based on the ^{60}Co experiment (Figure 5.4d) and the background experiment (Figure 5.5d) such that the electronic recoil band is excluded and the RPRs are included. The result is the blue dotted line, above which is the nuclear recoil band and below which is the electronic recoil band.

Discrimination: ^{60}Co Selection Cuts

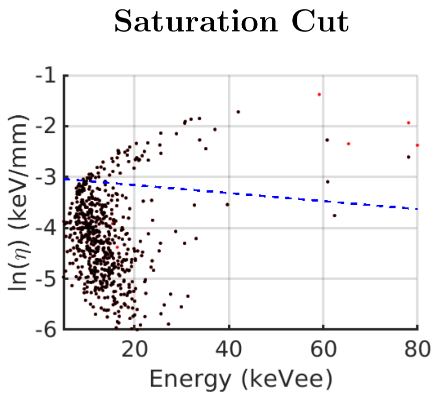

(a) The saturation cut rejects the events where the voltage signal saturates the vertical scale of the oscilloscope ($76mV$).

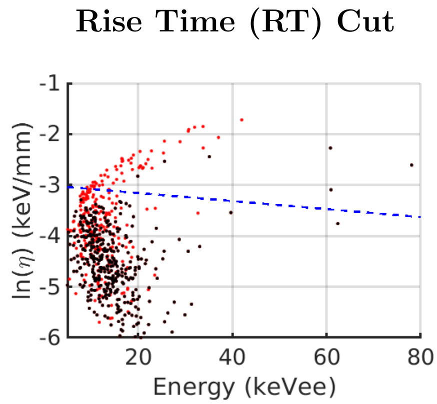

(b) The Rise time (RT) cut rejecting events with $RT < 5\ \mu s$.

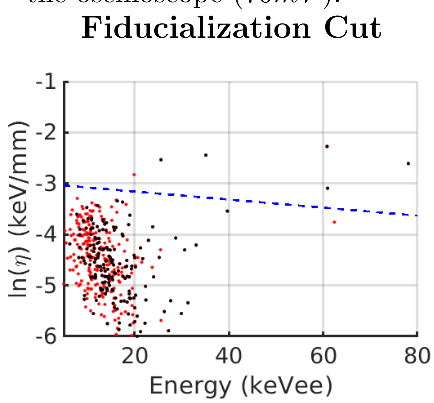

(c) The fiducialization cut rejects events where $Z_{CF_3^-}$ or $Z_{SF_5^-}$ lie outside of ($10\ cm < Z_{CF_3^-} < 60\ cm$) or ($10\ cm < Z_{SF_5^-} < 60\ cm$).

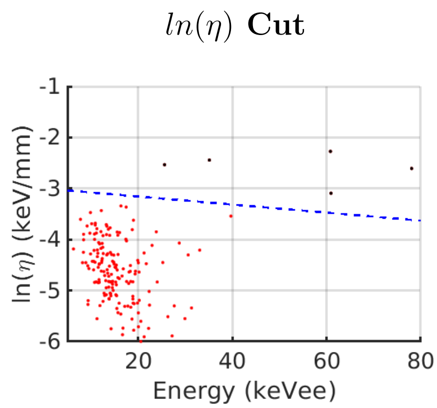

(d) The $ln(\eta)$ cut, where the nuclear recoil band lies above the boundary line (blue dotted line).

Figure 5.4: Discrimination: The selection cuts for the ^{60}Co experiment in 20-3 Torr CF_4-SF_6. The black events pass the given cut and the red tracks pass all previous cuts but fail the given cut. The blue dotted line is the boundary line defined in Section 5.3.2.

Discrimination: Background Selection Cuts

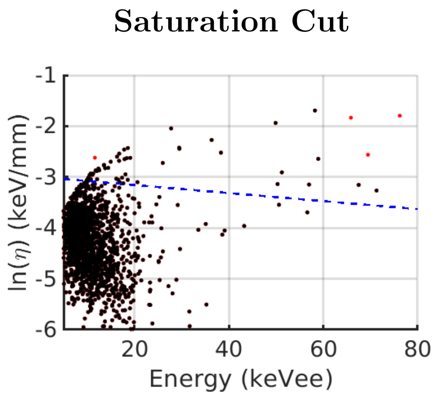

(a) The saturation cut rejects the events where the voltage signal saturates the vertical scale of the oscilloscope ($76 mV$).

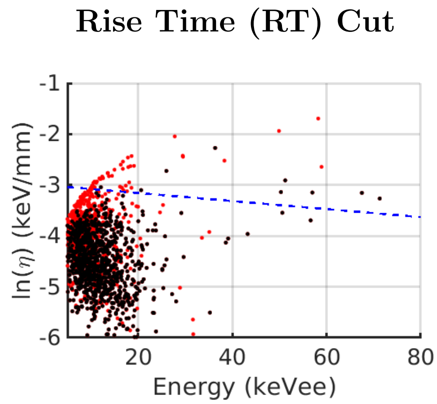

(b) The Rise time (RT) cut rejecting events with $RT < 5\ \mu s$.

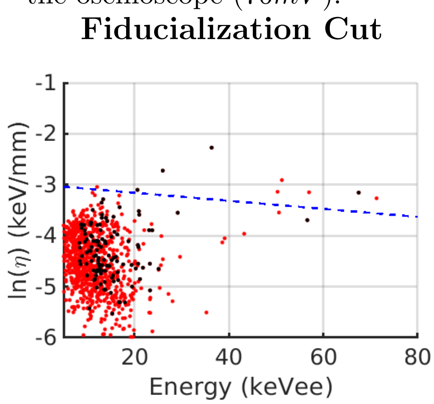

(c) The fiducialization cut rejects events where $Z_{CF_3^-}$ or $Z_{SF_5^-}$ lie outside of ($10\ cm < Z_{CF_3^-} < 60\ cm$) or ($10\ cm < Z_{SF_5^-} < 60\ cm$).

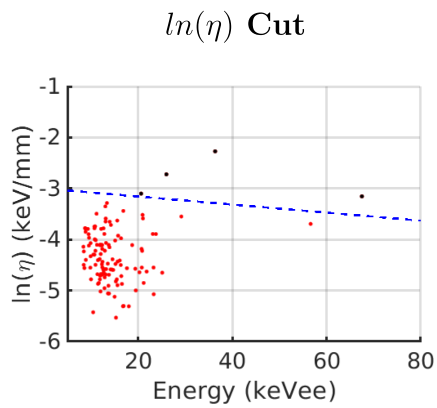

(d) The $ln(\eta)$ cut, where the nuclear recoil band lies above the boundary line (blue dotted line).

Figure 5.5: Discrimination: The selection cuts for the background experiment in 20-3 Torr CF_4-SF_6. The black events pass the given cut and the red tracks pass all previous cuts but fail the given cut. The blue dotted line is the boundary line defined in Section 5.3.2.

The location of the boundary line is consistent with the range (ΔZ) versus energy for the ^{60}Co experiment and the background experiment shown in Figures 5.6 and

5.7. The events that lie below the boundary line (red) in Figures 5.4d and 5.5d reside in the vertical band (red) in Figures 5.6b and 5.7b. Due to their low $\frac{dE}{dx}$, electronic recoils form a vertical band in range versus energy space. Also, although the statistics are few the RPR events (black) lie in the beginnings of a horizontal band, which is the nuclear recoil band.

Discrimination: ^{60}Co Experiment

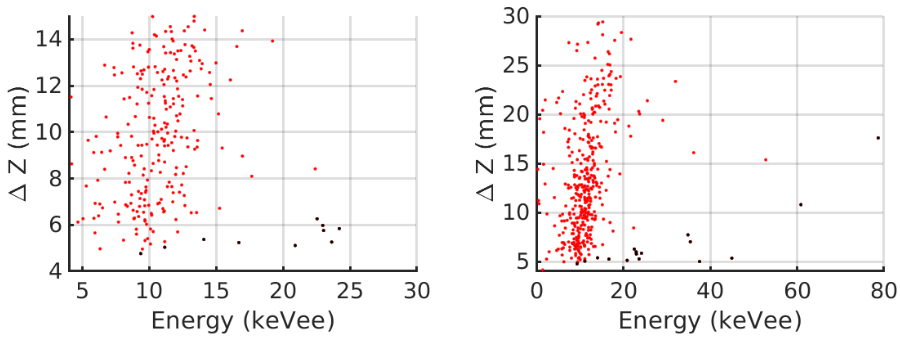

(a) (b)

Figure 5.6: Discrimination: The range (ΔZ) versus Energy for the ^{60}Co experiment in 20-3 Torr CF_4-SF_6.

Discrimination: Background Experiment

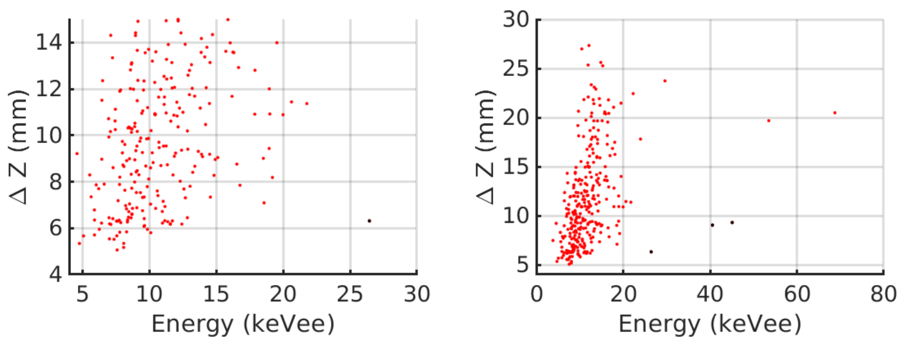

(a) (b)

Figure 5.7: Discrimination: The range (ΔZ) versus Energy for the background experiment in 20-3 Torr CF_4-SF_6.

5.3.3 Discrimination: Results and Discussion

The result of the discrimination measurement is shown in Figure 5.8 by utilizing the range versus energy of the DD neutron generator experiment. The red, vertical band is the electronic recoil band, and the horizontal band (located at the bottom of the black events) is the nuclear recoil band that consists mostly of F recoils. Unfortunately, the separation between the nuclear recoil band and the electronic recoil band is blurred by the what we call the "haze". The "haze" are the events that lie between the nuclear recoil band and the electronic recoil band in range versus energy.

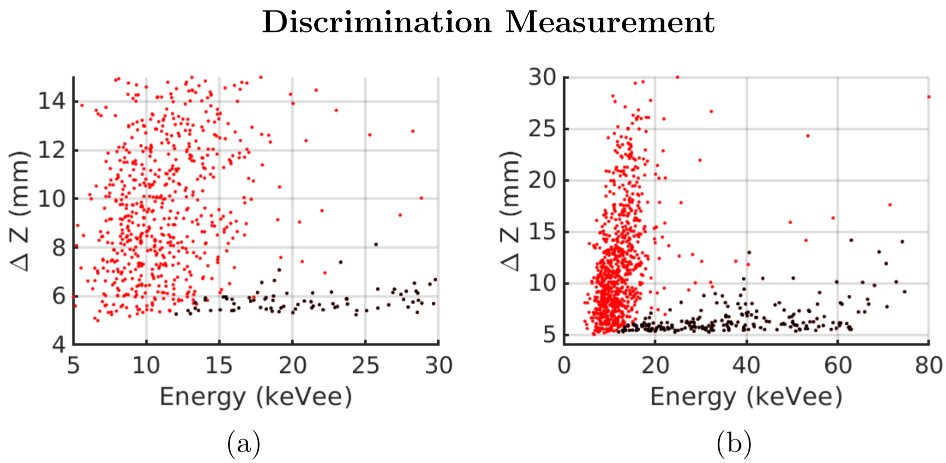

Figure 5.8: Discrimination: The range (ΔZ) versus Energy for the DD neutron generator experiment in 20-3 Torr CF_4-SF_6.

The "haze" will be considered in detail in the next paragraph. Even despite the "haze", E_{Disc} can be estimated from Figure 5.8a, which focuses on the low energy region of the range versus energy. It indicates there is discrimination down to $\approx 15keVe$. Also, the range verse energy for the ^{60}Co experiment (Figure 5.6) and the background experiment (Figure 5.7) are consistent with discrimination down to $\approx$ 15 $keVee$. Consequently, this work measures the E_{Disc} utilizing a 1D readout to be $E_{Disc} \approx 15$ $keVee$, where the "haze" and the nuclear recoil statistics are the biggest issues limiting the discrimination measurement.

We believe the "haze" are proton recoils that cross the entire active region of the THGEM (3 *cm* by 3 *cm*). They are the result of neutrons from the DD generator interacting in the acrylic cylinder of the detector, liberating a proton from the acrylic, and sending the proton recoiling through the gas. The nuclear recoils that correspond to the nuclear recoil band are mostly F recoils, which are much heavier than protons. Consequently, proton recoils (like the "haze") are longer than the F recoils (nuclear recoil band). Also supporting the idea that the "haze" consists of neutron-induced proton recoils from the acrylic are the range versus energy for the ^{60}Co experiment (Figure 5.6b) and the background experiment (Figure 5.7b), which do not have a "haze". Although it is possible to estimate the expected rate of neutron-induced proton recoils, the rate is not estimated. This is because it is difficult to take into account the effect of the oscilloscope dead-time and estimate the "true" rate of "haze" events.

Finally, we attempted to perform a "null" skewness experiment, where the DD generator was positioned along the side of the acrylic cylinder. For this "null" skewness experiment, the expected skewness distribution is centered on zero skewness. However, immediately upon powering the DD generator we observed a high rate of long, high energy, nuclear recoil-like events, which were different from the typical nuclear recoil events or the electronic recoil events seen when the DD generator is positioned at the THGEM or the cathode. The "null" experiment was immediately aborted for fear of damaging the THGEM. Afterwards, we concluded the most likely cause for these events are neutron-induced proton recoils, where the high rate is the result of having no aluminum or steel material between the DD generator and the acrylic to attenuate the neutrons. Whereas, for the "GEM-side" experiment and the "Cathode-side" experiment the neutrons must pass through the aluminum anode ("GEM") or the steel cathode ("Cathode").

Based on these results and the "null" experiment, all/most of the black events in the range versus energy in Figure 5.8b are nuclear recoils, but we cannot say that all are F recoils. Since the protons cross the entire active region of the THGEM, adding a veto wire to the readout is the best way to remove the "haze" and thereby make the distinction between the nuclear recoil band (F recoils) and the electronic recoil band clearer a future discrimination measurement.

5.4 Directionality Measurement

This section presents the directionality (skewness) measurement utilizing a 1D readout in 20-3 Torr CF_4-SF_6. The directionality measurement requires many nuclear recoil tracks in order to statistically measure the directionality. Unfortunately, the DD generator produces a high flux of gamma-rays, which interact in the detector at a high rate and create lots of low energy electronic recoils. Consequently, due to the oscilloscope dead-time the electronic recoil rate dominates the nuclear recoil rate, and it is difficult to acquire nuclear recoil statistics (see Section 3.4).

In order to resolve the issue of the low nuclear recoil rate either the detector must be shielded with lead (as is done for the discrimination measurement discussed in Section 5.3) or the trigger threshold must be increased. For the case of utilizing lead shielding, the neutrons are frequently scattered within the lead shielding, which causes the initially directional beam of neutrons to enter and to interact in the detector at potentially large angles. Consequently, the intrinsic directionality available to measure is diluted using the lead shielding. Therefore, the directionality experiment utilizes a high trigger threshold and no lead shielding. The trigger threshold is determined experimentally by raising the trigger threshold until the nuclear recoil rate is about the same as the electronic recoil rate. This occurred at a trigger threshold of approximately 20 $keVee$.

Similar to the discrimination section (Section 5.3), first the selection cuts for the directionality measurement are discussed in terms of $ln(\eta)$ versus energy in Section 5.4.1. Next, in Section 5.4.2 the magnitude of the directionality is quantified by the skewness difference versus energy between the "GEM-side" experiment and the "Cathode-side" experiment ($Skew_{GEM} - Skew_{Cathode}$). This same skewness difference quantity was discussed in Section 3.9.2 to quantify the directionality for the 30 Torr SF_6 directionality measurement.

5.4.1 Directionality: Selection Cuts

The selection cuts for the directionality measurement are similar to the selection cuts for the discrimination measurement discussed in Section 5.3.1. The effect of each cut on the "GEM-side" experiment (DD generator on the GEM-side) and the "Cathode-side" experiment (DD generator on the Cathode-side) are shown in Figures 5.9 and 5.10.

First, consider the saturation cut shown in Figures 5.9a and 5.10a. For the directionality experiments the vertical scale of the oscilloscope is increased in order to contain higher energy events. Consequently, the saturation cut is 0.39 V. The saturation cut rejects the events lying on the upper right of these Figures.

Next, the RT cut ($RT > 5$ μs) is applied to the events passing the saturation cut. Figures 5.9b and 5.10b shows the effect of the RT cut. The RT cut removes the "unphysically" fast RT events, which have the largest $ln(\eta)$ at a given energy (see Section 2.6.1). Due to the higher trigger threshold (≈ 20 $keVee$) compared to the discrimination experiment (≈ 5.9 $keVee$) these events do not form a completely independent band from the nuclear recoil band. Nevertheless, the RT cut ($RT > 5$ μs) removes them. The collection of events at zero energy are sparks, which also fail the RT cut.

The events that pass the RT cut are sent to the fiducialization cut, which rejects events that fail 60 $cm < Z_{CF_3^-} < 10$ cm and 60 $cm < Z_{SF_5^-} < 10$ cm. The result of the fiducialization cut is shown in Figures 5.9c and 5.10c. Similarly to the discrimination fiducialization cut (Figure 5.3c), many events are cut by the fiducialization cut. Nevertheless, unlike the discrimination experiment there remains a large number of statistics after the fiducialization cut.

Finally, the nuclear recoil band and the electronic recoil band are located based on the boundary line (blue dotted line in Figures 5.9d and 5.10d), which defines the separation between the electronic recoil band and the nuclear recoil band. The location of the boundary line is adjusted slightly relative to the location discussed in Section 5.3.2. This is because the energy range of the directionality experiments (≈ 20 $keVee$-≈ 400 $keVee$) are higher than the discrimination experiments (≈ 5.9 $keVee$-≈ 80 $keVee$). As a result, the signal-to-noise is higher for the directionality experiments, which allows the software filtering to be reduce compared to the discrimination experiments (see Section 5.2). The reduced filtering causes the measured track lengths at a given energy to be slightly shorter and I_{Max} to be slightly larger than the discrimination experiment. Therefore, the $ln(\eta)$ for the directionality experiments (Figures 5.9d and 5.10d) are systematically shifted upward relative to the $ln(\eta)$ for the discrimination experiment (Figure 5.3d). Figures 5.9d and 5.10d indicate the shift is roughly constant for all energies, so the slope of the discrimination boundary line (see Section 5.3.2) is utilized for the slope of the directionality boundary line. Whereas, the intercept of the boundary line is adjust to the appropriate location based on the directionality data (Figures 5.9d and 5.10d).

Directionality: "GEM-side" Selection Cuts

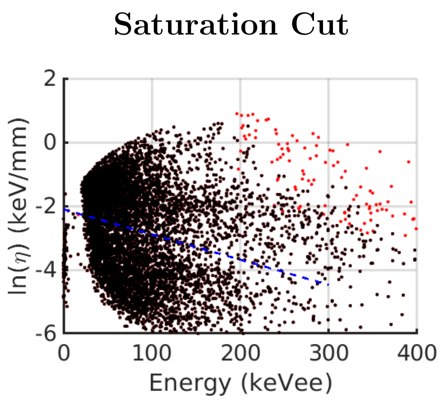

(a) The saturation cut rejects the events with voltage pulses that saturate the vertical scale of the oscilloscope ($0.39V$).

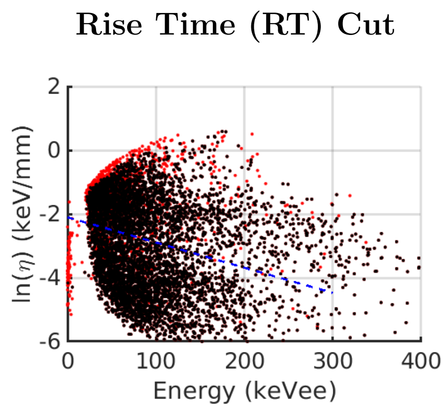

(b) The Rise time (RT) cut rejecting events with $RT < 5\ \mu s$.

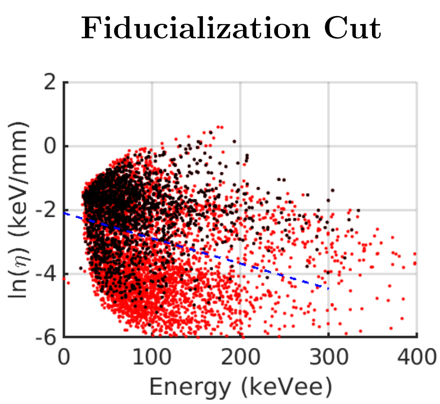

(c) The fiducialization cut rejects events where $Z_{CF_3^-}$ or $Z_{SF_5^-}$ lie outside of ($10\ cm < Z_{CF_3^-} < 60\ cm$) or ($10\ cm < Z_{SF_5^-} < 60\ cm$).

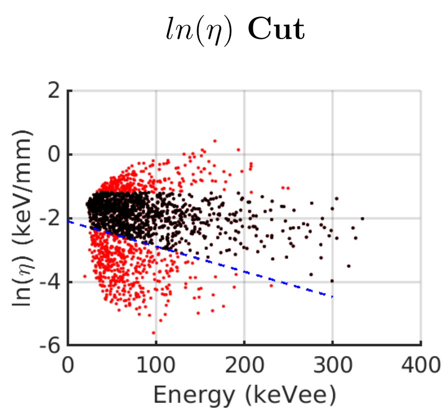

(d) The $ln(\eta)$ cut, where the nuclear recoil band lies above the boundary line (blue dotted line). The red events above the boundary line have $ln(\eta) > -1.2\ keV/mm$ and are part of the nuclear recoil band, but are excluded from the directionality measurement (see Section 5.4.1).

Figure 5.9: Directionality: The "GEM-side" experiment selection cuts in 20-3 Torr CF_4-SF_6, where the black tracks pass the given cut and the red tracks pass all previous cuts but fail the given cut. The blue dotted line is the boundary line defined in Section 5.3.2 with the intercept adjusted as described in Section 5.4.1.

Unfortunately, unlike the discrimination measurement, the location of what we call the nuclear recoil band (consisting of F recoils) is only approximate in the directionality experiments. A more precise localization of the nuclear recoil band would require a ^{60}Co experiment and a background experiment conducted at the $\approx 20\ keVee$ trigger threshold. These experiments were attempted, but the event rate above 20 $keVee$ for either experiment was very low (about a few events an hour) and obtaining enough statistics would take an excessive amount of time. Nevertheless, regardless of a fraction of the electronic recoils or the "haze" leaking into the nuclear recoil band, the systematics caused by these are subtracted in the skewness difference quantity. Therefore, the skewness difference allows the directionality to be measured even with the imperfect nuclear recoil band.

In order to enhance the directionality measurement, the directionality is measured for the longest nuclear recoil tracks at a given energy. (This technique was also found in Ref. [98] to improve the directionality measurements.) For the directionality measurement, the part of the nuclear recoil band with $ln(\eta) < -1.2\ keV/mm$ is utilized to measure directionality. Since the tracks with $ln(\eta) > -1.2\ keV/mm$ are the most narrow, highly peaked tracks, they have intrinsically the smallest available skewness to measure. After the noise reduction and the filtering this skewness is often removed entirely for these short tracks. Figures 5.11 and 5.12 show the range versus energy for the "GEM-side" experiment and the "Cathode-side" experiment respectively, which shows that the tracks with $ln(\eta) > -1.2\ keV/mm$ are indeed the shortest nuclear recoil tracks at a given energy (below black events). Also, we have measured and verified the skewness for the short nuclear recoils is consistent with zero skewness. Consequently, the short nuclear recoil tracks act only to dilute the skewness distributions and are excluded from the directionality measurement.

Directionality: Cathode Selection Cuts

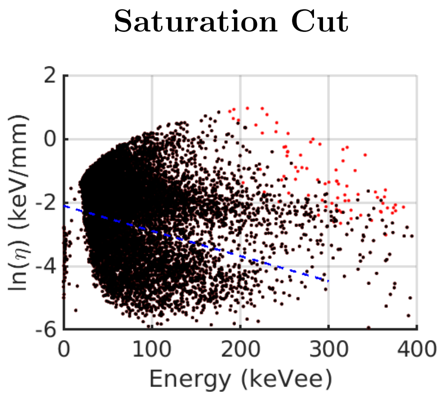

(a) The saturation cut rejects the events with voltage pulses that saturate the vertical scale of the oscilloscope ($0.39V$).

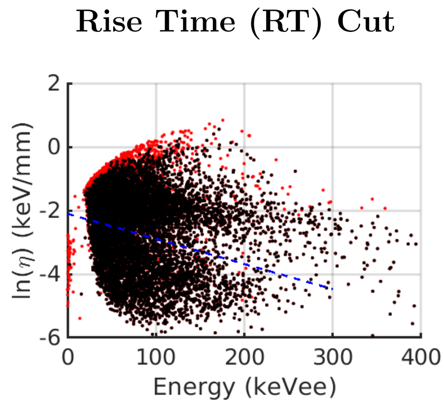

(b) The Rise time (RT) cut rejecting events with $RT < 5\ \mu s$.

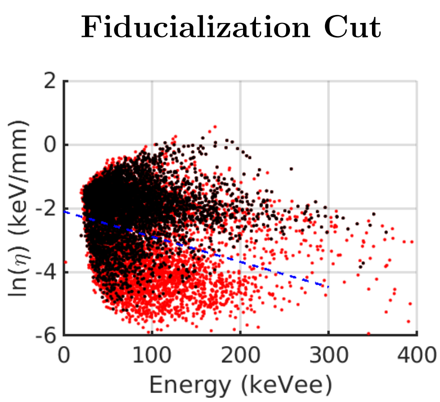

(c) The fiducialization cut rejects events where $Z_{CF_3^-}$ or $Z_{SF_5^-}$ lie outside of ($10\ cm < Z_{CF_3^-} < 60\ cm$) or ($10\ cm < Z_{SF_5^-} < 60\ cm$).

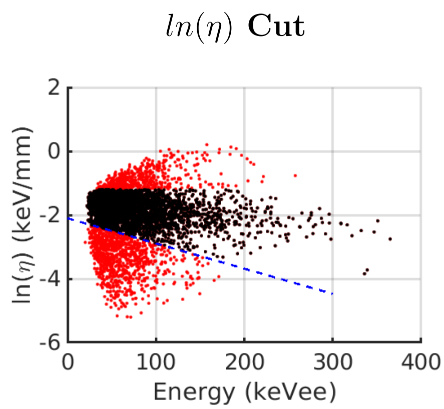

(d) The $ln(\eta)$ cut, where the nuclear recoil band lies above the boundary line (blue dotted line). The red events above the boundary line have $ln(\eta) > -1.2\ keV/mm$ and are part of the nuclear recoil band, but are excluded from the directionality measurement (see Section 5.4.1).

Figure 5.10: Directionality: The "Cathode-side" experiment selection cuts in 20-3 Torr CF_4-SF_6, where the black tracks pass the given cut and the red tracks pass all previous cuts but fail the given cut. The blue dotted line is the boundary line defined in Section 5.3.2 with the intercept adjusted as described in Section 5.4.1.

Lastly, consider the "haze", which lies above the nuclear recoil band (black) in the range versus energy shown in Figures 5.11 and 5.12. Recall, in Section 5.3.3 we argued the "haze" consists of neutron-induced, high energy proton recoils, which are long and cross the entire active region of the THGEM (3 cm by 3 cm). This is consistent with the high energies and long lengths of the "haze" events. Since the "haze" is only present in the DD generator experiments, this means the "haze" is correlated with the DD generator. Therefore, it is possible the proton recoils in the "haze" could contribute to the skewness difference, and if they are directional even enhance the measured directionality. The amount that they might contribute cannot be quantified or separated from the contribution from the F recoils. Nevertheless, despite the difficulty/handicap of the "haze" this directionality measurement represents the first measurement of directionality in 20-3 Torr CF_4-SF_6. In future work, result might be improved with a veto to remove the "haze".

Directionality "GEM-side"

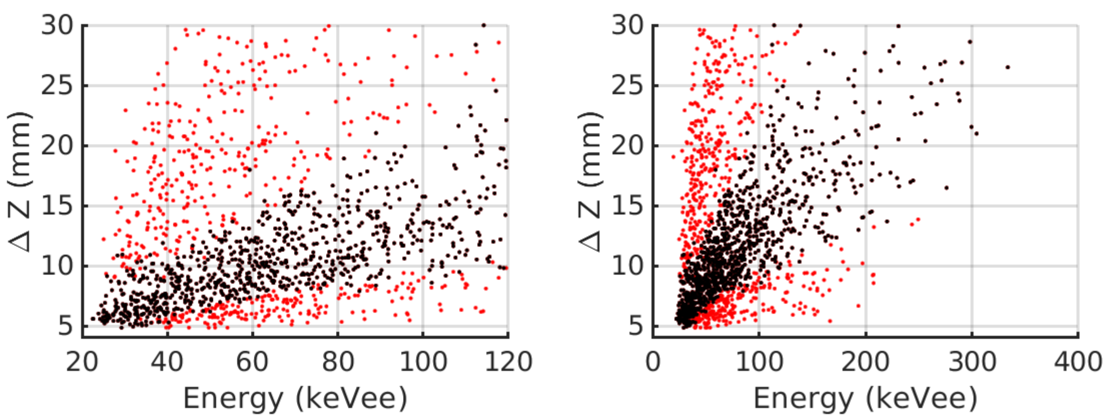

(a) (b)

Figure 5.11: Directionality: The range (ΔZ) versus energy for the "GEM-side" experiment at 20-3 Torr CF_4-SF_6 showing a close-up view (5.11a) and a full view (5.11b).

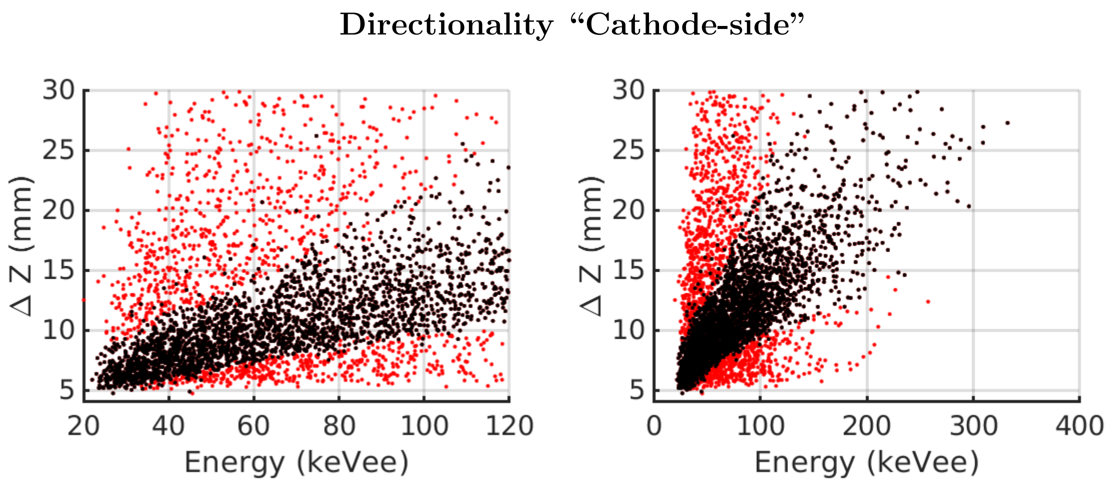

(a) (b)

Figure 5.12: Directionality: The range (ΔZ) versus energy for the "Cathode-side" experiment at 20-3 Torr CF_4-SF_6 showing a close-up view (5.12a) and a full view (5.12b).

5.4.2 Directionality Results and Discussion

This section presents the results of the directionality measurement in terms of the skewness difference ($Skew_{GEM} - Skew_{Cathode}$). First, the nuclear recoil band for the "GEM-side" experiment and the "Cathode-side" experiment are broken up into 20 $keVee$ energy bins starting with the minimum energy $E = 20$ $keVee$ and ending at $E = 120$ $keVee$. Figure 5.13 shows the measured skewness distributions, where the red and the blue are the "GEM-side" experiment and the "Cathode-side" experiment, respectively. The distributions are unnormalized to emphasis the total statistics in each distribution. Interestingly, the "GEM-side" experiment distributions all have fewer statistics than the "Cathode-side" experiment distributions despite similar acquisition times. Although the cause is unknown, it should have only a small effect on the directionality. The Figures also indicate an unknown systematic, which shifts the distributions toward negative skewness. This systematic is either due to the readout electronics or an artifact of the analysis.

Directionality: Skewness Distributions

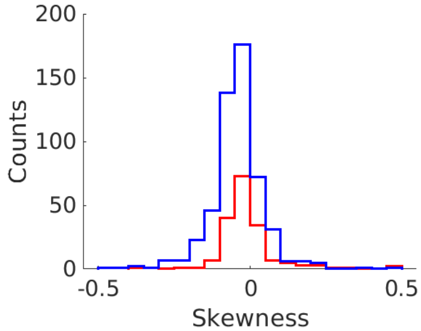

(a) 20 $keVee < E < 40$ $keVee$

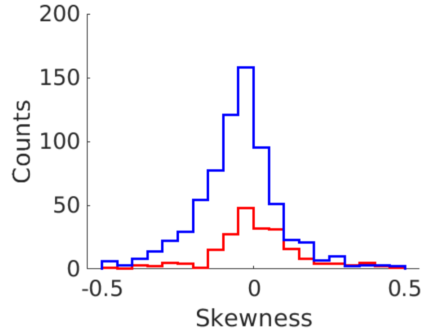

(b) 40 $keVee < E < 60$ $keVee$

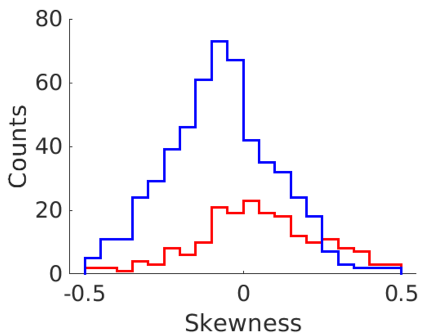

(c) 60 $keVee < E < 80$ $keVee$

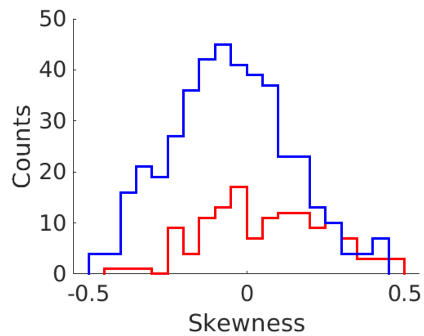

(d) 80 $keVee < E < 100$ $keVee$

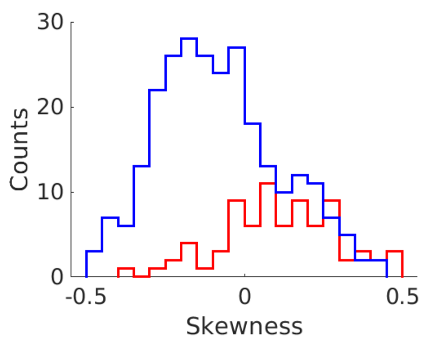

(e) 100 $keVee < E < 120$ $keVee$

Figure 5.13: Directionality: Skewness distributions for the nuclear recoil band (black events in Figures 5.11 and 5.12) in 20 $keVee$ energy bins from 20 $keVee$ to 120 $keVee$. The red and blue distributions are the distributions for the "GEM-side" experiment and the "Cathode-side" experiment, respectively.

Figure 5.14a plots the mean and standard error of the mean for the "GEM-side" experiment skewness distribution (red), and the "Cathode-side" experiment skewness distribution (blue). The horizontal bars represent the range of track energies contained at each point. The *Sum* (black) is $Sum = GEM + Cathode$, which is zero when no systematic is present. Figure 5.14b shows the skewness difference ($Skew_{GEM} - Skew_{Cathode}$) versus energy, where the red curve calculates the directionality over the entire nuclear recoil band and the black curve ($1/3 - 1$) measures the directionality for the upper 2/3 longest tracks of the nuclear recoil band. Both curves show the skewness difference is increasing with energy and is 2-3σ above zero skewness in the lowest energy bin ($20 - 40 keV$). Therefore, the E_{Skew} is measured to be $\approx 30\ keVee$ in 20-3 Torr CF_4-SF_6 utilizing 1D readout. However, since the skewness difference is 2-3σ above zero skewness in the lowest energy bin the intrinsic E_{Skew} might be lower than 30 $keVee$.

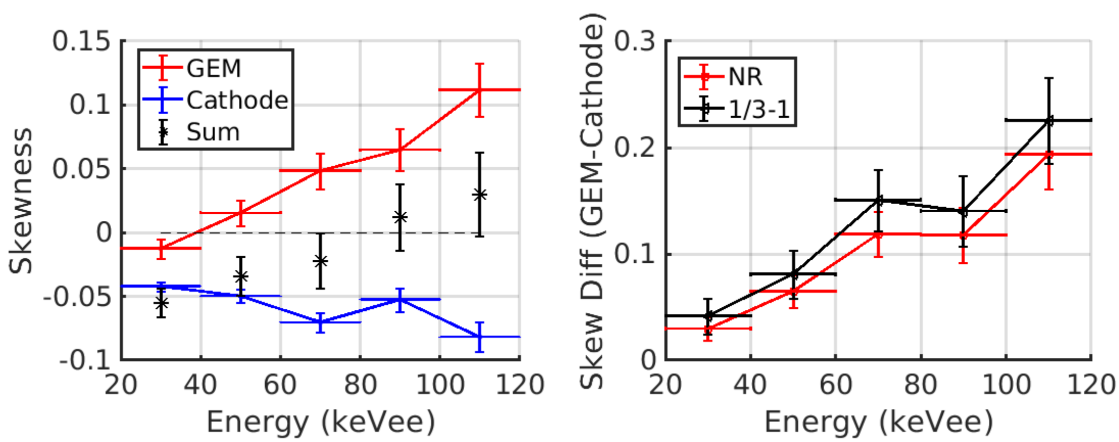

(a) The skewness versus energy. The "GEM-side" experiment, the "Cathode-side" experiment, and the Sum ("GEM" + "Cathode") are the red, the blue, and the black curves, respectively.

(b) The skewness difference ("GEM"-"Cathode") versus energy for the directionality nuclear recoil band (red) and the upper 2/3 of the nuclear recoil band by length (black).

Figure 5.14: The results of the directionality measurement in 20-3 Torr CF_4-SF_6 utilizing a 1D readout show statistically significant directionality down to the lowest energy bin. Consequently, $E_{Skew} \approx 30\ keVee$.

5.5 Range Versus Energy Measurement in 20-3-100 Torr CF_4-SF_6-He

This section presents a preliminary experiment measuring the range (ΔZ) versus energy in 20-3-100 Torr CF_4-SF_6-He. The motivation for studying a helium rich gas target is based on the following. Since the next generation of WIMP dark matter experiments will push the standard $100GeV$-$1TeV$ WIMP exclusion curves to the so called "neutrino floor" [39, 40, 41], there is now a push toward searching for low-mass ($1GeV$ scale) WIMPs [108, 109]. For these low-mass WIMP searches He is attractive for several reasons [110, 111]. First, He is kinematically well-matched to maximize the energy deposited in the detector per low mass WIMP-nuclear interaction due to their similar masses. Second, at a given pressure tracks are longer in He than other gases, which should improve discrimination compared to higher mass targets in TPCs.

For this experiment, the experimental apparatus and the data analysis algorithms are the same as discussed in Section 5.2. Similarly to the discrimination measurement in 20-3 Torr CF_4-SF_6 (see Section 5.3), the lead shielding is added to reduce the electronic recoil rate and the trigger threshold is set to ≈ 5.9 $keVee$. Finally, due to the low signal-to-noise of these experiments only a DD neutron generator experiment (with the DD generator oriented in front of the cathode) and a background experiment are performed. Therefore, a precise discrimination measurement is not performed. Instead, E_{Disc} is roughly estimated based on the range versus energy of the DD neutron generator experiment.

5.5.1 Discrimination Selection Cuts in 20-3-100 Torr CF_4-SF_6-He

This section will briefly present the selection cuts that preceded the range versus energy measurement. The $ln(\eta)$ cut is not applied because a boundary line, which separates the nuclear recoil band and the electronic recoil band, cannot be determined. Consequently, only the saturation cut, the RT cut, and the fiducialization cut are utilized. (The reader is referred to Section 5.3.1 for the description of the selection cuts.)

First, consider the selection cuts for the background experiment shown in Figure 5.15. Despite an ≈ 8 hour background experiment and the low trigger threshold (≈ 5.9 $keVee$), the overall statistics after the cuts are applied are low as shown in Figure 5.15d. This is because the signal-to-noise for the 20-3-100 Torr CF_4-SF_6-He experiments is very poor (for an unknown reason) and many events fail the fiducialization cut (Figure 5.15c). Similarly, Figure 5.16 shows the selection cuts applied to the DD neutron generator experiment. The distribution after all prior cuts is shown in Figure 5.16d.

Selection Cuts For The Background Experiment in 20-3-100 Torr CF_4-SF_6-He

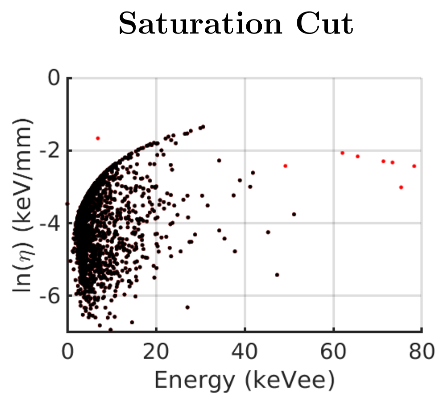

(a) Saturation cut rejects the voltage signals that saturate the vertical scale of the oscilloscope.

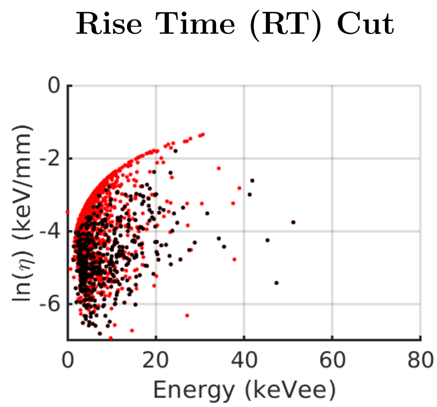

(b) Rise time (RT) cut: $RT < 5$ μs.

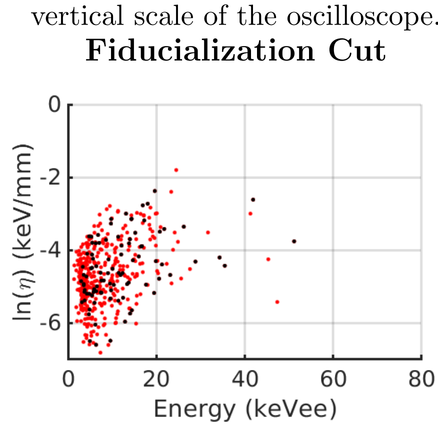

(c) The fiducialization cut rejects events where $Z_{CF_3^-}$ or $Z_{SF_5^-}$ lie outside of ($10\ cm < Z_{CF_3^-} < 60\ cm$) or ($10\ cm < Z_{SF_5^-} < 60\ cm$).

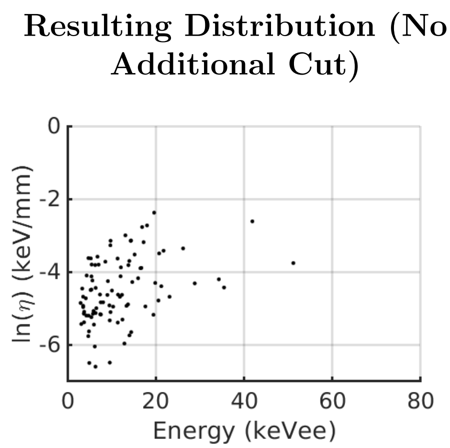

(d) The resulting distribution passing all prior cuts.

Figure 5.15: The selection cuts for the background experiment in the 20-3-100 Torr CF_4-SF_6-He mixture. The black events pass the given cut and the red tracks pass all previous cuts but fail the given cut.

Selection Cuts For The DD Neutron Generator Experiment In 20-3-100 Torr CF_4-SF_6-He

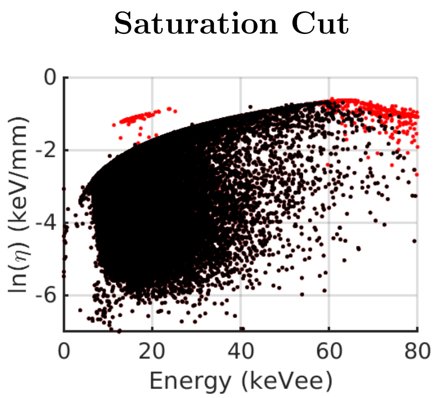

(a) Saturation cut rejects the voltage signals that saturate the vertical scale of the oscilloscope.

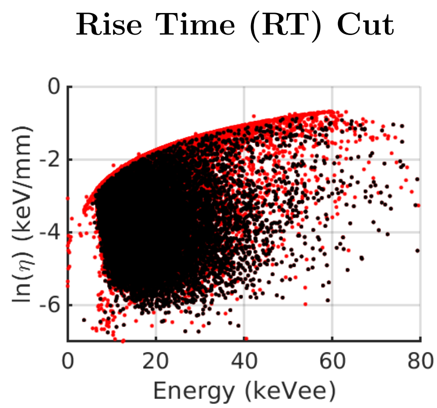

(b) Rise time (RT) cut: $RT < 5$ μs.

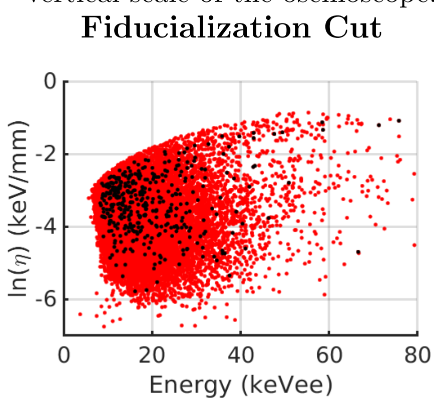

(c) The fiducialization cut rejects events where $Z_{CF_3^-}$ or $Z_{SF_5^-}$ lie outside of ($10\ cm < Z_{CF_3^-} < 60\ cm$) or ($10\ cm < Z_{SF_5^-} < 60\ cm$).

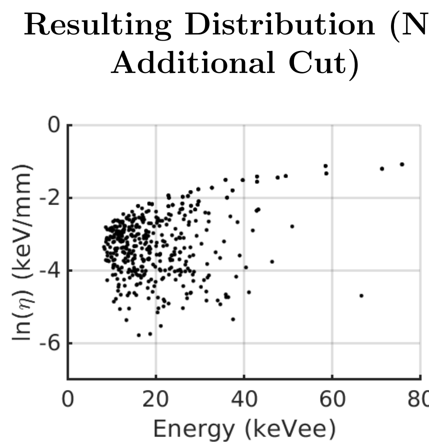

(d) The resulting distribution passing all prior cuts.

Figure 5.16: The selection cuts for the DD neutron generator experiment in 20-3-100 Torr CF_4-SF_6-He. The black events pass the given cut and the red tracks pass all previous cuts but fail the given cut.

5.5.2 Range Versus Energy In 20-3-100 Torr CF_4-SF_6-He

The result of the range versus energy is shown in Figure 5.17. The discrimination can be estimated based on Figure 5.17a and the location where the vertical band and horizontal band begin to overlap. These suggests there is some discrimination down to $E_{Disc} \approx 30\ keVee$. This is consistent with the range versus energy of the background experiment shown in Figure 5.17b. In order to precisely measure the discrimination in 20-3-100 Torr CF_4-SF_6-He using a 1D readout, a ^{60}Co experiment must be performed and the signal-to-noise improved. This is reserved for future work.

20-3-100 Torr CF_4-SF_6-He Discrimination

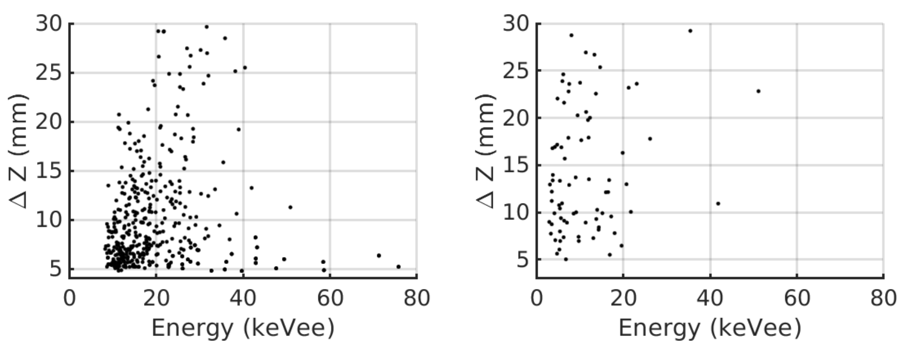

(a) "Cathode-side" (b) Background

Figure 5.17: The range (ΔZ) versus Energy in 20-3-100 Torr CF_4-SF_6-He.

5.6 Conclusion

In this chapter we presented the threshold energies for measuring directionality and discrimination in our 1D detector in 20-3 Torr CF_4-SF_6. The results indicate that $E_{Skew} \approx 30\ keVee$ and $E_{Disc} \approx 15\ keVee$. Unfortunately, a major limiting factor for each measurement is low nuclear recoil statistics due to the high gamma-ray interaction rate in the detector from the DD neutron generator. As a result, the directionality and the discrimination measurements were performed in dedicated experiments. For the directionality experiment the nuclear recoil rate is increased by increasing the trigger threshold to 20 $keVee$. For the discrimination experiment the trigger level is lowered to ≈ 5.9 $keVee$ and lead shielding is utilized to reduce the gamma-ray flux entering the detector. Another major issue is the “haze”, which are the event that lie between the nuclear recoil band and the electronic recoil band. Consequently, the “haze” blurs the separation between the nuclear recoil band and the electronic recoil band and is detrimental to the discrimination measurement. We asserted that the “haze” is due to neutron-induced proton recoils from the acrylic of the detector, which can be removed if a veto is added to the readout.

The following improvements to the experiment could result in better measurements of the discrimination and the directionality. First, by utilizing a data acquisition system with a shorter dead-time the nuclear recoil collection rate can be increased, which would improve nuclear recoil statistics. Second, reducing the noise or increasing the signal would allow for less software filtering and less distortion of the signal shape. An option is to stack two THGEMs to increase the gas gain. A different approach is to reduce the noise by reading the charge from a readout board instead of the THGEM. A benefit of this approach is that the readout board can be designed with a veto wire, which would allow the “haze” to be removed.

Chapter 6

Characterization of Novel 2D Readout Scheme

6.1 Introduction

This chapter discusses an entirely different topic than the previous chapters: the novel 2D readout scheme called the Tilted GEM that was developed by Nguyen Phan. Building off of his work, this chapter presents measurements of the 2D track reconstruction for neutron-induced nuclear recoils. Before we discuss the Tilted GEM, here is a brief motivation for his scheme.

As discussed in Section 1.4.3, the daily modulation of the nuclear recoil direction may be required in order to verify the galactic origin of a WIMP signal [41]. The current best directional detection technology are low pressure TPC detectors, which utilize the low pressure gases in order to lengthen WIMP induce nuclear recoils within the detector to a few $mm's$, thereby resolving the directionality [44, 45]. Another directional detector technology is nuclear emulsions [38], but they are currently in the development stage.

Unfortunately, low pressure TPC track reconstruction requires complex, fast, and/or expensive readout electronics. However, the requirements on the readout electronics can be relaxed considerably by the use of negative ion gases, which have ≈ 3 orders of magnitude slower drift speeds. In the case of the DRIFT TPC discussed in Section 1.6, 512, 2 mm pitch, 20 μm diameter steel anode wires are utilized in order to readout two 1 m (along X-dimension) by 50 cm (along Z-dimension) drift volumes [49]. Notice the spacial resolution along X is 2 mm (the pitch of the wires), which is far too coarse to resolve the predicted WIMP induced nuclear recoils ($\approx 1mm$) [44]. This is in contrast to the Z-dimension. Similar to the 1D readout scheme utilized for the prior measurements in this work, the Z- dimension has spatial resolution limited by the timing resolution of the readout electronics. Traditional methods to improve the spatial resolution in X require finely pitched strip or pixel detectors, which increases the number of readout channels. Also, since the size of dark matter detectors continues to increase (now to ton-scale experiments), the number of readout channels could be order 10^6, depending on the multiplexing and the pitch [44]. This section describes the advancement of the novel 2D readout scheme invented and tested by Nguyen Phan [112, 113], which achieves timing-based spacial resolution with only two readout channels. The work discussed in this section was performed in collaboration with Alex Mills.

The key features of the scheme are the following. First, the scheme requires at least two GEMs. The first GEM is called the "Z-GEM". It is utilized to amplify the track and to precisely measure the track along the drift dimension (Z). The novel approach is the orientation of the second GEM relative to the Z-GEM, where the second GEM is referred to as the "U-GEM". The U-GEM is rotated/tilted so that the plane of the U-GEM is at an angle relative to the Z-GEM. Nguyen Phan demonstrated that the orthogonal track dimension along the tilt of the U-GEM (X) can be reconstructed based on the relative timing of the signals at the Z-GEM and the U-GEM [112, 113]. This type of detector is referred to by us as the "Tilted GEM" detector. This chapter describes work toward characterizing the track reconstruction for low energy nuclear recoils within the Tilted GEM detector.

The chapter will proceed first with a description of the experimental setup in Section 6.2. In Section 6.3 the working principles, the track reconstruction, and the induced signals of the Tilted GEM are described. Also, in Section 6.3.1 a typical calibration alpha track is presented and the important features pointed out in the Z-GEM and the U-GEM signals. The algorithm utilized to calculate the track properties is described in Section 6.4. Next, in Section 6.5 the alpha source and the detector calibrations are presented. The detector calibration is compared for several different detector operating parameters with the goal of optimizing the ion backflow signal (described in Section 6.3.1). Utilizing the optimal detector parameters, we performed a DD neutron experiment, creating neutron-induced nuclear recoils preferentially directed along X. This experiment is presented and discussed in Section 6.6. Lastly, potential improvements/modification are considered in Section 6.7.

6.2 Experimental Setup

Figure 6.1 depicts the Tilted GEM. It is comprised of three 9.5 cm by 9.5 cm active area thin GEMs and a 2 μm thin film mylar cathode. The first GEM is "GEM1", which provides preliminary amplification of the track and is positioned 9.7mm below the cathode and above the Z-GEM. Although important for gas gain, GEM1 is not involved in the track reconstruction. However, discussed in Section 6.7.1 will be how reading out the signal induced on the bottom surface of GEM1 (facing the Z-GEM) improves the measurement of the ion backflow signal. The region between the cathode and GEM1 defines the drift volume (interaction region). The Z-GEM is 0.8mm below GEM1. The Z-GEM serves the dual function of track amplification and signal readout. The Z-GEM signal is utilized to measure the extent of the track along Z (ΔZ). Below the Z-GEM and tilted at 30° relative to the Z-GEM is the U-

GEM. Section 6.3.1 describes how the X extent of the track (ΔX) is extracted from the U-GEM signal. This extraction requires a precise calibration of the detector (see Section 6.5.3), which utilizes the structure above the cathode. This structure will be referred to as the "alpha calibration structure". The alpha calibration structure was designed by Eric Lee. Although for calibration purposes, it is left in place during the DD neutron generator experiments rather than opening the detector to remove it. This is because opening the detector requires pumping on the detector for several days in order to pump out the CS_2 utilized in the gas mixture, which is toxic.

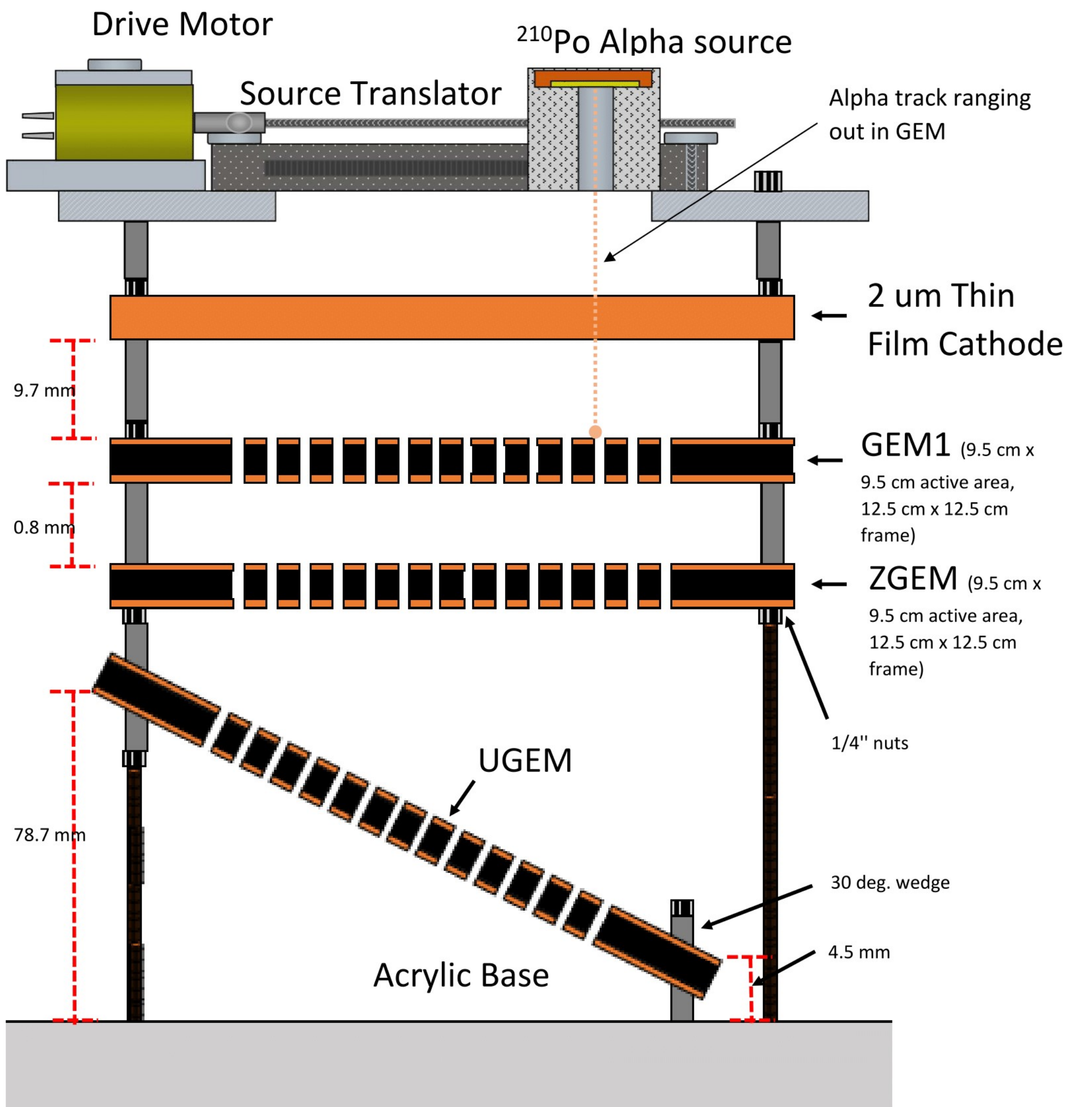

Figure 6.1: Schematic of the Tilted GEM detector. See section 6.2 for a description of each component.

Figure 6.2 shows the several intermediate steps in the assembly of the Tilted GEM. Figure 6.2a shows the mounting of the U-GEM on the four torlon support rods. Next, Figure 6.2b shows the subsequent attachment of the Z-GEM (middle) and GEM1 (top). In Figure 6.2c the entire assembly along with the alpha calibration structure is placed into the vacuum vessel. The alpha calibration structure is removed for the DD neutron experiment.

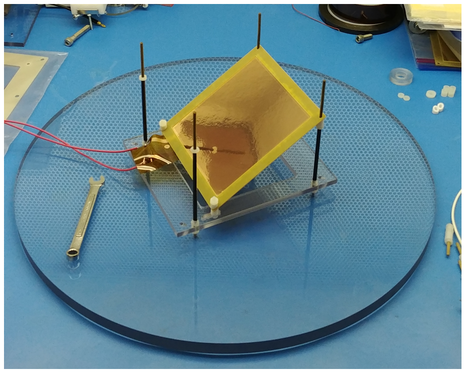

(a) The positioning of the U-GEM at 30° relative to the horizontal (Z-GEM).

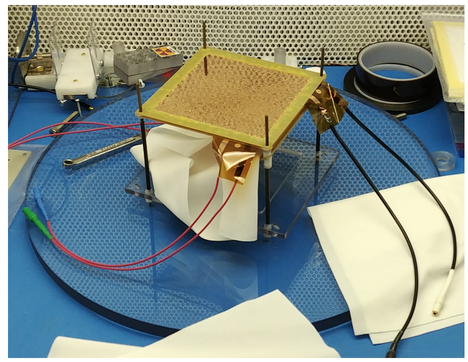

(b) The attachment of the Z-GEM (midde) and GEM1 (top).

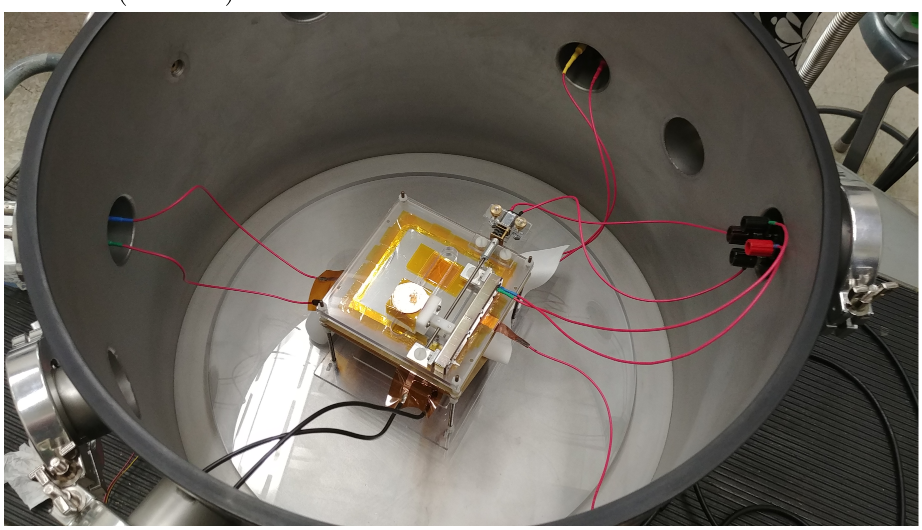

(c) The final Tilted GEM assembly including the alpha calibration structure (top) is placed and wired in the vacuum vessel.

Figure 6.2: The assembly of the Tilted GEM detector.

Once the detector is ready the vessel is pumped out for several days to remove impurities ingassed into the interior detector surfaces. Next, the following back fill and powering procedure is utilized in order to bring the detector to operating pressure and voltage. First, the vessel is flushed with 100-200 Torr CF_4. Once the vessel is pumped back to baseline pressure (minimum baratron pressure reading) the final 100 Torr CF_4 is added to the gas volume. After a few minutes to allow the gas to equilibrate within the detector, the negative ion gas CS_2 is slowly and carefully added to the mixture. Care must be taken with CS_2 since it is toxic. The operating gas mixture utilized through this chapter is 100-50 Torr CF_4-CS_2, which was selected due to its stability and high gas gain.

6.2.1 Signals and Data Acquisition

The signals in this chapter consist of the Z-GEM signal and the U-GEM signal. The Z-GEM signal is read out using an ORTEC 142 charge sensitive preamplifier from the bottom surface of the Z-GEM (facing the U-GEM). Similarly, the U-GEM signal is read out with a separate ORTEC 142 charge sensitive preamplifier from the bottom surface of the U-GEM (facing the acrylic base). Both signals are acquired with the Tektronix TDS 3054C digital oscilloscope and written to text with custom python code I developed.

6.2.2 GEM Powering Schemes

The GEMs are powered through a resistor chain (voltage divider) as depicted in Figure 6.3, where each resistor chain is housed within a dedicated aluminum voltage divider box. Figure 6.3a represents the resistor chain for GEM1, and Figure 6.3b represents the resistor chains for the Z-GEM and the U-GEM. R_1 is a protection resistor, utilized to help prevent damaging the GEM when a spark occurs on or near the GEM. R_2 and R_3 constitute the first and second resistors of the voltage divider. HV refers to the high voltage input, V_{In} is the high voltage output of the box ($V_{In} = HV$), and V_{Out} is the reduced/divided output voltage of the box. The capacitor $C1$ is added between V_{Out} and ground for the Z-GEM and U-GEM resistor chains (Figure 6.3b) in order to suppress the slow, induced ion backflow signal, which will be discussed in Section 6.3.1. Table 6.1 lists the resistor and capacitor values for three different boxes, where each box is numbered for convenience. Box 1 and Box 2 are utilized to power GEM1 and the Z-GEM. Boxes 3 and 4 are two different boxes for powering the U-GEM.

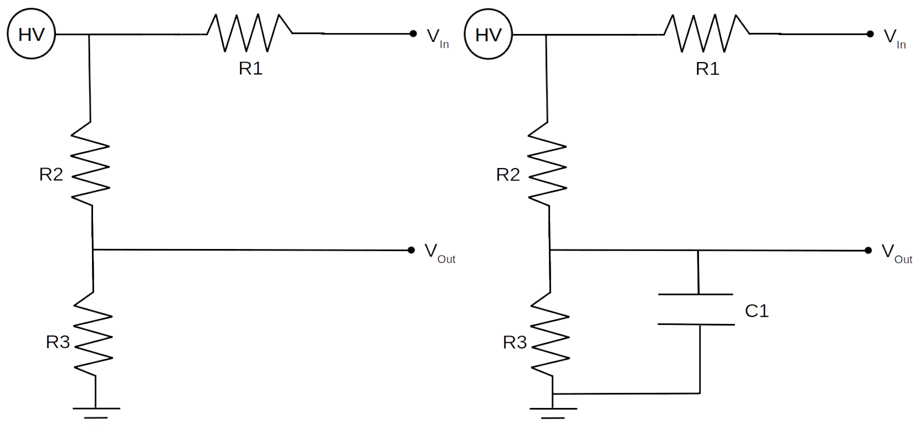

(a) GEM1 (b) Z-GEM and U-GEM

Figure 6.3: GEM powering scheme with voltage dividers.

Voltage Divider Boxes

Box	$R1(M\Omega)$	$R2(M\Omega)$	$R3(M\Omega)$	$C1(nF)$
1	100	14.9	10	-
2	100	56	1	5
3	100	14.9	66.5	5.3
4	100	9.8	55.8	5.3

Table 6.1: Resistor and capacitors utilized for the resistor boxes.

6.3 Working Principle, Track Reconstruction, and Induced Signals

6.3.1 Working Principle

This section describes the working principle of the Tilted GEM. First, consider Figure 6.4 which depicts the coordinate system, several important components of the Tilted GEM, and the passage of a track through these components. Not shown are the cathode or the GEM1. "Top" and "Bottom" refer to the GEM surface nearest to the vessel lid and base respectively. "Vertex" and "Opening" refer to the locations in the transfer region where the Z-GEM and U-GEM approach and diverge respectively.

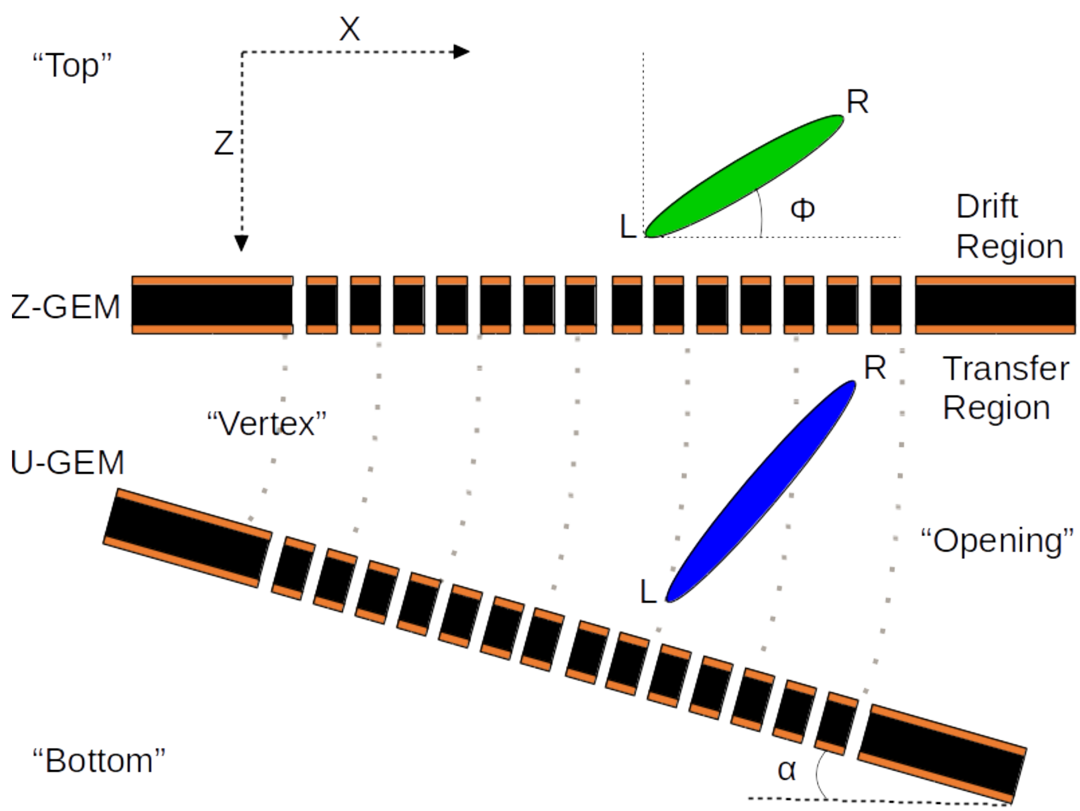

Figure 6.4: Working principle for the Tilted GEM Detector.

Next, consider a particle interaction in the drift region. The interacting particle creates an ionization track (green) that drifts uniformly to the Z-GEM, where the L edge and the R edge refer to the left and right edges of the track. Depending on the angle ϕ the track makes with the X-axis, the L edge or the R edge may arrive at the Z-GEM first. For the case of the green track, the L edge arrives first. At the Z-GEM, the track is amplified and a fraction of the charge is collected on the bottom surface of the Z-GEM. This charge contributes to the primary Z-GEM signal. Figure 6.5 shows the typical Z-GEM (red) and the U-GEM (black) signal for a calibration alpha track. The track edge that arrives first at the Z-GEM corresponds to T_{Z1} and the later edge to T_{Z2}. The charge that is not collected by the bottom surface of the Z-GEM is drawn into the region between the Z-GEM and the U-GEM, which is referred to as the transfer region. This charge is the blue track in Figure 6.4.

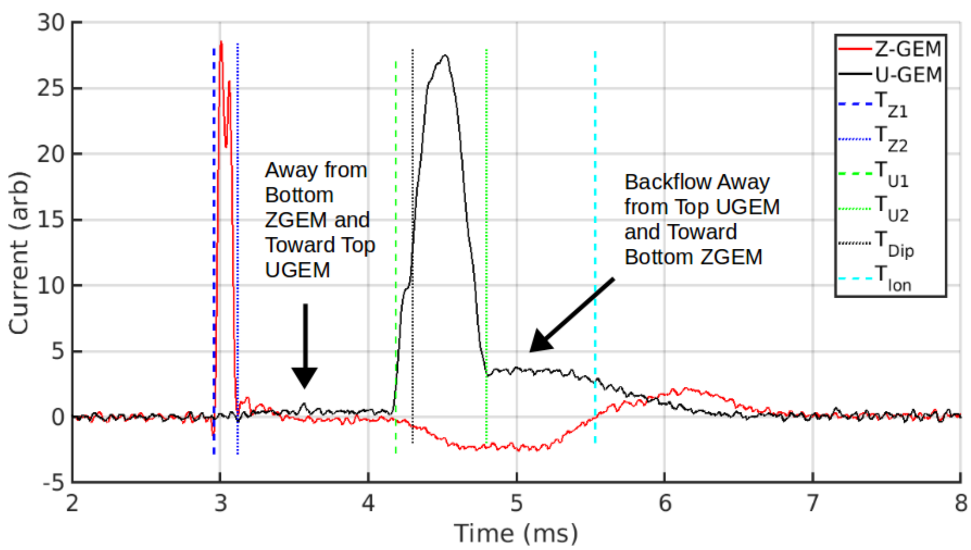

Figure 6.5: Calibration alpha track with the alpha source located close to the opening ($R = 14.5k\Omega$). Current signal for the Z-GEM and U-GEM are red and black respectively. The vertical dashed and dotted lines identify the edges of each signal and the location of the T_{Dip} and T_{Ion}. See Section 6.3.1 for details. The gas pressure is 100-50 Torr CF_4-CS_2.

The transfer field is nonuniform, larger near the vertex than the opening, and the field lines follow a curved path to the U-GEM, where each circular-dotted line in Figure 6.4 represents a field line. The transfer distance, path length traveled by a point charge along each field line, is longer in the opening than in the vertex. As a result, the side of the track closer to the opening drifts more slowly and has a longer distance to travel to the U-GEM than the side of the track closer to the vertex. In the case of the blue track, the L edge drifts more quickly and has a shorter distance to travel to the U-GEM than the R edge. The net effect of this is a monotonically increasing drift time as a function of where a piece of charge arrives at a given X along the Z-GEM. This results in the following one-to-one relationship: the time it takes the L edge (the R edge) of the track to traverse the transfer region corresponds uniquely to the X location of the L edge (the R edge). Therefore, by injecting charge at a know X location and measuring the time it takes the charge to traverse the transfer region the one-to-one relationship can be precisely measured. The procedure to measure the one-to-one function (the detector calibration procedure) is described in detail Section 6.5.3. Once the one-to-one function is measured, the X location of each edge of the track can be extracted, and the full extent of the track along X (ΔX) can be found. Once the track reaches the U-GEM it is amplified and collected on the bottom surface of the U-GEM. This charge constitutes the primary U-GEM signal (black). In Figure 6.5, the first charge arriving at the U-GEM is T_{U1}, and the end of the track arrives at T_{U2}.

The last feature to consider before describing the track reconstruction is the so-called "ion backflow". The ion backflow is the motion of the positive ions created during the track amplification by the U-GEM toward the Z-GEM. The positive ions retrace the field lines traveled by the negative ions back to the Z-GEM. As they do, they induce signals on the Z-GEM and the U-GEM. The arrival time of the first ion at the Z-GEM is called T_{Ion} (cyan). How T_{Ion} is measured from the induced signal on the Z-GEM and its importance is discussed in Section 6.3.2. The time T_{Dip} in the Z-GEM signal corresponds roughly to the start of the induced signal on the Z-GEM as the ion backflow begins to drift to the Z-GEM. In the U-GEM signal T_{Dip} corresponds roughly to when the track reaches the U-GEM and starts to be amplified by the U-GEM. The calculation of T_{Dip} and its usefulness will be discussed in Section 6.3.2.

6.3.2 Track Reconstruction

In this section the procedure for the track reconstruction is discussed. Instead of describing the detector calibration in this section, it will be reserved for Section 6.5.3. This section describes the track reconstruction using the measured one-to-one relationship between the time it takes a charge to traverse the transfer region ΔT_{U-Z} and the X location of the charge (calibration curve). This relationship will be calibrated in Section 6.5.3, but it is utilized here to describe the track reconstruction.

First, ΔZ is reconstructed from the Z-GEM signal by:

$$\Delta Z = (T_{Z2} - T_{Z1})V_{CS_2^-}, \tag{6.1}$$

where $V_{CS_2^-}$ is the drift velocity of CS_2^-, and T_{Z1} and T_{Z2} are the times corresponding to the arrival of the first and the second track edge at the Z-GEM. The ΔX reconstruction requires the detector calibration. A typical calibration curve (black) is shown in Figure 6.6. ΔT_{UL-ZL} and ΔT_{UR-ZR} are the measured times it takes the L edge and the R edge of the track to traverse the transfer region. Ignoring for now the degeneracy which is discussed in the next paragraph, $\Delta T_{UL-ZL} = T_{U1} - T_{Z1}$ and $\Delta T_{UR-ZR} = T_{U2} - T_{Z2}$. Next, the intersection of ΔT_{UL-ZL} and ΔT_{UR-ZR} with the calibration curve are located, and the corresponding X (X_L and X_R) are extracted. Lastly, the extent of the track in X is $\Delta X = X_R - X_L$. Note that ΔX can be negative for track orientations with $X_L > X_R$.

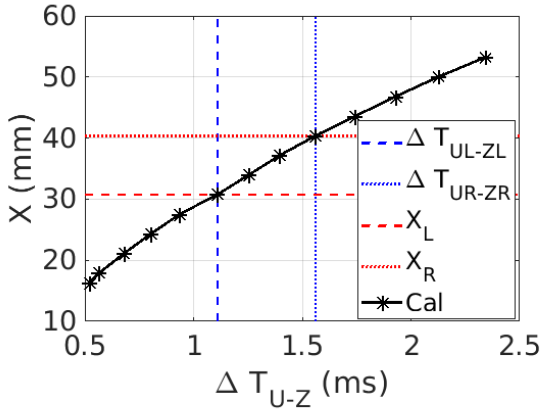

Figure 6.6: A typical calibration curve depicting the ΔX reconstruction with the vertical blue lines and the horizontal red lines. ΔT_{UL-ZL} and ΔT_{UR-ZR} correspond to the time it takes for the L edge and the R edges of the track to traverse the transfer region respectively. X_L and X_R are the extracted X locations corresponding to the L edge and the R edge, and $\Delta X = X_R - X_L$.

Unfortunately, there is a factor complicating the track reconstruction with the Tilted GEM; the track edges that arrive at T_{U1} and at T_{U2} in the U-GEM signal do not always correspond to the same edges T_{Z1} and T_{Z2} in the Z-GEM signal. This is because the nonuniformity of the transfer field and the transfer length causes the arrival ordering of the track edges at the Z-GEM to be reversed at the U-GEM for certain track orientations ϕ. This results in a degeneracy in the reconstructed ΔX. However, the degeneracy was cleverly resolved by Nguyen Phan by considering the ion backflow signal and T_{Ion} [112, 113]. Since T_{Ion} corresponds to the time it takes the first positive ion created at the U-GEM to retrace the transfer field lines and arrive at the Z-GEM, T_{Ion} is roughly the same as the time it took the first negative ion that arrived at the Z-GEM to drift along the same field lines and arrive at the U-GEM. The times are equal if the positive and negative ions have the same drift velocity, which is approximately the case [99]. Consequently, comparing the travel time through the transfer region for the ion backflow ($\Delta T_{Ion-U1} = T_{Ion} - T_{U1}$) with the time $\Delta T_{11} = T_{U1} - T_{Z1}$ and the complementary time $\Delta T_{12} = T_{U1} - T_{Z2}$ the correct ordering is discovered and the degeneracy resolved.

6.3.3 Induced Signals

This section describes the induced signals in the Z-GEM and the U-GEM waveforms by reconsidering Figure 6.5, which shows the waveform for a calibration alpha track near the opening. In our case, positively induced signals occur either when negative charge moves toward or when positive charge drifts away from the readout electrode. The opposite is the case for negatively induced signals. Between the Z-GEM and the U-GEM primary signals (indicated by the left-most arrow), there are induced negative and positive signals on the Z-GEM and U-GEM respectively. They correspond to the track drifting away from the bottom surface of the Z-GEM and to the top surface of the U-GEM. For the Z-GEM it "sees" negative charge moving away, and thus the Z-GEM induced signal is negative. Whereas, for the U-GEM it "sees" negative charge moving toward, and thus the U-GEM induced signal is positive.

The right-most arrow points the the ion backflow signal, where positive ions are drifting away from the U-GEM and toward the Z-GEM. Consequently, the ion backflow induces a negative signal in the Z-GEM and a positive signal in the U-GEM. T_{Dip} is a rough estimation of start of the induced signal in the Z-GEM. The method to find T_{Dip} is discussed in Section 6.4. When the first positive ions reach the bottom surface of the Z-GEM, the slope of the induced signal in the Z-GEM changes because fewer positive charges reside in the transfer region (the "kink" between T_{U2} and T_{Ion}). The Z-GEM signal becomes positive as more positive ions have passed through the Z-GEM and are drifting away from the Z-GEM and toward GEM1. The Z-GEM signal finally goes to zero when the positive ions have all passed through

GEM1, where GEM1 acts to shield the Z-GEM from the ion backflow as it continues to drift toward the cathode. As for the U-GEM, the ion backflow induces a positive shoulder, which similarly to the Z-GEM signal can be flat between T_{U2} and T_{Ion}. The subtle change in the slope of the U-GEM signal preceding T_{Ion} is where the first charges of the ion backflow reach the Z-GEM and begin to leave the transfer region. Once all positive ions have passed through the Z-GEM, the U-GEM signal goes to zero, because the Z-GEM acts to shield the U-GEM from the ion backflow. Notice the U-GEM signal goes to zero before the Z-GEM signal. This is because the Z-GEM continues to "see" the ion backflow as it drifts the small distance to GEM1, which the U-GEM does not "see".

Since the zero-crossing is easier to identify than the slope change (kink), currently T_{Ion} systematically overestimates the time it takes the positive ions to reach the Z-GEM. However, if this overestimation is approximately the same for every event the degeneracy is resolved in the same manner as discussed in Section 6.3.2. In any case, a more precise method to calculate T_{Ion} is discussed in Section 6.7.1. Unfortunately, the induced shoulder in the U-GEM signal makes it difficult to precisely locate the R edge of the primary U-GEM signal. This uncertainty is an issue for track reconstruction, which will become apparent in Section 6.6 for the results of the DD neutron experiment.

6.4 Track Property Algorithm

The track properties are identified with a method similar to Section 3.7. The first and second edges of the Z-GEM and U-GEM signal are located by calculating the quantity $I\frac{dI}{dt}$ and searching for positive-negative peaks in $I\frac{dI}{dt}$. The edge is then found by locating where I falls below 5% of I_{Max}, except for the second edge of the U-GEM signal. Unfortunately, the second edge of the U-GEM signal is blurred by the positive shoulder induced by the ion backflow. In this work the second edge of the U-

GEM signal T_{U2} is estimated to be the location where the slope of the U-GEM signal drops below a fixed threshold; i.e. where the U-GEM signal starts to flatten. Based on the calibration experiments discussed in Section 6.5.3, the uncertainty/jitter in this location results in fluctuations on the order of $\pm 100\ \mu s$. This in turn results in uncertainty/jitter in the ΔX of the track of order $0.5mm$. This is a significant issue, since typical low energy nuclear recoils are a few $mm's$. Potential resolutions to this issue are described in Section 6.7.1. Lastly, T_{Dip} is calculated to be where the slope of the Z-GEM signal falls below a negative threshold. This corresponds roughly with the start of the U-GEM signal, and is meant only as a consistency check with the U-GEM signal.

6.5 Detector Calibration

This section describes how the detector is calibrated. First, consider the alpha source structure above GEM1 in Figure 6.1. The alpha source structure has a rectangular, acrylic base with a 9 cm -10 cm slot drilled through along the X dimension. The ^{210}Po alpha source is placed inside of the alpha source holder, which is allowed to travel along the slot. The holder is moved along the slot with the drive motor and the source translator, which consists of a threaded rod that connects the holder to the drive motor. Depending on the polarity of the power supplied to the drive motor, the drive motor rotates the source translator, which in turn pushes or pulls the holder along the slot. The holder has a contact that touches the potentiometer that runs parallel to the source translator. Therefore, the resistance measured by the potentiometer corresponds uniquely to the location of the holder and thus the precise location of the alpha source along X.

In order to determine the X location of the alpha source from the potentiometer resistance, the potentiometer must be calibrated by precisely mapping the measured X location of the holder (measured with calipers relative to a reference location X_0)

to the corresponding potentiometer resistance. The choice of X_0 is not crucial for this work since it is subtracted away in the difference ($\Delta X = X_L - X_R$). The results of the potentiometer calibration are presented in Section 6.5.1.

Figure 6.1 shows that the emitted alpha particles pass through a narrow collimator, through the slot, through the thin film cathode, into the drift volume, and range out in GEM1. Within the drift volume, the ionization created by the alpha particle extends over the entire drift distance. This means the ΔZ of the track equals the total drift distance ($\Delta Z = 9.7$ cm). Due to the narrow collimation, the alpha tracks are contained within a narrow cone. This results in the tracks being highly directed along Z, where the ΔX of the track are small. In fact, the mean ΔX of the tracks is zero. Consequently, the mean of the distribution of transfer field arrival times (time difference ΔT_{UZ} between the U-GEM and Z-GEM signals) corresponds uniquely to the X location of the alpha source. By measuring the mean transfer field travel time over a range of X locations, the relationship between transfer field travel time and the X location can be mapped out. The results of several alpha calibration experiments are presented in Section 6.5.3. The track reconstruction from the alpha calibration was described in Section 6.3.2.

6.5.1 Potentiometer Calibration

This section presents the results of the potentiometer calibration. Figure 6.7a shows potentiometer resistance R versus the distance from the reference location X_0. The relationship is linear. Consequently, the curve is linearly fit (dotted line), where the fit results are given in the legend. Utilizing the fit, the X location of the alpha source can be calculated from the potentiometer resistance R.

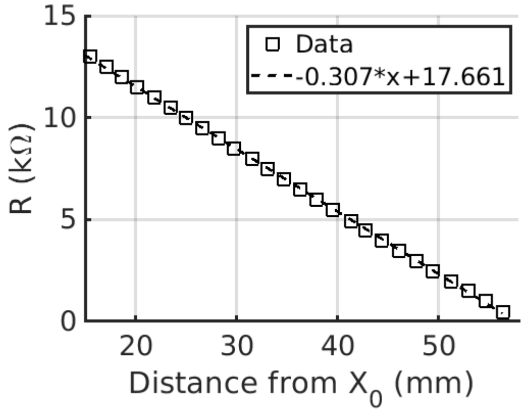

(a) R versus distance from X_0.

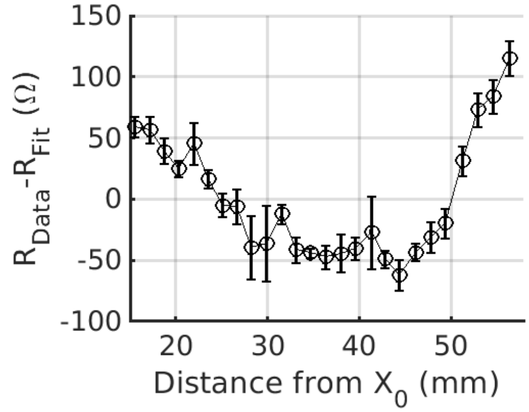

(b) Residual versus distance from X_0.

Figure 6.7: (6.7a) Potentiometer resistance R and (6.7b) Residual ($R_{Data} - R_{Fit}$) versus the distance from the reference location X_0.

Although difficult to see by eye, there is a small periodicity underlying the curve. Figure 6.7b shows the difference between the data and the fit ($R_{Data} - R_{Fit}$) versus distance from X_0. There appears to be two different periodicities; one with a wavelength of $\approx 1\ cm$, and a longer one with a wavelength of $\approx 6\ cm$. The most likely source for the periodicities is the precession of the threaded rod due to the rod not being straight. Nevertheless, the effect is small and should have a negligible effect on the track reconstruction.

6.5.2 Alpha Calibration Waveforms Versus X Location

Before considering the results of the alpha calibration, this section will describe another way to visualize the alpha calibration and the track reconstruction degeneracy. First consider Figure 6.8, which shows signals for typical calibration alpha tracks at three different X locations: $X = 47.8mm$, $28.2mm$, and $11.9mm$ ($R = 3k\Omega$, $9k\Omega$, and $14k\Omega$). The Z-GEM signal and the U-GEM signal are red and black respectively. They show that as the alpha source is moved closer to the vertex (toward smaller X and higher transfer fields), the time difference ΔT_{UZ} between the first edge of the

U-GEM T_{U1} and the first edge of the Z-GEM T_{Z1} decreases.

In order to resolve the track reconstruction degeneracy, consider the ion backflow. Similar to the primary signal, the time T_{Ion} (corresponding to the arrival of the ion backflow at the Z-GEM) decreases as the alpha source is moved closer to the vertex. Comparing $\Delta T_{Ion} = T_{Ion} - T_{U1}$ with $\Delta T_{UZ11} = T_{U1} - T_{Z1}$ and $\Delta T_{UZ12} = T_{U1} - T_{Z2}$, it is clear by eye that ΔT_{Ion} is closer to ΔT_{UZ11} than ΔT_{UZ21}. This indicates the track edge that arrived first at the Z-GEM T_{Z1} corresponds to the edge T_{U1} at the U-GEM, which we know to be the case since the alpha tracks are emitted downward along Z.

Lastly, consider the flat regions and sloped regions of the ion backflow. They are shorter and sharper respectively as the alpha source is moved closer to the vertex. These are the result of the higher transfer field near the vertex, which increases the drift velocity of the positive ions and in turn the rate at which the positive ions leave the transfer region.

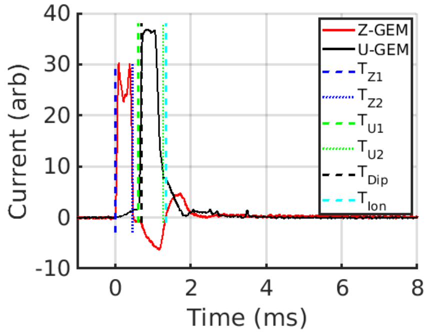

(a) Near vertex at $X = 11.9mm$ ($R = 14k\Omega$).

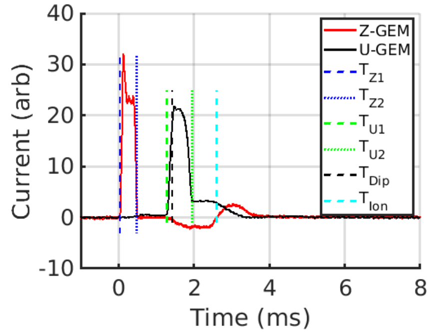

(b) Near middle at $X = 28.2mm$ ($R = 9k\Omega$).

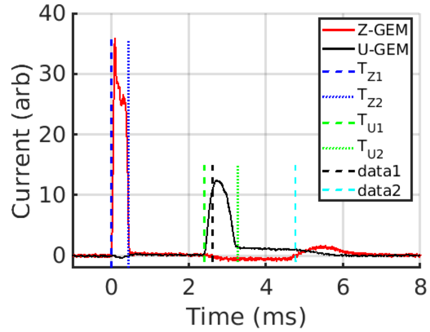

(c) Near opening at $X = 47.8mm$ ($R = 3k\Omega$).

Figure 6.8: Alpha signals at three different X locations. The left edge of the Z-GEM signal is set to $T = 0$. The gas mixture utilized is 100-50 Torr CF_4-CS_2.

If we assume that the mean ΔX's are zero, then $X_L = X_R$ and $\Delta T_{UZ11} = T_{U1} - T_{Z1}$ equals $\Delta T_{UZ22} = T_{U2} - T_{Z2}$. Unfortunately, the distribution of ΔT_{UZ22} is systematically larger and is broader than the distribution of ΔT_{UZ11} at a given alpha source location. This is because the ion backflow signal is blurring the T_{U2} edge of the U-GEM signal. Based on the broadness of the distributions and the location of T_{U2} that would cause $X_R = X_L$, the fluctuations of T_{U2} are on the order of $\pm 100\mu s$. Converting these fluctuations to ΔX with the calibration curve in Figure 6.6 gives fluctuations on the order of $0.5mm$. This is an issue since typical low energy nuclear recoil tracks are a few mm's long. Based on this and the results of the DD neutron generator experiment that will be presented in Section 6.6, in order to take full advantage of the potential of the Tilted GEM concept the improvements that are presented in Section 6.7.1 need to be implemented.

6.5.3 Alpha Calibration

This section presents the alpha calibration experiments for several different powering configurations. Table 6.2 shows the operating voltages for each powering configuration C. ΔV_{G1}, ΔV_Z, and ΔV_U are the voltage differences across GEM1, the Z-GEM, and the U-GEM. ΔV_{UZ} is the voltage difference between the top surface of the U-GEM and the bottom surface of the Z-GEM. Consequently, a large ΔV_{UZ} corresponds to a larger transfer field. The experiments corresponding to configurations $C1$, $C2$, and $C3$ were performed in order to study the behavior of the ion backflow signal and to determine a configuration where the ion backflow is maximized. Recall the ion backflow is important in order to resolve the track reconstruction degeneracy (see Section 6.3.2). "Phan" refers to Nguyen Phan's previous calibration in Ref [112], and "DD" refers to the final/optimal configuration utilized for the DD neutron experiment (discussed in Section 6.6).

C	G1 Box	Z Box	U Box	ΔV_{G1}	$\Delta V_Z(V)$	$\Delta V_{UZ}(V)$	$\Delta V_U(V)$	$E(V/cm)$
C1	1	2	3	360	422	1122	348	914
C2	1	2	3	360	422	1122	348	482
C3	1	2	3	360	452	1137	403	1005
Phan	1	2	3	360	422	1122	348	482
DD	1	2	4	400	437	2488	312	1000

Table 6.2: Powering schemes of several different alpha calibration experiments. C2 and Phan are the same powering configurations, but C2 refers to the implementation of Nguyen Phan's configuration (Phan) in this work.

The calibration curves for each configuration are displayed in Figure 6.9b. The "Phan" calibration is shifted vertically relative to C2, which employs the same powering scheme, because a different X_0 is utilized. Comparing C1 and C2 shows increasing

E_{Drift} has no affect on the calibration. In C3, ΔV_Z and ΔV_U are increased in order to observe their effect on the ion backflow. Ultimately, the ion backflow signal is the largest when ΔV_{UZ} is increased relative to ΔV_U. Based on these results, "DD" is chosen to be the configuration where the ion backflow signal is maximized. For the DD configuration, the calibration alpha signals had a peak voltage greater than $3V$, and ion backflow had a peak voltage of several hundred mV. Unfortunately, maximizing the ion backflow becomes an issue for track reconstruction, where the T_{U2} edge of the U-GEM signal becomes difficult to precisely identify.

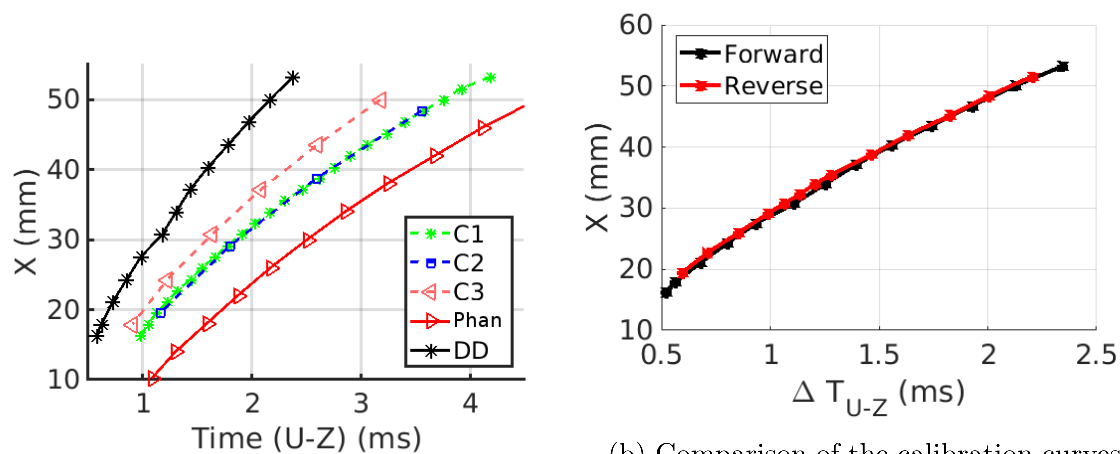

(a) Comparison of the calibration curves for different operating voltages (see Table 6.2).

(b) Comparison of the calibration curves using the DD powering configuration that result from moving the alpha source only away from the vertex (Forward) and toward the vertex (Reverse).

Figure 6.9: Alpha calibration curves (one-to-one relationship) in 100-50 Torr CF_4-CS_2.

As a verification that the effect of the periodicity in the potentiometer calibration is small, we performed an alpha calibration with the alpha source moving only away from the vertex (Forward) and only toward the vertex (Reverse). The result is shown in Figure 6.9b, which verifies the calibration has no systematics resulting from the direction of the calibration.

6.6 Nuclear Recoil Track Reconstruction Experiment

The DD neutron generator is utilized to create neutron induced nuclear recoil tracks preferentially directed away from the interaction plane of the DD generator. For a description of the DD generator see Section 3.4. For this experiment the DD generator is positioned so that the neutrons are directed along the positive x-axis of the detector. The powering configuration is the DD configuration in Table 6.2. This section presents and discusses the results of this DD neutron experiment.

Figure 6.10 shows each of the reconstructed track dimensions versus energy E. First, consider Figure 6.10a, which shows the ΔZ versus E. The vertical band are the electronic recoils, and the horizontal band are the nuclear recoils. It suggests discrimination in 1D down to $\approx 20\ keVee$. Unfortunately, Figure 6.10b shows that ΔX versus E is very poor. As discussed in Section 6.5.2, this is due to the fluctuations/jitter in the T_{U2} edge of the U-GEM signal caused by the induced ion backflow signal on the U-GEM. This results in a jitter in ΔX on the order of $0.5mm$. Consequently, there is little discrimination power in ΔX, because typical low energy nuclear recoil tracks are a few mm. Figure 6.11 shows $R2$ versus E is worse than ΔZ versus E, which should not be the case. Therefore, in order to better reconstruct the track along X, the induced ion backflow signal must be removed from the U-GEM signal while maintaining the ability to measure T_{Ion}. In Section 6.7.1 ideas for achieving this are discussed.

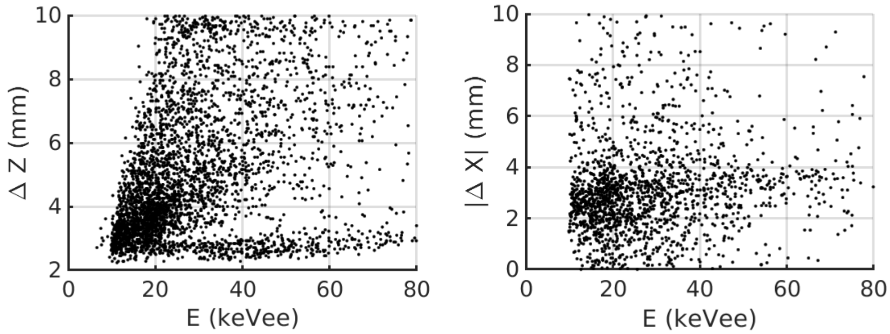

(a) (b)

Figure 6.10: The results of the DD neutron generator experiment in 100-50 Torr CF_4-CS_2. The ΔZ versus E curve (6.10a) shows discrimination down to ≈ 20 $keVee$. Unfortunately, the jitter in ΔX is on the order of 0.5 mm due to the uncertainty in the T_{U2} edge of the U-GEM. Consequently, there is little discrimination power in ΔX (6.10b).

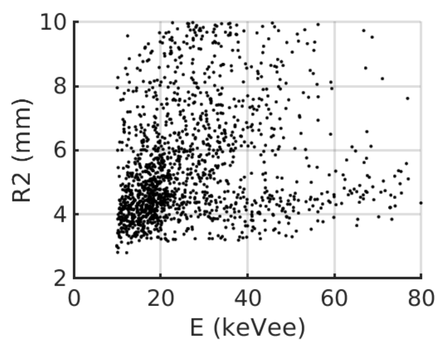

Figure 6.11: The R^2 versus energy for the DD neutron experiment. Unfortunately, these results show no advantage of $R2$ over ΔZ (6.10a), which should not be the case.

6.7 Improvements and Future Work

6.7.1 Resolving Induced Backflow Signal in U-GEM

This section describes future work toward suppressing the signal induced on the U-GEM due the ion backflow. A potential improvement to the detector is depicted in Figure 6.12, where the U-GEM signal is read out with a readout board. The readout board is oriented parallel to the U-GEM so that the field between the U-GEM and the readout board is uniform. The readout board should not "see" the positive ions drifting in the transfer region because: (1) the U-GEM acts as a shield blocking induced signals from the readout board [117, 118]; and (2) the readout board is not an amplification device. Therefore, the positive ions from the avalanche are localized near the GEM and are not seen by the readout board [114, 115, 116]. In fact, this is one of the advantages of the GEM; i.e. the GEM allows the amplification device and the readout device to be separate devices [114]. Consequently, the readout board signal is comprised of negative ions, which should result in sharp, well-defined edges for the U-GEM primary signal and in greatly improved track reconstruction compared to the result presented in this chapter (Section 6.6).

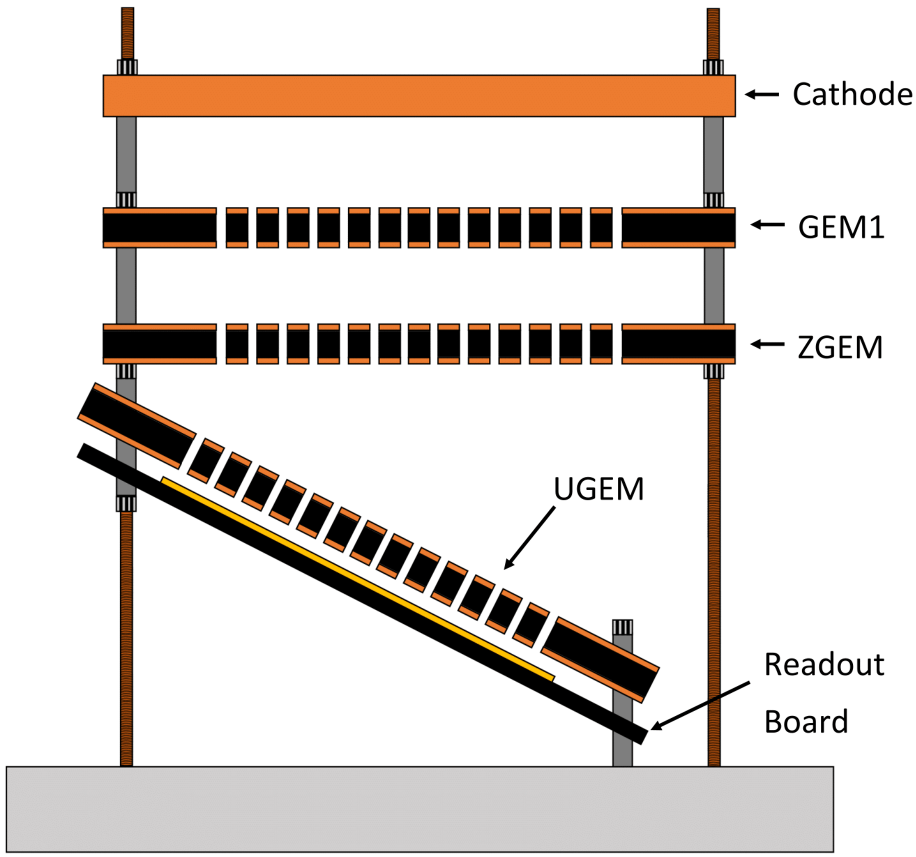

Figure 6.12: Tilted GEM detector with a readout board utilized to readout the U-signal. The readout board is oriented parallel to the U-GEM in order to have a uniform field between the U-GEM and the readout board. The readout board is a potential solution to the ion backflow blurring the U-GEM primary signal, because the readout board should not "see" the ion backflow.

6.7.2 Locating Ion Backflow

The other issue is to effectively and precisely locate T_{Ion} without the need of a large ion backflow. One idea is to read out the induced ion backflow signal from the bottom surface of GEM1. In this way the Z-GEM will act to shield GEM1 from the ion backflow as it drifts in the transfer region. However, when the ion backflow passes through the Z-GEM, GEM1 will "see" the ion backflow as it drifts from the Z-GEM to GEM1. Therefore, since the travel time through the Z-GEM is small compared to the travel time through the transfer region, the time T_{Ion} it takes the ion backflow to reach the Z-GEM is approximately the same as when GEM1 first sees the ion backflow.

We performed a basic test of this idea using the calibration alpha source, and reading out the signals from the bottom of the U-GEM and the bottom of GEM1. Figure 6.13 shows a typical signal from the U-GEM (black) and GEM1 (red). The negative dip at $T = 8.5ms$ corresponds to the primary track as it arrives and is amplified by the Z-GEM. The arrival of the ion backflow at the Z-GEM T_{Ion} corresponds to where the slope of the GEM1 signal suddenly changes from zero to a large negative slope. For this track, this occurs at $T \approx 11.4ms$. Also, notice that between the arrival of the primary track at the Z-GEM ($T = 8.5ms$) and T_{Ion} ($T \approx 11.4ms$) the GEM1 signal is completely flat. This verifies that GEM1 does not see the ion backflow in the transfer region, which makes the identification of T_{Ion} simpler and potentially more reliable and precise than the procedure to measure T_{Ion} utilized in this chapter.

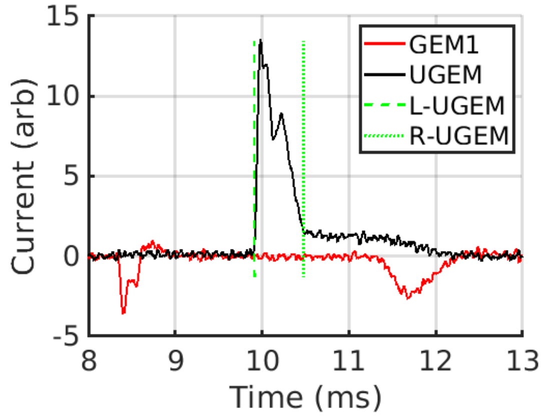

Figure 6.13: A typical calibration alpha track read out with the U-GEM (black) and from the bottom surface of GEM1. The transition from zero slope to negative slope at $T \approx 11.4ms$ corresponds to the arrival of the ion backflow at the Z-GEM (T_{Ion}).

6.8 Conclusion

This chapter presented work toward advancing the track reconstruction with the Tilted GEM detector, which was invented and tested by Nguyen Phan [112, 113]. We optimizing the detector powering configuration in order to maximize the ion backflow signal, which Nguyen Phan realized can be used in order to efficiently remove the degeneracy in the track reconstruction. Unfortunately, we measure the track reconstruction along X (ΔX) very poorly because the ion backflow induces a large signal on the U-GEM, which blurs the primary U-GEM signal and distorts the ΔX track reconstruction.

Therefore, future work is require to discover a way to suppress the induced ion backflow signal in the U-GEM, while maintaining the reliable and precise measurement of the ion backflow arrival time at the Z-GEM (T_{Ion}), which is crucial in order to remove the degeneracy. The following two experimental changes might resolve both issues. The first is to read out the U-GEM signal from a readout board. Since the readout board is not an amplification device, and the U-GEM acts as a shield against the ion backflow motion in the transfer region (similarly as the Z-GEM shielding GEM1 as shown in Figure 6.13), the readout board should not see the ion backflow, and the readout board signals should be well-defined. The second change is to measure T_{Ion} by reading out the bottom surface of GEM1. We demonstrated that the GEM1 signal does not see the ion backflow until it passes through the Z-GEM (see Figure 6.13). Therefore, T_{Ion} corresponds to the location in the GEM1 signal where the signal suddenly dips away from zero. After these improvements to the experiment, the Tilted GEM detector should result in good 2D track reconstruction with only three readout channels (Z-GEM, U-GEM, and GEM1).

Chapter 7

Summary/Conclusions

In this chapter the motivations, results, and conclusions of this work are summarized. The reader is referred to the appropriate chapter for details. The work began with an introduction to dark matter: the evidence for its existence (Section 1.1); the overview of dark matter candidates (Section 1.3), where this work focuses on the Weakly Interacting Massive Particle (WIMP) [26]; the dark matter detection techniques (Section 1.4); and the annual [36] and the daily (sidereal) [37] modulation signals for dark matter (Section 1.4.3). The daily modulation signal, which is the motivation for the R&D performed for this thesis, requires a detector capable of reconstructing nuclear recoil tracks resulting from dark matter interactions.

In Section 1.6 the leading directional dark matter experiment, the Directional Recoil Identification From Tracks (DRIFT) experiment [44, 45, 46, 57], was discussed. The DRIFT experiment is a Negative Ion Time Projection Chamber (NITPC) operated in 30-10-1 Torr CS_2-CF_4-O_2. The CS_2 component of the gas is required for negative ion drift, which results in low diffusion down to the thermal limit [44, 53]. The fluorine in the CF_4 component is the target for spin-dependent (SD) WIMP-nucleon interactions. The O_2 component elicits the production of minority negative ion species required for fiducialization along the drift dimension. The drawback of the multi-component DRIFT gas mixture is the low target mass of the fluorine, needed for SD WIMP interactions, and the toxicity and flammability of the CS_2.

This motivated our group to study SF_6 due to its high fluorine content and negative ion behavior. What was not known was whether gas gain was possible, or whether fiducialization could be made to work. Our studies showed that we could achieve sufficient gas gain using THGEMs in low pressure SF_6, and we discovered that a minority carrier (SF_5^-) is also produced in small quantities, enabling fiducialization [101].

My first project, presented in Chapter 2, was to measure the diffusion in a low pressure SF_6 TPC as a function of pressure, drift field, and drift distance. Besides verifying the thermal drift behavior seen in Ref. [101], a secondary goal was to measure the smearing due to the capture length of the primary electrons and the pitch of the THGEM, which are important to quantify as they impact track reconstruction. The diffusion measurements, summarized in Figure 2.18, indicate the onset of non-thermal behavior at 20 Torr, 30 Torr, and 40 Torr at drift fields of approximately 600 V/cm, 800 V/cm, and 800 V/cm, respectively. Our results for the capture length as a function of the drift field are shown in Figure 2.17, and we measured the smearing due to the THGEM pitch to be $\sigma_{THGEM} = 99\mu m \pm 11\ \mu m$.

In Chapter 3 we presented the first results of directionality and discrimination in a TPC operating with SF_6. Furthermore, to our knowledge these are the first measurements of these quantities using a 1D readout in a TPC. As described in Section 3.4, the DD neutron generator used for these studies also produced a large flux of gamma-rays, which led to a much higher rate of electron recoils than nuclear recoils. This was further compounded by a large dead-time in our data acquisition system. Nevertheless, good discrimination between electron and nuclear recoils and head-tail directionality was demonstrated down to 50 $keVee$.

Although our work with SF_6 demonstrated the promise of this negative ion gas for directional dark matter experiments, fiducialization using the SF_5^- minority peak is hampered by its small size ($\approx 2.5\%$ [101]) relative to the main SF_6^- peak. Consequently, detectors must have good signal-to-noise, otherwise the SF_5^- peak can be easily misidentified and the fiducialization unreliable. This led our group to search for new methods to enhance the production of SF_5^-. It is known that the SF_5^- production increases with electron energy, so we hypothesized that this could be achieved in CF_4-SF_6 gas mixtures with SF_6 in low concentrations. In this case the primary electrons are accelerated to higher energies before they are captured.

Operating a low pressure CF_4-SF_6 TPC with low SF_6 concentration, we made an unexpected discovery of a new negative ion species that is arbitrarily tunable by adjusting the drift field and the SF_6 concentration. In Chapter 4 of this work the characterization of the new species is presented. In Section 4.3, I propose a model for the production of the new species that is hypothesized to be CF_3^-. In Section 4.4, measurements are presented that map out the properties of the new species as a function of drift field and SF_6 concentration. These are shown to be qualitatively consistent with the predictions of the CF_3^- production model. In addition, gas properties such as diffusion and mobility, which are relevant to the use of CF_4-SF_6 gas mixtures in TPCs, are also presented. After this, I focused on the 20-3 Torr CF_4-SF_6 mixture, where the CF_3^- production is 9.8% by charge (see Figure 4.6), the diffusion is low (see Figure 4.12a), and the track lengths are long. In 20-3 Torr CF_4-SF_6 I measured the fiducialization utilizing the CF_3^- peak and the SF_5^- peak (see Section 4.4.8). The results of the fiducialization measurements demonstrate the fiducialization efficiency utilizing the CF_3^- peak is approximately a factor two better than with the SF_5^- peak.

The successful enhancement of the fiducialization efficiency in 20-3 Torr CF_4-SF_6 motivated our group to measure the discrimination and directionality in 20-3 Torr

CF_4-SF_6 utilizing our TPC with a THGEM-based 1D readout. These measurements, shown in Figures 5.8 and 5.14b, indicate discrimination and directionality down to 15 $keVee$ and 20 $keVee$, respectively. For more details see Chapter 5.

The final work in my thesis, presented in Chapter 6, made further studies of directionality and discrimination using a novel 2D readout invented by Nguyen Phan that utilizes timing alone to measure two dimensions of a particle track [112, 113]. The scheme utilizes two thin GEMs where one GEM is tilted along one dimension relative to the other. This results in a non-uniform field between the GEMs and a unique travel time for each location along the tilt dimension as the charges drift between the GEMs. The working principle of the detector is described in more detail in Refs. [112, 113] and in Section 6.3.1 of this thesis. Our measurements in Chapter 6 focus on the track reconstruction with the Tilted GEM for neutron-induced nuclear recoils. Unfortunately, an issue with the experimental setup resulted in poor track reconstruction along the tilt dimension (see Section 6.6). Several improvements to the experiment are discussed in Section 6.7, which should resolve this issue and result in good track reconstruction.

References

[1] K. Garrett, G Duda. *Dark Matter: A Primer*. Advances in Astronomy, Volume 2011, Sep 2010.

[2] Ken Freeman, Geoff McNamara (2006). In Search of Dark Matter. Springer. ISBN 978-0-387-27616-8. "the story of the emergence of the dark matter problem, from the initial 'discovery' of dark matter by Jan Oort" 1.2.1

[3] F. Zwicky, Helvetica Physica Acta, 6, 110, (1933) 1.2.1

[4] de Swart, Jaco; Bertone, Gianfranco; van Dongen, Jeroen (2017). "How dark matter came to matter". Nature Astronomy. 1 (59): 0059. arXiv:1703.00013. 1.2.1

[5] Nerlich, Steve. Could Dark Matter Not Matter? Phys.org, Phys.org, 5 Dec. 2011, phys.org/news/2011-12-dark.html. (document), 1.1

[6] Milgrom, M. (1983). "A modification of the Newtonian dynamics as a possible alternative to the hidden mass hypothesis". Astrophysical Journal. 270: 365370. Bibcode:1983ApJ...270..365M. doi:10.1086/161130. 1.2.1

[7] Clowe, Douglas, et al. A Direct Empirical Proof of the Existence of Dark Matter. The Astrophysical Journal, vol. 648, no. 2, 2006, doi:10.1086/508162. 1.2.2

[8] Lee, Chris. Science-in-Progress: Did the Bullet Cluster Withstand Scrutiny? Ars Technica, 21 Sept. 2017, arstechnica.com/science/2017/09/science-in-progress-did-the-bullet-cluster-withstand-scrutiny/. (document), 1.2

[9] Waynehu. CMB Introduction, background.uchicago.edu/ whu/beginners/ introduction.html. (document), 1.2.3, 1.3

[10] Partridge, R. B. A Measurement of Excess Antenna Temperature at 4080 Mc/s. 3 K: The Cosmic Microwave Background Radiation, pp. 355356., doi:10.1017/cbo9780511525070.010. 1.2.3

[11] Hinshaw, G., et al. Nine-Yearwilkinson Microwave Anisotropy Probe(Wmap) Observations: Cosmological Parameter Results. The Astrophysical Journal Supplement Series, vol. 208, no. 2, 2013, p. 19., doi:10.1088/0067-0049/208/2/19. 1.2.3, 1.4b

[12] NASA, NASA, map.gsfc.nasa.gov/media/121238/index.html. 1.4a

[13] Big Bang Nucleosynthesis, w.astro.berkeley.edu/ mwhite/darkmatter/bbn.html. 1.2.4

[14] Aarseth, Sverre J. Direct Methods for N-Body Simulations. Galactic Dynamics and N-Body Simulations Lecture Notes in Physics, pp. 275312., doi:10.1007/3-540-57983-422. 1.2.4

[15] Popolo, Antonino Del, and Morgan Le Delliou. Small Scale Problems of the CDM Model: A Short Review. Galaxies, vol. 5, no. 1, 2017, p. 17., doi:10.3390/galaxies5010017. 1.2.4

[16] Crittenden, Robert G. Structure Formation in the Universe. Kluwer Academic Publishers, 2001. 1.3

[17] Tisserand, P., et al. Limits on the Macho Content of the Galactic Halo from the EROS-2 Survey of the Magellanic Clouds. Astronomy & Astrophysics, vol. 469, no. 2, 2007, pp. 387404., doi:10.1051/0004-6361:20066017. 1.3

[18] Anonymous. Meetings: WIMP Alternatives Come Out of the Shadows. Physics, American Physical Society, 14 May 2018, physics.aps.org/articles/v11/48. (document), 1.5

[19] Bertone, Gianfranco, et al. Particle Dark Matter: Evidence, Candidates and Constraints. Physics Reports, vol. 405, no. 5-6, 2005, pp. 279390., doi:10.1016/j.physrep.2004.08.031. 1.3

[20] Ellis, John, and Ricardo A. Flores. Elastic Supersymmetric Relic-Nucleus Scattering Revisited. Physics Letters B, vol. 263, no. 2, 1991, pp. 259266., doi:10.1016/0370-2693(91)90597-j.

[21] J. Engel and P. Vogel, Phys. Rev. D 40, 31323135 (1989). 37

[22] P. C. Divari, T. S. Kosmas, J. D. Vergados, and L. D. Skouras, Phys. Rev. C 61, 054612 (2000). 37

[23] M. T. Ressell et al., Phys. Rev. D 48, 55195535 (1993). 37

[24] J. Engel, S. Pittel, E. Ormand, and P. Vogel, Phys. Lett. B 275, 119123 (1992). 33, 37

[25] M. T. Ressell and D. J. Dean, Phys. Rev. C 56, 535546 (1997) 1.4

[26] Bertone, Gianfranco. The Moment of Truth for WIMP Dark Matter. Nature, vol. 468, no. 7322, 2010, pp. 389393., doi:10.1038/nature09509. 1.4

[27] Servant, Graldine, and Tim M.p. Tait. Is the Lightest KaluzaKlein Particle a Viable Dark Matter Candidate? Nuclear Physics B, vol. 650, no. 1-2, 2003, pp. 391419., doi:10.1016/s0550-3213(02)01012-x. 1.4

[28] Axions and Axion-like Particles as Dark Matter. An Introduction to Particle Dark Matter, 2017, pp. 147166., doi:10.1142/97817863400230007. 1.4

[29] Gopalakrishna, Shrihari, et al. Hidden Sector Dark Matter and LHC Signatures. 2010, doi:10.1063/1.3327728. 1.4

1.4

[30] Dodelson, S., and L.m. Widrow. Sterile Neutrinos as Dark Matter. 1993, doi:10.2172/10146636. 1.3.1, 7

[31] Kiryluk, J., and Icecube Collaboration. The Latest Results from the IceCube Experiment. 2012, doi:10.1063/1.3700583. 1.3.2

[32] Cameron, Robert. The Fermi Large Area Telescope: 9 Years of on-Orbit Performance. Proceedings of 7th International Fermi Symposium PoS(IFS2017), 2017, doi:10.22323/1.312.0128. 1.3.3

[33] Fox, Patrick J., et al. Missing Energy Signatures of Dark Matter at the LHC. Physical Review D, vol. 85, no. 5, 2012, doi:10.1103/physrevd.85.056011. 1.3.4

[34] Urquijo, Phillip. Searching for Dark Matter at the Stawell Underground Physics Laboratory. EPJ Web of Conferences, vol. 123, 2016, p. 04002., doi:10.1051/epjconf/201612304002. 1.3.5

[35] Dark Matter Research, www.hep.shef.ac.uk/research/dm/intro.php. 1.4.1

[36] Drukier, Andrzej K., et al. Detecting Cold Dark-Matter Candidates. Physical Review D, vol. 33, no. 12, 1986, pp. 34953508., doi:10.1103/physrevd.33.3495. 1.4.1

[37] Spergel, David N. Motion of the Earth and the Detection of Weakly Interacting Massive Particles. Physical Review D, vol. 37, no. 6, 1988, pp. 13531355., doi:10.1103/physrevd.37.1353. 1.4.2

[38] Naka, Tatsuhiro. Status of Nuclear Emulsion for Directional Dark Matter Search. Proceedings of Identification of Dark Matter 2010 PoS(IDM2010), 2011, doi:10.22323/1.110.0040. (document), 1.4.3, 1.6

[39] Anderson, A. J., et al. Coherent Neutrino Scattering in Dark Matter Detectors. Physical Review D, vol. 84, no. 1, 2011, doi:10.1103/physrevd.84.013008. (document), 1.7

[40] Grothaus, Philipp, et al. Directional Dark Matter Detection beyond the Neutrino Bound. Physical Review D, vol. 90, no. 5, 2014, doi:10.1103/physrevd.90.055018. 1.4.3, 1.4.3, 7

[41] Ruppin, F., et al. Complementarity of Dark Matter Detectors in Light of the Neutrino Background. Physical Review D, vol. 90, no. 8, 2014, doi:10.1103/physrevd.90.083510. 1.4.3, 1.4.3, 1.4.3, 7

1.4.3, 6.1

[42] Marx, Jay N., and David R. Nygren. The Time Projection Chamber. Physics Today, vol. 31, no. 10, 1978, pp. 4653., doi:10.1063/1.2994775. 1.5, 5.5

[43] Hargrove, C. K. The Time Projection Chamber (TPC): An Overview. AIP Conference Proceedings, 1984, doi:10.1063/1.34317. 1.5, 5.5

[44] Snowden-Ifft, D. P., et al. Neutron Recoils In The Drift Detector. The Identification of Dark Matter, 2001, doi:10.1142/97898128113630060. 1.5, 5.5, 6.1

[45] Alner, G.j., et al. The DRIFT-II Dark Matter Detector: Design and Commissioning. Nuclear Instruments and Methods in Physics Research Section A: Accelerators, Spectrometers, Detectors and Associated Equipment, vol. 555, no. 1-2, 2005, pp. 173183., doi:10.1016/j.nima.2005.09.011. 1.4.3, 1.6.2

[46] Battat, J.b.r., et al. First Background-Free Limit from a Directional Dark Matter Experiment: Results from a Fully Fiducialised DRIFT Detector. Physics of the Dark Universe, vol. 9-10, 2015, pp. 17., doi:10.1016/j.dark.2015.06.001. 1.4.3, 1.6.2

[47] S. Burgos, et al., "Studies of neutron detection and backgrounds with the DRIFT-IIa dark matter detector." Astropart. Phys. 28 (2007) 409421. doi.org/10.1016/j.astropartphys.2007.08.007. 1.6, 1.6.1, 2.1, 6.1, 7

[48] J.B.R. Battat, et al., "Radon in the DRIFT-II directional dark matter TPC: emanation, detection and mitigation." J. Instrum. 9 (2014) 11004. doi.org/10.1088/1748-0221/9/11/P11004. arXiv:1407.3938. 1.6, 1.6.2, 2.1, 6.1, 7

[49] J. Brack, et al., "Long-term study of backgrounds in the DRIFT-II directional dark matter experiment." J. Instrum. 9 (2014) arXiv:1307.5525. 1.6, 1.6.3, 1.6.3, 1.6.4, 7

[50] J. Brack, et al., "Background assay and rejection in DRIFT." Phys. Procedia 00 (2014) 17. arXiv:1404.2253. 1.6.3

[51] P.J. Smith, et al., "Simulation studies of neutron shielding, calibration and veto systems for gaseous dark matter detectors." Astroparticle Phys. 22 (2005) 409. 1.6.3

[52] Murphy, Alex, and Sean Paling. The Boulby Mine Underground Science Facility: The Search for Dark Matter, and Beyond. Nuclear Physics News, vol. 22, no. 1, 2012, pp. 1924., doi:10.1080/10619127.2011.629920. 1.6.3, 3.1, 6.1

[53] Martoff, C.j., et al. Suppressing Drift Chamber Diffusion without Magnetic Field. Nuclear Instruments and Methods in Physics Research Section A: Accelerators, Spectrometers, Detectors and Associated Equipment, vol. 440, no. 2, 2000, pp. 355359., doi:10.1016/s0168-9002(99)00955-9. 1.6.3

[54] Snowden-Ifft, D. P., et al. Low Pressure Negative Ion Time Projection Chamber for Dark Matter Search. Physical Review D, vol. 61, no. 10, 2000, doi:10.1103/physrevd.61.101301. 1.6.3

[55] Bednyakov, V. A. Is It Possible to Discover a Dark Matter Particle with an Accelerator? Physics of Particles and Nuclei, vol. 47, no. 5, 2016, pp. 711774., doi:10.1134/s1063779616050026. 1.6, 1.6.3

[56] Directional Recoil Identification from Tracks. Wikipedia, Wikimedia Foundation, 8 Jan. 2019, en.wikipedia.org/wiki/Directional Recoil Identification from Tracks. 1.6.1, 1.6.2, 7

[57] J.B.R. Battat, A.C. Ezeribe, J.*L. Gauvreau,. . . "Low Threshold Results and Limits from the DRIFT Directional Dark Matter Detector" 1.6.2

[58] Weekend Plot: Spin-Dependent Dark Matter. RSONAANCES, resonaances.blogspot.com/2015/01/weekend-plot-spin-dependent-dark-matter.html. (document), 1.8

(document), 1.9, 1.10

[59] Christophorou, L.g., et al. Gas Breakdown and High Voltage Insulating Gases. Special Topics, 1982, pp. 87167., doi:10.1016/b978-0-12-478805-3.50010-2. 1.6, 1.6.4, 7

[60] Coyner, E. C., and D. Hanesian. Electrical Insulating Gases: Hexafluoroethane and Octafluorocyclobutane. Symposium on Electrical Insulating Gases, doi:10.1520/stp44526s. (document), 1.6.4, 1.11

[61] Eisele, K. M. SF_6, a Preferable Etchant for Plasma Etching Silicon. Journal of The Electrochemical Society, vol. 128, no. 1, 1981, p. 123., doi:10.1149/1.2127351. 2.1

[62] Plasma Etching Using SF6 and Chlorine Gases. Microelectronics Reliability, vol. 25, no. 2, 1985, p. 394., doi:10.1016/0026-2714(85)90125-8. 2.1

[63] Gases for Electrical Insulation and Arc Interruption: Possible Present and Future Alternatives to Pure SF/Sub 6/ [Book Review]. IEEE Power Engineering Review, vol. 18, no. 6, 1998, pp. 3131., doi:10.1109/mper.1998.1236737. 2.1

[64] Christophorou, L. G., and J. K. Olthoff. Electron Interactions With SF6. Journal of Physical and Chemical Reference Data, vol. 29, no. 3, 2000, pp. 267330., doi:10.1063/1.1288407. 2.1

[65] Hinkley, David. Bootstrap Methods: Another Look at the Jackknife. Springer Series in Statistics The Science of Bradley Efron, pp. 178206., doi:10.1007/978-0-387-75692-9 9. 2.1

[66] Efron, Bradley, and Robert Tibshirani. The Bootstrap Method for Assessing Statistical Accuracy. 1985, doi:10.21236/ada161257. 2.1

[67] Tibshirani, Robert J. Bootstrap Confidence Intervals. 1984, doi:10.21236/ada147572. 2.6.2, 2.6.2

2.6.2

2.6.2

[68] Scintillation and Inorganic Scintillators. Inorganic Scintillators for Detector Systems Particle Acceleration and Detection, pp. 134., doi:10.1007/3-540-27768-4 3.1

[69] Lecoq, Paul, et al. Scintillation Mechanisms in Inorganic Scintillators. Inorganic Scintillators for Detector Systems Particle Acceleration and Detection, 2016, pp. 125174., doi:10.1007/978-3-319-45522-8 4. 3.1

[70] Pustovot, V I. Effects Connected with Phonon Production in Semiconductors. Soviet Physics Uspekhi, vol. 15, no. 6, 1973, pp. 832833., doi:10.1070/pu1973v015n06abeh005082. 3.1

[71] Nam, Sae Woo. Development of Phonon-Mediated Cryogenic Particle Detectors with Electron and Nuclear Recoil Discrimination. 1998, doi:10.2172/1421523. 3.1

[72] Fermi, Enrico. The Ionization Loss of Energy in Gases and in Condensed Materials. Physical Review, vol. 57, no. 6, 1940, pp. 485493., doi:10.1103/physrev.57.485. 3.1

[73] Halpern, Otto, and Harvey Hall. The Ionization Loss of Energy of Fast Charged Particles in Gases and Condensed Bodies. Physical Review, vol. 73, no. 5, 1948, pp. 477486., doi:10.1103/physrev.73.477. 3.1

[74] Lowry, Ralph A. Measurement of the Ionization Yield of Low Energy Atomic Particles in Gases. doi:10.31274/rtd-180813-14335. 3.1

[75] Sigmund, P. Energy Loss and Ranges of Charged Particles in Matter. Radiation Research, 1975, pp. 278286., doi:10.1016/b978-0-12-523350-7.50030-4. 3.1

[76] Gascon, Jules. Review of Dark Matter Direct Searches. Proceedings of Frontiers of Fundamental Physics 14 PoS(FFP14), 2016, doi:10.22323/1.224.0052. 3.1

[77] Brink, P. L. Review of Dark Matter Direct Detection Using Cryogenic Detectors. Journal of Low Temperature Physics, vol. 167, no. 5-6, 2012, pp. 10481055., doi:10.1007/s10909-012-0517-7. 3.1

[78] Meunier, P., et al. Discrimination between Nuclear Recoils and Electron Recoils by Simultaneous Detection of Phonons and Scintillation Light. Applied Physics Letters, vol. 75, no. 9, 1999, pp. 13351337., doi:10.1063/1.124685. 3.1

[79] Stefano, P. Di, et al. Background Discrimination Capabilities of a Heat and Ionization Germanium Cryogenic Detector. Astroparticle Physics, vol. 14, no. 4, 2001, pp. 329337., doi:10.1016/s0927-6505(00)00127-4. 3.1

[80] Spooner, N.j.c., et al. Demonstration of Nuclear Recoil Discrimination for Low Temperature Dark Matter Detectors, by Measurement of Simultaneous Ionization and Thermal Pulses in Silicon. Physics Letters B, vol. 273, no. 3, 1991, pp. 333337., doi:10.1016/0370-2693(91)91693-p. 3.1

[81] Tsukuda, Masahiro, and Hiroyuki Murakami. Pulse Shape Discrimination Applied to Nuclear Radiation Measurement. Radioisotopes, vol. 21, no. 3, 1972, pp. 186192., doi:10.3769/radioisotopes.21.3 186. 3.1

[82] Edkins, Erin Elisabeth. Detailed Characterization of Nuclear Recoil Pulse Shape Discrimination in the DarkSide-50 Direct Dark Matter Experiment. 2017, doi:10.2172/1354860. 3.1

[83] Arnaboldi, C., et al. A Novel Technique of Particle Identification with Bolometric Detectors. Astroparticle Physics, vol. 34, no. 11, 2011, pp. 797804., doi:10.1016/j.astropartphys.2011.02.006. 3.1

[84] Boulay, M.g., and A. Hime. Technique for Direct Detection of Weakly Interacting Massive Particles Using Scintillation Time Discrimination in Liquid Argon. Astroparticle Physics, vol. 25, no. 3, 2006, pp. 179182., doi:10.1016/j.astropartphys.2005.12.009. 3.1

[85] Hitachi, Akira. Quenching Factor and Electronic LET in a Gas at Low Energy. Journal of Physics: Conference Series, vol. 65, 2007, p. 012013., doi:10.1088/1742-6596/65/1/012013. 3.1, 3.1, 3.1

[86] Hitachi, A., et al. Luminescence Quenching in Liquid Argon under Charged-Particle Impact: Relative Scintillation Yield at Different Linear Energy Transfers. Physical Review B, vol. 46, no. 18, 1992, pp. 1146311470., doi:10.1103/physrevb.46.11463. 3.1, 3.1

[87] Simon, E., et al. SICANE: a Detector Array for the Measurement of Nuclear Recoil Quenching Factors Using a Monoenergetic Neutron Beam. Nuclear Instruments and Methods in Physics Research Section A: Accelerators, Spectrometers, Detectors and Associated Equipment, vol. 507, no. 3, 2003, pp. 643656., doi:10.1016/s0168-9002(03)01438-4. 3.1, 3.1, 3.1

[88] Graichen, J, et al. Efficiency and Directional Effects in the Detection of Low-Energy Recoil Nuclei in a NaI(Tl) Single Crystal. Nuclear Instruments and Methods in Physics Research Section A: Accelerators, Spectrometers, Detectors and Associated Equipment, vol. 485, no. 3, 2002, pp. 774779., doi:10.1016/s0168-9002(01)02103-9. 3.1, 3.1

[89] Akimov, D, et al. Measurements of Scintillation Efficiency and Pulse Shape for Low Energy Recoils in Liquid Xenon. Physics Letters B, vol. 524, no. 3-4, 2002, pp. 245251., doi:10.1016/s0370-2693(01)01411-3. 3.1, 3.1

[90] Collar, J. I. Quenching and Channeling of Nuclear Recoils in NaI(Tl): Implications for Dark-Matter Searches. Physical Review C, vol. 88, no. 3, 2013, doi:10.1103/physrevc.88.035806. 3.1, 3.1

[91] Skewness. Wikipedia, Wikimedia Foundation, 17 June 2019, en.wikipedia.org/wiki/Skewness. (document), 3.2

[92] Luo, Jianwen, et al. SavitzkyGolay Smoothing and Differentiation Filter for Even Number Data. Signal Processing, vol. 85, no. 7, 2005, pp. 14291434., doi:10.1016/j.sigpro.2005.02.002. 3.6.1, 3.6.1

[93] Press, William H., and Saul A. Teukolsky. Savitzky-Golay Smoothing Filters. Computers in Physics, vol. 4, no. 6, 1990, p. 669., doi:10.1063/1.4822961. 3.6.1

[94] Bromba, Manfred U. A., and Horst. Ziegler. Application Hints for Savitzky-Golay Digital Smoothing Filters. Analytical Chemistry, vol. 53, no. 11, 1981, pp. 15831586., doi:10.1021/ac00234a011. 3.6.1

[95] Numerical Differentiation. Wikipedia, Wikimedia Foundation, 14 June 2019, en.wikipedia.org/wiki/Numerical differentiation. 3.6.1

[96] Gaussian Filter. Wikipedia, Wikimedia Foundation, 21 May 2019, en.wikipedia.org/wiki/Gaussian filter. 3.6.1

[97] Dep. Properties of Co-60 Radiation. PTB.de, 29 Mar. 2016, www.ptb.de/cms/en/ptb/fachabteilungen/abt6/fb-62/621-high-energy-photon-and-electron-radiation/gamma-irradiation-facility/properties-of-co-60-radiation.html. 3.4

[98] Phan, N.s., et al. GEM-Based TPC with CCD Imaging for Directional Dark Matter Detection. Astroparticle Physics, vol. 84, 2016, pp. 8296., doi:10.1016/j.astropartphys.2016.08.006. 3.9.2, 4.1, 4.3, 5.4.1

[99] E. Basurto, J. de Urquijo. "Mobility of CF_3^+ in CF_4 , CHF_2^+ in CHF_3 , and C^+ in Ar" Journal of Applied Physics, Vol 91 Num 1, January 2002 (document), 4.10, 4.4.5, 6.3.2

[100] J. de Urquijo, F. B. Yousif. "Negative ion motion in the mixtures of SF_6 with CF_4 and $CH_4 - Ar$" Physical Review E 68, January 2003 (document), 4.3, 4.4.5, 4.8

[101] Nguyen Phan, Randy Lafler, and Dinesh Loomba. "The novel properties of SF6 for directional dark matter experiments". JINST, Dec 2016. (document), 2.1, 2.7.1, 2.7.1, 3.2, 3.4, 3.5, 3.3, 3.4, 3.5, 3.5, 3.8a, 3.8b, 3.8, 3.5, 3.9.3, 4.1, 4.2.1, 4.3, 4.3, 4.4.1, 4.4.2, 4.4.5, 4.4.9, 7

[102] Christophorou, L. G., et al. Electron Interactions with CF4. Journal of Physical and Chemical Reference Data, American Institute of Physics, 30 June 1996, aip.scitation.org/doi/10.1063/1.555986. 4.1, 4.3

[103] Kebarle, Paul, Swapan Chowdhury "Electron Affinities and Electron-Transfer Reactions." Chemical Reviews, vol. 87, no. 3, 1987, pp. 513534., doi:10.1021/cr00079a003. 4.1, 4.3, 4.3, 4.3, 4.4.1

[104] Gennady L. Gutsev, Ludwik Adamowicz. "The structure of the CF4 anion and the electron affinity of the CF4 molecule." The Journal of Chemical Physics 102, 9309 (1995); doi: 10.1063/1.468797 4.1, 4.3

[105] Grimsrud, E. P., et al. Electron Affinity of SF6 and Perfluoromethylcyclohexane. The Unusual Kinetics of Electron Transfer Reactions $A+B=A+B$, Where $A=SF6$ or Perfluorinated CycloAlkanes. The Journal of Chemical Physics, vol. 83, no. 3, 1985, pp. 10591068., doi:10.1063/1.449468. 4.1, 4.3, 4.3

[106] Lotter, Johannes., and Eugen. Illenberger. Electron Capture Induced Reactions in Tetrafluoromethane Clusters. The Journal of Physical Chemistry, vol. 94, no. 26, 1990, pp. 89518956., doi:10.1021/j100389a019. 4.3

[107] Illenberger, Eugen. Electron-Attachment Reactions in Molecular Clusters. Chemical Reviews, vol. 92, no. 7, 1992, pp. 15891609., doi:10.1021/cr00015a006. 4.3

[108] Anderson, Adam J. "A Search for Light Weakly-Interacting Massive Particles with SuperCDMS and Applications to Neutrino Physics. 2015, doi:10.2172/1352057. 5.5

[109] Agnese, R. "New Results from the Search for Low-Mass Weakly Interacting Massive Particles with the CDMS Low Ionization Threshold Experiment." 2016, doi: 10.1103/PhysRevLett.116.071301. 5.5

[110] G. Mazzitelli et al., "A high resolution TPC based on GEM optical readout," 2017 IEEE Nuclear Science Symposium and Medical Imaging Conference (NSS/MIC), Atlanta, GA, 2017, pp. 1-4. doi: 10.1109/NSSMIC.2017.8532631 5.5

[111] "CYGNO: a CYGNUs Collaboration 1 m3 Module with Optical Readout for Directional Dark Matter Search," ISTITUTO NAZIONALE DI FISICA NUCLEARE (INFN-19/2/LNF), 2019, arXiv:1901.04190v1 5.5

[112] Phan, Nguyen. "Extending the Reach of Directional Dark Matter Experiments Through Novel Detector Technologies." Physics & Astronomy ETDs (2016). 2.7.1, 4.1, 4.3, 6.1, 6.3.2, 6.5.3, 6.8, 7

[113] Phan, Nguyen. "Novel Readout Design for Hi-Resolution Tracking TPCs." Cygnus Conference, 2015. 6.1, 6.3.2, 6.8, 7

[114] Sauli, F., et al. Ion Feedback Suppression in Time Projection Chambers. Nuclear Instruments and Methods in Physics Research Section A: Accelerators, Spectrometers, Detectors and Associated Equipment, vol. 560, no. 2, 2006, pp. 269277., doi:10.1016/j.nima.2005.12.239. 6.7.1

[115] Sauli, Fabio. The Gas Electron Multiplier (GEM): Operating Principles and Applications. Nuclear Instruments and Methods in Physics Research Section A: Accelerators, Spectrometers, Detectors and Associated Equipment, vol. 805, 2016, pp. 224., doi:10.1016/j.nima.2015.07.060. 6.7.1

[116] Sauli, F. GEM: A New Concept for Electron Amplification in Gas Detectors. Nuclear Instruments and Methods in Physics Research Section A: Accelerators, Spectrometers, Detectors and Associated Equipment, vol. 386, no. 2-3, 1997, pp. 531534., doi:10.1016/s0168-9002(96)01172-2. 6.7.1

[117] Bondar, A, et al. Further Studies of GEM Performance at Cryogenic Temperatures. Nuclear Instruments and Methods in Physics Research Section A: Accelerators, Spectrometers, Detectors and Associated Equipment, vol. 535, no. 1-2, 2004, pp. 299302., doi:10.1016/s0168-9002(04)01665-1. 6.7.1

[118] Bondar, A., et al. Cryogenic Avalanche Detectors Based on Gas Electron Multipliers. Nuclear Instruments and Methods in Physics Research Section A: Accelerators, Spectrometers, Detectors and Associated Equipment, vol. 524, no. 1-3, 2004, pp. 130141., doi:10.1016/j.nima.2004.01.060. 6.7.1